UNIVERSITÀ
DEGLI STUDI
DI PADOVA

Sede Amministrativa: Università degli Studi di Padova

Dipartimento di Scienze Chimiche

CORSO DI DOTTORATO DI RICERCA IN: Scienza ed Ingegneria dei Materiali e delle Nanostrutture

CICLO XXXII

ENGINEERED PEPTIDES ON GOLD NANOSTRUCTURES FOR CELL TARGETING AS SERRS BIOSENSORS FOR CANCER DIAGNOSTICS

Coordinatore: Ch.mo Prof. Giovanni Mattei

Supervisore: Ch.mo Prof. Marina Gobbo

Co-Supervisore: Ch.mo Prof. Moreno Meneghetti

Dottoranda: Francesca Biscaglia

Table of Contents

Abstract ……...1

Acknowledgments ……...3

Chapter 1: Introduction ……4

An introduction to Nanotechnology ……5

Nanomedicine ……..7

Cancer Nanotechnology ……10

Gold nanoparticles in cancer research ……....15

Localized Surface Plasmon Resonance ……....17

Surface Enhanced Raman Scattering ……...20

Aim of the thesis……24

References ……..28

Chapter 2: Methodologies ……37

Strategies of Peptides Synthesis ……38

Synthesized peptides: peptides for colorectal and liver cancer biosensors ……..43

Strategies of Gold Nanoparticles Synthesis ……..45

Laser Ablation Synthesis in Solution ……46

Synthesis and Characterization of Gold Nanostructures ……...53

Molecular Dynamics calculations ……...58

References ……60

Chapter 3: Engineering of GE11 peptide to enhance EGFR targeting activity of SERRS nanostructures ……67

Results and Discussion ……..70

Experimental Section ……79

Appendix ……....85

References ……..94

Chapter 4: Understanding the efficient $\alpha_v\beta_3$ integrin targeting of SERRS nanostructures functionalized with engineered cyclic RGD peptides ……..….98

Results and Discussion ……101

Experimental Session ……..110

Appendix ……114
References ……...120
Chapter 5: The role of PEG on the targeting activity of SERRS nanostructures……125
Results and Discussion ……128
Experimental Session ……...137
Appendix ……..141
References ……....143
Chapter 6: Stability to proteolysis of SERRS nanostructures engineered with GE11 peptide analogues ……147
Results and Discussion ……150
Experimental Session ……..158
Appendix ……161
References ……...167
Chapter 7: Efficient Liver Cancer Targeting with PreS1 Peptide-Functionalized Gold Nanostructures ……..171
Results and Discussion ……174
Experimental Session ……..181
Appendix ……187
References ……...196
Conclusions ……200
Publications ……203

Abstract

Due to their optical properties, facile surface chemistry and biocompatibility, Gold Nanoparticles (AuNP) have attracted an increasing interest in the last years for Nano-biotechnological applications. Their targeted delivery to malignant tumours, in particular, has become a powerful tool in cancer nanomedicine exploiting AuNP as promising platform for imaging, using for example SERS spectroscopy, diagnosis and therapy. In order to fully exploit their potentialities, AuNP have to be conjugated with active targeting ligands which could improve their pharmacokinetic and pharmacodynamic profiles. Among many targeting agents, such as antibodies, proteins and small molecules, peptides have achieved great success in cancer nanotechnology for their low toxicity and immunogenicity as well as for their relatively low synthetic costs. To achieve an efficient cancer cell targeting a convenient design of the targeting ligands is necessary to optimize the association of the nanostructures with the receptor, reducing the interactions with healthy tissues. However, the effect of the organization of the targeting units on the nanostructures surface has never been studied in detail.

In this PhD thesis the engineering of peptide targeted gold nanostructures, as SERRS biosensors for colorectal and liver cancer diagnostics, is described. The targeting activity of the nanostructures was studied both *in vitro* on cancer cells and *in vivo* on murine tumour models. Experimental results were combined to Molecular Dynamics (MD) calculations and spectroscopic analysis to investigate the role of the peptide organization on the nanostructures surface for the receptor recognition. In Chapter 2 methodologies used to synthesize and characterize peptides as well as gold nanostructures are described. Chapters 3-6 are focused on colorectal cancer targeting achieved by conjugating gold nanostructures with peptides specific for the Epidermal Growth Factor receptor (GE11 peptide) and $\alpha_v\beta_3$ Integrins (RGD peptide), two receptors overexpressed in cancer cells and tissues. In Chapters 3 and 4 the exposure of the targeting units on the nanostructures surface for achieving an efficient association with the receptor is investigated with the help of molecular dynamics. To achieve this goal, several peptide analogues were conveniently synthesized to present the targeting unit in different arrangements on the nanostructure surface and the targeting properties of the resulting nanosystems were assessed. Since among many ligands those engineered by conjugating the peptide to polyethylene glycol (PEG) showed the best targeting activity, the role of the polymer was investigated in dept by studying the targeting activity of nanostructures coated with a mixed monolayer of PEG and peptides (Chapter 5). For in vivo applications of peptide functionalized nanoparticles, the stability to proteolysis of the targeting units is an important issue that was evaluated

by incubation of the nanostructures with different proteolytic enzymes and in serum (Chapter 6). Chapter 7 concerns liver cancer cells targeting achieved by functionalizing gold nanostructures with properly designed analogues of the peptide PreS1, known as specific ligand of the Squamous Cell Carcinoma Antigen 1 which is overexpressed in hepatoma and hepatoblastoma. The arguments developed in the thesis are introduced in the Chapter 1.

Acknowledgments

I would like to thank the Ph.D. School in Science and Engineering of Materials and Nanostructures for the opportunity of developing the research which is reported in this thesis. A special remark to my supervisor Prof. Marina Gobbo, of the BioOrganic Chemistry (BOC) group of the Department, for the support and the ideas which conducted to the successful results. My work developed also in the Nanostructures and Optics Laboratory (NOL) group headed by Prof. Moreno Meneghetti, who supported in particular the realization of the SERRS nanostructures.

The entire work has been possible also thanks to the collaboration of my friends and colleagues Dr. Valentina Piotto, Dr. Lucio Litti and Dr. Simone Sansoni.

For the realization of all experiments with cells special thanks goes to the group of Prof. Patrizia Pontisso of the Department of Medicine, the groups of Prof. Simone Mocellin and Prof. Antonio Rosato of the Department of Surgery Oncology and Gastroenterology of the University of Padova and the group of Prof. F. Rizzolio of the Department of Molecular Sciences and Nanosystems of the University Ca' Foscari in Venezia.

For the realization of the Molecular Dynamics calculations, I would like to thank the group of Prof. Antonio Palleschi of the Department of Chemical Sciences and Technologies of the University of Roma Tor Vergata.

I would also thank all undergraduate students that actively participated in the realization of this project: Dr. Andrea Braga and Dr. Nicole Dal Caso.

Parts of this project were possible only thanks to the collaboration of: Dr. Francesco Boldrin and Dr. Federico Caicci for TEM images (University of Padova, Department of Biology), Dr. Barbara Biondi (University of Padova, Department of Chemical Sciences) for ESI-MS analysis, Prof. Fabrizio Mancin for the possibility of performing DLS and Z-potential measurements in his lab.

Chapter 1: Introduction

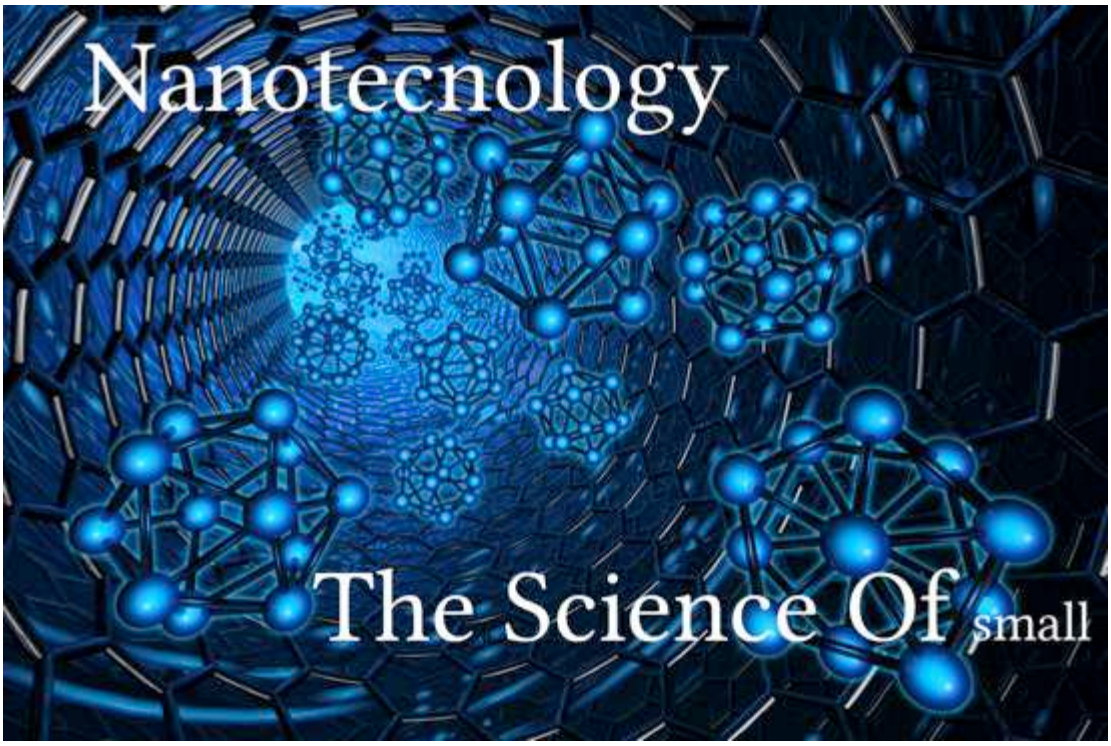

An introduction to Nanotechnology

Nowadays “Nanotech” products are on the worldwide market and are an integral part of our daily routine. Companies manufacturing from different forms of “nano-enabled material” or using “nanotech processes” make up the majority across many industries. As a consequence, “Nanotechnology” is an over-used term in non-scientific contexts and one of the main facing problems of this technology is the confusion about its definition. Richard Feynman first introduced the concept of Nanoscience at an American Physical Society meeting at the California Institute of Technology in 1959. In his lectures, entitled “There’s plenty of a room at the bottom”[1], he described the possibility for scientists to manipulate and control individual atoms and molecules. However, the term “Nanotechnology” was coined in 1974, over a decade later, by Norio Taniguchi of the Tokyo Science University to describe semiconductor processes with a control on the order of nanometres [2]. His definition still stands as the basic statement today: "Nano-technology mainly consists of the processing of separation, consolidation, and deformation of materials by one atom or one molecule”. But, in some sense, Nanoscience is not new. Early examples of nanostructured materials date back to the Pre-modern Era and were based on the empirical knowledge and manipulation, such as the use of high heat, to produce materials with novel properties. The Lycurgus Cup at the British Museum of London (Figure 1) is an example of dichroic glass looking opaque green when lit from outside but translucent red when light shines through the inside. This effect is due to the absorption and scattering of the colloidal gold and silver nanoparticles in the glass.

Figure 1. Lycurgus Cup, 4th Century, British Museum, London

Other examples are “luster” Islamic ceramic glazes and stained-glass windows in European cathedrals (Figure 2) containing metallic nanoparticles. But only after 1981, when Gerd Binnig and Heinrich Rohrer at IBM’s Zurich lab invented the scanning tunnelling microscope (STM)[3], that allows scientist to image surfaces at atomic resolution and to control nanodimensions, Nanotechnology had a huge

growth surge. In the following years, researches at the nanoscale explosive grew leading to the discovery of colloidal semiconductor nanocrystals [4,5] and carbon nanotubes [6,7]. Nanomaterials, at first promising just for semiconductors science, spread in multiple fields and integrated knowledge from chemistry, biology, materials and pharmaceuticals sciences, physics, mathematics and engineering making a meaningful contribution.

Figure 2. Rose window of Notre Dame cathedral, Paris.

Nanomedicine

Nanomedicine is the application of nanotechnology for medical purposes and refers to the use of nanoscale materials for diagnosis, prevention, control and treatment of diseases [8]. Despite a joint definition for various scientific and international regulatory bodies has not been reached yet, commonly "nanomaterial" termed to an engineered material that has at least one dimension in the nanometre range, approximately from 1 to 100 nm. Nanomaterial is therefore a wide term comprising materials of different compositions. Few examples are reported in Figure 3[8].

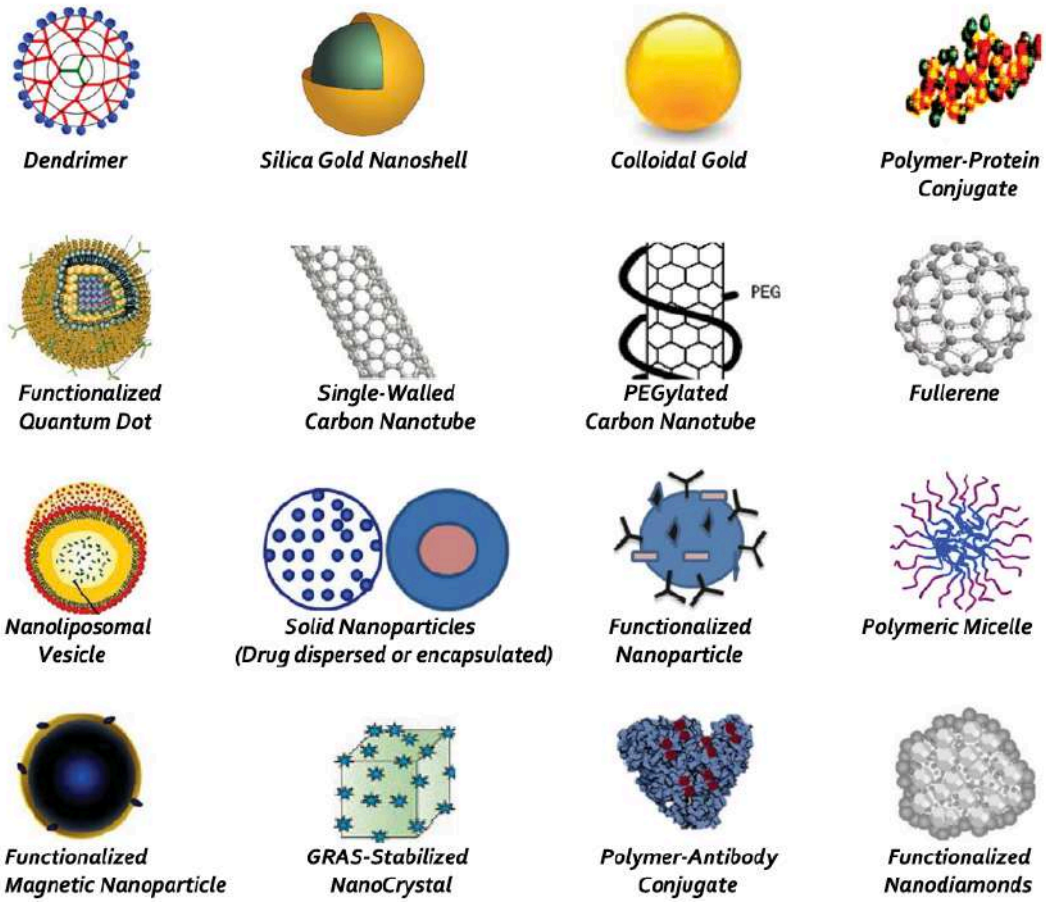

Figure 3. Example of Nanomaterials.

The majority of them are nanoparticles that can be divided in two main groups [9]:

a) Hard nanoparticles, consisting of gold, silver or other noble metals, iron oxide, ceramic and carbon;

b) Soft nanoparticles, including liposomes, micelles, polymers and proteins nanoparticles.

Due to the small size, nanomaterials have a high surface area in relation to volume that increases the particle surface energy making them very reactive and prone to adsorb or be chemically functionalized with several ligands. They can be engineered to have different size, shape, chemical composition and their surface can be rationally designed to address specific purposes, which could be the target of a specific site in the body or the integration of both diagnostic and therapeutic agents. Furthermore, they exhibit optical, magnetic and electrical properties distinctively different from either bulk materials or atoms and that are tuneable with the dimension [10]. Due to these intrinsic properties, nanomaterials create opportunities not available for common medicines or other medical constructs and are consequently expected to satisfy clinical needs unmet to date. For instance, nanomedicine is promising to maximize the drug efficiency by increasing the bioavailability and to reduce unwanted side effects of systemic delivery, if compared to the standard care, by promoting the preferential accumulation in the diseased area within the body. Furthermore, it could improve transport across biological barriers and integrate different biomedical functions on the same construct [11]. Nanomedicine products can be divided in two main groups:

a) Nanopharmaceuticals, which are nanocompounds formulated to treat and prevent diseases by correcting, restoring or modifying physiological functions;

b) Medical devices, that are tools designed to prevent, control, diagnose and treat diseases (e.g. products for in vitro testing and in vivo imaging, medical textiles).

Nanomedicine applies to a vast class of therapeutic indications such as cancer or infections treatments, palliative cares, vitamins and minerals deficiency and so on. Subsequently, it is not surprising that several nanoproducts have been successfully introduced in the clinical practice in the last decades. Figure 4 shows some examples of nanopharmaceuticals that are commercially available in the EU market (Figure 4 [11]). Furthermore, nanomaterials have proved to be useful to understand complex and dynamic disease processes. Despite the large and challenging gap between the preclinical space and the regulatory requirements for clinical applications, ever more novel nanomedicines show great promises. Results are expected in the near future.

Nanomedicine class	Active substance/brand name	Pharmaceutical form	Therapeutic indications
Nanoparticles	*Nab-paclitaxel* Abraxane®	Powder for suspension for infusion	Breast neoplasms Carcinoma non-small-cell lung Pancreatic neoplasma
	Yttrium-90 radiolabelled ibritumomab tiuxetan Zevalin®	Solution for infusion	Follicular Lymphoma
	Glatiramer acetate Copaxone®, Synthon®	Solution for injection	Multiple sclerosis
Liposomes	*Doxorubicin hydrochloride* Caelyx®	Concentrate for solution for infusion	Breast neoplasms Multiple myeloma Ovarian neoplasms Kaposi's sarcoma
	Doxorubicin hydrochloride Myocet®	Powder, dispersion and solvent for concentrate for dispersion for infusion	Metastatic breast cancer
	Amphotericin B AmBisome®	Powder for solution for infusion	Fungal infection
	Daunorubicin DaunoXome®	Concentrate for Solution for Infusion	Advanced HIV-related Kaposi's Sarcoma
	Cytarabine DepoCyte®	Suspension for injection	Lymphomatous meningitis
	Mifamurtide Mepact®	Powder for concentrate for dispersion for infusion	Osteosarcoma
	Morphine DepoDur®	Suspension for injection	Pain
Nanocomplex	*Verteporfin* Visudyne®	Powder for solution for infusion	Degenerative myopia, age-related macular degeneration
	Ferumoxytol Rienso®	Solution for infusion	Iron deficiency anemia in adult patients with chronic kidney disease
	Ferric carboxymaltose Ferinject®	Solution for injection/infusion	Iron deficiency
	Iron(III) isomaltoside Monofer®	Solution for injection/infusion.	Iron deficiency
	Iron(III)-hydroxide dextran complex Ferrosat®	solution for infusion or injection	Iron deficiency
Nanoemulsions	*Cyclosporine* Sandimmun Neoral®	Capsule, soft	Solid organ, bone marrow transplantation Endogenous uveitis Nephrotic syndrome Rheumatoid arthritis Psoriasis Atopic dermatitis
	Pegaspargase Oncaspar®	Solution for injection/infusion.	Acute lymphoblastic leukemia
Nanocrystals	*Paliperidone palmitate* Xeplion®	Prolonged release suspension for injection	Schizophrenia
	Olanzapine pamoate Zypadhera®	Powder and solvent for prolonged release suspension for injection	Schizophrenia
	Aprepitant Emend®	Capsule	Nausea and vomiting
	Fenofibrate Tricor® Lipanthyl® Lipidil®	Tablet	Hiperlipidemia
Polymer-protein conjugates	*Perginterferon ahpha-2b* PegIntron®	Powder and solvent for solution for injection	Chronic hepatitis C
	Perginterferon ahpha-2a Pegasys®	Solution for injection	Chronic hepatitis B and C
	Pegfilgastrim Neulasta®	Solution for injection	Leukopenia by chemotherapy
	Methoxy polyethylene glycol-epoetin beta Mircera®	Solution for injection in pre-filled syringe	Anemia associated with chronic kidney disease
	Certolizumab pegol Cimzia™	Solution for injection	Rheumatoid arthritis
	Pegvisomant Somavert®	Powder and solvent for solution for injection	Acromegaly

Figure 4. Examples of nanopharmaceuticals currently in the EU market.

Cancer Nanotechnology

Despite recent advances in diagnosis and treatment, cancer still remains the major cause of mortality throughout the world. The National Cancer Institute indicates that tumours kill 163.5 for each 10000 individuals every year and that approximately 38.4% of men and women will be diagnosed with cancer at some point during their lifetimes. The number of new cases per year is expected to rise from 14 million estimated in 2012 to 24 million by 2030 (Accessible at *https://www.cancer.gov/about-cancer/understanding/statistics*). Cancer is a general term used to describe more than 100 distinct diseases affecting many different tissues and cells types [12]. Listed in descending order, the most common are breast, lung, prostate, colorectal cancers and melanoma of the skin [13]. All forms are a collection of related diseases characterized by the abnormal growth of cells that begin to divide without stopping and spread into surrounding tissues as a result of hereditary or environmentally induced genetic mutations. Cancer cells show specific features that allow them to grow out of control and became invasive: producing their own growth signals, they are able to ignore growth-inhibition signals and escape from death; they are able to evade the immune system and benefit from it to stay alive; they can sustain angiogenesis inducing nearby normal cells to form blood vessels that supply the tumour with nutrients and oxygen; they can invade other tissues by a process known as metastasis [14]. Currently there are different kinds of methods for cancer diagnostic including laboratory and genetic tests, physical exams and imaging procedures just as much as the types of therapeutic approaches such as surgery, radiotherapy, chemotherapy, immunotherapy, hormone therapy, targeted therapy, stem cells transplant and precision medicine. Although the types of screening and treatment are carefully adjusted on the kind of tumour and the number of the cancer survivors is expected to increase, there is still a long way to fight off this disease. The main reason is that there is still a lack of diagnostic techniques for early stage detection, that is important since when cancer is diagnosed before it causes symptoms it is easier to be treated, and of therapies that are selective against cancer cells and can penetrate into the tumour without damaging healthy tissues. In this scenario, due to the unique chemical, physical and biological features provided by their dimension, the ability to cross wide range biological barriers and the possibility to be loaded with several agents at the same time, nanomaterials have raised as promising alternatives to conventional cares and have made important contributes to oncology over the past several decades (Figure 5 [15]). They can be considered as modern "magic bullet", a concept proposed in 1906 by Paul Ehrlich to describe compounds capable of carrying active molecules towards their targets as well as interacting highly specifically with them [16].

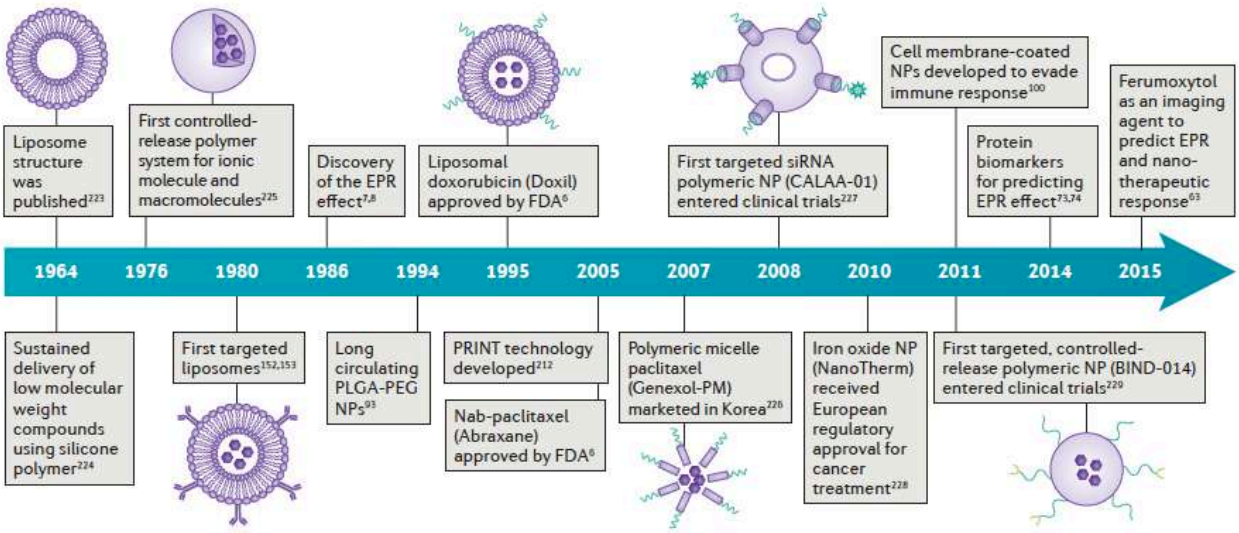

Figure 5. Historical timeline of major developments in the field of cancer nanomedicine.

Food and Drug Administration (FDA) approved the first class of nanoparticles for cancer treatment composed of liposomes (e.g. liposomal doxorubicin Doxil for ovarian cancer and multiple myeloma) and other lipid-based nanomaterials in the 1960s. More than a decade later, nanoparticle albumin-bound paclitaxel (Abraxane) proved to be superior to conventional paclitaxel either in terms of response rate and time of progression for patients with breast cancer and was released to the market. Polymeric micelles or nanoparticles and inorganic nanomaterials form the novel class of cancer nanomedicines. Polymeric micelles paclitaxel (Genexol) for breast and non-small lung cancer and iron oxide nanoparticles (NanoTherm) for thermal treatment of glioblastoma are already commercially available [15].

Most nanomaterials are delivered intravenously for systemic transport to the tumour and preferentially accumulate in that through the enhanced permeability and retention (EPR) effect [17] (Figure 6 [18]). This passive mechanism is generally ascribed to defective tumour vessels, which show branching and leaky walls because of the rapid proliferation of endothelial cells, and defective lymphatic functions. As a result, firstly nanomaterials cross the permeable tumour microvasculature thought the fenestrations of the discontinuous vascular bed and enter into the tumour interstitial space. Secondly, the suppression of the lymphatic drainage causes their retention within the tissue [19]. In turn, nanoparticles properties such as size, shape, surface and composition can influence these processes determining the efficacy of the EPR effect. For instance, the optimal size emerging from many studies is apparently in the range from 20 to 100 nm since nanoparticles smaller than 20 nm rapidly extravasate but scarcely accumulate into the tumour whereas particles larger than 100 nm slowly permeate the tumour vasculature [20]. Negatively- charged nanoparticles demonstrated to be preferable for clinical applications with respect to positive-charged nanoparticles that are responsible of

significant immune reactions [21]. Furthermore, elongated shapes proved to faster extravasate and diffuse more in depth into the tumour than spherical constructs [22]. Unfortunately, there is no obvious dependence between the nanoparticles properties and their delivery systems. Consequently, the differences of the formulation design lead to difficulties in comparing pre-clinical trials. Another reason that complicates the interpretation of pre-clinical studies and causes the failure of a successful nanomaterial in murine tumour models once translated into the clinic lies in the diversity of animals and humans' cancers (e.g. morphology, nature of the microenvironment, metabolic and clearance rate). Since studies on murine models do not provide direct information on human tumour response, physicochemical properties required for an optimal EPR effect in animals could be different from those requested for humans. Diverse types of human cancers show also different predispositions to the EPR effect due to the complex heterogeneity within tumours [22, 23]. A meaningful exploitation of the EPR effect requires, therefore, not only the precise control of the nanomaterial properties but also a full understanding of the inter-cancer's variability. Moreover, several studies demonstrated that nanoparticles are caught by the reticuloendothelial system and, remaining mainly trapped in spleen and liver due to clearance by mononuclear phagocytes, their passive delivery to the tumour is limited [17]. As a conclusion, even though the EPR effect has predominated on the delivery of nanomedicines to tumours in the last decades, it has several and challenging drawbacks that must be resolved.

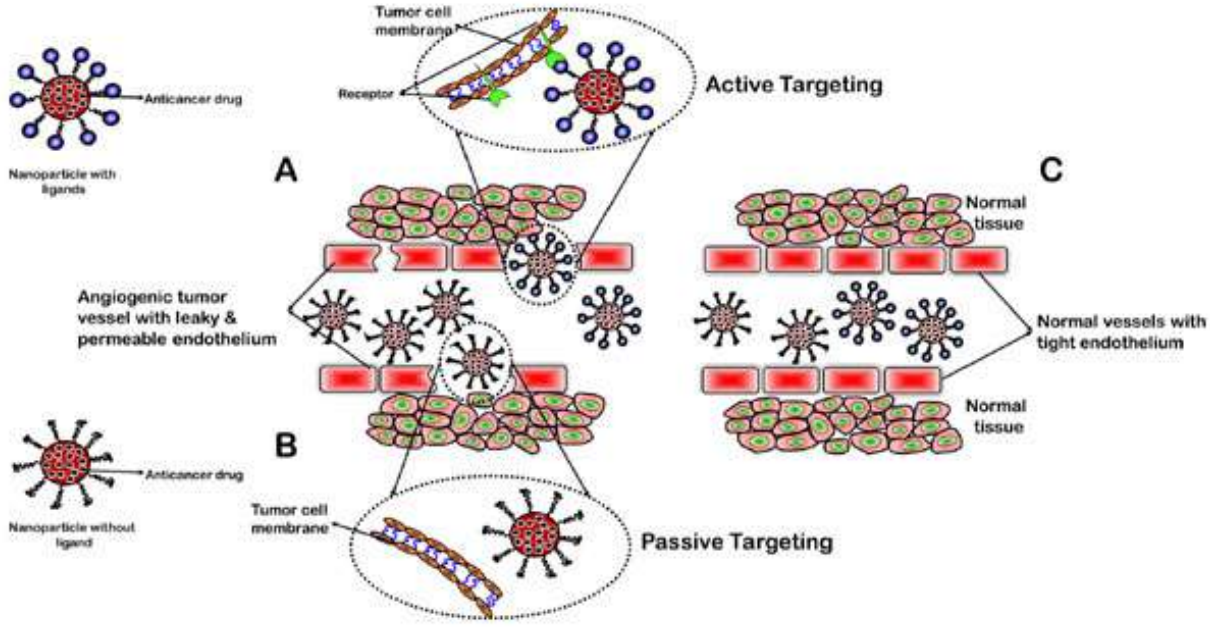

Figure 6. Passive and active delivery of Nanomaterials.

A promising strategy is the active tumour targeting (Figure 6), which should deliver the nanomaterial toward specific diseased sites and, by increasing the affinity for cancer cells, it should extend the retention in the tumour. The fundamental basis behind the active delivery is the recognition of a ligand decorating the nanomaterial surface by its biomarker, which is overexpressed in cancerous tissues, cells or subcellular domains, but represented at low levels in other healthy areas. The recognition process may also trigger the receptor-mediated endocytosis facilitating the uptake of the nanoparticles and the diffusion into the tumour [24]. Representative ligands used to modify the nanomaterial surface include antibodies, proteins, peptides, nucleic acids, sugars, vitamins, aptamers and small molecules. Monoclonal antibodies (Figure 7 [25]) are the most widely used for targeted applications since they have two epitope binding sites on the light chain and on the heavy chain in the fragment antigen-binding (Fab) domain capable of binding the biomarker with high affinity and selectivity.

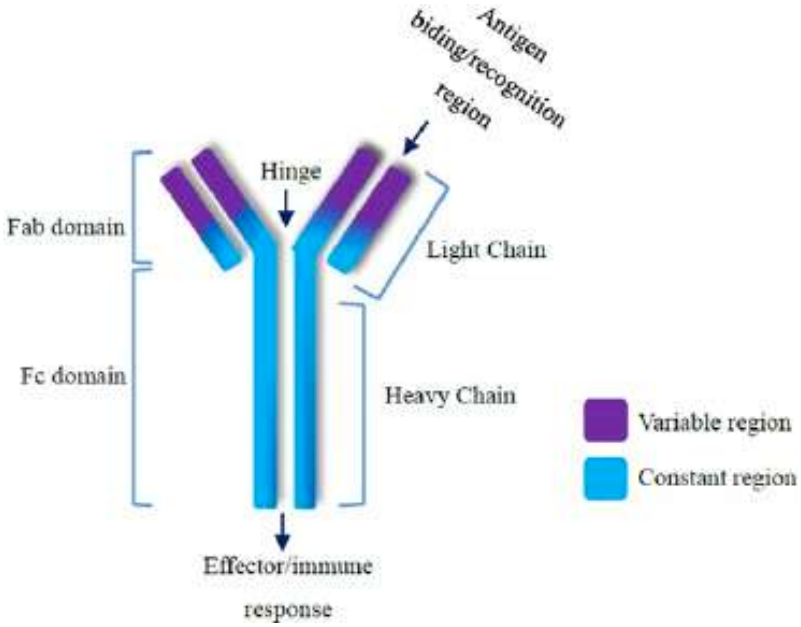

Figure 7. Structure of a monoclonal antibody.

However, the fragment crystallizable (Fc) region is responsible of immune response and, if it is accessible to macrophages, may lead to the accumulation in liver and spleen hampering the targeted delivery [26]. These undesirable effects may be overcome by the use of antibody fragments, which maintain only the variable region of one arm of the antibody, or more recently, with peptides. In addition to a lower immunogenicity, peptides offer other several advantages over antibodies such the room temperature storage, the deeper tissue penetration, the possibility to be produced more cheaply in larger quantities. Furthermore, they are safer since their metabolic cleavage products are less or non-toxic. Over other small molecules, peptides usually show higher affinity and selectivity to the target and a lower toxicity profile [27,28]. However, in spite of these strong points, the widespread use

of peptides is hampered by problems like proteolytic degradation and fast clearance from the body through renal filtration and uptake by the reticuloendothelial system. These drawbacks result in an average half-life in the range from minutes to hours, that is not enough to assure the delivery to the target. In addition, having lower specificity and binding affinity to biomarkers with respect to antibodies, peptides must be engineered not just to limit the enzymatic degradation but also to optimize the receptor recognition process [27]. Despite a number of active targeting nanomaterials proved to be effective in preclinical studies and, in some cases, in early clinical trials, the efficacy of these systems in humans has not been demonstrated overall. This is mainly due to the complex design of these systems, which must be carefully developed. Other reasons are the interactions with physiological proteins that, creating a protein corona around the system, hinder the targeting ligand thus reducing the nanomaterial targeting ability [29].

Gold nanoparticles in cancer research

Gold has ever had a special place in human history because of its chemical inertness and physical properties. Nowadays is the most extensively studied nanomaterial not merely to its unique physical and chemical features but also for its biocompatibility, which is an essential requirement for biomedical applications. Taking into account that every substance can be toxic in high doses, the toxicity of a nanomaterial is strongly influenced by its morphology and surface modification, in addition to concentration. As an example, if on one hand gold nanoparticles smaller than 2 nm are extremely toxic since they can penetrate cells and cellular compartments [30], on the other those larger than 10 nm usually do not induce cytotoxicity and can be safely intravenously administered. Furthermore, escaping the renal filtration, nanoparticles of this dimension show optimal blood retention and for this reason are the favoured for applications in nanomedicine [31]. Several studies also demonstrated that the rather little toxicity observed for these nanosystems is induced by capping agents used as stabilizers and not to the gold core itself, that is inert and non-toxic [32]. Therefore, a suitable surface modification can solve any possible toxicity problem. Because of their facile surface chemistry, gold nanoparticles can be conjugated with different molecules, including unstable drugs or poorly soluble imaging agents that can't be otherwise delivered to the diseased site, allowing simultaneous targeting, diagnostic and therapeutic functionalities. By varying the density of the ligands on the surface, the biomedical activity can be also precisely tuned. Molecules can be attached to the gold surface by a rich variety of functional groups such as thiolate, dithiolate, amine, carboxylate, isothiocyanate and phosphine moieties or by simple physical methods including hydrophobic entrapment and electrostatic adsorption (Figure 8 [33]). The choice depends on the desired liability of the ligand for the specific application. Since the Au-S bond proved to be stable in physiological condition for weeks [34], thiols are usually the preferred anchoring groups for applications, so as the targeting, that do not require the release of the molecule. Gold nanoparticles possess also unique optical and localized plasmon resonance properties useful for the development of ultrasensitive detection and therapeutic techniques. Regarding diagnostic, in addition to the most diffuse imaging modalities exploiting this nanomaterial (e.g. Two-photon Fluorescence imaging [35,36] and Photoacoustic imaging [37,38]), a novel approach based on the Surface Enhanced Raman Scattering (SERS) effect is rising steadily due to the great sensitivity and the possibility to perform multiplexed analysis [39]. SERS effect consists on the enhancement of the Raman signal of a molecule once in close contact with the surface of noble metal nanoparticles and will be discuss in detail in the next following subparagraph. Concerning cancer treatment, the simplest way to use gold nanoparticles is to load them with drugs (e.g. Doxorubicin [40,41], Paclitaxel [42,43]) and to trigger their release in the diseased

area by an external stimulus, like the change of pH and temperature or the presence of enzymes [44].

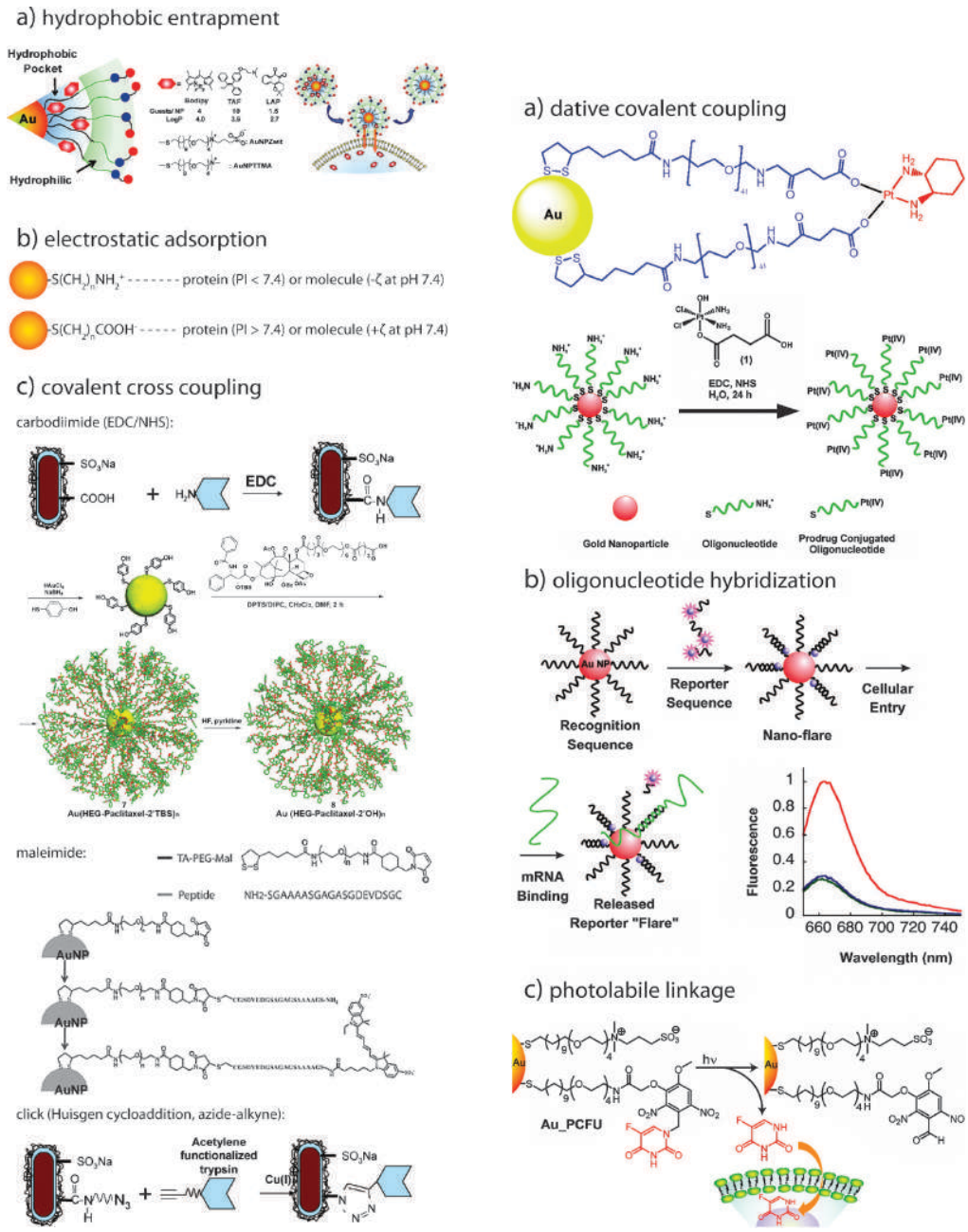

Figure 8. Schematic illustration of methods used for anchoring molecules to gold nanoparticles.

More interesting is Photothermal Therapy. Based on the ability of gold nanoparticles to efficiently convert light into heat if appropriately irradiated with a laser source, this technique allows the highly specific thermal ablation of cells and tissues without damaging healthy ones [45,46]. Finally, the nanoparticles ability to absorb copious amounts of X-ray radiation and to increase the deposition in the tumour tissues can be used to enhance radiotherapy [47,48].

Localized Surface Plasmon Resonance

Materials characterized by a negative real and small positive imaginary dielectric constant show a coherent oscillation of the surface conduction electrons with the electromagnetic radiation, called Surface Plasmon Resonance (SPR). A particular type of SPR is the one possessed by metallic nanoparticles, the Localized Surface Plasmon Resonance (LSPR), which is also responsible of the different properties that nanoparticles own with respect to bulk materials. It can be defined as the collective and resonant oscillation of free electrons in the conduction band of the nanoparticles with the electric field of the radiation and it is generated when the dimension of the nanoparticles is comparable or smaller to the incident wavelength. The term "Localized" refers to the confinement of SPR in the nanoscale region on the particle [49].

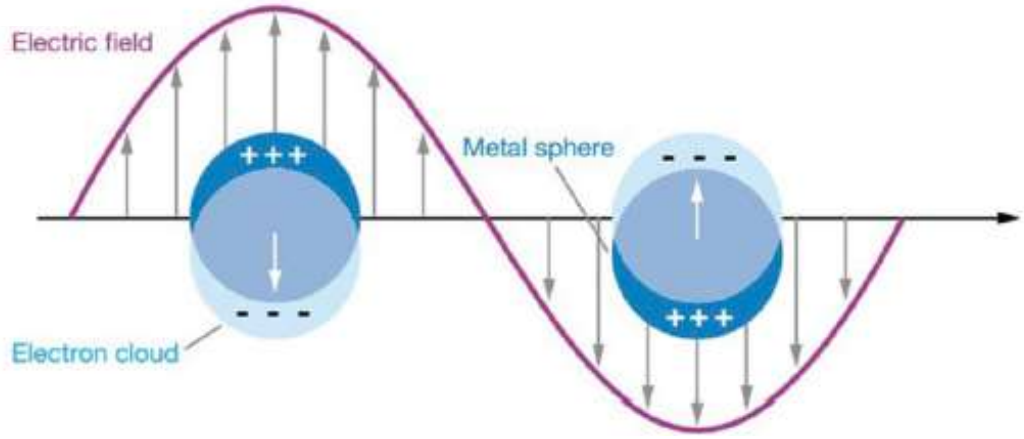

Figure 9. Schematic representation of the Localized Surface Plasmon Resonance (LSPR).

In Figure 9 [50] a schematic representation of the LSPR is shown. The incident electric field induces the polarization of the electrons in the conduction band with respect to the positive charged core of the spherical nanoparticle that, being much heavier, is assumed to be immobile. The movement of the electrons under the influence of the external field induces a net charge difference at the nanoparticle boundaries that, in turn, generates a linear restoring force. As a consequence, a dipolar oscillation of electrons, called Surface Plasmon Oscillation, is created. The term "Surface" arises from the fact that the surface, altering the boundary condition for the polarizability of the metal, determines the plasmon oscillation [51].

The first interpretation of the LSPR was rationalized by Mie in 1908 [52] who demonstrated, by solving the Maxwell's equations for spherical nanoparticles with the appropriate boundary conditions, that the red colour of a colloidal solution of gold nanoparticles arises from the absorption and scattering

of light by the particles contained in it. The Mie's theory is based on two main assumptions:

a) the particle and the surrounding medium are homogeneous and describable by their optical dielectric functions;

b) the radius of the particles is much smaller than the incident wavelength of light.

In these conditions, also called quasi-static approximation, the electric field can be considered constant all along the nanoparticle and the interaction governed by electrostatics rather than electrodynamics. The theory is summarized by the expression of the extinction cross-section σ_{ex} ($\sigma_{ext}= \sigma_{abs} + \sigma_{sca}$= absorption cross-action + scattering cross-section (Equation 1):

$$\sigma_{ext}(\omega) = 9\frac{\omega}{c}\varepsilon_m^{3/2}V\frac{\varepsilon_2(\omega)}{[\varepsilon_1(\omega)+2\varepsilon_m]^2+[\varepsilon_2(\omega)]^2}$$

Equation 1. Expression of the extinction cross-action in Mie's theory.

where ω is the angular frequency of the exciting light, c is the velocity of light, $V=(4/3)\pi R^3$ is the volume of the spherical particle and ε_m and $\varepsilon(\omega)= \varepsilon_1(\omega) + i\varepsilon_2(\omega)$ are, respectively, the dielectric functions of the surrounding medium and of the material itself (real and imaginary part).

When $\varepsilon_1(\omega) =- 2\varepsilon_m$ and ε_2 is small and weakly dependent on ω, the extinction cross-section maximizes reaching the resonant condition [51]. Depending on the dielectric functions, the relevance of the material and of the solvent in determining the position of the localized plasmon is obvious. The resonant condition can be fulfilled only for materials with negative values of the dielectric function. This condition occurs for noble metals in the visible region (e.g. for gold nanoparticles with a diameter of 20 nm the LSPR in water is located at 520 nm). The LSPR is also strongly influenced by the particle's size and shape, the presence of ligands bounded to the surface and the charge of the metal core. As an example, as the size of gold nanoparticles increases (Figure 10 [53]), the LSPR shifts to longer visible wavelengths giving solutions colouring from red to violet. On the contrary, if the size reduces below 5-4 nm, the LSPR decreases in intensity and shifts to shorter wavelength due to quantum size effects, which became predominant for nanoparticles smaller than 2 nm [54].

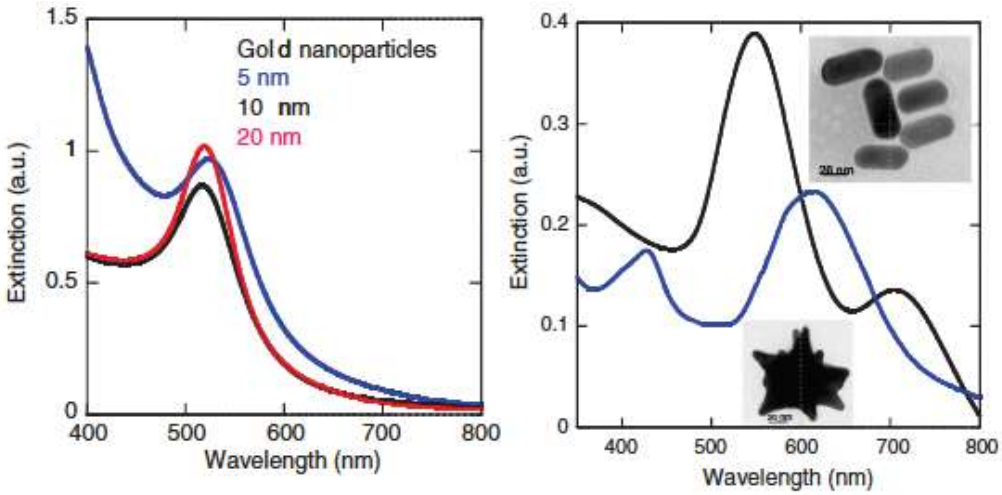

Figure 10. UV-Vis absorption spectra of gold nanoparticles of different size (on the left) and of gold nanorods and nanostars (on the right).

The Mie's theory was complemented by the Gans theory to take into account also non-spherical particles for which the dipole approximation is not valid. In particular, the Mie-Gans theory has been drafted for ellipsoidal nanoparticles showing two plasmon resonances, the longitudinal and the transverse plasmon, referring respectively to the oscillation of electrons along or perpendicular to the major axes of the ellipse. This results in two different maximums of absorption in the spectrum, one red-shifted and broader and the other identical to that of spherical nanoparticles (Figure 10). If the morphology of the nanoparticle becomes more asymmetric, multiple plasmon bands form causing a more pronounced broadening and red- shifting of the LSPR [55] (Figure 10). An even more complicated extinction spectrum is that of aggregated gold nanoparticles that typically shows the conventional plasmon resonance of a single spherical nanoparticle and a novel red-shifted broaden maximum resulting from interparticle interactions (Figure 11 [56]).

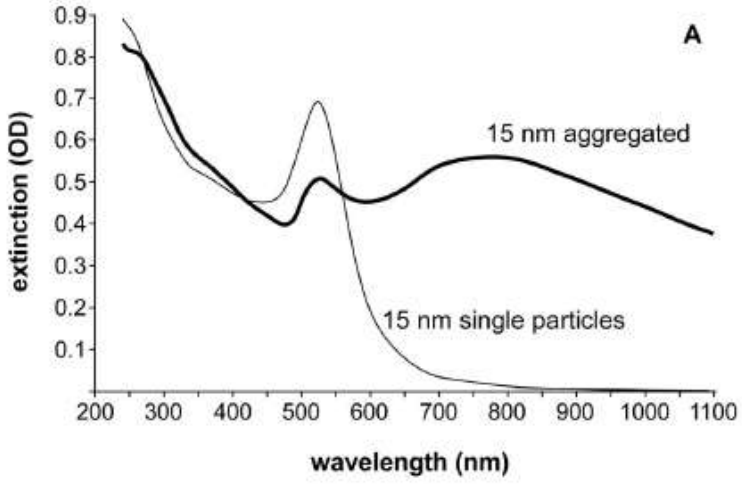

Figure 11. Spectral extinction shift upon aggregation of gold nanoparticles of 15 nm.

This can be ascribed to the electronic coupling between the nanoparticles in the aggregates that causes the red-shifting and the broadening of the longitudinal plasmon resonance. The spectrum is also strongly influenced by the size and shape of the aggregates.
LSPR properties also allow the intense plasmon-assisted scattering of molecules on or nearby noble metal surfaces, a phenomenon that is the base of the Surface Enhanced Raman Scattering spectroscopic technique.

Surface Enhanced Raman Scattering

Surface Enhanced Raman Scattering (SERS) is a phenomenon first observed in 1973 by M. Fleischmann [57], but correctly interpreted only in 1977 by D. L. Jeanmaire and R. P. Van Duyne [58], when the spontaneous Raman signal of adsorbed pyridine was measured at a roughened silver electrode. Since Raman signals are usually weak, even in resonant condition, because of the low Raman cross-section, it was of great excitement that the intensities could be amplified several orders of magnitude by simply absorbing the molecule on the metallic surface. Requiring depth knowledge of optics and lasers at that time, SERS was initially employed by a relatively small community of scientists but, from the year 1977, when a single molecule was observed [59,60] and the potentialities over the most common fluorescence spectroscopy emerged, SERS had a bootstrap. Nowadays it is known that the signal intensities can be enhanced up to factors of 10^{14}–10^{15} over spontaneous Raman signals and SERS is employed in numerous multidisciplinary approaches.
The Enhancement Factor (EF, Equation 2) describes the experimental evaluation of the overall enhancement of the Raman bands:

$$EF = \frac{I_{SERS}/N_{surface}}{I_{RFM}/N_{bulk}}$$

Equation 2. Expression of the Enhancement Factor.

where I_{SERS} and $N_{surface}$ are, respectively, the intensity of the Raman spectra and the number of molecules in the excitation volume on the metal surface. I_{RFM} and N_{bulk} are the Raman signal intensity for the free molecule and the number of molecules in the excitation volume in the bulk, respectively [61]. Despite several mechanisms contributes to this equation, the amplification of the Raman signal can be ascribed to two main effects: the electromagnetic (EM) field enhancement, that gives the greatest contribution to the overall signal amplification, and the chemical enhancement. The EM mechanism relies on plasmonic properties of nanoparticles: upon excitation of the LSPR, particles

emit their own dipole field increasing the electromagnetic field strength of the incident radiation. As a consequence, when the enhanced radiation excites the molecule nearby the nanoparticle surface, the scattered field from the molecule is increased by the nanoparticle as well [62]. Equation 3 [61] describes the total EM enhancement (G_{SERS}):

$$G_{SERS} \approx \left|\frac{E_{loc}}{E_0}\right|^4 = \left|\frac{\varepsilon_m - \varepsilon_s}{\varepsilon_m + 2\varepsilon_s}\right|^4 \left(\frac{R}{R+d}\right)^{12}$$

Equation 3. Expression of the EM Enhancement.

where E_{loc} and E_0 are respectively the amplitude of the local and of the incident field. ε_m is the dielectric constant of the metal spherical nanoparticle and ε_s is the permittivity of the surrounding medium. R is the nanoparticles radius and d is the distance of the molecule from the metal surface. Equation 3 suggests that theoretically the highest EM enhancement occurs when $\varepsilon_m=2\varepsilon_s$. This suggests that excitation of the LSPR of the nanoparticles produces the largest enhancements. Since noble metal nanoparticles show LSPR in the visible range, most common lasers are suitable sources to achieve huge Raman signals. Other parameters like irradiation time, number of acquired spectra and laser power can also be tuned to optimize the EM enhancement. The size and the shape of the nanoparticle also strongly affect the EM mechanisms. Typically, the hugest EM for silver and gold spherical nanoparticles is observed in the radius range of 40-60 nm since, when the size of the particles increases, scattering contributions increase and, as a result, the nanoparticle show a weakening of the electromagnetic field on its surface with a consequent lowering of the EM enhancement [63, 64].

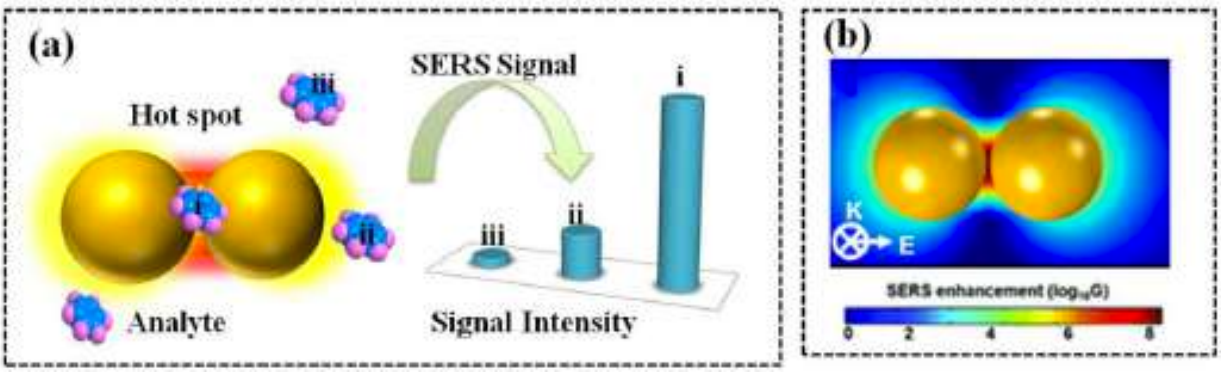

Figure 12. (a) Schematic representation of hot spots between two nanoparticles and corresponding SERS intensity; (b) SERS enhancement of 2 nm gapped gold nanoparticles dimer in water.

The effect of the shape on the EM mechanisms is more pronounced than that of the size. For instance, anisotropic nanostructures show highly enhanced field strengths located at sharp edges or vertices that rapidly drop off with the distance from the surface. This is due to the higher curvature and smaller effective radius in these specific locations, named Hot Spots. In addition to sharp tips and vertices in single nanostructures, Hot Spots can be also found in the junctions between metal nanoparticles aggregated or in close contact (Figure 12 [65]). In this case the extreme field enhancement origins from the constructive coupling of localized surface plasmons which leads to the increase of induced dipole magnitude that, in turn, causes the amplification of the polarization [66-68].

When the molecule is absorbed or chemically bonded to metal nanoparticles undergoes electronic coupling that lead to resonances in the Raman cross-section with new contributions to the enhancement. The electronic coupling with the surface underlies the Chemical Enhancement (CE) mechanism [69-71]. As illustrated in Figure 13 [61], four inter-related processes contribute to the CE: a) the increase of the polarizability of the molecule once absorbed on the nanoparticle surface; b) charge transfer resonance of the molecule-metal complex; c) Raman resonance scattering; d) Plasmon resonance scattering. The most attractive way is the charge transfer between the adsorbed molecule and the metal surface: the chemisorption of the molecules on the surface induces the formation of new molecular electronic accessible states that, serving as resonant intermediate states, lead to the increase of the signal intensity. Requiring the close contact between the molecule and the surface, the CE is a short-range effect and, compared to EM, is weaker. The enhancement is in the order of 10^2-10^3.

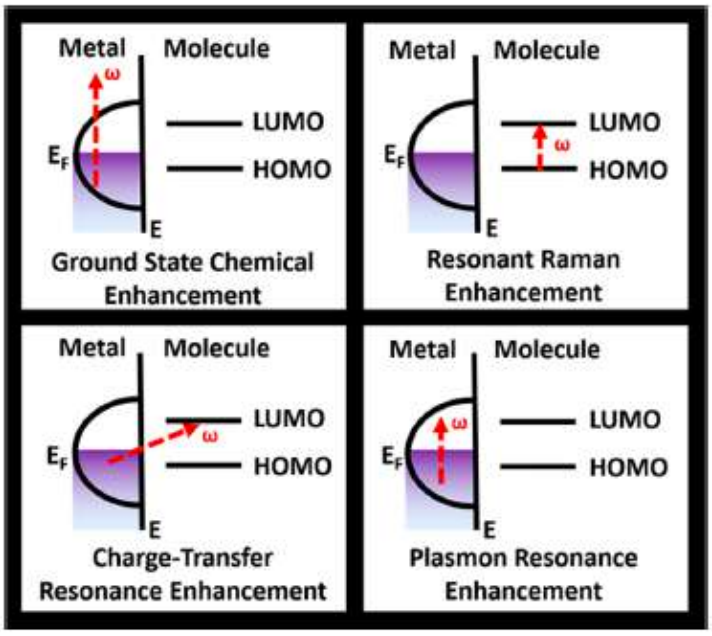

Figure 13. Schematic mechanisms of the four inter-related processes contributing to CE.

In SERS spectroscopy the molecule adsorbed on the metal surface is the prefixed analyte and it is called SERS label (or SERS reporter). It could be a drug, a contaminant, a chromophore et cetera. In any case, to be a suitable reporter, it should own specific features: a) high Raman cross section; b) peak pattern simplicity to allow multiplexed experiments; c) stability to laser light; d) ability to bind the metal surface. Showing stronger SERS signals due to the major polarizability induced by molecular vibrations, conjugated molecules like Malachite Green, Cyanine Dyes, Nile Blue and Texas Red are usually preferred to unconjugated ones [72]. To further increase the SERS response of the label, two main strategies can be also exploited. The first is the invoking of the Surface Enhanced Resonance Raman Scattering (SERRS) by using "resonant" molecules as SERS reporter, namely molecules with an electronic transition energy that overlaps the LSPR energy [73]. The second is the formation of strong bonds between the label and the surface [74]. Besides, preventing the molecules desorption from the substrate, the formation of the ligand-metal bond generates metal-to-ligand or ligand-to-metal charge transfer that contributes to the CE enhancement. Furthermore, the EM enhancement increases since electromagnetic fields are greater when the molecule is anchored to the surface [70].

Raman spectrum can provide rich information about the analyte molecule and, exploiting SERS, it is possible to detect very low concentrations. This fosters the application of SERS spectroscopy in various fields including trace chemical [75,76], food additives [77] and explosives detection [78]. There is also a considerable interest in SERS for biomedical purposes since, besides being a non-destructive method with simple or no preparation of the sample, it is highly effective in the near-infrared (NIR) where light attenuation and autofluorescence from tissues are low. Furthermore, SERS spectroscopy offers several distinct advantages over other spectroscopic techniques. In contrast to IR spectroscopy, it allows the detection of fine spectral details of biomarkers and biomolecules in living cells or in physiological fluids without the interference of vibrational peaks of water [79]. Possessing single molecule sensitivity, Raman scattering is comparable or more sensitive than Fluorescence spectroscopy, on which most of the biological assays are based [79]. Compared to fluorescence ones, SERS signals are also more stable against photodegradation and photobleaching due to the faster relaxation of the excited states [80]. Moreover, since Raman peaks show narrow spectral width of 1-2 nm, nanostructures labelled with various molecules can be designed for the simultaneous excitation using the same wavelength. This allows multiplexed analysis obtaining, on a single spectrum, information coming from different reporters easily distinguishable in their fingerprint region. This approach is not possible in the case of fluorescence as only a finite number of dyes can be simultaneously employed due to the overlap of their broad bands [39].

Aim of the thesis

The aim of this PhD project is to engineer gold nanostructures to be used as SERRS biosensors for colorectal and liver cancer diagnostics by functionalization with peptides, as specific ligands of tumor associated receptors. Therefore, a deep knowledge of colorectal and liver cancers, as well as a careful study of the state of art regarding receptors and ligands involved in these diseases, are necessary to take the first step of this work: the choice of the tumor targeting peptides. Subsequently, a general overview of colorectal and liver cancers, followed by the selection of the targeting ligands, is emphasized.

Colorectal cancer (CRC) is the third most commonly occurring cancer in men and the second in women. In 2018 over 1.8 million of new cases were estimated (*Accessible at www.wcrf.org*). Comparing cancer statistics in more and less developed countries, the strong evidence that the tumours widespread is related to the Western lifestyles emerges [81,82]. Smoking and consuming of processed meat and alcoholic drinks in association with overweight and physical inactivity are the stronger cancer risks whereas the changing of foods habits embedding wholegrain, fibres, dairy products and calcium supplements proved to reduce this burden [83,84]. Epidemiological studies also suggest that the risk of CRC in a first-degree relative increases an individual's lifetime risk [85]. Death from CRC can be prevented by detecting the disease in the early stage and several effective, safe and relatively inexpensive screening methods, including Faecal Occult Blood Testing, Flexible Sigmoidoscopy and Colonoscopy Screening, are currently available [86]. However, to reduce potential harms and imperfect acceptability to patients and to improve the accuracy of the early stage detection, novel and individualized to patients screening tests must be introduced into the routine clinical practice. A promising approach is the detection of biomarkers such as proteins, cytological, DNA and mRNA markers in blood specimens or on tumour tissues [87,88]. Among them, Integrins and the Epidermal Growth Factor receptor (EGFR) have attracted much attention for CRC targeted diagnostic and therapy.

EGFR is a cell-surface receptor belonging to the ErbB family of tyrosine kinase overexpressed in colorectal tumours, so as in many other cancers having epithelial origin. It is involved in cancerous cell proliferation and survival in malignant states [89]. Various endogenous ligands bind EGFR leading to the autophosphorylation of the intracellular domain that, in turn, activates multiple signalling pathways modulating cell responses and inducing cellular growth, angiogenesis and metastasis [89]. Examples of these ligands are the Epidermal Growth Factor (EGF) [90], betacellulin [91], epigen [92] and heparin binding EGF [93]. In the last decade novel therapeutic and diagnostic agents able to target EGFR and compete with endogenous ligands inhibiting or non-activating the downstream signalling

have been designed with remarkable results. The most exploited and promising are monoclonal antibodies (e.g. Cetuximab [94], Panitumumab [95]), small Tyrosine Kinases molecules [96] and peptides (e.g. D-K6L9 [97], GE11 [98]).

Integrins are a family of adhesion receptors for the extracellular matrix playing important roles in different physiological processes such as inflammation, regulation of cell growth, cell migration and angiogenesis [99,100]. Among different integrins, the $\alpha_v\beta_3$ integrin has attracted much attention for CRC targeted nanomedicine since its up-regulation is associated with increased cell invasion and metastasis [101]. Moreover, an abnormal expression is usually found in patients who have metastatic disease [102]. Integrins $\alpha_v\beta_3$ are recognized by several proteins such as vitronectin, fibronectin and fibrinogen and various agents containing the tripeptide sequence Arg-Gly-Asp (RGD) [99, 103] such as the cycloRGD peptide [102]. Many of them are currently in clinical trials for cancer treatment since are promising as potential inhibitors of tumour growth as well as tumour angiogenesis [104].

Although being only the sixth common cancer worldwide, Liver cancer is the second most common cause of death from cancer (*Accessible at www.wcrf.org*). The most widespread form is the Hepatocellular carcinoma (HCC) that shows a broad geographic variability with the highest incidence in less developed countries (*Accessible at www.wcrf.org*). This evidence points out that in addition to high fats/low fibres diet, alcohol consuming and smoking, which are common causes of various cancers, other sources facilitate the occurrence of this disease. Consumption of foods contaminated by aflatoxins and chronicle hepatitis B (HBV) and hepatitis C (HPC) virus infections represent established causes [105]. The relation between viral hepatitis and HCC is supported by the evidence that chronic liver infections cause the recurrent turnover of hepatocytes that, in turn, lead to liver inflammation and cirrhosis, which are conditions that may trigger hepatocarcinogenesis [106]. HCC shows a poor survival rate of approximately 12% at five years in US and Europe but a substantially decrease to 5% in low-income countries [105]. In part, this is because the early stages of this disease do not usually produce symptoms and consequently HCC is generally diagnosed in advanced states. Another significant reason lies in the absence of satisfactory tests for early diagnosis in clinical laboratories. Currently available tests, such as the Alpha-Fetoprotein (AFP) tumour marker test, suffer, in fact, of low diagnostic sensitivity combined with an unsatisfactory specificity. It is not surprisingly that several studies aim to identify additional or complementary biomarkers or to develop novel diagnostic methods for the HCC early state screening. Among a number of biomarkers including the s-carboxyprothrombin, interleukin-6, osteopontin and circulating miRNAs [107,108], recent studies revealed that the Squamous Cell Carcinoma Antigen 1, named also SerpinB3 (SB3), a soluble serine protease inhibitor of the ovalbumin−serine protease family (ov-serpins), is a promising target for HCC early detection. Interestingly, in fact, SB3 is frequently overexpressed in dysplastic

nodules, HCC and hepatoblastoma but not in healthy hepatocytes [109]. Highest levels of SB3 in HCC patients are also related to subtype of the most aggressive liver tumours [110]. A natural ligand of SerpinB3 is the hepatitis B virus (HBV) that involves a fragment of the envelope proteins, which is the N-terminal HBV PreS1 (21–47) sequence, in the recognition process and in particular in cell attachment and internalization [111, 112]. The PreS1 peptide is therefore of a great interest for the development of novel methods for the early screening of liver cancer.

Taking into account abovementioned information, peptides shown in Table 1 were chosen as specific targeting ligands of gold nanostructures synthesized for this work for colorectal and liver cancer early stage screening. In particular, GE11 [98] and cycloRGD [102] peptides, which respectively bind to EGFR and $\alpha_v\beta_3$ integrin receptors, were selected to target the colorectal cancer. The peptide PreS1 [111, 112] was chosen to target SerpinB3 overexpressed in liver tumours. As already discussed, although peptides have achieved great success in biomedical and biotechnological realms, they suffer from poor stability and fast renal clearance that reduce the efficiency of the delivery to the diseased site. In addition, peptides for peptide-based materials must be optimized for applications in nanomedicine. The rational peptide design is therefore required. For this project, a number of peptide analogues, which will be described in detail in the following chapters, were designed to optimize the nanostructures targeting properties.

Table 1. Synthesized peptides for colorectal and liver cancer biosensors.

Peptide	*Sequence* [a]	*Associated Receptor*	*Targeted tumor*
GE11	YHWYGYTPQNVI-NH_2	EGFR	Colon rectum
cycloRGD	cyclo[RGDyK]	$\alpha_v\beta_3$ integrin	Colon rectum
PreS1	PLGFFPDHQLDPAFGANSNNPDWDFNP-NH_2	SerpinB3	Liver

[a] Abbreviations: Amino acids are represented by one letter symbol.

The targeting activity of the nanostructures was studied both *in vitro* on cancer cells and *in vivo* on murine tumour models. In order to investigate on the most functional composition of the surface coating, experimental results were combined to Molecular Dynamics (MD) calculations and spectroscopic analysis. Methodologies used to synthesize and characterize peptides as well as gold nanostructures are described in Chapter 2, that gives also an overview on MD computer simulations. Chapters 3-6 regard colorectal cancer cells targeting achieved by loading the nanosystems with GE11

and cycloRGD peptides. Several studies have demonstrated that an efficient targeting activity can be achieved only if the ligands on the nanosystems are properly designed to optimize the association with the targeted receptors on cells [113, 114]. Actually, the effect of the ligands organization on the surface has not been deeply investigated. In order to contribute to fill this gap, a number of analogues of GE11 (Chapter 3) and cycloRGD (Chapter 4) peptides were rationally designed to obtain nanosystems presenting the targeting motif with different arrangements on the nanoparticles surface. Experimental results associated to MD simulations highlighted the relevance of the targeting motif exposure on the nanosystems for the efficient receptor recognition. Since among a number of analogues those conveniently engineered by conjugating the peptide to polyethylene glycol (PEG) showed the best targeting activity, the role of the polymer was further investigated. For this purpose, several nanostructures were loaded with a mixture of GE11 peptides and PEG chains. By studying the targeting activity of the nanostructures on cancer cells and by rationalizing experimental results by MD calculations and spectroscopic measurements, the presence of PEG in the system coating was proved to be essential for an effective receptor binding (Chapter 5).

As already discussed in previous paragraphs, peptides offer numerous advantages over other targeting units such as the possibility of being chemically modified to be easily attached to nanoparticles without reducing their affinity to receptors and the relatively low synthetic cost and toxicity. However, they suffer from sensitivity to proteolytic enzymes that limits their circulation in the blood to not more than few minutes. Peptides stability to proteases is expected to be even greater on nanostructures since the presence of thousands of nearby molecules on the nanoparticles contrasts the action of the enzymes [115]. However, the influence of the peptides organization on the surface is not known. In order to contribute to this knowledge, the proteolytic stability of several analogues of GE11 presenting the targeting motif with different arrangements on the nanosystems was studied. Results are presented in Chapter 6.

Chapter 7 concerns liver cancer cells targeting. Firstly, nanostructures were loaded with different analogues of PreS1 peptide to evaluate the proper presentation of the targeting unit on the nanosystem for the association to receptors on cells. Then, once verified the stability to proteolytic enzymes and the biocompatibility, the nanostructures showing the best targeting in vitro were tested in vivo on murine tumour models. Results demonstrated that the nanostructures are really promising to be used for diagnostic and SERRS imaging of hepatocarcinoma.

References

1. Feynman, R., There's plenty of room at the bottom. *Engineering and science*. **1960**, 23, pp 22-36.

2. Taniguchi, N., On the basic concept of nanotechnology. Proc. Intl. Conf. Prod. Eng. Tokyo, Part II, Japan Society of Precision Engineering. **1974**. pp 18-23.

3. Binnig, G., Fuchs, H., Gerber, C., Rohrer, H., Stoll, E., Tosatti, E., Energy-dependent state-density corrugation of a graphite surface as seen by scanning tunneling microscopy. *Europhysics Letters.* **1986**. 1 (1), pp 31-36.

4. Brus, L., Electron-electron and electron-hole interactions in small semiconductor crystallites: the size dependence of the lowest excited electronic state. *J. Chem. Phys*. **1984**. 80, pp 4403–4409.

5. Brus, L., Electronic wave functions in semiconductor clusters: experiment and theory. *J. Phys. Chem.* **1986**. 90, pp 2555–2560.

6. Iijima, S., Helical microtubules of graphitic carbon. *Nature.* **1991**. 354 (6348), pp 56-58.

7. Iijima, S., Ichihashi, T., Single-shell carbon nanotubes of 1-nm diameter. *Nature.* **1993**. 363 (6430), pp 603-605.

8. Tinkle, S., McNeil, S. E., Muhlebach, S., Bawa, R., Borchard, G., Barenholz, Y., Tamarkin, L., Desai, N., Nanomedicines: addressing the scientific and regulatory gap. In *Annals Reports*, *Blackwell Science Publ: Oxford*. **2014**. 1313, pp 35-56.

9. Etheridge, M. L., Campbell, S. A., Erdman, A. G., Haynes, C. L., Wolf, S. M., McCullough, J., The big picture on nanomedicine: the state of investigational and approved nanomedicine products. *Nanomedicine-Nanotechnology Biology and Medicine.* **2013**. 9 (1), pp 1-14.

10. Rao, C. N. R., Müller, A., Cheetham, A. K., The Chemistry of Nanomaterials: Synthesis, Properties and Applications. *John Wiley & Sons*. **2006**.

11. Soares, S., Sousa, J., Pais, A., Vitorino, C., Nanomedicine: Principles, Properties, and Regulatory Issues. *Frontiers in Chemistry.* **2018**. 6 (15).

12. Hoskin, D. W., Ramamoorthy, A., Studies on anticancer activities of antimicrobial peptides. *Biochimica Et Biophysica Acta-Biomembranes.* **2008**. 1778 (2), pp 357-375.

13. https://www.cancer.gov/about-cancer/understanding/statistics.

14. Leite, M. L., da Cunha, N. B., Costa, F. F., Antimicrobial peptides, nanotechnology, and natural metabolites as novel approaches for cancer treatment. *Pharmacology & Therapeutics.* **2018**. 183, pp 160-176.

15. Shi, J. J., Kantoff, P. W., Wooster, R., Farokhzad, O. C., Cancer nanomedicine: progress, challenges and opportunities. *Nature Reviews Cancer.* **2017**. 17 (1), pp 20-37.

16. Strebhardt, K., Ullrich, A., Paul Ehrlich's magic bullet concept: 100 years of progress. *Nature Reviews Cancer.* **2008**. 8 (6), pp 473-480.

17. Xu, X. Y., Ho, W., Zhang, X. Q., Bertrand, N., Farokhzad, O., Cancer nanomedicine: from targeted delivery to combination therapy. *Trends in Molecular Medicine.* **2015**. 21 (4), pp 223-232.
18. Kamath, P. R., Sunil, D., Nano-Chitosan Particles in Anticancer Drug Delivery: An Up-to-Date Review. *Mini-Reviews in Medicinal Chemistry.* **2017**. 17 (15), pp 1457-1487.
19. Wang, A. Z., Langer, R., Farokhzad, O. C., Nanoparticle Delivery of Cancer Drugs. *Annual Review of Medicine.* **2012**. 63, pp 185-198.
20. Perrault, S. D., Walkey, C., Jennings, T., Fischer, H. C., Chan, W. C. W., Mediating Tumor Targeting Efficiency of Nanoparticles Through Design. *Nano Letters.* **2009**. 9 (5), pp 1909-1915.
21. Gratton, S. E. A, Ropp, P. A., Pohlhaus, P. D., Luft, J. C., Madden, V. J., Napier, M. E., DeSimone, J. M., The effect of particle design on cellular internalization pathways. *Proceedings of the National Academy of Sciences of the United States of America.* **2008**. 105 (33), pp 11613-11618.
22. Bertrand, N., Wu, J., Xu, X. Y., Kamaly, N., Farokhzad, O. C., Cancer nanotechnology: The impact of passive and active targeting in the era of modern cancer biology. *Advanced Drug Delivery Reviews.* **2014**. 66, pp 2-25.
23. Danhier, F., To exploit the tumor microenvironment: Since the EPR effect fails in the clinic, what is the future of nanomedicine? *Journal of Controlled Release.* **2016**. 244, pp 108-121.
24. Zhang, X. Q., Xu, X., Bertrand, N., Pridgen, E., Swami, A., Farokhzad, O. C., Interactions of nanomaterials and biological systems: Implications to personalized nanomedicine. *Advanced Drug Delivery Reviews.* **2012**. 64 (13), pp 1363-1384.
25. ul Haque Saeed, A. F., Awan, S. A., Advances in Monoclonal Antibodies Production and Cancer Therapy. *MOJ Immunol*. **2016**. 3, pp 00099-00103.
26. Dawidczyk, C. M., Russell, L. M., Searson, P. C., Nanomedicines for cancer therapy: state-of-the-art and limitations to pre-clinical studies that hinder future developments. *Frontiers in Chemistry.* **2014**. 2, pp 13.
27. Tu, Z. G., Ha, J., Kharldia, R., Meng, X. G., Liang, J. F., Improved stability and selectivity of lytic peptides through self-assembly. *Biochemical and Biophysical Research Communications.* **2007**. 361 (3), pp 712-717.
28. Bellmann-Sickert, K., Beck-Sickinger, A. G., Peptide drugs to target G protein-coupled receptors. *Trends in Pharmacological Sciences.* **2010**. 31 (9), pp 434-441.
29. Chrastina, A., Massey, K. A., Schnitzer, J. E., Overcoming in vivo barriers to targeted nanodelivery. *Wiley Interdisciplinary Reviews-Nanomedicine and Nanobiotechnology.* **2011**. 3 (4), pp 421-437.
30. Alkilany, A. M., Murphy, C. J., Toxicity and cellular uptake of gold nanoparticles: what we have learned so far? *Journal of Nanoparticle Research.* **2010**. 12 (7), pp 2313-2333.

31. Longmire, M., Choyke, P. L., Kobayashi, H., Clearance properties of nano-sized particles and molecules as imaging agents: considerations and caveats. *Nanomedicine.* **2008**. 3 (5), pp 703-717.
32. Gharatape, A., Salehi, R., Recent progress in theranostic applications of hybrid gold nanoparticles. *European Journal of Medicinal Chemistry.* **2017**. 138, pp 221-233.
33. Dreaden, E. C., Alkilany, A. M., Huang, X. H., Murphy, C. J., El-Sayed, M. A., The golden age: gold nanoparticles for biomedicine. *Chemical Society Reviews.* **2012**. 41 (7), pp 2740-2779.
34. Flynn, N. T., Tran, T. N. T., Cima, M. J., Langer, R., Long-term stability of self-assembled monolayers in biological media. *Langmuir.* **2003**. 19 (26), pp 10909-10915.
35. Yin, J. C., Chen, D. Q., Wu, S. S., Li, C. R., Liu, L. Z., Shao, Y. Z., Tumor-targeted nanoprobes for enhanced multimodal imaging and synergistic photothermal therapy: core-shell and dumbbell Gd-tailored gold nanorods. *Nanoscale.* **2017**. 9 (43), pp 16661-16673.
36. Jiang, Y. Q., Horimoto, N. N, Imura, K., Okamoto, H., Matsui, K., Shigemoto, R., Bioimaging with Two-Photon-Induced Luminescence from Triangular Nanoplates and Nanoparticle Aggregates of Gold. *Advanced Materials.* **2009**. 21 (22), pp 2309.
37. Lee, D., Beack, S., Yoo, J., Kim, S. K., Lee, C., Kwon, W., Hahn, S. K., Kim, C., In Vivo Photoacoustic Imaging of Livers Using Biodegradable Hyaluronic Acid-Conjugated Silica Nanoparticles. *Advanced Functional Materials.* **2018**. 28 (22), pp 9.
38. Bao, S. J., Huang, S. N., Liu, Y., Hu, Y. R., Wang, W. P., Ji, M. F., Li, H. L., Zhang, N. X.;, Song, C. Z., Duan, S. F., Gold nanocages with dual modality for image-guided therapeutics. *Nanoscale.* **2017.** 9 (21), pp 7284-7296.
39. Laing, S., Gracie, K., Faulds, K., Multiplex in vitro detection using SERS. *Chemical Society Reviews.* **2016**. 45 (7), pp 1901-1918.
40. Liu, X. T., Wang, L., Xu, X. W., Zhao, H. Y., Jiang, W., Endogenous Stimuli-Responsive Nucleus-Targeted Nanocarrier for Intracellular mRNA Imaging and Drug Delivery. *Acs Applied Materials & Interfaces.* **2018**. 10 (46), pp 39524-39531.
41. Shi, H., Gao, T., Shi, L., Chen, T. S., Xiang, Y., Li, Y. Y., Li, G. X., Molecular imaging of telomerase and the enzyme activity-triggered drug release by using a conformation-switchable nanoprobe in cancerous cells. *Scientific Reports.* **2018**. 8, pp 11.
42. Chen, Y., Li, N., Yang, Y., Liu, Y., A dual targeting cyclodextrin/gold nanoparticle conjugate as a scaffold for solubilization and delivery of paclitaxel. *Rsc Advances.* **2015**. 5 (12), pp 8938-8941.
43. Gao, Y. Y., Chen, H., Zhou, Y. Y., Wang, L. T., Hou, Y. L., Xia, X. H., Ding, Y., Intraorgan Targeting of Gold Conjugates for Precise Liver Cancer Treatment. *Acs Applied Materials & Interfaces.* **2017**. 9 (37), pp 31458-31468.

44. Qiao, Y. T., Wan, J. Q., Zhou, L. Q., Ma, W., Yang, Y. Y., Luo, W. X., Yu, Z. Q., Wang, H. X., Stimuli-responsive nanotherapeutics for precision drug delivery and cancer therapy. *Wiley Interdisciplinary Reviews-Nanomedicine and Nanobiotechnology.* **2019**. 11 (1), pp 20.

45. Yang, S. Y.. Yao, D. F,. Wang, Y. S., Yang, W. T., Zhang, B. B., Wang, D. B., Enzyme-triggered self-assembly of gold nanoparticles for enhanced retention effects and photothermal therapy of prostate cancer. *Chemical Communications.* **2018**. 54 (70), pp 9841-9844.

46. Wang, S. J., Xin, J., Zhang, L. W., Zhou, Y. C., Yao, C. P., Wang, B., Wang, J., Zhang, Z. X., Cantharidin-encapsulated thermal-sensitive liposomes coated with gold nanoparticles for enhanced photothermal therapy on A431 cells. *International Journal of Nanomedicine.* **2018**. 13, pp 2143-2160.

47. Choi, J., Jung, K. O., Graves, E. E., Pratx, G., A gold nanoparticle system for the enhancement of radiotherapy and simultaneous monitoring of reactive-oxygen-species formation. *Nanotechnology.* **2018**. 29 (50), pp 8.

48. Borran, A. A., Aghanejad, A., Farajollahi, A., Barar, J., Omidi, Y., Gold nanoparticles for radiosensitizing and imaging of cancer cells. *Radiation Physics and Chemistry.* **2018**. 152, pp 137-144.

49. Michael, D., Mingos, P., Gold Clusters, Colloids and Nanoparticles *I. Springer International Publishing Switzerland*. **2014**.

50. Cao, Y. Q., Zhang, J. W., Yang, Y., Huang, Z. R., Long, N. V., Fu, C. L., Engineering of SERS Substrates Based on Noble Metal Nanomaterials for Chemical and Biomedical Applications. *Applied Spectroscopy Reviews.* **2015**. 50 (6), pp 499-525.

51. Ghosh, S. K., Pal, T., Interparticle coupling effect on the surface plasmon resonance of gold nanoparticles: From theory to applications. *Chemical Reviews.* **2007**. 107 (11), pp 4797-4862.

52. Mie, G., *Ann. Phys. (Leipzig)*. **1908**. 25, pp 377-445.

53. Szunerits, S., Spadavecchia, J., Boukherroub, R., Surface plasmon resonance: signal amplification using colloidal gold nanoparticles for enhanced sensitivity. *Reviews in Analytical Chemistry.* **2014**. 33 (3), pp 153-164.

54. Hutter, E., Fendler, J. H., Exploitation of localized surface plasmon resonance. *Advanced Materials.* **2004**. 16 (19), pp 1685-1706.

55. Sprunken, D. P., Omi, H., Furukawa, K., Nakashima, H., Sychugov, I., Kobayashi, Y., Torimitsu, K., Influence of the local environment on determining aspect-ratio distributions of gold nanorods in solution using Gans theory. *Journal of Physical Chemistry C.* **2007**. 111 (39), pp 14299-14306.

56. Hainfeld, J. F.; O'Connor, M. J.; Lin, P.; Qian, L. P.; Slatkin, D. N.; Smilowitz, H. M., Infrared-Transparent Gold Nanoparticles Converted by Tumors to Infrared Absorbers Cure Tumors in Mice by Photothermal Therapy. *Plos One* **2014**. *9* (2), 11.

57. Fleischmann, M., Hendra, P. J., McQuillan, A. J., Raman spectra of pyridine adsorbed at a silver electrode. *Chemical Physics Letters*. **1974**. 26, pp 163-166.

58. Jeanmaire , D. L., Van Duyne, R. P., Surface raman spectroelectrochemistry : Part I. Heterocyclic, aromatic, and aliphatic amines adsorbed on the anodized silver electrode. *Journal of Electroanalytical Chemistry and Interfacial Electrochemistry*. **1977**. pp 1-20.

59. Nie, S. M., Emery, S. R., Probing single molecules and single nanoparticles by surface-enhanced Raman scattering. *Science.* **1997**. 275 (5303), pp 1102-1106.

60. Kneipp, K., Wang, Y., Kneipp, H., Perelman, L. T., Itzkan, I., Dasari, R. R., Feld, M. S., Single Molecule Detection Using Surface-Enhanced Raman Scattering (SERS). *Physical Review Letters*. **1997**. 78, pp 1667-1670.

61. Lane, L. A., Qian, X. M., Nie, S. M., SERS Nanoparticles in Medicine: From Label-Free Detection to Spectroscopic Tagging. *Chemical Reviews.* **2015**. 115 (19), pp 10489-10529.

62. Schlucker, S., Surface-Enhanced Raman Spectroscopy: Concepts and Chemical Applications. *Angewandte Chemie-International Edition.* **2014**. 53 (19), pp 4756-4795.

63. Stamplecoskie, K. G., Scaiano, J. C., Tiwari, V. S., Anis, H., Optimal Size of Silver Nanoparticles for Surface-Enhanced Raman Spectroscopy. *Journal of Physical Chemistry C.* **2011**. 115 (5), pp 1403-1409.

64. Hong, S. M., Li, X., Optimal Size of Gold Nanoparticles for Surface-Enhanced Raman Spectroscopy under Different Conditions. *Journal of Nanomaterials.* **2013**. 9.

65. Joseph, M. M., Narayanan, N., Nair, J. B., Karunakaran, V., Ramya, A. N., Sujai, P. T., Saranya, G., Arya, J. S., Vijayan, V. M., Maiti, K. K., Exploring the margins of SERS in practical domain: An emerging diagnostic modality for modern biomedical applications. *Biomaterials.* **2018**. 181, pp 140-181.

66. Le Ru, E. C., Grand, J., Sow, I., Somerville, W. R. C., Etchegoin, P. G., Treguer-Delapierre, M., Charron, G., Felidj, N., Levi, G., Aubard, J., A Scheme for Detecting Every Single Target Molecule with Surface-Enhanced Raman Spectroscopy. *Nano Letters.* **2011**. 11 (11), pp 5013-5019.

67. Michaels, A. M., Jiang, J., Brus, L., Ag nanocrystal junctions as the site for surface-enhanced Raman scattering of single Rhodamine 6G molecules. *Journal of Physical Chemistry B.* **2000**. 104 (50), pp 11965-11971.

68. Kleinman, S. L., Frontiera, R. R., Henry, A. I., Dieringer, J. A., Van Duyne, R. P., Creating, characterizing, and controlling chemistry with SERS hot spots. *Physical Chemistry Chemical Physics.* **2013**. 15 (1), pp 21-36.

69. Campion, A., Ivanecky, J. E., Child, C. M., Foster, M., On the mechanism of chemical enhancement in surface-enhanced raman-scattering. *Journal of the American Chemical Society.* **1995**. 117 (47), pp 11807-11808.

70. Qian, X. M., Nie, S. M., Single-molecule and single-nanoparticle SERS: from fundamental mechanisms to biomedical applications. *Chemical Society Reviews.* **2008**. 37 (5), pp 912-920.

71. Cao, Y. Q., Li, D., Jiang, F., Yang, Y., Huang, Z. R., Engineering Metal Nanostructure for SERS Application. *Journal of Nanomaterials.* **2013**. 12.

72. Fabris, L., Gold-based SERS tags for biomedical imaging. *Journal of Optics.* **2015**. 17 (11), pp 114002-114016.

73. Le Ru, E. C., Blackie, E., Meyer, M., Etchegoin, P. G., Surface enhanced Raman scattering enhancement factors: a comprehensive study. *Journal of Physical Chemistry C.* **2007**.111 (37), pp 13794-13803.

74. McHugh, C. J., Docherty, F. T., Graham, D., Smith, W. E., SERRS dyes - Part 2. Syntheses and evaluation of dyes for multiple labelling for SERRS. *Analyst.* **2004**. 129 (1), pp 69-72.

75. Yang, Y., Li, Z. Y., Yamaguchi, K., Tanemura, M., Huang, Z. R., Jiang, D. L., Chen, Y. H., Zhou, F., Nogami, M., Controlled fabrication of silver nanoneedles array for SERS and their application in rapid detection of narcotics. *Nanoscale.* **2012**. 4 (8), pp 2663-2669.

76. Costa, J. C. S., Ando, R. A., Sant'Ana, A. C., Rossi, L. M., Santos, P. S., Temperini, M. L. A., Corio, P., High performance gold nanorods and silver nanocubes in surface-enhanced Raman spectroscopy of pesticides. *Physical Chemistry Chemical Physics.* **2009**. 11 (34), pp 7491-7498.

77. Zhang, B., Xu, P., Xie, X. M., Wei, H., Li, Z. P., Mack, N. H., Han, X. J., Xu, H. X., Wang, H. L., Acid-directed synthesis of SERS-active hierarchical assemblies of silver nanostructures. *Journal of Materials Chemistry.* **2011**. 21 (8), pp 2495-2501.

78. Sajanlal, P. R., Pradeep, T., Functional hybrid nickel nanostructures as recyclable SERS substrates: detection of explosives and biowarfare agents. *Nanoscale.* **2012**. 4 (11), pp 3427-3437.

79. Taylor, J., Huefner, A., Li, L., Wingfield, J., Mahajan, S., Nanoparticles and intracellular applications of surface-enhanced Raman spectroscopy. *Analyst.* **2016**. 141 (17), pp 5037-5055.

80. Doering, W. E., Nie, S. M., Spectroscopic tags using dye-embedded nanoparticles and surface-enhanced Raman scattering. *Analytical Chemistry.* **2003**. 75 (22), pp 6171-6176.

81. Center, M. M., Jemal, A., Smith, R. A., Ward, E., Worldwide Variations in Colorectal Cancer. *Ca-a Cancer Journal for Clinicians.* **2009**. 59 (6), pp 366-378.

82. Bray, F., Jemal, A., Grey, N., Ferlay, J., Forman, D., Global cancer transitions according to the Human Development Index (2008-2030): a population-based study. *Lancet Oncology.* **2012**. 13 (8), pp 790-801.

83. Santarelli, R. L., Pierre, F., Corpet, D. E., Processed meat and colorectal cancer: A review of epidemiologic and experimental evidence. *Nutrition and Cancer-an International Journal.* **2008**. 60 (2), pp 131-144.

84. Ma, Y. L., Yang, Y. Z., Wang, F., Zhang, P., Shi, C. Z., Zou, Y., Qin, H. L., Obesity and Risk of Colorectal Cancer: A Systematic Review of Prospective Studies. *Plos One.* **2013**. 8 (1), pp 16.

85. Johns, L. E., Houlston, R. S., A systematic review and meta-analysis of familial colorectal cancer risk. *American Journal of Gastroenterology.* **2001**. 96 (10), pp 2992-3003.

86. Walsh, J. M. E., Terdiman, J. P., Colorectal cancer screening - Scientific review. *Jama-Journal of the American Medical Association.* **2003**. 289 (10), pp 1288-1296.

87. Hundt, S., Haug, U., Brenner, H., Blood markers for early detection of colorectal cancer: A systematic review. *Cancer Epidemiology Biomarkers & Prevention.* **2007**.16 (10), pp 1935-1953.

88. Vacante, M., Borzi, A. M., Basile, F., Biondi, A., Biomarkers in colorectal cancer: Current clinical utility and future perspectives. *World Journal of Clinical Cases.* **2018**. 6 (15), pp 869-881.

89. Yewale, C., Baradia, D., Vhora, I., Patil, S., Misra, A., Epidermal growth factor receptor targeting in cancer: A review of trends and strategies. *Biomaterials.* **2013**. 34 (34), pp 8690-8707.

90. Bodnar, R. J., Epidermal growth factor and epidermal growth factor receptor: the Yin and Yang in the treatment of cutaneous wounds and cancer. *Adv. Wound Care*. **2013**. 2, pp 24-29.

91. Riese, D. J., Bermingham, Y., vanRaaij, T. M., Buckley, S., Plowman, G. D., Stern, D. F., Betacellulin activates the epidermal growth factor receptor and erbB-4, and induces cellular response patterns distinct from those stimulated by epidermal growth factor or neuregulin-beta. *Oncogene.* **1996**. 12 (2), pp 345-353.

92. Strachan, L., Murison, J. G., Prestidge, R. L., Sleeman, M. A., Watson, J. D., Kumble, K. D., Cloning and biological activity of epigen, a novel member of the epidermal growth factor superfamily. *Journal of Biological Chemistry.* **2001**. 276 (21), pp 18265-18271.

93. Raab, G., Klagsbrun, M., Heparin-binding EGF-like growth factor. *Biochimica Et Biophysica Acta-Reviews on Cancer.* **1997**. 1333 (3), F179-F199.

94. Baselga, J., Pfister, D., Cooper, M. R., Cohen, R., Burtness, B., Bos, M., D'Andrea, G., Seidman, A., Norton, L., Gunnett, K., Falcey, J., Anderson, V., Waksal, H., Mendelsohn, J., Phase I studies of anti-epidermal growth factor receptor chimeric antibody C225 alone and in combination with cisplatin. *Journal of Clinical Oncology.* **2000**. 18 (4), pp 904-914.

95. Yang, X. D., Jia, X. C., Corvalan, J. R. F., Wang, P., Davis, C. G., Development of ABX-EGF, a fully human anti-EGF receptor monoclonal antibody, for cancer therapy. *Critical Reviews in Oncology Hematology.* **2001**. 38 (1), pp 17-23.

96. Azemar, M., Schmidt, M., Arlt, F., Kennel, P., Brandt, B., Papadimitriou, A., Groner, B., Wels, W., Recombinant antibody toxins specific for ERBB2 and EGF receptor inhibit the in vitro growth of human head and neck cancer cells and cause rapid tumor regression in vivo. *International Journal of Cancer.* **2000**. 86 (2), pp 269-275.

97. Papo, N., Seger, D., Makovitzki, A., Kalchenko, V., Eshhar, Z., Degani, H., Shai, Y., Inhibition of tumor growth and elimination of multiple metastases in human prostate and breast xenografts by systemic inoculation of a host defense-like lytic peptide. *Cancer Research.* **2006**. 66 (10), pp 5371-5378.

98. Li, Z. H., Zhao, R. J., Wu, X. H., Sun, Y., Yao, M., Li, J. J., Xu, Y. H., Gu, J. R., Identification and characterization of a novel peptide ligand of epidermal growth factor receptor for targeted delivery of therapeutics. *Faseb Journal.* **2005**. 19 (14), pp 1978-1985.

99. Jin, H., Varner, J., Integrins: roles in cancer development and as treatment targets. *British Journal of Cancer.* **2004**. 90 (3), pp 561-565.

100. Hwang, R., Varner, J., The role of integrins in tumor angiogenesis. *Hematology-Oncology Clinics of North America.* **2004**. 18 (5), pp 991-1006.

101. Pilch, J., Habermann, R., Felding-Habermann, B., Unique ability of integrin alpha(v)beta(3) to support tumor cell arrest under dynamic flow conditions. *Journal of Biological Chemistry.* **2002**. 277 (24), pp 21930-21938.

102. Vonlaufen, A., Wiedle, G., Borisch, B., Birrer, S., Luder, P., Imhof, B. A., Integrin alpha(v)beta(3) expression in colon carcinoma correlates with survival. *Modern Pathology.* **2001**. 14 (11), pp 1126-1132.

103. Hynes, R. O., A reevaluation of integrins as regulators of angiogenesis. *Nature Medicine.* **2002**. 8 (9), pp 918-921.

104. Kerr, J. S., Slee, A. M., Mousa, S. A., The alpha(v) integrin antagonists as novel anticancer agents: an update. *Expert Opinion on Investigational Drugs.* **2002**. 11 (12), pp 1765-1774.

105. Bosetti, C., Turati, F., La Vecchia, C., Hepatocellular carcinoma epidemiology. *Best Practice & Research Clinical Gastroenterology.* **2014**. 28 (5), pp 753-770.

106. Montagnana, M., Danese, E., Lippi, G., Squamous cell carcinoma antigen in hepatocellular carcinoma: Ready for the prime time? *Clinica Chimica Acta.* **2015**. 445, pp 161-166.

107. Boye, A., Yang, Y., Hepatic MicroRNA Orchestra: A New Diagnostic, Prognostic and Theranostic Tool for Hepatocarcinogenesis. *Mini-Reviews in Medicinal Chemistry.* **2014**. 14 (10), pp 837-852.

108. Voiculescu, M., Nanau, R. M., Neuman, M. G., Non-invasive Biomarkers in Non-Alcoholic Steatohepatitis-induced Hepatocellular Carcinoma. *Journal of Gastrointestinal and Liver Diseases.* **2014**. 23 (4), pp 425-429.

109. Guido, M., Roskam, T., Pontisso, P., Fassan, M., Thung, S. N., Giacomelli, L., Sergio, A., Farinati, F., Cillo, U., Rugge, M., Squamous cell carcinoma antigen in human liver carcinogenesis. *J. Clin. Pathol.* **2008**. 61 (4), pp 445-447.

110. Turato, C., Vitale, A., Fasolato, S., Ruvoletto, M., Terrin, L., Quarta, S., Morales, R. R., Biasiolo, A., Zanus, G., Zali, N., Tan, P. S., Hoshida, Y., Gatta, A., Cillo, U., Pontisso, P., SERPINB3 is associated with TGF-beta 1 and cytoplasmic beta-catenin expression in hepatocellular carcinomas with poor prognosis. *British Journal of Cancer.* **2014**. 110 (11), pp 2708-2715.

111. Dash, S., Rao, K. V. N., Panda, S. K., Receptor for Pre-S1(21-47) component of hepatitis-B on the liver-cell-role in virus-cell interaction. *J. Med. Virol.* **1992**. 37 (2), pp 116-121.

112. Deng, Q., Zhai, Q., Michel, M. L., Zhang, J., Qin, J., Kong, J. J., Zhang, X. X., Budkowska, A., Tiollais, P., Wang, Y., Xie, Y. H., Identification and characterisation of peptides that interact with hepatitis B virus via the putative receptor binding site. *J. Virol.* **2007**. 81, pp 4244–54.

113. Fasolato, C., Giantulli, S., Silvestri, I., Mazzarda, F., Toumia, Y., Ripanti, F., Mura, F., Luongo, F., Costantini, F., Bordi, F., Postorino, P., Domenici, F., Folate-based single cell screening using surface enhanced Raman microimaging. *Nanoscale.* **2016**. 8 (39), pp 17304-17313.

114. Stefanick, J. F., Kiziltepe, T., Bilgicer, B., Improved Peptide-Targeted Liposome Design Through Optimized Peptide Hydrophilicity, Ethylene Glycol Linker Length, and Peptide Density. *Journal of Biomedical Nanotechnology.* **2015**. 11 (8), pp 1418-1430.

115. Tassa, C., Duffner, J. L., Lewis, T. A., Weissleder, R., Schreiber, S. L., Koehler, A. N., Shaw, S. Y., Binding Affinity and Kinetic Analysis of Targeted Small Molecule-Modified Nanoparticles. *Bioconjugate Chemistry.* **2010**. 21 (1), pp 14-19.

Chapter 2: Methodologies

Strategies of Peptides Synthesis

Peptide-based materials have been extensively investigated over the last decades because of their versatility and potentiality as alternative to synthetic materials. In particular, being naturally bioactive, biodegradable and biocompatible, peptides are building blocks of great interest for materials for biomedical applications. Peptide-based materials can be made up of solely amino acids or combined with other polymers [1] or nanoparticles [2]. Combination of peptides to other moieties allows obtaining hybrid conjugates that benefit from the synergistic behaviour of both components and overcome some of their respective intrinsic limitations. For instance, polymers like PEG can be conjugated to peptides to improve biocompatibility and to prolong blood circulation time whereas the peptides impart biofunctional properties to the conjugate, which can be thus employed in therapeutics and sensing [3]. Examples of peptide-based materials are biosensors obtained by integrating peptides either as recognition units or as sensor constituents [4], and stimuli responsive materials, which exploit the switching of the peptide conformation triggered by an external stimulus such as pH, ionic strength, temperature, photons and enzymes [5]. The expansion of peptide-based materials in various research fields have requested the development of diverse strategies for a relatively easy, quick and versatile synthesis of peptides. The two major chemical techniques for peptide production are Solution Phase Synthesis (SPS) and Solid Phase Peptide Synthesis (SPPS). Solution Phase Synthesis is based on the coupling of single amino acids in solution and, thanks to the isolation and purification of the intermediates, gives a high pure final peptide. However, SPS can't be easily and cheaply scaled up and requires long reaction times. Moreover, long peptides can be produced only by condensing short fragments [6]. Pioneered by Merrifield in 1963 [7], who won the Nobel Prize in Chemistry in 1984 [8], Solid Phase Peptide Synthesis (SPPS) have rapidly developed into one of the most powerful and versatile strategy for the production of long and complex peptides. SPPS is based on the use of a solid phase support, an insoluble polymeric resin, combined to repetitive coupling and deprotection steps. The resin has a central role and is responsible of the simplicity, speed and efficiency of this synthetic strategy. By filtration through the resin, in fact, unreacted reagents (introduced in large quantities to achieve the final product with high yields) and soluble by-products can be discarded. Consequently, all reactions can be carried out in a single vessel and isolation and purification of intermediates, requested by the classic SPS, are not necessary. One should only remember that SPPS has high costs, due to the excess of reactants used, and reactions can't be easily controlled meanwhile occurring [9].
The general scheme of SPPS is illustrated in Figure 1 [10]. SPPS starts with the loading of the first amino acid (AA_1) from the C-terminal residue (carboxyl group) to the resin via linker functionality. AA_1 is protected on the N-terminus (amino group) with a temporary group. Then the synthesis

proceeds with the peptide sequence construction to the N-terminal end by repetitive cycles of:
a) deprotection of the N-terminus of the amino acid already attached to the resin;
b) coupling of the subsequent amino acid (AA_2) by the carboxyl group, that must be activated for the coupling, to the N-terminal end of the amino acid sequence on the resin.

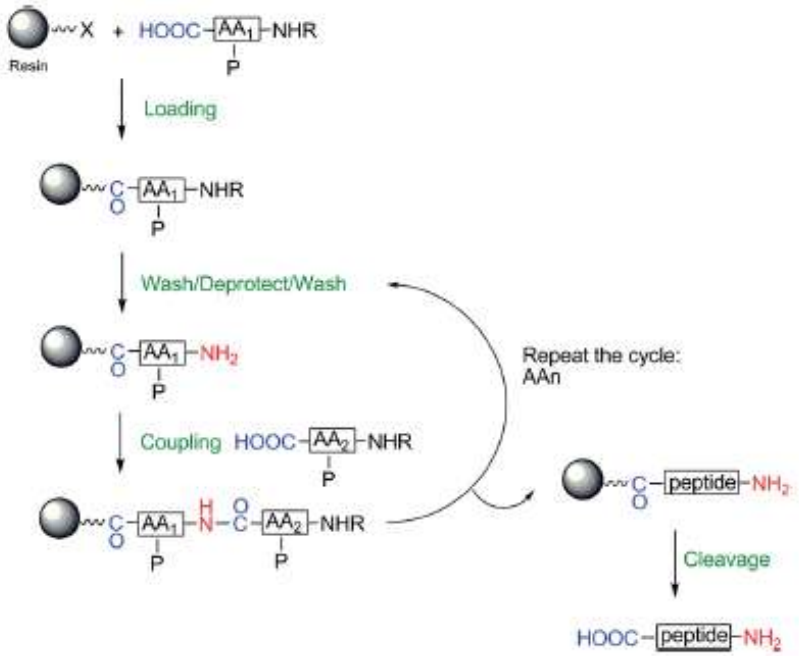

Figure 1. General scheme of Solid Phase Peptide Synthesis.

In addition to the amino group, temporary protecting groups must also protect reactive side chains of amino acids to avoid secondary reactions. The resin is filtered and washed to remove by-products and unreacted reagents at each step of the synthesis. Once the sequence is complete, the peptide is cleaved from the solid support and, typically, all protecting groups are contemporary removed. Subsequently, a more comprehensive view of SPPS and how this protocol has been successfully applied in the preparation of different peptides for this Ph.D. project are emphasized.

Resin material and linkers for SPPS: Polystyrene (PS) support containing 1% or 2% divinylbenzene (DVB), as a cross-linking agent, is the most common resin in SPPS. Typically, it is composed by small and spherical beads of two different sizes: 100–200 mesh (75–150 μm) and 200–400 mesh (35–75 μm). The swelling of the resin in a proper solvent has a huge influence on the diffusion and accessibility of the reagents into the core of the polymer and therefore to the synthetic efficiency [7]. 1-2% DVB cross-linked PS resin is well solvated in common organic solvents for SPPS (e.g. toluene, dichloromethane, dimethylformamide) but shows a decrease of solubility in more polar solvents (e.g.

methanol, acetonitrile) up to no swelling properties in water [11]. For this reason, polyamines and polyethylene glycols (PEG)-PS resins have been developed to perform the synthesis even in aqueous solutions [10].

Linkers are bifunctional chemical moieties used to attach the first amino acid to the resin. The chemical nature of the linker determines the chemistry to be used for the synthesis, the conditions under those the products can be cleaved from the solid support and the C-terminal functionalization of the final peptide. A wide variety of linkers for PS core resin have been developed. Most of them requests acidic conditions for the cleavage and yields peptides ending with a carboxylic acid (e.g. Wang resin) or an amide (e.g. Rink Amide) at the C-terminus [10,12]. The percentage of the linker attached to the solid support needs to be lower than the 2 % since higher percentages, inducing problems related to steric effects (e.g. formation of secondary rigid structures), reduce the efficiency of the synthesis. The density of the linker on the resin is usually given in mmol/g (number of linkers in millimoles per gram of resin).

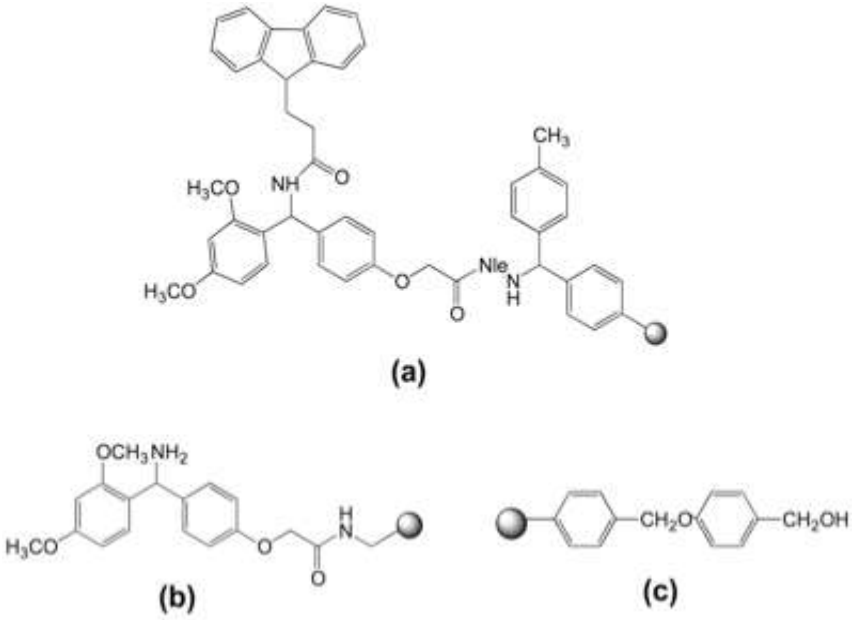

Figure 2. Resins for SPPS: (a) Rink Amide MBHA (b) Rink Amide PEGA (c) Wang.

In this work three kinds of resins (Figure 2) enabling the cleavage of the peptide under acidic conditions were used: Rink Amide-MBHA resin (polymeric core: PS, loading: 0.52 mmol/g, mesh: 100-200), Rink Amide PEGA resin (polymeric core: PS-PEG, loading: 0.35 mmol/g, mesh: 100-200) and Wang resin (polymeric core: PS, loading: 0.3 mmol/g, mesh: 100-200). The detachment of the peptide from these supports was performed in a single step by treatment with 95 % Trifluoroacetic Acid (TFA).

Orthogonal strategy of protecting groups: There are two categories of SPPS known as Tert-butyloxycarbonyl (Boc-) and Fluorenylmethyloxycarbonyl (Fmoc-) SPPS. The name refers to the temporary protecting group in N-terminal amino group of the amino acid. Initially, Boc-SPPS was the main form of SPPS but it was rapidly replaced by the more accessible Fmoc-SPPS technique that requires the use of relatively safer chemicals compared to strong acids requested by the Boc chemistry. Fmoc group (Figure 3), in fact, is sensitive to soft bases due to the electron-withdrawing properties of the fluorene system, which makes the hydrogen in position 9 acidic.

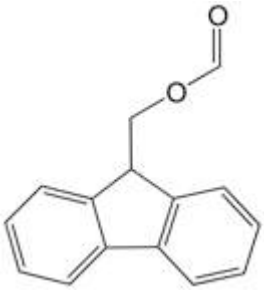

Figure 3. Fmoc protecting group.

In this work, the Fmoc deprotection was achieved with 20% piperidine in DMF. The reaction mechanism is illustrated in Figure 4. The first step is the removal of the proton in position 9 by piperidine that leads to the formation of the aromatic intermediate cyclopentadienyl-anion, which decomposes through β-elimination in dibenzofulvene and carbonic anhydride. Then, dibenzofulvene is blocked by the generation of a compound with the secondary amines [13].

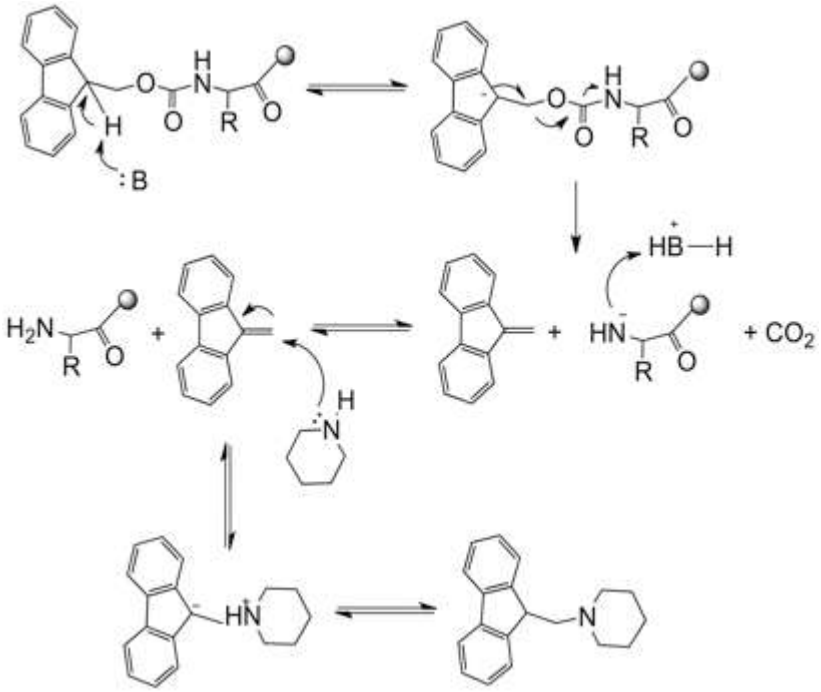

Figure 4. Mechanism of Fmoc deprotection by piperidine.

The correct choice of the protecting groups of the amino acid side chains is a crucial step for an efficient peptide synthesis. Different protecting groups for each amino acid exist and the deprotection conditions depend on the specific amino acid [14]. In this work an orthogonal approach is used for SPPS: amino acids present the amino group protected by the Fmoc group, removable in alkaline conditions, while the lateral chains are protected by acid labile protecting groups. Protecting groups chosen for each amino acid are reported in the Experimental Sections of the following Chapters.

Activation of the carboxyl group of the amino acids: The unification between carboxylic acids and amines to form amide bonds does not occur spontaneously at ambient temperature due to the adverse thermodynamic that promotes the side hydrolysis rather than the bond formation. This barrier is overcome in nature through complex and selective processes catalysed by enzymes, that enables protein and peptide synthesis activating the carboxyl group prior the coupling to the amino group. Miming nature, the carboxylic acid can be also activated for the chemical synthesis of peptides using coupling reagents that convert the hydroxyl group of the carboxyl group into a better leaving group. The choice of the coupling reagent ranges from acyl halides, acyl azides, acylimidazoles, anhydrides, esters et cetera but is however critical due to benefits and limitations of each reactants [15,16].

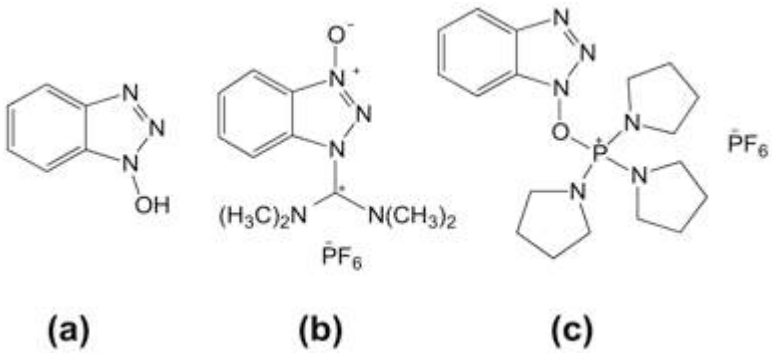

Figure 5. Coupling reagents (a) HOBt (b) HBTU (c) PyBop.

In this work 1H-benzotriazoles (HOBt) associated with uronium salt O-(1Hbenzotriazol-1-yl)-N,N,N0,N0-tetramethyluronium hexafluorophosphate (HBTU) or with phosphonium salt benzotriazol-1-yl-oxy-tris-pyrrolidinophosphonium hexafluorophosphate (PyBop) are mainly used as coupling agents (Figure 5). HOBt / HBTU and HOBt/ PyBop associations allow the activation of the carboxyl group as aromatic ester, which easily reacts with amines under mild conditions. A drawback of these activation strategies is the steric hindrance during the aminolysis step. The activation mechanism using HOBt / HBTU is reported in Figure 6. The first step is the deprotonation of the carboxyl group by a tertiary amine, usually Diisopropylethylamine (DIPEA). Then the

carboxylate reacts with HBTU generating a reactive intermediate that forms, in turn, an activated ester with HOBt. Being the anion -OBt an excellent leaving group, the activated ester quickly reacts with the terminal amino group of the growing peptide [17].

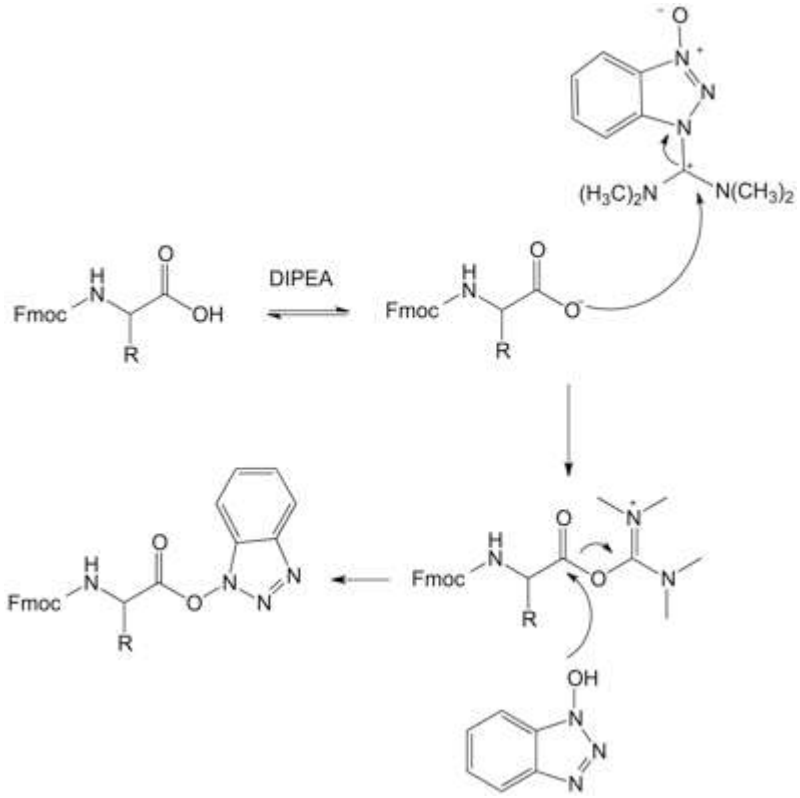

Figure 6. Mechanism of ester active formation using HOBt/HBTU.

Synthesized peptides: peptides for colorectal and liver cancer biosensors

The aim of this PhD project is to engineer gold nanostructures to be used as SERRS biosensors for colorectal and liver cancer diagnostic by functionalization with peptides, as specific ligands of tumor associated receptors. An overview of colorectal and liver cancer diseases was provided in Chapter 1 followed by the choice of the peptide sequences (Table 1) selected as targeting motifs among those proposed in recent literature. In particular, GE11 [18] and cycloRGD [19] peptides, which respectively bind to EGFR and $\alpha_v\beta_3$ integrin receptors, were identified for colorectal cancer targeting while the peptide PreS1 [20,21] was chosen to target SerpinB3 overexpressed in liver cancers. As discussed in Chapter 1, the rising of peptides for biomedical applications is dampened mainly by their poor stability and fast clearance. In addition, peptides must be rationally designed for effective use in nanomedicine. For this PhD project, a number of peptide analogues were designed to optimize the nanostructures targeting properties. The synthesis was performed on solid phase following the

procedures described above and yields around 80% were achieved. All peptide derivatives were enriched with a thiol group for exploiting the sulphur affinity for gold to strongly bond the peptides to the nanostructures surface, as already described in Chapter 1. After the sidechains deprotection and the detachment from the resin, the synthesized compounds were purified by Semipreparative High Pressure Liquid Chromatography (HPLC) separations. Products were characterized by Analytical HPLC and Electrospray Ionisation Time-of-Flight mass spectroscopy (ESI-TOF MS) or Matrix Assisted Laser Desorption Ionization Time-of- Flight mass spectroscopy (MALDI-TOF MS).

Table 1. Synthesized peptides for colorectal and liver cancer biosensors.

Peptide	*Sequence* [a]	*Associated Receptor*	*Targeted tumor*
GE11	YHWYGYTPQNVI-NH_2	EGFR	Colon rectum
cycloRGD	cyclo[RGDyK]	$\alpha_v\beta_3$ integrin	Colon rectum
PreS1	PLGFFPDHQLDPAFGANSNNPDWDFNP-NH_2	SerpinB3	Liver

[a] Abbreviations: Amino acids are represented by one letter symbol.

Strategies of Gold Nanoparticles Synthesis

In the past decades, several methods for the synthesis of gold nanoparticles of different size, shape, and morphology have been presented. Synthetic strategies encompass two main approaches: the "top-down" and the "bottom-up" approach [22].

In the "bottom-up" approach, also called "molecular nanotechnology", nanoparticles are formed starting from atoms, molecules or smaller particles through an assembling process. Most common bottom-up strategies are chemical syntheses based on the controlled reduction of solvated gold salt in the presence of surface capping agents, which prevent nanoparticles aggregation due to electrostatic and physical interactions. Among all of these chemical syntheses, the citrate reduction method, presented in 1951 by John Turkevich [23], is already the most used. It consists on the reduction of Au^{3+} of gold (III) chloride hydrate salt to Au^0 by trisodium citrate dehydrate, which plays also as stabilizer. The gold salt-to-citrate concentration ratio controls the particle size. As a result of the presence of deprotonated carboxylic groups of citrates on the gold surface, nanoparticles show a negative surface charge and the surface functionalization requires ligand-exchange reactions. Furthermore, citrate-capped nanoparticles must be accurately washed to remove citrate residues that can interfere in biomedical applications. In 1973 the Turkevich reduction was implemented by Frens to produce monodisperse spherical gold nanoparticles of diameter ranging from 16 to 150 nm [24]. Along with these citrate methods, other chemical approaches were propounded to synthesize gold nanoparticles. Examples are:

a) the reduction of chloro(triphenylphosphine)gold(I) by diborane in benzene, proposed by Schmid in 1981 to produce phosphine-stabilized gold particles with diameters from 1.4 to 0.4 nm [25];

b) the synthesis of thiol-stabilized gold clusters proposed by Brust in 1994. This method uses a two-phase system: in the organic phase (toluene) gold chloride is solvated by way of a phase-transfer reagent (tetraoctylammonium bromide) and dodecanethiol is added as a stabilizer for gold clusters formed whereas, in the aqueous phase, sodium borohydrate is used as reducing agent [26].

Controlling the chemistry of the process (e.g. pH, temperature, solvents, stabilizing and reducing agents et cetera) it is therefore possible to synthesize nanoparticles of desired properties and functionalities. Moreover, by varying the content and the nature of gold salt, reducing agent ad capping ligand it is possible to control the nanoparticle dimension, which usually shows a narrow size distribution. Drawbacks of these approaches are the complex synthesis and the toxicity that chemicals could impart to the particles, limiting their applicability for biomedical purposes [27,28].

In the "top-down" approach the starting material in the macro or micro scale is reduced to the nanoscale size through mechanical or physical processes including ball milling, lithography,

radiolysis, thermolysis, sonolysis and laser ablation [29]. An example is the photochemical synthesis proposed by Shang, who synthesized gold nanoparticles in the presence of anionic or cationic surfactants by Uv-radiation of gold (III) chloride hydrate without alternative reducing agents [30]. Another interestingly approach was propounded by Yusof who produced gold nanoparticles showing different shapes using High Intensity Focused Ultrasound (HIFU) [31]. In the late 1990's Van Duyne developed a template-base synthesis using a shadow-mask approach: after assembling polymer nanospheres on a flat surface creating a two-dimensional close-packed array, gold was deposited into the interstitial spaces. Then, removing the template, an ordered array of gold nanoparticles is obtained [32]. Usually, top-down methods are less used than bottom-up approaches since requiring a dedicated instrumentation and, if not well optimized, produce nanoparticles of wide size and morphology distribution. However, the minor using of chemical substances than that requested for the chemical synthesis makes them appealing as greener methodologies, which may also overcome limits of green strategies actually exploited. Nowadays, green syntheses of gold nanoparticles are performed by using a natural component extracted by plants [33,34], bacteria [35,36] or fungi [37] as reducing agent. These methods provide a simple and safe approach to synthesize gold nanoparticles but suffer of the presence of unnecessary substances and relatively low particles stability. Among many physical methods may overcome some of these grave drawbacks, the most promising is the Laser Ablation Synthesis in Solution (LASiS) since combines benefits of chemical and green strategies. Gold nanoparticles used for this work were synthesized by this approach. For this reason, LASiS is discussed in detail in the following sub-paragraph.

Laser Ablation Synthesis in Solution

Laser Ablation is a low-cost, versatile and easy to execute technique applied in heterogeneous disciplines (e.g. in surgery to resect tissues, in mass spectroscopy for the matrix assisted laser desorption ionization of samples) for the removal of material from the surface of an object through vaporization and erosion processes [38]. The application in liquids for the synthesis of nanoparticles was pioneered by Henglein, who produced colloidal solutions of gold, nickel and carbon ablating the corresponding bulk materials in water and various organic solvents [39].

The basic experimental set-up for LASiS (Figure 7 [40]) consists in a pulsed laser and optics focusing the laser beam on a metal bulk target, which can be either a single piece or pressed power, immersed in a liquid solution. Due to the complexity of the process, the current understanding of LASiS is still partly fragmented. The main known stages are reassumed in Figure 8 [40]. The process starts with the penetration of the laser beam into the liquid. At this stage, the solvent absorption of the laser light

must be reduced to assure that the laser energy requested for the ablation reaches the target.

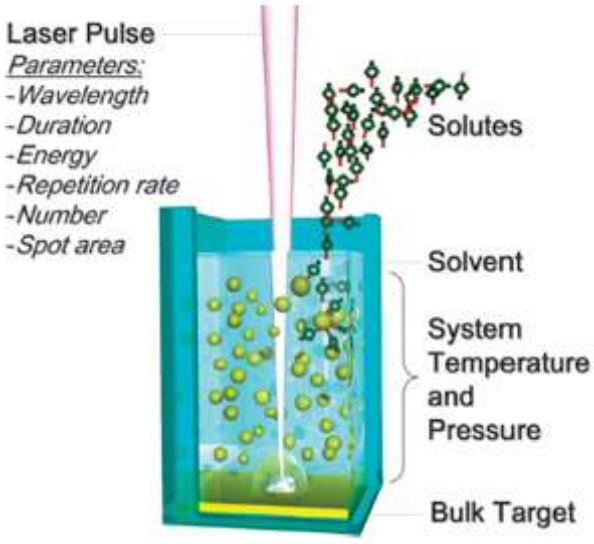

Figure 7. Experimental set-up and main experimental parameters for LASiS.

To reduce the solvent absorption, besides having no more than 1-2 cm of liquid above the target, the solution should be transparent to the laser wavelength or, at least, the energy delivered to the target should be orders of magnitude larger than that absorbed by the liquid [41]. For this purpose, gold nanoparticles were synthesized for this work using nanosecond pulses at 1064 nm from a Nd:YAG laser and water as solvent: in this condition the solvent absorption is negligible. When the laser pulse reaches the metal target instantaneous multiphoton absorption induces the detachment of the ablated material from the irradiated area [42]. The huge temperature difference between the irradiated and non-irradiated zones allows the target to efficiently dissipate heat [43]. As a result, the detachment of ablated materials occurs mainly by thermal processes, such as vaporization, normal boiling and explosive boiling, in a region almost coincident with the laser spot. If the laser pulse is shorter than 10^{-7} s the prevalent mechanism is the explosive boiling: the material, superheated above its critical temperature, expellees in the form of a plasma plume containing highly ionized species and simultaneously emits light and shockwaves. If the laser pulse is of the order of 10^{-11} s the laser beam overlap with the plasma plume in time and space. As a result, a phenomenon called “plasma shielding” occurs: due to the absorption of the laser energy, the temperature and the lifetime of the plume increase leading to the reduction of the energy delivered to the target [44,45]. From 10^{-10} s to 10^{-7} s the plasma plume containing the ablated material expands into the surrounding liquid and cools down. At this stage liquid drops, solid fragments and molecular clusters composing the ablated material induce nucleation and growth of small nuclei of metal particles, which act as preferential site of growth and coalescence

for the final particles. Usually, nanoparticles produced are almost spherical because the interface energy minimizes if the lattice rearranges to this shape, although multiple laser pulses are needed to be absorbed by a single particle to produce a spherical shape [46]. After 10^{-7} s the plasma plume extinguishes releasing an energy that generates a cavitation bubble, which, expands and then collapses emitting a second shockwave [47]. Nanoparticles mainly form during the bubble collapses. If LASiS occurs in water, a relevant modification is the surface oxidation of a small part (less than 10%) of its surface [48,49].

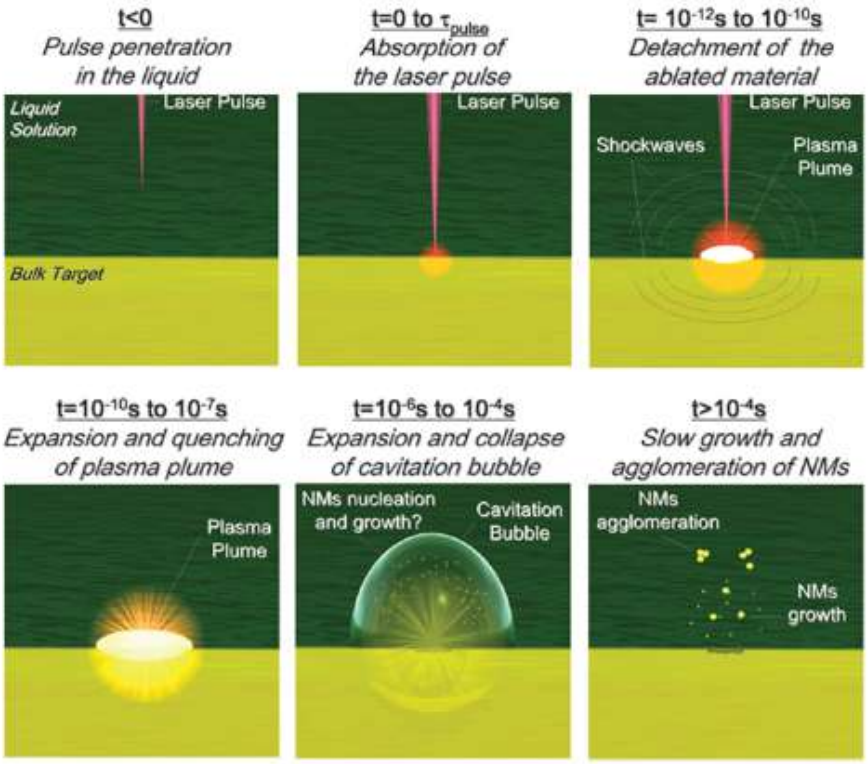

Figure 8. Timeline of LASiS.

Many parameters influence the nanoparticles synthesis by laser ablation. Several of them concern the materials involved in the process such as the bulk target, the solvent and the presence of solutes. Others deal with the laser and include the wavelength, the duration, the fluence and the number of pulses. The main obvious parameter is the target material. It has been proved that different materials, besides showing different reactivity, yield diverse products under the same experimental conditions. Moreover, products may differ from the bulk target regarding the phase and the composition. Being the nanoparticles used for this work made of gold, parameters influencing the LASiS of gold nanoparticles are discussed subsequently.

Material parameters: during LASiS, in addition to the ablated material, several species can participate to chemical reactions including both other solutes and the solvent. Solutes can influence the laser ablation by either modifying physical and chemical properties of the solvent but especially because they interact directly with the ablated material. The physical interaction between the solutes and the material may occur at different levels of intensity. Usually solutes adsorb by electrostatic interactions or chemical bonds on the nanoparticles surface creating a molecular layer that limits the particles growth [48]. However, they can also strongly interact with the ablated material modifying the nanoparticle composition, mainly on their surface.

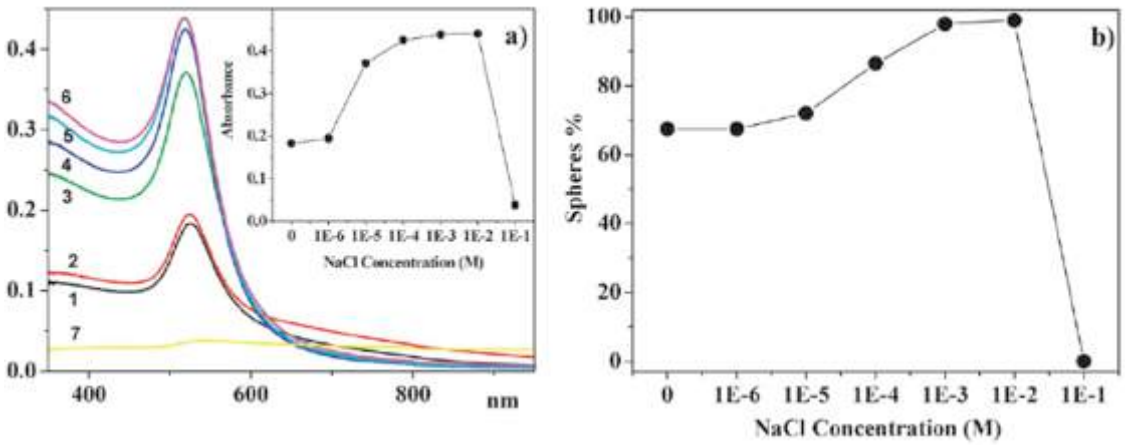

Figure 9. LASiS of gold nanoparticles in water with increasing concentration of NaCl (a) UV-vis spectra. The inset shows the absorbance of the LSPR for the solutions. (b) Percentage of spherical nanoparticles obtained by the fitting of the spectra using the Mie-Gans theory.

An example is the oxidation of the gold nanoparticles surface that occurs during the laser ablation in water (Figure 9 [50]). In particular the presence in solution of chloride anions promote the dissociation of Au-O-Au bonds leading to the formation of $Au\text{-}O^-$ and $Au\text{-}Cl^-$ groups. These groups, increasing the negative charge on the particles surface, enhance the stability of the colloidal system. However, if the anions concentration excessively increases, the electrostatic interaction due to the modified dielectric constant is reduced and particles aggregate and precipitate. In order to obtain stable solutions of nanoparticles, a proper amount of salt has to be added to the solvent. Previous works in the laboratory in which this thesis was developed found that if gold nanoparticles are synthetized in a NaCl 10^{-5} M water solution, mainly spherical particles with dimension ranging from 18 nm to 22 nm are obtained. The colloidal solution is stable for months without the use of any stabilizing agent due to the negative charges generated by the partial oxidation of the surface, that is less than 10 % [50]. If the synthesis is performed in organic solvents rather than in water, gold nanoparticles of different composition and structure are obtained pointing out the impact of the solvent on LASiS. In particular,

gold nanoparticles synthesized in solvents like ethanol, tetrahydrofuran, dimethylsulphoxide, acetonitrile and dimethylformamide show a lower average size and a higher fraction of non-spherical particles than those obtained in water. These effects are ascribed to the capping action of the organic solvent or its by-products generated during the ablation process. Adsorbing on the gold surface, these agents prevent the nuclei coalescence and, if the capping coating is not complete, allow the nanoparticle growth only along the portion of the surface remained uncovered. Moreover, the coating makes the nanoparticles more prone to aggregate and precipitate on the medium-long term by reducing the surface charge and inhibiting the surface oxidation processes [49,51].

Laser parameters: the main laser parameters involved in LASiS are: pulse wavelength, energy and duration. Since the overlap between the already formed nanoparticles and the laser light reduces the amount of energy that reaches the target and induces particles modifications such as photofragmentation or melting, laser wavelengths that are not absorbed by the particles are preferred. To synthesize gold nanoparticles, which absorb the Uv and visible (Uv-vis) light, the use of lasers in the near infrared (NIR) is suggested [50,52]. Rising the pulse energy, multiple mechanisms of material detachment from the target such as fragmentation, vaporization and boiling become possible increasing the amount of the ablated material in the plume and, consequently, enhancing the nanoparticles productivity [53]. However, high energies induce nanoparticles modifications and the extension of size and morphology distributions [41]. Regarding the pulse duration, several studies demonstrated the huge impact on particles size, structure and composition [45,53]. With ns laser pulses, like these used in this thesis project, the laser pulse and the ablated material coexist for a certain time due to the plasma shielding. Under these conditions, melted drops ejected from the target can more easily vaporize creating a homogeneous plume that, cooling down, generates nanoparticles with a sharper size distribution with respect to those obtained with fs and ps pulses. Other laser parameters influencing the LASiS are the spot area, the number of pulses and the repetition rate. Therefore, experimental conditions must be optimized to increase the productivity without altering the desired nanoparticles features [40].

To sum up, LASiS is a technique that owns more pro than cons compared to the more conventional chemical strategies. The LASiS pro are:

a) the possibility to synthesize a variety of nanomaterials in several liquid solutions with the same experimental equipment;

b) the eco sustainability, because LASiS does not require chemical reagents and does not produce waste;

c) the relative low cost since, besides the experimental set-up, minimal chemical precursors are

requested;

d) the absence of surfactants on the nanoparticles surface. This provides great opportunities for an easier procedure of surface functionalization that does not require ligands exchange reactions. Moreover, the toxicity of the system, usually ascribed to thiols and disulphides frequently used as capping agents, is reduced.

On the other hand, the main cons are:

a) the difficulty to scale the production up to the gram scale;

b) the lower control over the size and shape distributions.

Among a number of investigation techniques such as Dynamic Light Scattering (DLS) and X-ray, TEM analysis and Uv-vis-NIR spectroscopy are the most exploited to evaluate LASiS results. Uv-vis-NIR spectroscopy provides information about the particles shape and size through the analysis of the LSPR: the presence of a sharp plasmon band close to 520 nm is the proof that gold nanoparticles with a spherical shape and a diameter of about 20 nm have been obtained [54]. Besides confirming the nanoparticles spherical shape, TEM analysis is complemented to Uv-vis-NIR spectroscopy to identify the concomitant presence of particles with spheroidal or irregular forms, which contribute to the overall plasmon band at wavelength longer than the plasmon peak [55].

Previous works in the research group in which this project was developed, found that gold nanoparticles with a sharp size distribution centred at 20 nm of diameter and with a mainly spherical morphology can be synthesized by LASiS under specific experimental conditions. In particular, gold nanoparticles synthesized for this work were obtained by the laser ablation under weak magnetic stirring of a 99.999% pure gold target in 10^{-5} NaCl bidistilled aqueous solution. A ns pulsed Nd-YAG laser operating at 1064 nm with a repetition rate of 10 Hz, a pulse duration of 9 ns and a fluence of 1 J/cm^2 was used [56]. In addition to TEM and UV-vis-NIR analysis, synthesis results were evaluated through a procedure based on the fitting of the Uv-vis-NIR spectrum of the colloidal solution with the Mie and Gans models [55].

The fitting program was used to evaluate the particles size with accuracy of the order of 6% and to estimate both the particles concentration and the fraction of non-spherical or aggregated nanoparticles (Figure 10 [50]). Gold nanoparticles synthesized under these conditions are stable in solution for long times because they are already charged when synthesized (estimated ζ-potential larger than −30 mV). Being the surface clean from surfactants, nanoparticles can be easily functionalized with various ligands. Biocompatibility problems usually ascribed to the presence of stabilizing molecules requested in many nanoparticles chemical syntheses are also avoided.

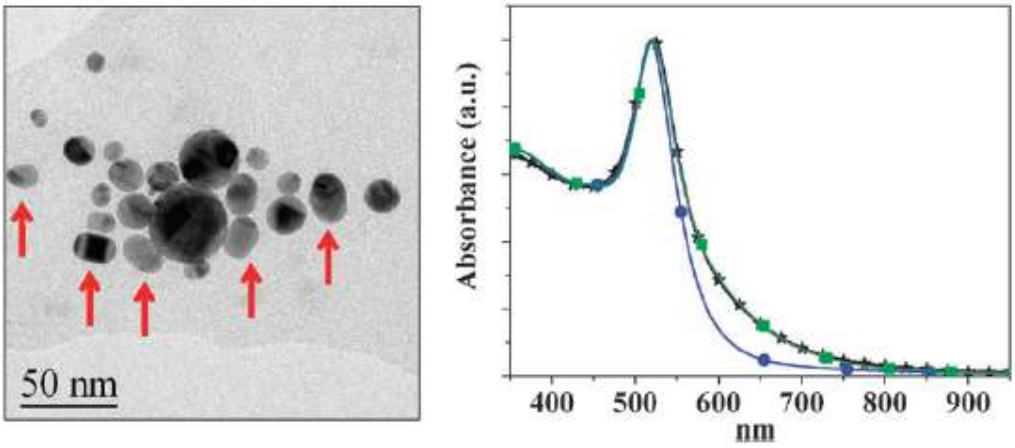

Figure 10. On the left, TEM image of gold nanoparticles obtained by LASiS in water. The red arrows indicate particles with spheroidal shape. On the right, experimental Uv-vis-NIR spectrum of the nanoparticles solution (stars) overlapped either to the Mie fitting model for spherical particles (circles) and to the Mie-Gans fitting model for spherical and spheroidal particles (squares).

Synthesis and Characterization of Gold Nanostructures

Gold nanostructures synthesized for this PhD project as SERRS biosensors for early stage cancer screening use an indirect detection approach: the analyte molecule, that is the receptor overexpressed in the tumour, is recognized by the targeting peptides on the nanosystems. Then, by mapping the area of interest that could be, for the preclinical evaluation of the biosensor a murine tumour model or in vitro specimens, the signals of the SERRS label anchored to the nanostructures surface are recorded both proving the presence of the target molecule and providing localization information. To build these SERRS biosensors, three main components are therefore claimed:

a) gold nanoparticles as substrate; b) the SERRS reporter; c) peptides as targeting moieties.

The strategies for the synthesis of gold nanoparticles and peptides have been deeply discussed in preceding paragraphs. Subsequently, the procedure used for assembling the components to the final structures (Figure 11), consisting in the preparation of the substrate followed by its functionalization with both the SERRS label and the peptides, is outlined.

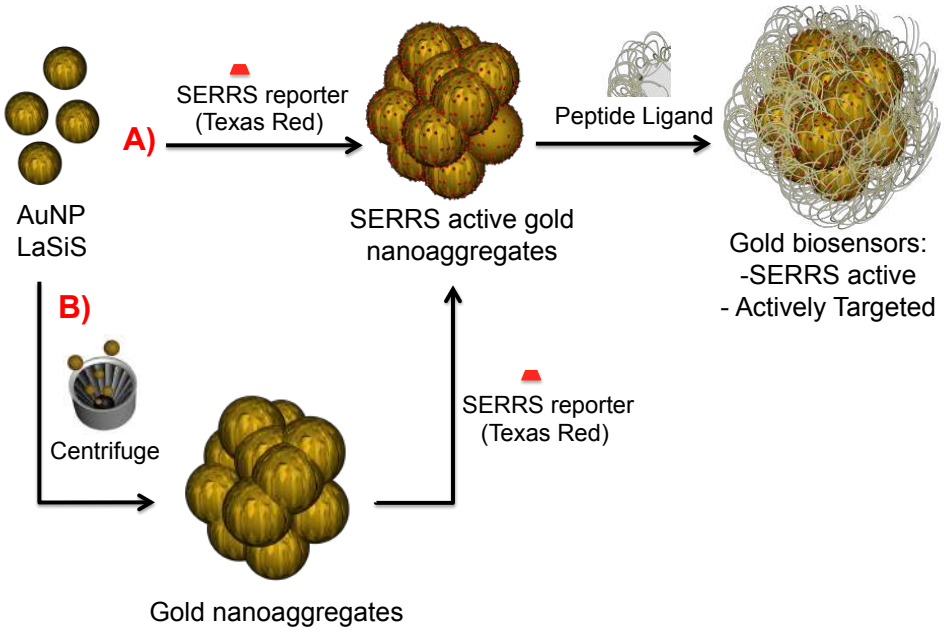

Figure 11. Synthetic scheme for the preparation of SERRS biosensors.

Substrate preparation and functionalization with the SERRS label: in order to achieve an efficient SERS enhancement, the rational design of the substrate material is of a great importance and several parameters must be taken into account. Nanoparticles as substrate can be employed as single or assembled particles. Regarding single nanoparticles, the size is a pivotal feature for SERS efficiency

and particles dimensions ranging from 10 to 100 nm demonstrate to exhibit the strongest enhancement. This is because particles smaller than 10 nm do not own enough surface conduction electrons to sustain significant plasmons whereas particles larger than 100 nm, interfering with the propagation of the radiation, reduce the overall enhancement [57]. On the other hand, the assembling of nanoparticles provides great opportunities to achieve extraordinary SERS enhancement due to the Hot Spots at the interparticle junctions. Moreover, the aggregation causes the red shift of the LSPR allowing the use of far visible and NIR laser. In this condition the laser beam penetrate more deeply into the tissues without damaging healthy cells, a very important benefit for biomedical applications [58]. However, it is important to remember that as the size of the substrate increases, the clearance from the body due to the uptake by the reticuloendothelial system is promoted and the cellular internalization is drastically reduced. Dimensions above 200 nm should be therefore avoided [59]. To date, different procedures have been extensively investigated to assemble nanoparticles such as layer-by-layer assembling [60], solvent-induced evaporation [61], liquid-liquid interface assembly [62] and ions, small molecules or polymers induced assembly [63]. By controlling the assembling process using molecular linkers [64], asymmetrically functionalized nanoparticles [65] or auditable aggregation kinetics [66], aggregates of different morphologies can be generated. Concerning gold nanoparticles, recently linear aggregates for SERS applications were obtained by using siloxane surfactants [67]. Chen et all. reported the use of inorganic salts (e.g. NaCl) to induce particles pre-aggregation followed by the isolation of gold assemblies composed by a mixture of monomers and polymers via gradient centrifugation [66]. In another approach, gold nanoparticles were repeatedly centrifuged and re-suspended to obtain aggregated particles with a sufficient number of Hot Spots for a strong SERS signal [56]. Marvellously, several studies demonstrated that bifunctional SERS labels could be exploited to induce gold nanoparticles to assemble into aggregates with a huge SERS enhancement. In this constructs, the SERS reporter not only produces the Hot Spots at the interparticle gaps, but also places within them providing an additional enhancement over substrates in which the label is exclusively bound to the external surface [59,68]. Even though former biosensors (see Chapter 3) were constructed by adopting the strategy of first aggregating gold nanoparticles by repeatedly centrifugation and re-suspension and then functionalizing the aggregates with the SERS label (Strategy B in Figure 11), as suggested by a previous work [56] of the laboratory in which this PhD project was developed, mainly biosensors (see Chapters 4-7) were obtained by using a bifunctional SERRS reporter (Strategy A in Figure 11). In order to further enhance the Raman signal invoking the SERRS effect, a bithiolated derivative of Texas Red (from here on TR) that satisfies the resonant conditions with the LSPR of gold aggregates and the excitation wavelength used to record the spectra (He-Ne laser operating at

633 nm) was chosen (Figure 12). The chemical modification of this dye with thiol groups guarantees the strong bond to the gold surfaces, as already discussed in Chapter 1.

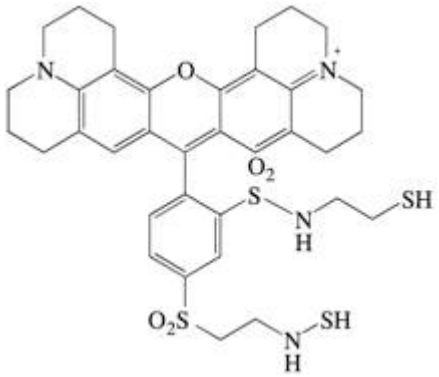

Figure 12. Bithiolated derivative of Texas Red (TR) used as SERRS label.

Both strategies (A and B in Figure 11) for the substrate preparation and functionalization with the SERRS reporter induce gold nanoparticles produced by LASiS to assemble into nanoaggregates of 10–20 particles with an overall dimension of the order of 100 nm, as demonstrated by transmission electron microscopy (TEM) images (Figure 13). Dynamic light scattering and ζ-potentials measurements revealed a hydrodynamic diameter of about 110 nm and a ζ-potential of -10 mV.

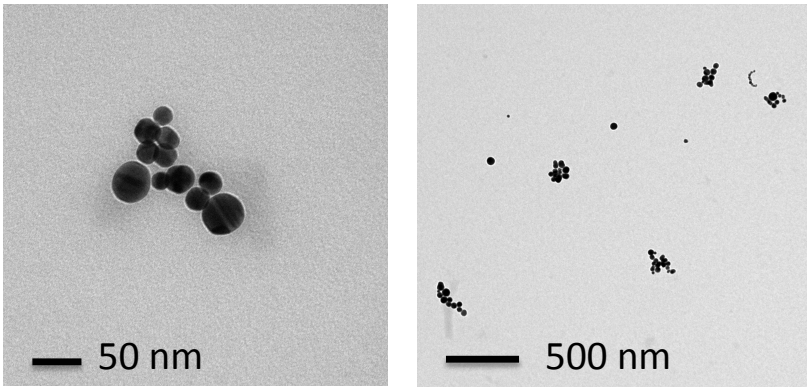

Figure 13. TEM images of aggregated nanoparticles.

The extent of aggregation and the colloidal stability were controlled by recording the UV-vis-NIR spectrum (Figure 14): plasmon resonance bands above 600 nm indicate the aggregation of gold nanoparticles but a large extinction above 900 nm points out that the aggregation is too extended and leads to the instability of the colloidal solution. Raman spectra allowed verifying the occurred functionalization with the SERRS reporter. The SERRS spectrum (Figure 14) show two intense bands at 1505 and 1649 $cm^{-1,}$ which have been assigned, respectively, to the stretching of carbon-nitrogen and carbon-carbon bonds and, in the first case, with the participation of the scissoring of the CH_2

group [69]. After cleaning from non-reacted SERRS labels by centrifugation, the sulphur affinity for gold was exploited to functionalize the aggregates with peptide ligands.

Functionalization with peptide ligands: to date, the most common methods to obtain targeted nanostructures involve the preparation of the nanoparticles followed by the bonding of the targeting ligands to the already formed nanostructures employing covalent or non-covalent conjugation strategies. Non-covalent methods proceed by physical association of the targeting moieties to the particles surface. Despite the advantage of avoiding rigorous chemical reactions, weak bonding and low control over the process and orientation of the ligand on the surface limit these strategies [70]. Among many covalent methods, some are based on the coupling of the reactive groups of the ligands with those on the particles (e.g. thiols, amines and carboxylic acids [71]). Many others exploit "click-reactions" (e.g. copper-catalysed azide–alkyne cycloaddition, strain-promoted azide–alkyne cycloaddition, thiol–ene reaction and oxime ligation) that, occurring with high efficiency, assure high yields [72]. However, these approaches result in significant batch-to-batch variations in coupling yields and lead to highly heterogeneous nanoparticle populations in number and conformation of peptides on the surface [73]. For this work, the strategy of first synthesizing the targeting ligand and then to link it to gold nanoaggregates already functionalized with the SERRS label was adopted. This approach assures the precise control over the peptides incorporation on the aggregates eliminating the batch-to-batch variability and guaranteeing homogeneous nanostructures. Peptides were synthesized on a solid support following the procedure described in the paragraph "Synthetic strategy of peptides". By exploiting the sulphur affinity for gold of the extra thiol group inserted in the peptide sequence, the ligands were conjugated to the nanoparticles by simply mixing the solution with that of the aggregates. The number of peptides covering on average each nanoparticle was estimated by exploiting the Ellman test for thiols [74] of the ligand solution before and after the functionalization of the nanostructures. Whenever possible, as in the case of peptides GE11 and PreS1, Uv-vis absorption of aromatic side chains of tryptophan and tyrosine amino acids in the sequence was also exploited. Several thousands of ligands were found to be linked per nanoparticle for all peptide derivatives. Moreover, by mixing ligands and particles at specific stoichiometry, the precise control over the number of peptides on each nanoparticle was achieved without altering the reproducibility of the process. The final nanostructures were characterized by recording Uv-vis-NIR and Raman spectra to confirm the particles aggregation and the presence of the SERRS reporter after the anchoring of the targeting motifs. Typical Uv-vis-NIR and Raman spectra are reported as an example in Figure 14. No significant variation was usually observed between the Uv-vis-NIR spectra of gold nanoaggregates before and after the anchoring of peptide ligands (see red and blue lines respectively in Figure 14).

This evidence indicates that the functionalization process does not induce substantial modification to gold nanoaggregates. Moreover, since an eventual entrapment of the ligands between the nanoparticles could induce modifications to their state of aggregation, it suggests that peptides are placed on the external surface of the nanostructures. Dynamic light scattering measurements demonstrated that the nanostructures have dimensions of on average 200 nm, also confirmed by TEM images, and ζ-potentials, showing small values, ensure the stability of the colloidal solution.

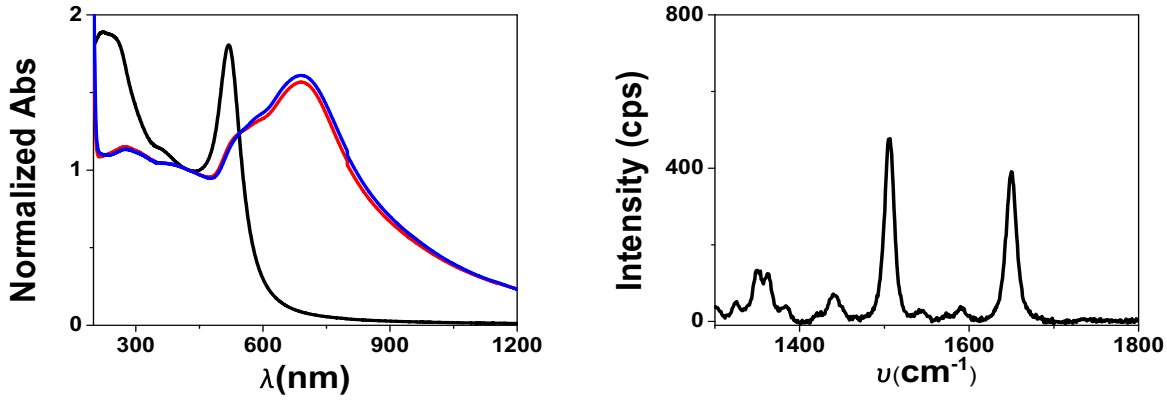

Figure 14. SERRS (on the right) and Extinction (on the left) spectra of the nanostructures and their evolution at various steps of functionalization: gold nanoparticles synthesized by LASiS (black line), functionalization with the SERRS reporter (red line) and with the targeting peptide (blue line). As aid to eyes, extinction spectra were normalized at 425 nm.

Molecular Dynamics calculations

Molecular dynamics (MD) simulations provide the methodology to understand the assembling properties of molecules in terms of their structure and the microscopic interactions between them as a function of time. As a complement to conventional experiments, MD calculations act as a bridge between theory and experiment allowing addressing specific questions about the properties of the system, which are usually not available from experimental measurements. Moreover, being the simulation completely under the control of the user, the removal or the modification of specific contributions make possible to investigate on their role in determining a given system property. Despite initially situated merely in the physics context, MD is nowadays used also by scientists interested in investigating chemical and biological problems. As examples, it has been used to interpret the single-walled carbon nanotubes nucleation and growth process as well as to predict their mechanical behaviour [75], to investigate on structural and physical properties of metal nanoparticles [76] and to study the self-assembling process of fullerene molecules [77]. In the biomedical realm, MD simulations proved to be useful for Drug Design [78] and have contributed to understand the physical basis of structure and function of biomolecules for those internal motions, resulting in conformational changes, play an essential role [79, 80]. Electrons transfer in biological systems [81], enzymatic-reaction mechanisms [82] and protein folding and unfolding [83] have also been studied. The aim of MD calculations is to predict the evolution of the atoms positions of the system over time. To this end, the evaluation of the Potential Energy Surface related to each conformation is required. The method uses a differentiable gradient of the energy function related to the forces acting on individual atoms, which can be derived from a set of many inter-atomic potential energy functions commonly named as Force Fields [84,85]. In literature many Force Fields used to describe various systems are reported. A general form used in GROMOS, an acronym of the GROningen MOlecular Simulation computer program package, is reported in Equation 1 [86]:

$$\vec{\mathbb{F}}_i = -\vec{\nabla}_{r_i} V(\vec{r}_1, \vec{r}_2 \ldots \vec{r}_N; p)$$

$$V = V_{\text{bond}} + V_{\text{angle}} + V_{\text{imp.dih.}} + V_{\text{tors.dih.}} + V_{\text{LJ}} + V_{\text{Coul.}}$$

Equation 1. Functional form of the Force Field used in GROMOS.

where F_i is the force acting on the atoms and $V(r_N)$, where $rN = (r_1; r_2; : : : r_N)$ represents the complete set of 3N atomic coordinates, is the potential energy of the system. p indicates a set of parameters depending on the system (e.g. stretching constant, bending constant) that implicitly takes into account electrons effects. These parameters are usually obtained from quantum-mechanic *ab-initio*

calculations (e.g. Density Functional Theory or other methods) or derived by fitting the experimental data collected by using various techniques such as Raman and IR spectroscopy. The total energy potential of the system of atoms is the sum of several contributions such as variations of bond length (V_{bond}, covalent bond interactions) and bond angles (V_{angle}, covalent bond-angle interactions; $V_{imp.\ dih.}$, improper dihedral interactions; $V_{tors.\ dih.}$, torsional dihedral interactions) with respect to reference values. Interactions between non-bonded atoms are calculated considering electrostatic ($V_{Coul.}$, Coulomb interactions) and van der Waals ($V_{L.J.}$, Lennard-Jones interactions) interactions. For this work, MD calculations were carried out thanks to the cooperation with the group of Professor A. Palleschi of the Department of Chemical Science and Technology of the University of Rome "Tor Vergata". Simulations were carried out using the GROMACS v5.0.7 software package [87]. The Gromos53A6 force field parameters were used for the simulation of peptides [86] while other parameters needed to describe other components of each system were taken from literatures [88,89]. Peptide density used for simulations were settled on around 0.3 peptides nm^{-2}. This value is lower than experimental results calculating the density as the number of peptides on a nanoparticle with a diameter of 20 nm, ranging from approximately 1 to 8 peptides nm^{-2} depending on the nanostructures. However, considering that the nanoparticles functionalization involves the formation of several peptide layers, as demonstrated in Chapter 5, experimental density of a peptide monolayer is supposed to be close to effective density in MD simulations. MD calculations are discussed in detail in the Experimental Section of the following chapters.

References

1. Gauthier, M. A., Klok, H. A., Peptide/protein-polymer conjugates: synthetic strategies and design concepts. *Chemical Communications.* **2008**. 23, pp 2591-2611.

2. Spicer, C. D., Jumeaux, C., Gupta, B., Stevens, M. M., Peptide and protein nanoparticle conjugates: versatile platforms for biomedical applications. *Chemical Society Reviews.* **2018**. 47 (10), pp 3574-3620.

3. Hamley, I. W., PEG-Peptide Conjugates. *Biomacromolecules.* **2014**. 15 (5), pp 1543-1559.

4. Liu, Q. T., Wang, J. F., Boyd, B. J., Peptide-based biosensors. *Talanta.* **2015**. 136, pp 114-127.

5. de la Rica, R., Matsui, H., Applications of peptide and protein-based materials in bionanotechnology. *Chemical Society Reviews.* **2010**. 39 (9), pp 3499-3509.

6. Chandrudu, S., Simerska, P., Toth, I., Chemical Methods for Peptide and Protein Production. *Molecules.* **2013**. 18 (4), pp 4373-4388.

7. Merrifield, R. B., Solid Phase Peptide Synthesis. I. The Synthesis of a Tetrapeptide. *J. Am. Chem. Soc*. **1963**. 8*5*, pp 2149–2154.

8. Merrifield, R. B., Solid Phase Synthesis (Nobel Lecture). *Angew. Chem., Int. Ed*. **1985**. 24, pp 799-810.

9. Hill, S. A., Gerke, C., Hartmann, L., Recent Developments in Solid-Phase Strategies towards Synthetic, Sequence-Defined Macromolecules. *Chemistry-an Asian Journal.* **2018**. 13 (23), pp 3611-3622.

10. Palomo, J. M., Solid-phase peptide synthesis: an overview focused on the preparation of biologically relevant peptides. *Rsc Advances.* **2014**. 4 (62), pp 32658-32672.

11. Merrifield, R. B., The role of the support in solid phase peptide synthesis. **1984**. 16, pp 173-178.

12. Gongora-Benitez, M., Tulla-Puche, J., Albericio, F., Handles for Fmoc Solid-Phase Synthesis of Protected Peptides. *Acs Combinatorial Science.* **2013**. (5), pp 217-228.

13. Chan, W. C., White, P. D., Fmoc solid phase peptide synthesis: a practical approach. *Oxford University Press*. **2000**.

14. Isidro-Llobet, A., Alvarez, M., Albericio, F., Amino Acid-Protecting Groups. *Chemical Reviews.* **2009**. 109 (6), pp 2455-2504.

15. Montalbetti, C., Falque, V., Amide bond formation and peptide coupling. *Tetrahedron.* **2005**. 61 (46), pp 10827-10852.

16. Valeur, E., Bradley, M., Amide bond formation: beyond the myth of coupling reagents. *Chemical Society Reviews.* **2009**. 38 (2), pp 606-631.

17. Lloyd-Williams, P. A., F.Giralt, E., Chemical Approaches to the Synthesis of Peptides and Proteins. *CRC Press*. **1997**.

18. Li, Z. H., Zhao, R. J., Wu, X. H., Sun, Y., Yao, M., Li, J. J., Xu, Y. H., Gu, J. R., Identification and characterization of a novel peptide ligand of epidermal growth factor receptor for targeted delivery of therapeutics. *Faseb Journal.* **2005**. 19 (14), pp 1978-1985.

19. Vonlaufen, A., Wiedle, G., Borisch, B., Birrer, S., Luder, P., Imhof, B. A., Integrin alpha(v)beta(3) expression in colon carcinoma correlates with survival. *Modern Pathology.* **2001**. 14 (11), pp 1126-1132.

20. Deng, Q., Zhai, Q., Michel, M. L., Zhang, J., Qin, J., Kong, J. J., Zhang, X. X., Budkowska, A., Tiollais, P., Wang, Y., Xie, Y. H., Identification and characterisation of peptides that interact with hepatitis B virus via the putative receptor binding site. *J. Virol.* **2007**. 81, pp 4244–54.

21. Dash, S., Rao, K. V. N., Panda, S. K., Receptor for Pre-S1(21-47) component of hepatitis-B on the liver-cell-role in virus-cell interaction. *J. Med. Virol.* **1992**. 37 (2), pp 116-121.

22. Sanchez, F., Sobolev, K., Nanotechnology in concrete - A review. *Construction and Building Materials.* **2010**. 24 (11), pp 2060-2071.

23. Turkevich, J. S., P.C. Hillier, J., A study of the nucleation and growth processes in the synthesis of colloidal gold. *Discuss. Faraday Soc*. **1951**. 11, pp 55-75.

24. Frens, G., Controlled Nucleation for the Regulation of the Particle Size in Monodisperse Gold Suspensions. *Nature Physical Science.* **1973**. 241, pp 20-22.

25. Schmid, G., Pfeil, R., Boese, R., Bandermann, F., Meyer, S., Calis, G. H. M., van der Velde, J. W. A., $Au_{55}[P(C_6H_5)_3]_{12}Cl_6$ a Gold Cluster of an Exceptional size. *European Journal of Inorganic Chemistry*. **1981**. 114, pp 3634-3642.

26. Brust, M., Walker, M., Bethell, D., Schiffrin, D. J., Whyman, R., Synthesis of thiol-derivatized gold nanoparticles in a 2-phase liquid-liquid system. *Journal of the Chemical Society-Chemical Communications.* **1994**. 7, pp 801-802.

27. Dreaden, E. C., Alkilany, A. M., Huang, X. H., Murphy, C. J., El-Sayed, M. A., The golden age: gold nanoparticles for biomedicine. *Chemical Society Reviews.* **2012**. 41 (7), pp 2740-2779.

28. Gharatape, A., Salehi, R., Recent progress in theranostic applications of hybrid gold nanoparticles. *European Journal of Medicinal Chemistry.* **2017**. 138, pp 221-233.

29. Kelsall, R., Hamley, I. W., Geoghegan, M., Nanoscale Science and Technology. *John Wiley & Sons*. **2005**.

30. Shang, Y. Z., Min, C. Z., Hu, J., Wang, T. M., Liu, H. L., Hu, Y., Synthesis of gold nanoparticles by reduction of $HAuCl_4$ under UV irradiation. *Solid State Sciences.* **2013**. 15, pp 17-23.

31. Yusof, N. S. M., Ashokkumar, M., Sonochemical Synthesis of Gold Nanoparticles by Using High Intensity Focused Ultrasound. *Chemphyschem.* **2015**. 16 (4), pp 775-781.
32. Hulteen, J. C., Vanduyne, R. P., Nanosphere lithography - a materials general fabrication process for periodic particle array surfaces. *Journal of Vacuum Science & Technology a-Vacuum Surfaces and Films.* **1995**. 13 (3), pp 1553-1558.
33. Wang, C., Mathiyalagan, R., Kim, Y. J., Castro-Aceituno, V., Singh, P., Ahn, S., Wang, D., Yang, D. C., Rapid green synthesis of silver and gold nanoparticles using Dendropanax morbifera leaf extract and their anticancer activities. *International Journal of Nanomedicine.* **2016**. 11, pp 3691-3701.
34. Kim, H. S., Seo, Y. S., Kim, K., Han, J. W., Park, Y., Cho, S., Concentration Effect of Reducing Agents on Green Synthesis of Gold Nanoparticles: Size, Morphology, and Growth Mechanism. *Nanoscale Research Letters.* **2016**. 11, pp 9.
35. Kumar, C. G., Poornachandra, Y., Chandrasekhar, C., Green synthesis of bacterial mediated anti-proliferative gold nanoparticles: inducing mitotic arrest (G2/M phase) and apoptosis. *Nanoscale* **2018**. 10 (41), pp 19639-19639.
36. Reddy, A. S., Chen, C. Y., Chen, C. C., Jean, J. S., Chen, H. R., Tseng, M. J., Fan, C. W., Wang, J. C., Biological Synthesis of Gold and Silver Nanoparticles Mediated by the Bacteria Bacillus Subtilis. *Journal of Nanoscience and Nanotechnology.* **2010**. 10 (10), pp 6567-6574.
37. Tidke, P. R., Gupta, I., Gade, A. K., Rai, M., Fungus-Mediated Synthesis of Gold Nanoparticles and Standardization of Parameters for its Biosynthesis. *Ieee Transactions on Nanobioscience.* **2014**. 13 (4), pp 397-402.
38. Phipps, C., Laser Ablation and its Applications. *Springer Heidelberg*. **2007**.
39. Fojtik, A., Henglein, A., Laser ablation of films and suspended particles in a solvent - formation of cluster and colloid solutions. *Berichte Der Bunsen-Gesellschaft-Physical Chemistry Chemical Physics.* **1993**. 97 (2), pp 252-254.
40. Amendola, V., Meneghetti, M., What controls the composition and the structure of nanomaterials generated by laser ablation in liquid solution? *Physical Chemistry Chemical Physics.* **2013**. 15 (9), pp 3027-3046.
41. Kabashin, A. V., Meunier, M., Synthesis of colloidal nanoparticles during femtosecond laser ablation of gold in water. *Journal of Applied Physics.* **2003**. 94 (12), pp 7941-7943.
42. Momma, C.;, Chichkov, B. N., Nolte, S., vonAlvensleben, F., Tunnermann, A., Welling, H., Wellegehausen, B., Short-pulse laser ablation of solid targets. *Optics Communications.* **1996**. 129 (1-2), pp 134-142.

43. Zhigilei, L. V., Kodali, P. B. S., Garrison, B. J., A microscopic view of laser ablation. *Journal of Physical Chemistry B.* **1998**. 102 (16), pp 2845-2853.
44. Miotello, A., Kelly, R., Laser-induced phase explosion: new physical problems when a condensed phase approaches the thermodynamic critical temperature. *Applied Physics a-Materials Science & Processing.* **1999**. 69, pp S67-S73.
45. Perez, D., Beland, L. K., Deryng, D., Lewis, L. J., Meunier, M., Numerical study of the thermal ablation of wet solids by ultrashort laser pulses. *Physical Review B.* **2008**. 77 (1), pp 9.
46. Piotto, V., Litti, L., Meneghetti, M., Synthesis and Shape Manipulation of Anisotropic Gold Nanoparticles by Laser Ablation in Solution. *Journal of Physical Chemistry C.* **2020**. 124 (8), pp 4820-4826.
47. Tsuji, T., Tsuboi, Y., Kitamura, N., Tsuji, M., Microsecond-resolved imaging of laser ablation at solid-liquid interface: investigation of formation process of nano-size metal colloids. *Applied Surface Science.* **2004**. 229 (1-4), pp 365-371.
48. Mafune, F., Kohno, J., Takeda, Y., Kondow, T., Sawabe, H., Formation of gold nanoparticles by laser ablation in aqueous solution of surfactant. *Journal of Physical Chemistry B.* **2001**. 105 (22), pp 5114-5120.
49. Amendola, V., Polizzi, S., Meneghetti, M., Laser ablation synthesis of gold nanoparticles in organic solvents. *Journal of Physical Chemistry B.* **2006**. 110 (14), pp 7232-7237.
50. Amendola, V., Meneghetti, M., Laser ablation synthesis in solution and size manipulation of noble metal nanoparticles. *Physical Chemistry Chemical Physics.* **2009**. 11 (20), pp 3805-3821.
51. Compagnini, G., Scalisi, A. A., Puglisi, O., Production of gold nanoparticles by laser ablation in liquid alkanes. *Journal of Applied Physics.* **2003**. 94 (12), pp 7874-7877.
52. Tsuji, T., Iryo, K., Nishimura, Y., Tsuji, M., Preparation of metal colloids by a laser ablation technique in solution: influence of laser wavelength on the ablation efficiency (II). *Journal of Photochemistry and Photobiology a-Chemistry.* **2001**. 145 (3), pp 201-207.
53. Zhigilei, L. V., Lin, Z. B., Ivanov, D. S., Atomistic Modeling of Short Pulse Laser Ablation of Metals: Connections between Melting, Spallation, and Phase Explosion. *Journal of Physical Chemistry C.* **2009**. 113 (27), pp 11892-11906.
54. Kreibig, U., Vollmer, M., Optical Properties of Metal Clusters. *Springer, Heidelberg*. **1995**.
55. Amendola, V., Meneghetti, M., Size Evaluation of Gold Nanoparticles by UV-vis Spectroscopy. *Journal of Physical Chemistry C.* **2009**. 113 (11), pp 4277-4285.
56. Meneghetti, M., Scarsi, A., Litti, L., Marcolongo, G., Amendola, V., Gobbo, M., Di Chio, M., Boscaini, A., Fracasso, G., Colombatti, M., Plasmonic Nanostructures for SERRS Multiplexed Identification of Tumor-Associated Antigens. *Small.* **2012**. 8 (24), pp 3733-3738.

57. Ghosh, S. K., Pal, T., Interparticle coupling effect on the surface plasmon resonance of gold nanoparticles: From theory to applications. *Chemical Reviews.* **2007**. 107 (11), pp 4797-4862.
58. Altunbek, M., Kuku, G., Culha, M., Gold Nanoparticles in Single-Cell Analysis for Surface Enhanced Raman Scattering. *Molecules.* **2016**. 21 (12), pp 18.
59. Fabris, L., Gold-based SERS tags for biomedical imaging. *Journal of Optics.* **2015**. 17 (11), pp 114002-114016.
60. Huang, Y. P., Yang, Y., Chen, Z., Li, X., Nogami, M., Fabricating Au-Ag core-shell composite films for surface-enhanced Raman scattering. *Journal of Materials Science.* **2008**. 43 (15), pp 5390-5393.
61. Peng, S., Lee, Y. M., Wang, C., Yin, H. F., Dai, S., Sun, S. H., A Facile Synthesis of Monodisperse Au Nanoparticles and Their Catalysis of CO Oxidation. *Nano Research.* **2008**. 1 (3), pp 229-234.
62. Duan, H. W., Wang, D. Y., Kurth, D. G., Mohwald, H., Directing self-assembly of nanoparticles at water/oil interfaces. *Angewandte Chemie-International Edition.* **2004**. 43 (42), pp 5639-5642.
63. Yang, Y., Shi, J. L., Tanaka, T., Nogami, M., Self-assembled silver nanochains for surface-enhanced Raman scattering. *Langmuir.* **2007**. 23 (24), pp 12042-12047.
64. Olson, M. A., Coskun, A., Klajn, R., Fang, L., Dey, S. K., Browne, K. P., Grzybowski, B. A., Stoddart, J. F., Assembly of Polygonal Nanoparticle Clusters Directed by Reversible Noncovalent Bonding Interactions. *Nano Letters.* **2009**. 9 (9), pp 3185-3190.
65. Sardar, R., Shumaker-Parry, J. S., Asymmetrically functionalized gold nanoparticles organized in one-dimensional chains. *Nano Letters.* **2008**. 8 (2), pp 731-736.
66. Chen, G., Wang, Y., Tan, L. H., Yang, M. X., Tan, L. S., Chen, Y., Chen, H. Y., High-Purity Separation of Gold Nanoparticle Dimers and Trimers. *Journal of the American Chemical Society.* **2009**. 131 (12), pp 4218.
67. Jia, H., Bai, X. T., Li, N., Yu, L., Zheng, L. Q., Siloxane surfactant induced self-assembly of gold nanoparticles and their application to SERS. *Crystengcomm.* **2011**. 13 (20), pp 6179-6184.
68. Fabris, L., Dante, M., Nguyen, T. Q., Tok, J. B. H., Bazan, G. C., SERS aptatags: New responsive metallic nanostructures for heterogeneous protein detection by surface enhanced Raman spectroscopy. *Advanced Functional Materials.* **2008**. 18 (17), pp 2518-2525.
69. Jiang, L. L., Liu, W. L., Song, Y. F., He, X., Wang, Y., Wang, C., Wu, H. L., Yang, F., Yang, Y. Q., Photoinduced intermolecular electron transfer and off-resonance Raman characteristics of Rhodamine 101/N,N-diethylaniline. *Chemical Physics.* **2014**. 429, pp 12-19.
70. Werengowska-Ciecwierz, K., Wisniewski, M., Terzyk, A. P., Furmaniak, S., The Chemistry of Bioconjugation in Nanoparticles-Based Drug Delivery System. *Advances in Condensed Matter Physics.* **2015**. 27.

71. Biju, V., Chemical modifications and bioconjugate reactions of nanomaterials for sensing, imaging, drug delivery and therapy. *Chemical Society Reviews.* **2014**. 43 (3), pp 744-764.
72. Tang, W., Becker, M. L., "Click" reactions: a versatile toolbox for the synthesis of peptide-conjugates. *Chemical Society Reviews.* **2014**. 43 (20), pp 7013-7039.
73. Nobs, L., Buchegger, F., Gurny, R., Allemann, E., Current methods for attaching targeting ligands to liposomes and nanoparticles. *Journal of Pharmaceutical Sciences.* **2004**. 93 (8), pp 1980-1992.
74. Riddles, P. W., Blakeley, R. L., Zerner, B., Ellman's reagent: 5,5-dithiobis(2-nitrobenzoic acid) a reexamination. *Analytical Biochemistry.* **1979**. 94, pp 75-81.
75. Rafiee, R., Moghadam, R. M., On the modeling of carbon nanotubes: A critical review. *Composites Part B-Engineering.* **2014**. 56, pp 435-449.
76. Chepkasov, I. V., Visotin, M. A., Kovaleva, E. A., Manakhov, A. M., Baidyshev, V. S., Popov, Z. I., Stability and Electronic Properties of PtPd Nanoparticles via MD and DFT Calculations. *Journal of Physical Chemistry C.* **2018**. 122 (31), pp 18070-18076.
77. Irle, S., Zheng, G., Wang, Z., Morokuma, K., The C-60 formation puzzle "solved": QM/MD simulations reveal the shrinking hot giant road of the dynamic fullerene self-assembly mechanism. *J. Phys. Chem. B.* **2006**. 110 (30), pp 14531-14545
78. Hernández-Rodríguez, M., C. Rosales-Hernández, M., E. Mendieta-Wejebe, J., Martínez-Archundia, M., Correa Basurto, J., Current Tools and Methods in Molecular Dynamics (MD) Simulations for Drug Design. *Current Medicinal Chemistry*. **2016**. 23 (34), pp. 3909-3924
79. Karplus, M., McCammon, J. A., Molecular dynamics simulations of biomolecules. *Nature Structural Biology.* **2002**. 9 (9), pp 646-652.
80. Woods, R. J., Predicting the Structures of Glycans, Glycoproteins, and Their Complexes. *Chemical Reviews.* **2018**. 118 (17), pp 8005-8024.
81. Narth, C., Gillet, N., Cailliez, F., Levy, B., de la Lande, A., Electron Transfer, Decoherence, and Protein Dynamics: Insights from Atomistic Simulations. *Accounts of Chemical Research.* **2015**. 48 (4), pp 1090-1097.
82. Zhao, Y., Cao, Z. X., Global Simulations of Enzymatic Catalysis. *Acta Physico-Chimica Sinica.* **2017**. 33 (4), pp 691-708.
83. Toofanny, R. D., Daggett, V., Understanding protein unfolding from molecular simulations. *Wiley Interdisciplinary Reviews-Computational Molecular Science.* **2012**. 2 (3), pp 405-423.
84. Allen, M. P., Introduction to Molecular Dynamics Simulation. Computational Soft Matter: From Synthetic Polymers to Proteins. *Lecture Notes, Norbert Attig, Kurt Binder, Helmut Grubm¨ uller, Kurt Kremer (Eds.),John von Neumann Institute for Computing*. **2004**. 23, pp 1-28.

85. Mackerell, A. D., Empirical force fields for biological macromolecules: Overview and issues. *Journal of Computational Chemistry.* **2004**. 25 (13), pp 1584-1604.
86. Oostenbrink, C., Villa, A., Mark, A. E., Van Gunsteren, W. F., A biomolecular force field based on the free enthalpy of hydration and solvation: The GROMOS force-field parameter sets 53A5 and 53A6. *Journal of Computational Chemistry.* **2004**. 25 (13), pp 1656-1676.
87. Abraham, M. J., Murtola, T., Schulz, R., Páil, S., Smith, J. C., Hess, B., Lindahl , E., GROMACS: High performance molecular simulations through multi-level parallelism from laptops to supercomputer. *SoftwareX*. **2015**. 1 (C), pp 19-25.
88. Fuchs, P. F. J., Hansen, H. S., Hunenberger, P. H., Horta, B. A. C., A GROMOS Parameter Set for Vicinal Diether Functions: Properties of Polyethyleneoxide and Polyethyleneglycol. *Journal of Chemical Theory and Computation.* **2012**. 8 (10), pp 3943-3963.
89. Pu, Q., Leng, Y. S., Zhao, X. C., Cummings, P. T., Molecular simulations of stretching gold nanowires in solvents. *Nanotechnology.* **2007**. 18 (42), pp 424007-424011.

Chapter 3: Engineering of GE11 peptide to enhance EGFR targeting activity of SERRS nanostructures

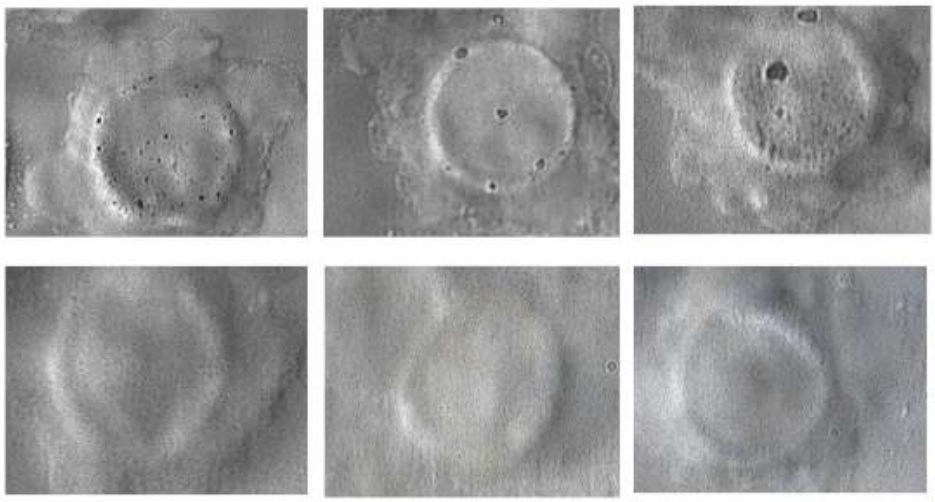

100x objective images after incubation with colorectal cancer cells overexpressing EGFR of engineered analogues of GE11 peptide (top) and of non specific-targeting nanostructures (bottom). Gold nanostructures are visible as dark spots.

As deeply discussed in Chapter 1, the aim of this PhD project is to engineer gold nanostructures to be used as SERRS biosensors for colorectal and liver cancer diagnostics by functionalization with peptides, as specific ligands of tumor associated receptors. To target colorectal cancer, GE11 [1] and cycloRGD [2] peptides, which respectively bind EGFR and $\alpha_v\beta_3$ integrin receptors, were chosen. In this Chapter, colorectal cancer cells targeting achieved by loading the nanosystems with GE11 is deeply investigated whereas nanostructures functionalized with cycloRGD peptides are discussed in Chapter 4. Recalling knowledge reported in Chapter 1, the Epidermal Growth Factor Receptor (EGFR) is a target protein overexpressed in various human tumors of epithelial origin, including non-small cell lung cancer, breast, gastric, colorectal, prostate, renal, pancreatic and ovarian carcinomas[3]. Traditionally, EGFR is targeted with antibodies [4,5] but a number of other moieties that selectively bind this receptor are currently available [6-8]. Among them the dodecapeptide GE11 (YHWYGYTPQNVI), recently identified by screening phage display libraries, is of a great interest since, as opposite to endogenous ligands such as the EGF, binds the receptor without activating the complex signaling cascade that modulates growth, differentiation, migration and survival of cancer cells [1]. For this reason, GE11 has been used to improve targeted gene delivery [9,10], as drug carrier [11-13] and for tumour imaging [14]. Moreover, it was linked to drug loaded micelles [15], liposomes [16, 17] and self-assembled amphiphilic peptide nanoparticles [18]. It is well known that in order to achieve an efficient cancer cell targeting, nanosystems must be functionalized with ligands properly engineered to assure an high affinity and specificity for receptors overexpressed by cancer cells but minimally expressed on healthy cells [19,20]. This guarantees long blood circulation and remaining time of the nanoparticles within the tumor and also triggers their transport across cell membranes. However, studies regarding the effect of the organization of the targeting units on the nanostructures surface are still lacking. With the aim to contribute to fill this gap, a number of analogues of the peptide GE11 were rationally designed to obtain nanosystems presenting the targeting motif with different arrangements on the gold surface. The targeting properties of the synthesized nanostructures were assessed on colorectal cancer cells overexpressing or not the receptor and compared to that of a non-specific targeting nanostructure obtained covering the surface of gold aggregates only with short thiolated PEG chains. Furthermore, the nanostructures targeting properties were compared to those of nanosystems functionalized with Cetuximab, an antibody specific for EGFR already used in the clinical settings [21]. In vitro experiments carried out in collaboration with the group of Prof. A. Rosato and Prof. S. Mocellin of Department of Surgery Oncology and Gastroenterology of the University of Padova, suggested that the organization of the targeting motif on the nanostructures surface strongly influences the selective binding of EGFR. Thanks to the partnership with the group of Prof. A. Palleschi of the Department of Chemical Sciences and Technologies of the University of Roma Tor

Vergata, Molecular Dynamics calculations were performed to understand the role of the peptide arrangement in the receptor recognition. Results demonstrated that by properly exposing the targeting motif on the nanostructures surface a very sensitive and selective receptor binding, even better than that obtained using the antibody as targeting unit, could be achieved. The work presented in this chapter has been recently published [22].

Results and Discussion

Gold nanostructures were synthesized following the synthetic procedure illustrated in Figure 1. A detailed description of methods employed for the synthesis and the characterization of peptides and nanosystems is reported in Chapter 2. All synthetic and analytical procedures are reported in the Experimental Section whereas characterizations of peptides and nanosystems are contained in the Appendix of this chapter. Colloidal aqueous solutions of naked gold nanoparticles with average diameters of about 20 nm were obtained by the laser ablation assisted in solution (LASiS) technique[23]. Gold nanoparticles were centrifuged and resuspended in water for three times to obtain aggregated particles with a sufficient number of hot spots for a strong SERS enhancement. Extent of aggregation was controlled recording UV-Vis-NIR spectra that showed a pronounced maximum at about 600–750 nm, which is essential for exciting the localized plasmon resonance of the nanoparticles in the NIR spectral region (Figure A5).

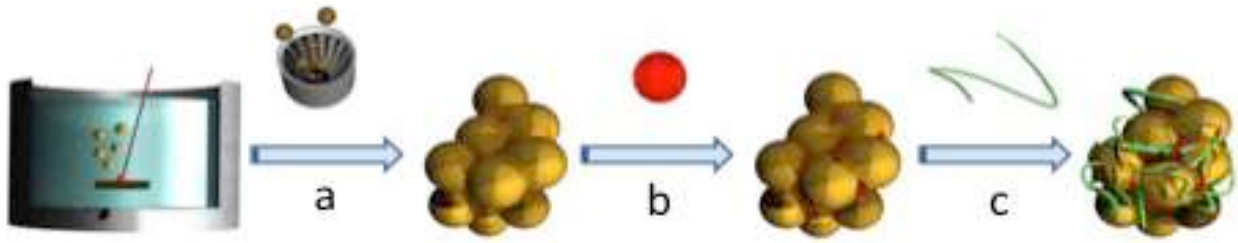

Figure 1. Synthesis steps of the preparation of the nanostructures: after the laser ablation synthesis in solution, gold nanoparticles are aggregated by centrifugation (a), functionalized with the SERRS reporter (b) and with the targeting molecules or only with PEG for a reference nanostructure (c).

Gold nanoaggregates were functionalized with Texas Red (TR) as SERRS label and characterized by recording Raman spectra to confirm the anchoring of the reporter to the surface (Figure A5). SERRS nanoaggregates were then functionalized with the targeting ligands and characterized recording UV-Vis-NIR e Raman spectra (Figure A5). DLS measurements revealed hydrodynamic diameters of the order of 100-300 nm (See Table 1). In particular, it can be noticed that nanostructures covered with PEG chains owned hydrodynamic diameter around 135 nm, smaller than that of nanostructures without the PEG coating. This evidence suggests that the presence of the polymer avoids further aggregation among the nanostructures, which can be present in AuNP@GE11^{N} and AuNP@GE11^{C} nanosystems. The nanostructures colloidal stability is the result of several factors including

electrostatic repulsion and steric hindrance between the nanosystems attributable to both the nanoparticles and the ligands decorating their surface. An estimation can be made measuring the nanostructures' ζ-potentials. In fact, AuNP synthesized by the LASiS synthetic approach, which are stable in absence of surfactants, show negative values due to the formation of $Au\text{-}O^-$ and $Au\text{-}Cl^-$ groups resulting from the dissociation of Au-O-Au bonds (See Chapter 2 for further details). ζ-potentials of nanostructures displayed small values (Table 1), that cannot perturb their colloidal stability. However, the differences of ζ-potentials among the nanosystems at currently are not explained. The quantification of the targeting units bound to the surface was estimated by comparing the absorbance of the peptide solution before and after the functionalization of the nanoparticles and is reported in Table 1. Nanostructures functionalized with PEG-peptide conjugates displayed a lower number of targeting units per nanoparticles, as one would expect considering the larger dimension of the conjugate with respect to the parent peptide. Interestingly, AuNP@PEG nanostructures showed the lowest number of ligands estimated on the surface. A possible explanation could be a greater reactivity of peptides compared to PEG molecules, that could be ascribed to the presence of functional groups, such as carboxyl groups or amines, that foster the interaction of the peptide ligand with the gold nanostructures or to the formation of multiple peptide layers as suggested by results reported in Chapter 5.

Table 1. Characterization of functionalized nanostructures.

Nanostructure	*Ligands per nanoparticle*	*Hydrodynamic diameter (nm)*	*ζ-potential (mV)*
AuNP@GE11^N	7000	280±10	-25±2
AuNP@GE11^C	5000	315± 10	0.1±1
AuNP@PEG-GE11	2000	125±5	4±1
AuNP@PEG-KKKGG-GE11	3000	145±1	13±1
AuNP@PEG	400	174±6	-15±1

The first step for understanding how the ligands organization on the nanostructures surface could affect the receptor recognition was the investigation on the influence of the peptide orientation. For

this purpose, two analogues of the peptide GE11 were synthesized by extending the N- or the C-terminal end with a cysteine residue and a short ethylene glycol spacer (Figure A1 and Table A1). By linking them to gold nanoaggregates two nanostructures, AuNP@GE11^{C} and AuNP@GE11^{N} respectively exposing the C- or N- peptide terminal end, were obtained (Figure A5 and Table 1). Gold nanostructures covered only with PEG (AuNP@PEG) were used as reference to detect non-specific interactions with cells (Figure A5 and Table 1). The targeting properties of the synthesized nanostructures were assessed by incubating different picomolar concentrations of the nanosystems with colorectal cancer cells overexpressing (Caco2 and SW480 cell lines) or not (SW620 cell line) the EGFR for 2 h at 37°C. After incubation, the cells were washed with PBS and fixed with paraformaldehyde. SERRS spectra were acquired for each single cell with a 20x objective. The presence in the recorded spectra of the characteristic signal of the SERRS label was evaluated using an automated homemade procedure based on the use of a reference spectrum of TR and a Pearson correlation coefficient of 0.6. Clearly, SERRS signals were detected only if the targeting units recognize the receptor and consequently the nanostructures are strongly bound to cells. However, Figure 2E reporting results obtained after the incubation of the three cell lines with the reference nanostructure AuNP@PEG, shows that SERRS signals can achieved up to a 20% for all cell lines at the highest nanostructure's concentration as a result of unspecific recognition events. This result suggests that the targeting activity of peptide functionalized nanostructures could be affected by, on average,10-20% of non-specific interactions which could generate false responses. In any case, as discussed as follows, the better results in terms of sensitivity (cells that must show SERRS signals) are far away from poorly non-specific interactions that consequently do not change the overall frameworks of results. On the contrary, the better specificities (cells that must not show SERRS signals) approach the AuNP@PEG targeting activity demonstrating that unspecific interactions of peptides functionalized nanostructures can be reduced up to the reference. Data of AuNP@GE11^{N} and AuNP@GE11^{C} are respectively report in Fig. 2A and Fig. 2B. An increase of the targeting activity with the concentration of the nanostructures was observed after incubation with both nanostructures. The better results in terms of sensitivity (cells that must show SERRS signals) and specificity (cells that must not show SERRS signals) were achieved for AuNP@GE11^{N}: at the highest explored concentration sensitivities of 81% and 74% for Caco2 and SW480, respectively, and a specificity of 87% for SW620 were observed. Lower sensitivities (71% and 42% for SW480 and Caco2, respectively) were found for AuNP@GE11^{C}. However, the targeting activity with the SW620 cell line was lower than 20% at higher concentrations as well as the nanostructure AuNP@GE11^{N}. These results are comparable to those recorded for the reference nanostructure AuNP@PEG for all cell lines and demonstrated that these SERRS signals are due to non-specific interactions with cells,

which reduce the specificity of the EGFR binding. Finally, considering the small differences of the targeting properties between the nanostructures AuNP@GE11^{N} and AuNP@GE11^{C}, it is possible to conclude that the orientation of the peptide on the surface does not significantly affect the receptor recognition.

The good targeting activity of AuNP@GE11^{C} and AuNP@GE11^{N} can be better appreciated considering results of the evaluation of the activity of the isolated peptides. For this purpose, two fluoresceinated peptides, Fluo-GE11^{C} and Fluo-GE11^{N}, were synthesized conjugating the dye respectively at the N- or C-terminus of the sequence (Figure A3 and Table A1). The affinity of both analogues for EGFR was estimated by cytofluorimetric assays and was found to be very low since very small differences were observed between the cells overexpressing or not the receptor (Figure A7). These measurements, in agreement with the large dissociation constant recently reported for the binding of GE11 to EGFR ($K_D = 4.59\ 10^{-4}$) by SPR methodology [24], highlights the importance of the peptide organization on the nanostructures surface to achieve an effective receptor binding. To increase the specificity of the recognition process exploiting the well-known stealth effect of a PEG coating [25] and simultaneously exploring the targeting activity of nanostructures presenting the peptide in a different arrangement, GE11 was covalently linked to a long thiolated PEG chain and used to prepare another nanosystem: AuNP@PEG-GE11 (See Figure A4 and Table A1 for the PEG-peptide conjugate; Figure A5 and Table 1 for the nanosystem). Results of incubation of this nanostructure with cells are reported in Figure 2C. Surprisingly, the polymeric layer not only reduced the non-specific interactions with cells, as expected, but also hampered the peptide binding to EGFR. The reason could be ascribed to the morphology of the long PEG chains. In fact, in aqueous media the PEG does not assume a linear conformation but is folded to form globular structures that, embedding the targeting motif within the polymeric coating, sterically hinder the association with the receptor[26]. Peptide hydrophilicity plays an important role in promoting the exposure of the targeting unit above the PEG layer [27]. Taking into account this information, another GE11 analogue was synthesized inserting a cationic spacer, constituted by three lysines and two glycines, between GE11 and the polymer and was used to prepare the nanostructure AuNP@PEG-KKKGG-GE11 (See Figure A4 and Table A1 for the peptide; Figure A5 and Table 1 for the nanosystem). This nanosystem showed a sensitivity higher than 90% for Caco2 and SW480 cell lines and a specificity of 89% considering SW620 cells, as reported in Figure 2D. The comparison of these results to those obtained for the nanostructures AuNP@PEG-GE11 points out that the targeting capability can be enhanced by increasing the hydrophilicity of the ligand. The improvement can also be noticed with respect to the nanosystems without the PEG chains, AuNP@GE11^{C} and AuNP@GE11^{N}.

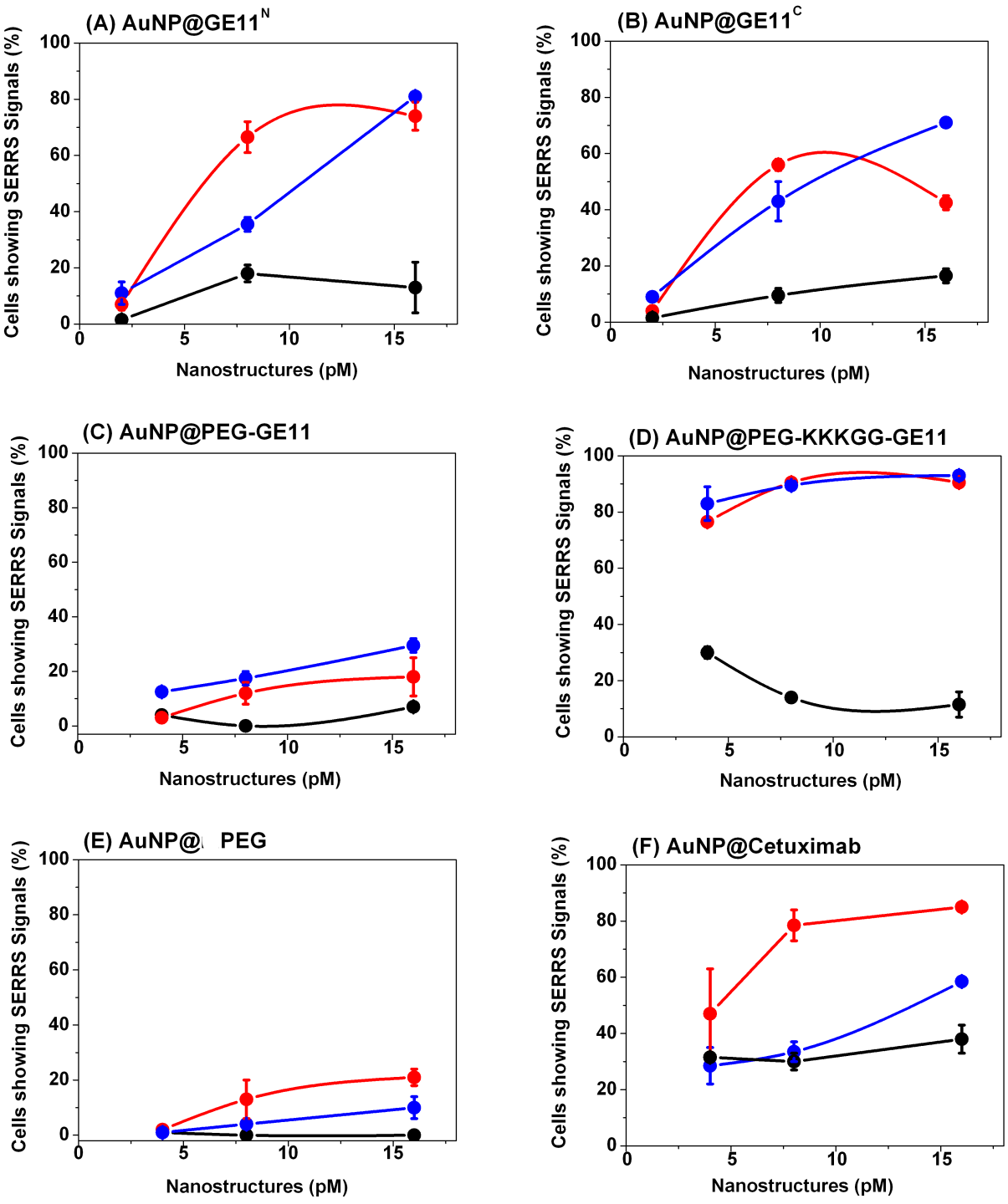

Figure 2. Targeting activity of synthesized nanostructures (A) AuNP@GE11^{N}, (B) AuNP@GE11^{C}, (C) AuNP@PEG-GE11, (D) AuNP@PEG-KKKGG-GE11, (E) AuNP@PEG and (F) AuNP@Cetuximab for Caco2 (EGFR+) (red lines), SW480 (EGFR+) (blue lines) and SW620 (EGFR-) (black lines) cells. 100 cells were considered for each measurement and error bars indicate variations of the results for three different selections of 100 cells within two or three preparations.

As gold nanoparticles strongly scatters, their presence on targeted cells can be easily evaluated by transmission microscopy in addition to SERRS measurements. As an example, images of SW480 cells incubated with AuNP@PEG-KKKGG-GE11 and with the reference nanostructure AuNP@PEG at the highest explored concentrations are shown in Figure 3. Dark spots, corresponding to the scattering clusters, are clearly visible only on SW480 cells after incubation with AuNP@PEG-KKKGG-GE11 and washing of the nanostructures for which the targeting did not occur. These images confirm the good targeting activity of this nanosystem.

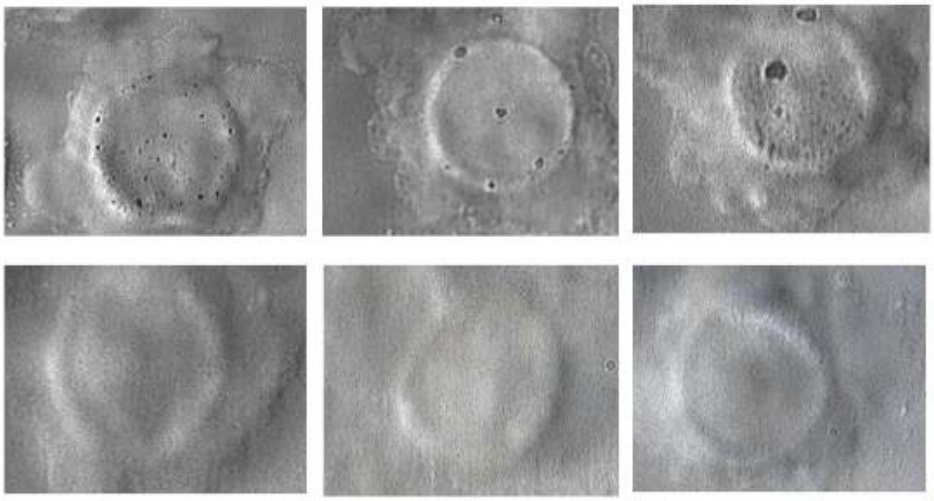

Figure 3. 100x objective images after incubation with colorectal cancer cells overexpressing EGFR of AuNP@PEG-KKKGG-GE11 (top) and of AuNP@PEG nanostructures (bottom). Gold nanostructures are visible as dark spots.

Finally, the targeting activity of nanosystems functionalized with GE11 peptide analogues were compared to that of a nanostructure presenting Cetuximab, an anti-EGFR antibody already used in the clinic, as targeting unit (AuNP@Cetuximab). Cetuximab was linked to the gold surface exploiting the Au-S affinity according to a defined procedure established for other antibodies in the group in which this PhD project was developed [23] (see Experimental Section for details). The average number of antibodies per nanoparticles was estimated by comparing the absorbance at 280 nm of the antibody solution before and after the nanostructures' functionalization. The presence of about 50 to 60 antibodies was estimated on each nanoparticle (Figure A6 and Table 1). Since it is known that the number of active antibodies on the surface of gold nanoparticles is less than 4% [28], this procedure guarantees a sufficient number of active antibodies on the nanostructure for a good targeting activity. Results obtained after incubation of AuNP@Cetuximab with the three cell lines in the same experimental conditions than those used for the nanostructures functionalized with peptides are reported in Figure 2E. AuNP@Cetuximab showed a good targeting activity for Caco2 (sensitivity of

85 %), although less sensitivity was observed for SW480 cells (59 %). A low specificity (62%) was also found considering that SW620 cells were targeted for 38% at the highest nanostructure concentration. Comparing these results to those achieved for AuNP@PEG-KKKGG-GE11, the more efficient targeting activity of the latter nanostructures is pointed out since both the sensitivity and the specificity are much higher.

To rationalize these findings, and in particular to build a model for the organization of the PEG-KKKGG-GE11 chains on the surface that could explain the reason of the excellent targeting activity of the AuNP@PEG-KKKGG-GE11 nanostructures, Molecular Dynamics calculations were performed. In particular, simulations were focused on the different organization of the PEG-peptide targeting units in which the cationic spacer is present (PEG-KKKGG-GE11) or not (PEG-GE11). In fact, the slightly less positive surface potential of AuNP@PEG-GE11 (+4 mV) than that of AuNP@PEG-KKKGG-GE11 (+13 mV) does not seem sufficient to justify the very different behavior of the two types of nanostructures. Molecular dynamics (MD) simulations of PEG-GE11 and PEG-KKKGG-GE11 were performed in water mimicking the bonding of PEG chains to the Au surface and constraining the position of the end sulfur atoms of PEG along the Z-directions. 36 replicas of the PEG-GE11 and PEG-KKKGG-GE11 were considered on a surface of 90 nm^2. Initially the ligands were set up in the extended conformation and peptides were considered in α-helical secondary structure (i.e. all the torsional angles equal to 180°). After approximately 100 ns the system reached the steady state, but the simulations were continued for further 20 ns to provide the portion of trajectories required for the analyses. During the equilibration time, the PEG disorder increased due to the formation of local gauche conformations. In the last 20 ns the number of torsional angles in gauche conformations resulted to be 22% and 23 % for PEG-GE11 and PEG-KKKGG-GE11, respectively, causing a significant reduction of the thickness of the PEG layer. After 100 ns, the thickness was found to be 6 nm on average in both cases. The last frames of the simulations for the two systems are reported in Figure 4A. The amount of α-helical structure evaluated in the last 20 ns of simulations for the twelve amino acids of GE11 was found to be significantly reduced, mostly for the GE11 in PEG-KKKGG-GE11 than for that in PEG-GE11 being, respectively, of the order of 16% and 22%. The positive ψ angle for the 79% of the analyzed trajectory for the sequence KKKGG of the PEG-KKKGG-GE11 demonstrated that the cationic linker adopts almost totally an extended conformation. For both systems, peptides were found to be located at the interface between PEG and water.

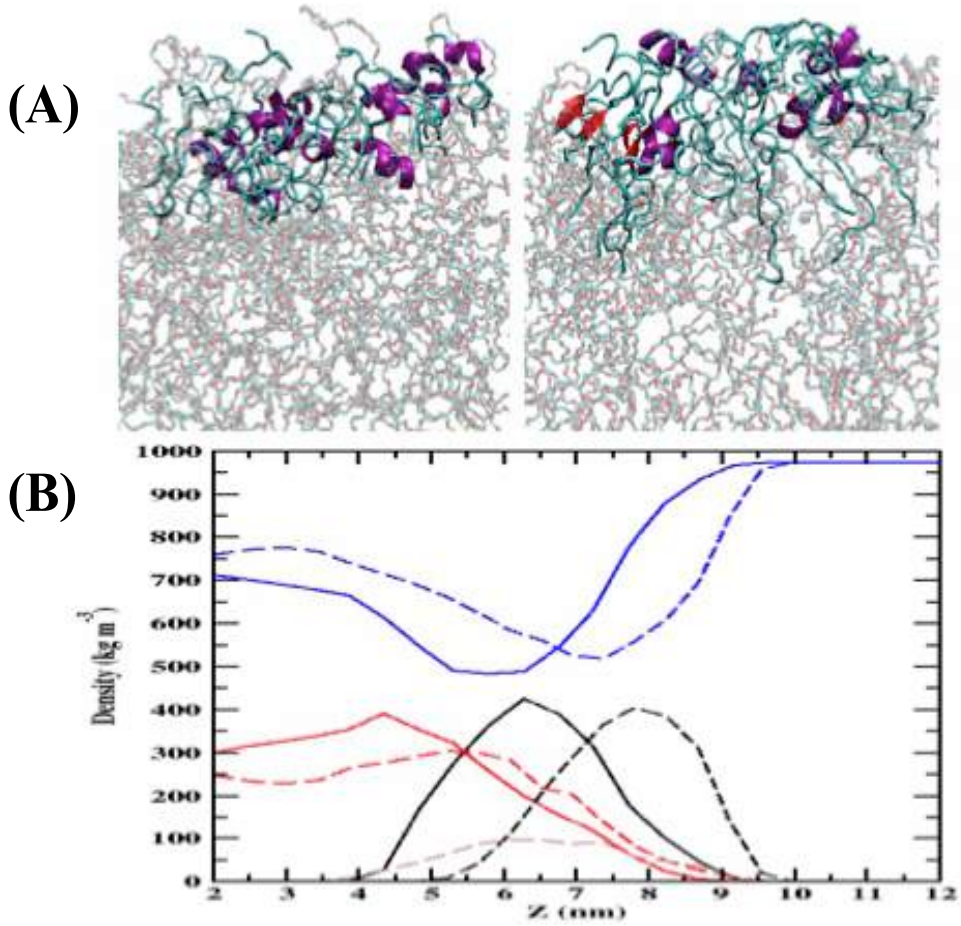

Figure 4 (A) Final structures obtained from MD simulations of PEG-GE11 (left) and PEG-KKKGG-GE11 (right). PEG is reported as semi-transparent sticks, the peptides as green ribbons with β-sheet and helical tracts colored in red and purple, respectively. For sake of clarity the water molecules are not reported but fill the white areas. KKKGG sequence is reported as blue ribbons attached to the green ribbons of GE11. (B) Density profiles evaluated along the Z direction in the last 20 ns of simulations of the peptide (black lines), PEG (red lines) and water (blue lines). Lines are continuous for PEG-GE11 and dashed for PEG-KKKGG-GE11. The density profile of the KKKGG sequence is reported with a dashed brown curve and is found in the top part of the PEG coating (compare brown and red dashed lines).

The density profile of the different parts of the simulated systems along the outward Z-direction points out that the peptide sequence of GE11 in PEG-KKKGG-GE11, being located at higher values of Z, is more exposed to the solvent than that in PEG-GE11 (Figure 4B). Besides the high value of the local charge density, the cationic spacer was found, on the contrary, almost completely embedded in the PEG layer. The high density for counterions (not reported) near this sequence confirms the location of the spacer. The water accessible surface for the two peptides (Figure 5A) was found to be larger for the PEG-KKKGG-GE11. Furthermore, the minimum distances between the N-terminal regions of the peptides (Figure 5B) showed that the linker, promoting higher distances between the peptides, prevents their aggregation. These results highlight the more availability of GE11 in PEG-KKKGG-GE11 than in the PEG-GE11 system for interactions in aqueous solutions. Consequently,

the much better targeting activity of AuNP@PEG-KKKGG-GE11 with respect to AuNP@PEG-GE11 relies on the more appropriate exposition of the targeting motif above the PEG layer for the interactions with EGFR on the cell surface.

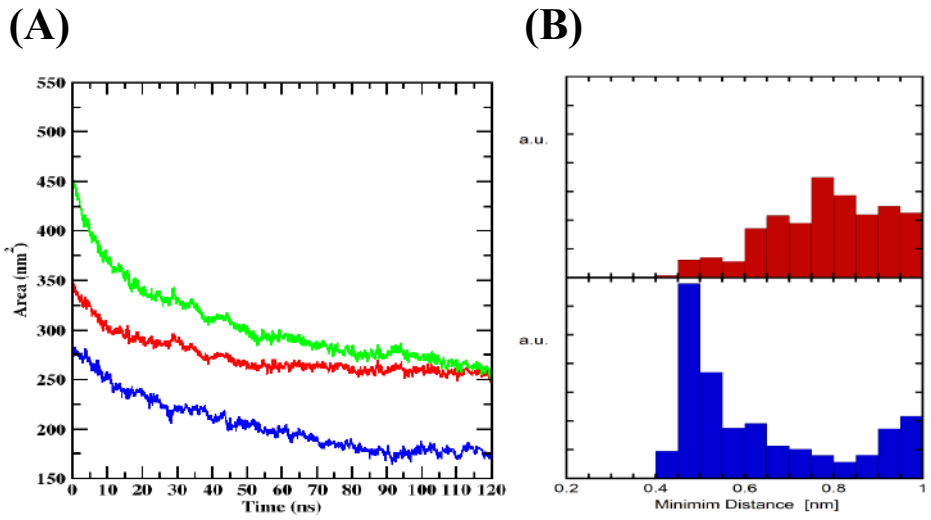

Figure 5. (A) Water accessible surface (WAS) during the 120 ns of the dynamic evolution of the ensemble for PEG-GE11 (blue line), PEG-KKKGG-GE11 (green line) and for only the GE11 sequence in the PEG-KKKGG-GE11(red line). In the last 20 ns, when the system reaches the equilibrium, GE11 in PEG-KKKGG-GE11 accounts for almost the complete water available surface. The great difference with the WAS of the whole PEG-GE11 shows that GE11 in PEG-KKKGG-GE11 is much more available to interactions in water with other molecules. (B) Distribution of the minimum distances between pairs of N atoms of the first tyrosine in the GE11 sequences for both PEG-GE11 (down) and PEG-KKKGG-GE11 (up). The distances are obtained as the minimum distance, for each N atom, among the 36 peptides of the ensemble, during the last 20 ns of simulations with a time interval of 10 ps.

To conclude, in this chapter experimental analysis were associated to MD calculations to demonstrate that the exposure of peptide ligands on the nanostructures surface has a huge impact on their association with the receptor. It was proved that if the ligands are conveniently engineered, the proper arrangement of the targeting units for effective receptor recognition, even better than that of nanosystem functionalized with specific antibodies, could be achieved. Moreover, although recent literature highlights that the peptide hydrophilicity plays a key role for the improvement of the receptor binding by promoting the presentation of the targeting motif above the PEG coating [27], this study suggests that this could be not a sufficient condition for guaranteeing a satisfactory association. Others features, such as a suitable presentation above the polymeric layer and the avoidance of peptides aggregation, are necessary. To further investigate on these findings, the influence of the arrangement on the nanostructures surface of another peptide, namely cycloRGD, for the recognition of $\alpha_v\beta_3$ integrin receptors on colorectal cancer cells was studied (Chapter 4).

Experimental Section

Materials and Methods

All chemicals were commercial products and were used without further purification, unless differently specified. 9-Fluorenylmethoxycarbonyl (Fmoc)-amino acids and all other chemicals for the solid phase peptide synthesis were purchased from Sigma-Aldrich, as well as 5(6)-carboxyfluorescein, fluorescein-5-maleimide and Bovine Serum Albumin (BSA). Fmoc-8-amino-3,6-dioxaoctanoic acid (Fmoc-PEG_1-OH) and the Rink Amide MBHA resin (loading 0.9-0.55 mmol/g) were supplied by Iris Biotech GMBH. α-tritylthio-ω-N-hydroxysuccinimide PEG (Trt-S-C_2H_4-CONH-PEG-O-C_3H_6-CONHS MW. ≈3000 Da) and α-methoxy-ω-mercapto PEG (CH_3O-PEG-SH MW.≈2000Da) by Rapp Polymer. Cetuximab was obtained through ultracentrifugal filtration of Erbitux (MerckSerono). Sulforhodamine 101-bis-cysteamide (TR) was prepared according to a previously published procedure [23].

Analytical HPLC separations were performed on a Dionex Summit dual-gradient HPLC instrument, equipped with four-channel UV-vis detector, using a Vydac 218TP54 column (250 x 4.6 mm, 5 μm, flow rate at 1.5 ml/min). The mobile phaseA (aqueous 0.1% Trifluoroacetic acid (TFA)) and B (90% aqueous acetonitrile containing 0.1%TFA) were used for preparing binary gradients. Except otherwise indicated, the elution condition was: isocratic 10% B for 3 min; linear gradient 10-90% B for 30 min. Preparative HPLC separations were performed on a Shimadzu series LC-6A chromatograph, equipped with two independent pump units, a UV-vis detector, using a Vydac column 218TP54 (250x22 mm, 10 μm, flow rate at 15 ml/min) and the same mobile phases described above. Mass spectral analyses were carried out on a Mariner API-TOF workstation (PerSeptiveBiosystemsInc), operating in positive mode with ESI technique or on a MALDI TOF/TOF Analyzer (ABSciex), operating in positive mode in the linear mid-mass range (2,5-dihydroxybenzoic acid as matrix). DLS and ζ-potential measurements were performed with a Malvern Nano-ZS instrument equipped with a 633 nm He-Ne Laser. SERRS spectra of cells were recorded with a micro-Raman spectrometer (inViaRenishaw) exciting at 633 nm (1.5mW) with a 20x objective for 1 s. SERRS spectra of the colloidal solutions were recorded with a 5x objective for 30 s. An internal Si reference was used as reference. UV-Vis-NIR spectra were recorded with a Cary5000 spectrometer (Varian) in 0.2 or 1 cm quartz cells**.** Microscopic cell images were acquired on cells fixed on a glass slide using a Leica microscope with a 100x objective.

Synthesis of Peptides and Conjugates

General Method: The peptide sequences were synthesized using Fmoc Chemistry on an automated Advanced Chemtech 348 Ω, starting from Rink amide MBHA resin (0.05 mmoles). The amino acid side chains were protected by the *tert*-butyl group (tyrosine and threonine), the *tert*-butyloxycarbonyl group (tryptophan and lysine) and the trityl group (histidine, glutamine, asparagine and cysteine). Fmoc deprotection was achieved with 20% piperidine in DMF (5 + 15 min). Couplings were carried out in DMF, using an excess of the Fmoc-amino acid (4 eq) and in the presence of *N,N,N′,N′*-tetramethyl-*O*-(1*H*-benzotriazol-1-yl)uroniumhexafluorophosphate**,** N-hydroxybenzotriazole and N,N,N-ethyldiisopropylamine (4 : 4 : 12 eq) (reaction time 45min). *N*-Acetylation was performed with a 0.5 M solution of acetic anhydride/N,N,N-ethyldiisopropylamine (2:1 v/v) in DMF for 30 min. Cleavage and deprotection of peptides from the solid support were achieved by treatment with a mixture of TFA/triisopropylsilane/H_2O (95:2.5:2.5 v/v/v) for 1h and 30 min at room temperature (RT). Alternatively, in the case of cysteine containing peptides, a mixture of TFA/triisopropylsilane/H_2O/1,2-ethanedithiol (94:1:2.5:2.5 v/v/v/v) was used. The resin was filtered off, the acid solution was reduced to a small volume and the crude peptide was precipitated by addition of cold diethyl ether. Peptides were purified by semi-preparative HPLC and characterized as shown in Table A1 and Figure A1-A2.

Fluoresceinated peptides. 5(6)-Carboxyfluorescein (0.018 mmol) was dissolved in 0.5 mL of DMF and reacted overnight with the amino terminal group of PEG_1-YHWYGYTPQNVI-Resin (0,007 mmol), in the presence of diisopropylcarbodiimide and N-hydroxybenzotriazole (0.018 mmol each one) as coupling reagents. Excess of reagents was filtered off and the resin was repeatedly washed with DMF and DCM, until the filtrate was colourless. Deprotection and cleavage were carried out as reported in the General Procedure. After HPLC purification (isocratic 22%B for 5 min; linear gradient 22-50%B in 20 min) the fluoresceinated peptide (Fluo-$GE11^C$) was characterized as shown in Table A1 and Figure A3.

GE11 fluoresceinated at C-terminus (Fluo-$GE11^N$) was prepared by reacting fluorescein-5-maleimide (0.019 mmol) with the thiol group of $GE11^N$ (0.002mmol), dissolved in 1.6 mL of acetonitrile/ 10 mM phosphate buffer (63/37 v/v). After 4h stirring at RT under inert atmosphere, the unreacted fluorescein-5-maleimide was quenched by addition of an excess of cysteine. The reaction mixture was shaken overnight, a solid residue was centrifuged off and the surnatant purified by semi-preparative HPLC in the same condition described for Fluo-$GE11^C$. Fractions containing the fluoresceinated peptide were collected and lyophilized to yield the pure Fluo-$GE11^N$, which was characterized as reported in Table A1 and Figure A3.

Synthesis of PEG-peptide Conjugates. A solution of the free peptide (GE11, 0.007 mmol or KKKGG-GE11, 0.005 mmol) in cold DMF (0.6 ml) was neutralized with N,N,N-ethyldiisopropylamine (1 or 4 eq respectively). The heterobifunctional PEG (Trt-S-C_2H_4-CONH-PEG-O-C_3H_6-CONHS, 1 eq) was added to these solutions and the reaction mixture was shaken for 48h at RT. After that, the solvent was removed under reduced pressure and the product was precipitated by addition of cold diethyl ether and dried under vacuum. To unmask the thiol group, the compound was dissolved in the TFA/triisopropylsilane/H_2O/1,2-ethanedithiol mixture and stirred for 1h at RT under inert atmosphere. The acid solution was reduced to a small volume and the thiolated PEG-peptide conjugate was collected by precipitation with cold diethyl ether. The conjugates were purified by semipreparative HPLC and characterized by analytical HPLC and MALDI-TOF MS (Figure A4, Table A1)

Preparation of SERRS nanostructures

Synthesis and PEGylation of SERRS nanoaggregates: Naked gold nanoparticles were synthesized with Laser Ablation Solution Synthesis methodology [23]. Nanoparticles average diameter, obtained by fitting their UV-Vis-NIR spectrum [29], is 20 nm and the ζ-potential is -30 mV. AuNP were centrifuged at 25000 g for 10 min and re-suspended in water for three times to obtain aggregated nanoparticles with a sufficient number of hot spots for a strong SERS enhancement. Extent of aggregation was controlled by the UV-Vis-NIR spectra (Figure A5). 1 mL of the colloidal solution of nanoaggregates (4 nM) was mixed with 100μL of a 34μM alcoholic solution of TR. The reporter in excess was discarded by centrifugation and nanoaggregates were redispersed in PBS buffer at nanomolar concentration and used for conjugation with ligands.

PEG coated nanoaggregates were prepared by mixing 1 ml of the colloidal solution of nanoaggregates (3 nM) with 0.1 ml of 0.25 mM CH_3O-PEG-SH in water. The mixture was shaken for 3 h at RT and the unbound ligands were removed by centrifugation (25000 g, 10 min). The resulting AuNP@PEG was redispersed in PBS (1ml) and 5 mg of BSA were added just before incubation with cells. At each step, UV-Vis-NIR and Raman Spectra were recorded (Figure 5A). DLS and ζ-potential measurements are reported in Table 1.

Conjugation with Peptide Ligands: 1 ml of the colloidal solution of gold nanoparticles (4 nM) was centrifuged at 25000 g for 10 min and redispersed in a 20 μM solution of the peptide in PBS (1ml). The mixture was shaken for 3h at RT and stored at 4° overnight. The excess of ligand was removed by centrifugation and the nanoaggregates were redispersed in 1 ml of PBS. The number of peptide ligands covering, on average, each nanoparticle was estimated by measuring the absorbance at 280 nm of the ligand solution (ε_{280nm} 6240 M^{-1} cm^{-1}) before and after removal of nanoparticles by

centrifugation (See Table 1). These values were further confirmed by the Ellman test. At each step, UV-Vis-NIR and Raman Spectra were recorded (Figure A5) and the fully functionalized nanostructures were also characterized by DLS and ζ-potential measurements (Table 1). Just before incubation with cells, gold nanostructures were mixed with BSA (5 mg/ml).

Coupling of the antibody Cetuximab to the nanostructures: Nanoparticles functionalized with Cetuximab were obtained according to a previously published protocol [23]. Briefly, 0.1 ml of a 50 μM solution of 2-iminothiolane hydrochloride in water (50 nmol) was added to 1 mL of 6 μM solution of the antibody in buffer (pH 8). The reaction mixture was shaken for 2h at RT and stored overnight at 4 °C. After then 15 mg of glycine were added to destroy the unreacted reagent. The antibody was purified by centrifugal ultrafiltration and the presence of 1.5 thiol groups per antibody was determined by the Ellman test. Gold nanoaggregates were isolated by centrifugation from 1 ml of a 3 nM colloidal solution and redispersed in 1ml of the thiolated antibody solution in PBS (5 μM). The mixture was gentle shaken for 6 hours at RT and then stored overnight at 4°C. Functionalized nanoparticles were collected by centrifugation at 25000 g for 10 min and redispersed in 1 ml PBS containing 5 mg of BSA. According to the absorption measurements at 280 nm of the antibody solution before and after the removal of the nanoparticles, about 50-60 antibodies per nanoparticle were estimated. The UV-Vis-NIR spectra recorded at different steps of the preparation and the final SERRS spectrum are reported in Figure A6.

Cell Lines and Receptor Expression Assay

Caco2, SW480 and SW620 cell lines were purchased from CLS Cell Lines Service GmbH (Eppelheim, Germany) and were cultured in the specific culture media suggested by the manufacturer following standard aseptic procedures. In brief, Caco2 cells were cultured in Eagle's minimum essential medium (EMEM) (Sigma-Aldrich, Irvine, UK) supplemented with L-glutamine, 1% nonessential amino acids, 1 mM sodium pyruvate, and 10% fetal bovine serum. SW480 cells were cultured in Ham's F12 medium (Sigma-Aldrich, Irvine, UK) supplemented with 2mM L-glutamine and 10% fetal bovine serum. SW620 cells were cultured in Dulbecco's modified eagle medium (DMEM) (Sigma-Aldrich, Irvine, UK) supplemented with 4,5 g/L glucose, 2 mM L-glutamine, and 10% fetal bovine serum. All the above-mentioned media were supplemented with 100 U/mL penicillin, and 100-μg/mL streptomycin (Gibco). All the cell cultures were maintained at 37 ° with 5% CO_2.

Receptor Expression and Peptide Binding Assay by Flow Cytometry: Caco2, SW480, and SW620 cells were grown in T75 flasks until about 80% confluence at which point they were sub cultivated. A 1:1 (v/v) solution of 0.25% trypsin and 0.02% ethylenediaminetetraacetic acid (EDTA) in PBS was

used to loosen the adherent cells. The cell pellet was washed with PBS. 500 000 cells were incubated with 20 µL of anti-Human EGFR-PE antibody (BD biosciences San Jose, CA, USA) in the dark for 15 min at room temperature and washed with PBS to remove excess unbound antibodies. The unmarked cells were used as negative controls. The samples were analysed using the FACS BD Calibur instrument (BD biosciences San Jose, CA, USA). Results were compared for relative EGFR expression and analysed with FlowJosoftware (TreeStar Inc.).

Peptide binding evaluation (Figure A7) was carried out by incubating cells with increasing concentrations of fluorescein-conjugated peptides Fluo-GE11^{N} and Fluo-GE11^{C} for 2 h at 37°C. Samples were washed twice with PBS and analysed on a FACS BD Calibur instrument (BD biosciences San Jose, CA, USA).

Cell Culture and SERRS Measurements

Cells were incubated the day after seeding with 160, 80 and 40 pM nanoparticles in culture medium for 2 h at 37 °C. Then slides were washed twice with PBS, fixed with 4% PFA and washed three times with distilled water to remove unbound nanoparticles before the SERRS measurements. Using an automated homemade procedure SERRS spectra were collected from each single cell totalling 100 cells randomly chosen from a total of about 75 000 cells/well at each concentration of nanostructures. The experiment was repeated twice and the presence of the typical SERRS signals was evaluated following the Pearson correlation method. In particular, the statistical evaluation of data collected for each cell was conducted using Pearson correlation coefficients calculated with the build-in function corrcoef of Matlab and as a reference the typical SERRS spectrum of the TR label. Using the WiRE 4 build-in routines of the micro-Raman instrument each spectrum was corrected subtracting the baseline and only the spectra with a correlation coefficient above 0.6 were considered to be positive. Data are reported as percentages of positive cells among the 200 cells considered for each experiment. Error bars are 95% confidence intervals. The homogeneity of the results of the two replicate experiments was checked using a two-tailed test. A p-value <0.01 was considered to be statistically significant. All statistical analyses were performed using R software (R Development Core Team, version 3.4; R Foundation for Statistical Computing, Vienna, Austria).

Molecular Dynamics Calculations

MD simulations were carried out using the software package Gromacs v4.6.5 [30] The Gromos53a6 force field parameters were used for peptides [31] while the PEG parameters were taken from Fuchs et al [32]. In the first part of simulations, the systems were described using 36 molecules composed by a PEG75 chain linked to a GE11 or a KKKGG-GE11 peptide and about 80 000 explicit simple point-

charge (SPC) water molecules [33]. To improve the computational performances, the amount of water molecules was reduced during the simulation that, in turn, leads to the significant reduction of the PEG phase thickness. At the end of the system dimension reduction, 58 000 water molecules were present. These systems were simulated for 120 ns in a triclinic box (10 x 9 x 32 nm dimension) in a constant particles, pressure and temperature (NPT) ensemble with a protocol similar to that previously used for other peptide simulations [34-36] Briefly, electrostatic interactions were calculated with the particle mesh Ewald (PME) algorithm [37] (cut-off 1.4 nm). Chloride ions were added to assure the electroneutrality and a double cut-off was used for the van der Waals interactions (1.0–1.4 nm). Using the Berendsen algorithm, pressure and temperature were maintained constant [38]. The system starting configurations were composed by extended PEG chains and peptides in α-helix conformation aligned next to each other in the x–y plane, with the main axis oriented along the Z axis of the box. Convergence was evaluated analysing PEG-peptides chains solvent accessible surface and partial densities, which were obtained using the g_sas, g_density, and g_densmap tools of the GROMACS software package. GE11 secondary structure and both GE11 and PEG dihedral distributions were analysed through define secondary structure of proteins (DSSP) and g_angle tools. The minimum distances between atoms belonging to different peptides were evaluated using a homemade program.

Appendix

(a) $GE11^N$ (Ac-YHWYGYTPQNVI-PEG_1-C-NH_2)

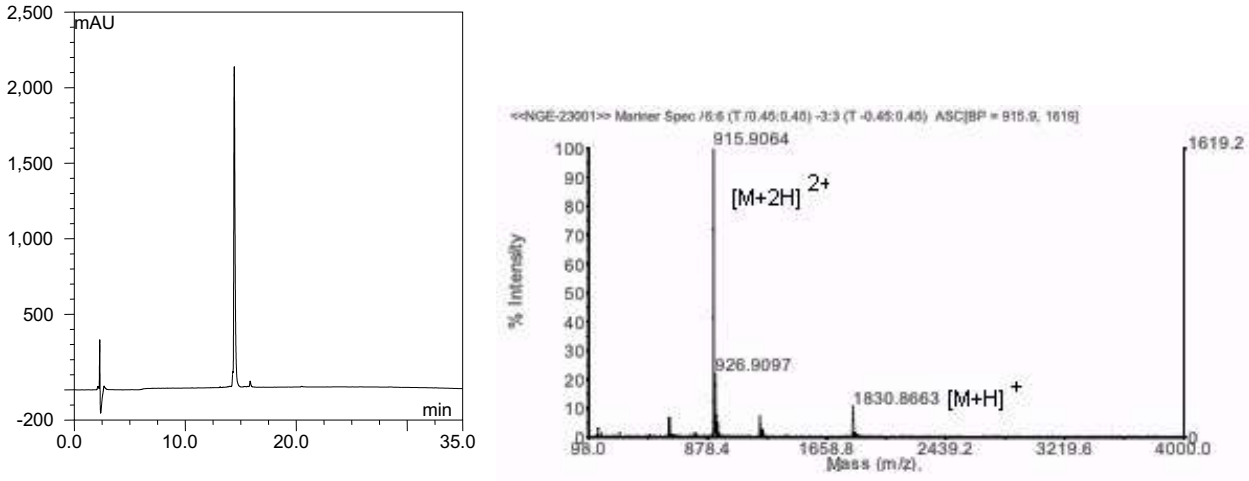

(b) $GE11^C$ (Ac-C-PEG_1-YHWYGYTPQNVI-NH_2)

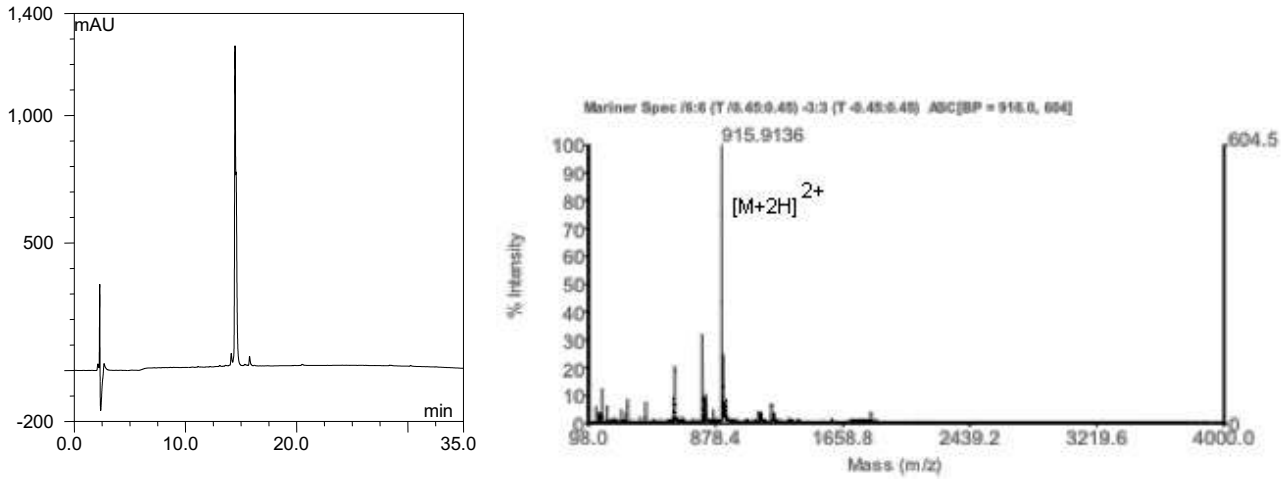

Figure A1. Analytical HPLC and ESI-MS spectra of peptides: (a) $GE11^N$ (b) $GE11^C$. Analytical HPLC separations were performed on a Vydac 218TP54 column (250 x 4.6 mm, 5 μm, flow rate at 1.5 ml/min). The elution condition was: isocratic 10% B for 3 min; linear gradient 10-90% B for 30 min. For preparing binary gradients the mobile phase A (aqueous 0.1% Trifluoroacetic acid (TFA)) and B (90% aqueous acetonitrile containing 0.1%TFA) were used. Mass spectral analyses were carried out on a Mariner API-TOF workstation operating in a positive mode with the ESI technique.

(a) GE11 (YHWYGYTPQNVI-NH_2)

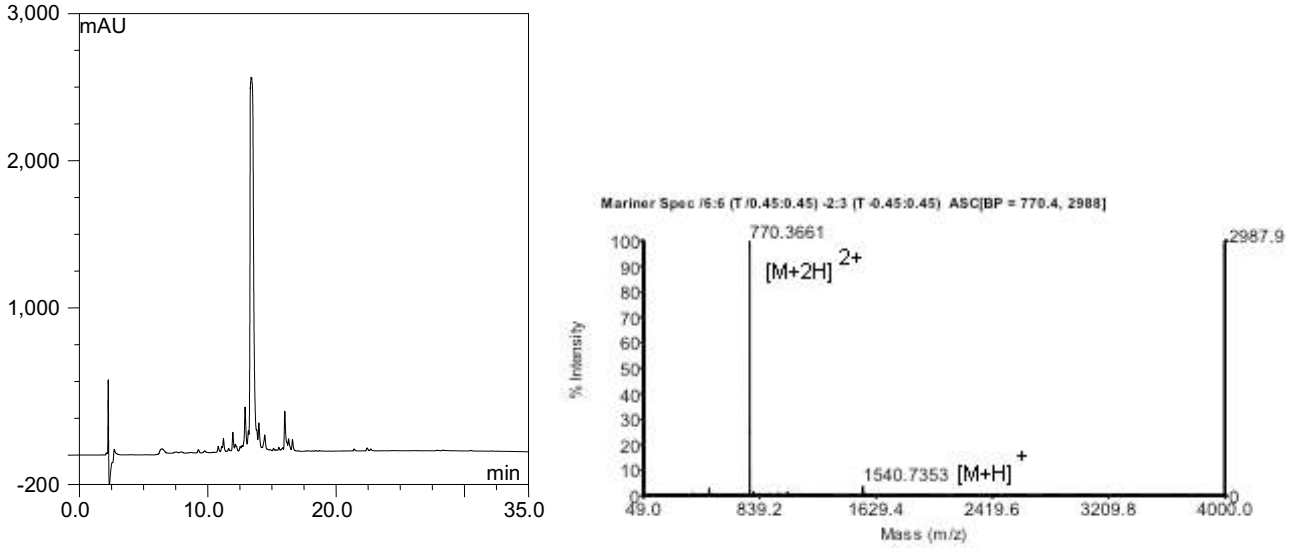

(b) KKKGG-GE11 (KKKGGYHWYGYTPQNVI-NH_2)

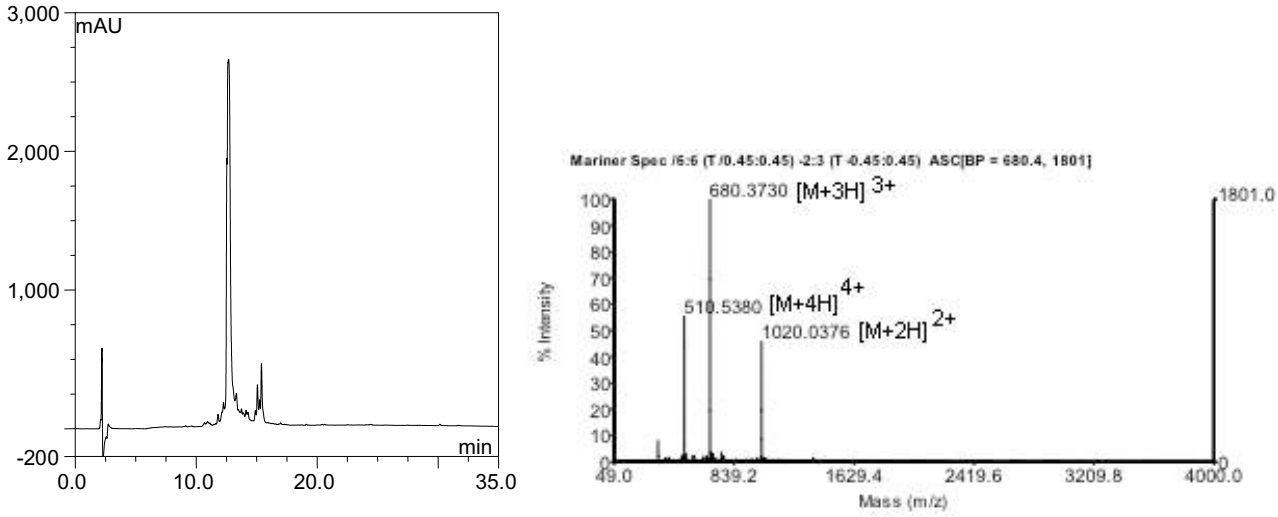

Figure A2. Analytical HPLC and ESI-MS spectra of peptides: (a) GE11 (b) KKKGG-GE11. Analytical HPLC separations and mass spectral analyses were carried out in the same conditions described in Figure A1.

(a) Fluo-GE11^{N} (Ac-YHWYGYTPQNVI-PEG$_1$-Cys (Fluo)-NH$_2$)

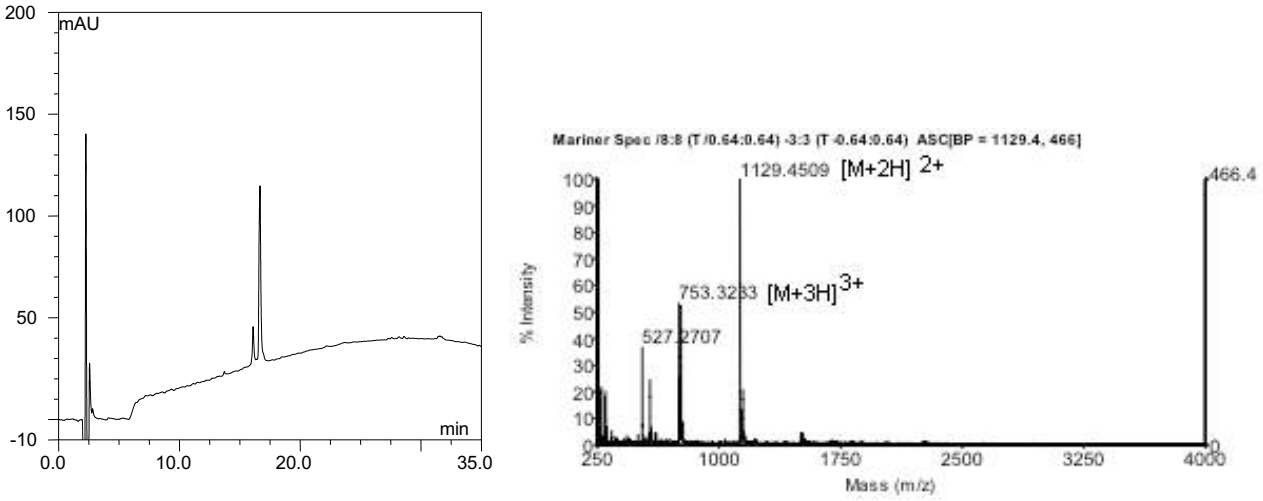

(b) Fluo-GE11^{C} (Fluo-PEG$_1$-YHWYGYTPQNVI-NH$_2$)

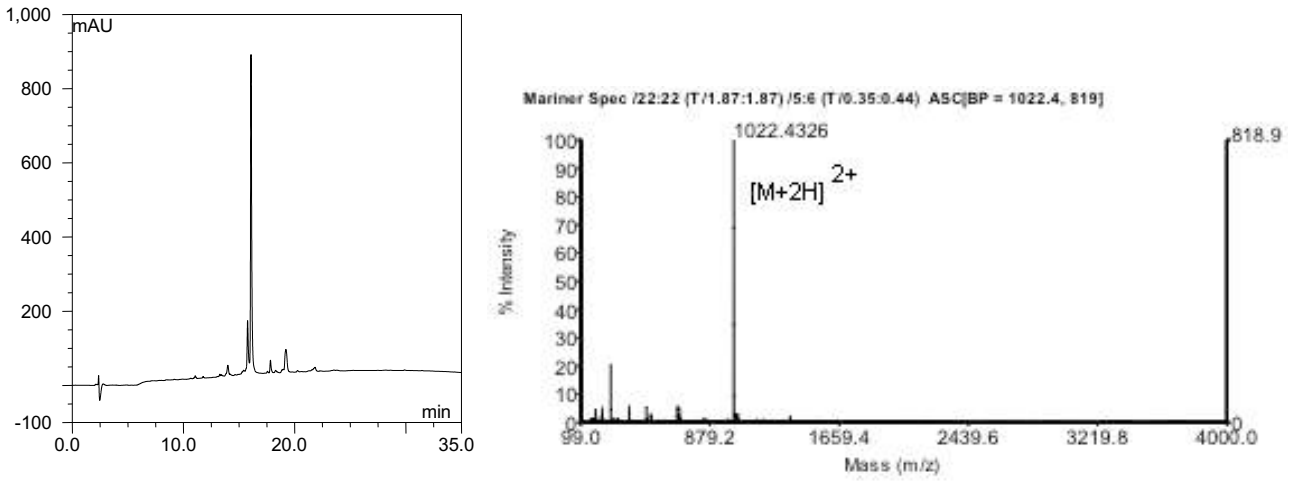

Figure A3. Analytical HPLC and ESI-MS spectra of fluoresceinated peptides: (a) Fluo-GE11^{N} (b) Fluo-GE11^{C}. Analytical HPLC separations and mass spectral analyses were carried out in the same conditions described in Figure A1.

(a) PEG-GE11 (HS-PEG-YHWYGYTPQNVI-NH_2)

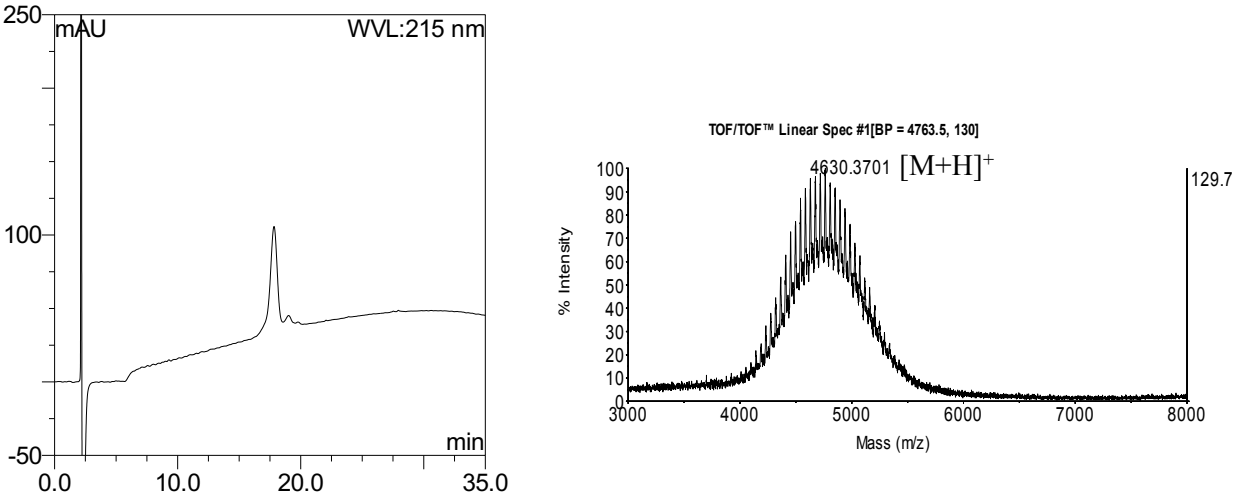

(b) PEG-KKKGG-GE11 (HS-PEG-KKKGGYHWYGYTPQNVI-NH_2)

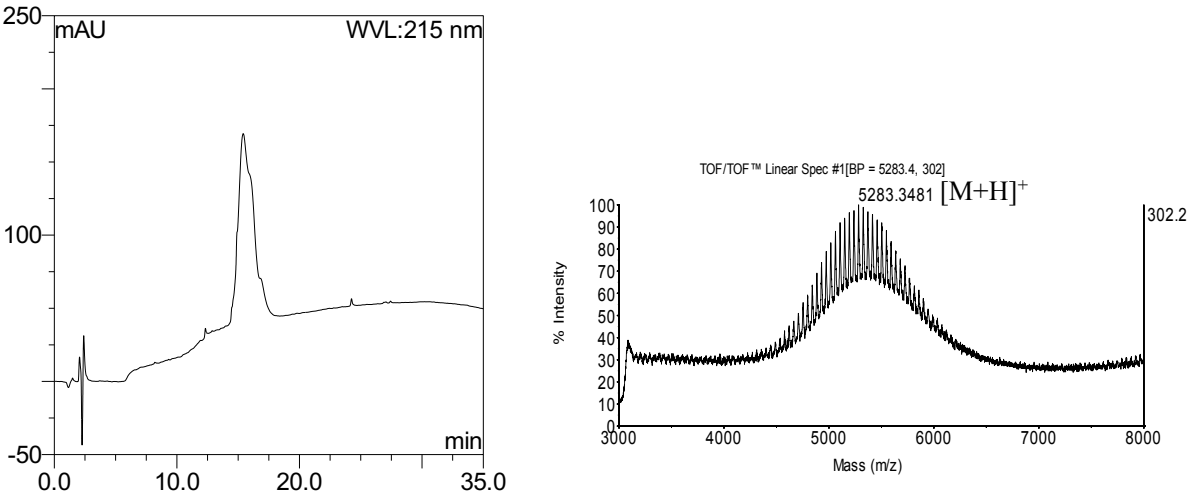

Figure A4. Analytical HPLC and MALDI TOF-TOF spectra of PEG-peptide conjugates (a) PEG-GE11 (b) PEG-KKKGG-GE11. Analytical HPLC separations were carried out in the same conditions described in Figure A1. Mass spectral analyses were performed on a MALDI TOF/TOF Analyser, operating in positive mode in the linear mid-mass range (2,5-dihydroxybenzoic acid as matrix).

Table A1. Analytical data of the synthesized ligands.

Peptide	*Sequence* [a]	*Yield %*	*HPLC*[b] t_R *(min)*	*Expected Mass* $[M+H]^+$	*Found Mass*[b] *m/z*
$GE11^C$	Ac-C-PEG_1-YHWYGYTPQNVI-NH_2	73	14.5	1829.8	915.4 $[M+H]^{+2}$
$GE11^N$	Ac-YHWYGYTPQNVI-PEG_1-C-NH_2	72	14.4	1829.8	1829.8$[M+H]^+$, 915.4$[M+2H]^{+2}$
GE11	YHWYGYTPQNVI-NH_2	94	13.4	1539.7	1540.7 $[M+H]^+$, 770.9$[M+2H]^{+2}$
KKKGG-GE11	KKKGGYHWYGYTPQNVI-NH_2	91	12.7	2038.1	1020.1$[M+2H]^{+2}$ 680.3$[M+3H]^{+3}$, 510.5$[M+4H]^{+4}$
Fluo-$GE11^C$	Fluo-PEG_1-YHWYGYTPQNVI-NH_2	92	16.1	2042.9	1021.9$[M+2H]^{+2}$
Fluo-$GE11^N$	Ac-YHWYGYTPQNVI-PEG_1-Cys(Fluo)-NH_2	91	16.7	2256.9	1128.9$[M+2H]^{+2}$ 753.1$[M+3H]^{+3}$
PEG-GE11	HS-PEG-YHWYGYTPQNVI-NH_2	91	17.8	4729	4630 $[M+H]^+$
PEG-KKKGG-GE11	HS-PEG-KKKGGYHWYGYTPQNVI-NH_2	94	15.4	5226	5283 $[M+H]^{+1}$

[a] Abbreviations: Amino acids are represented by one letter symbol. Fluo is 5(6)-carboxyfluorescein, PEG_1 is 8-amino-3,6-dioxaoctanoic acid, Ac is Acetyl group, PEG is α-tritylthio-ω-N-hydroxysuccinimide PEG

[b] For Analytical HPLC, ESI-MS and MALDI TOF-TOF spectra see Figures A1-A4.

(a) AuNP@GE11^{N}

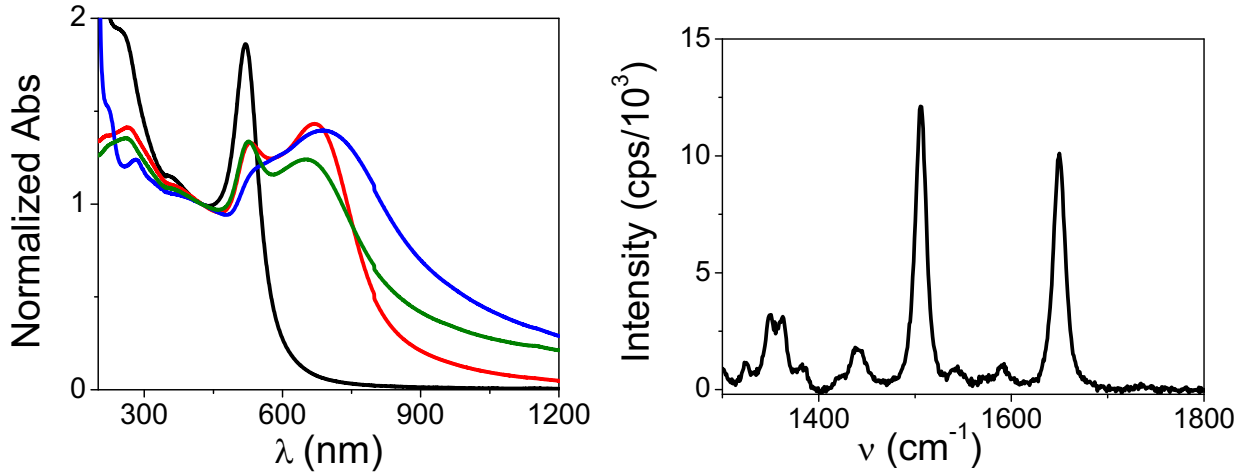

(b) AuNP@GE11^{C}

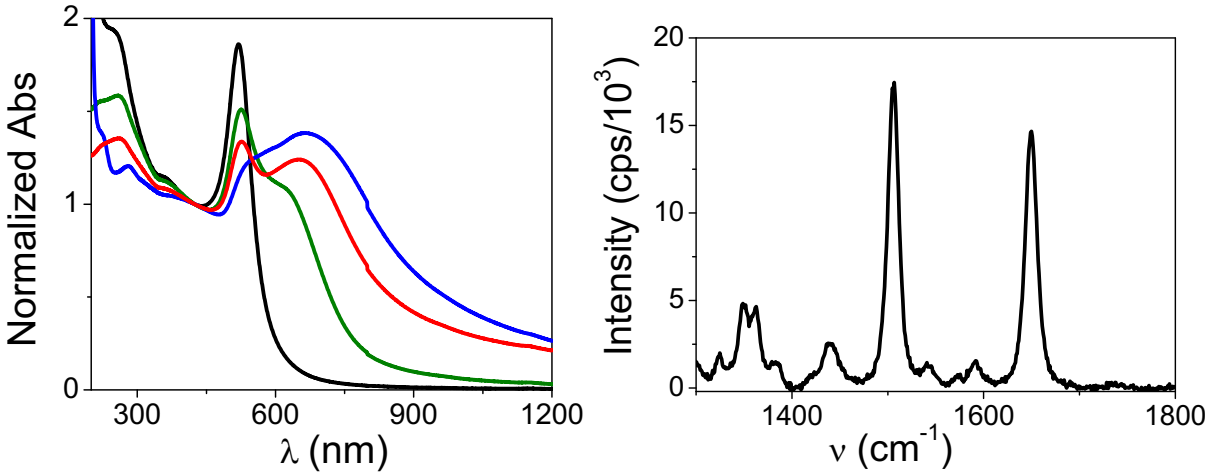

(c) AuNP@PEG-GE11

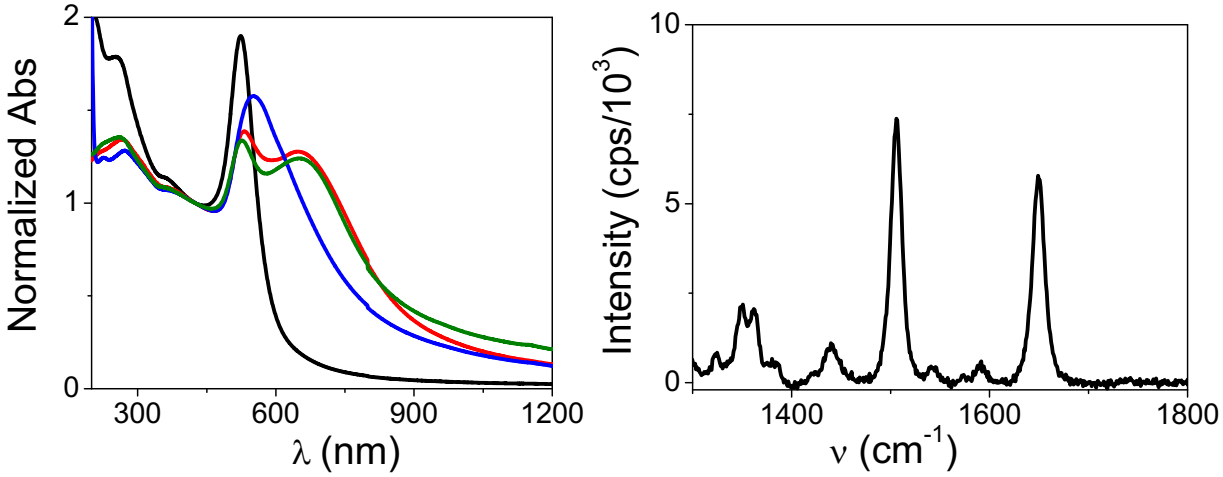

(d) AuNP@PEG-KKKGG-GE11

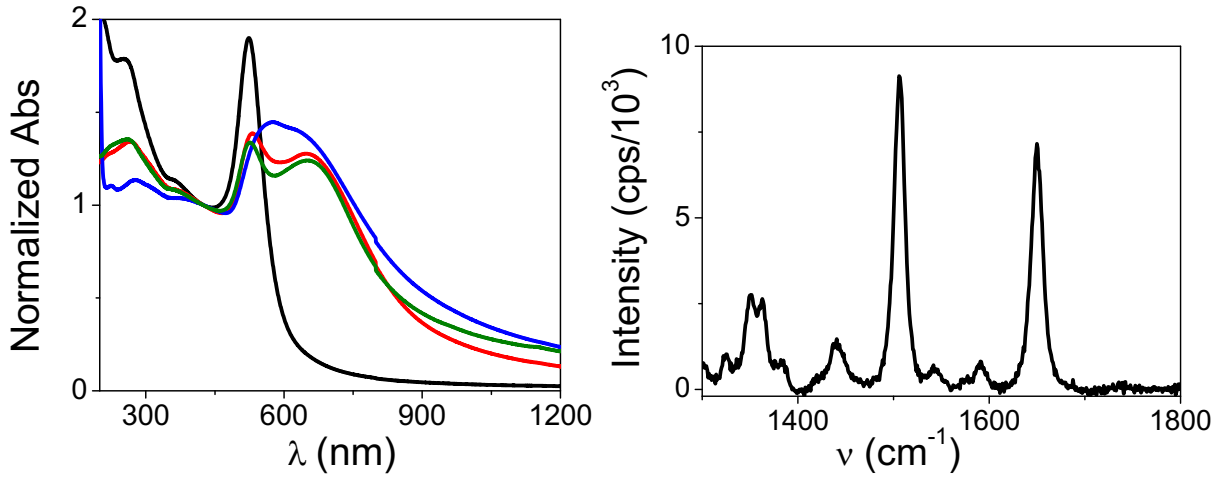

(e) AuNP@PEG

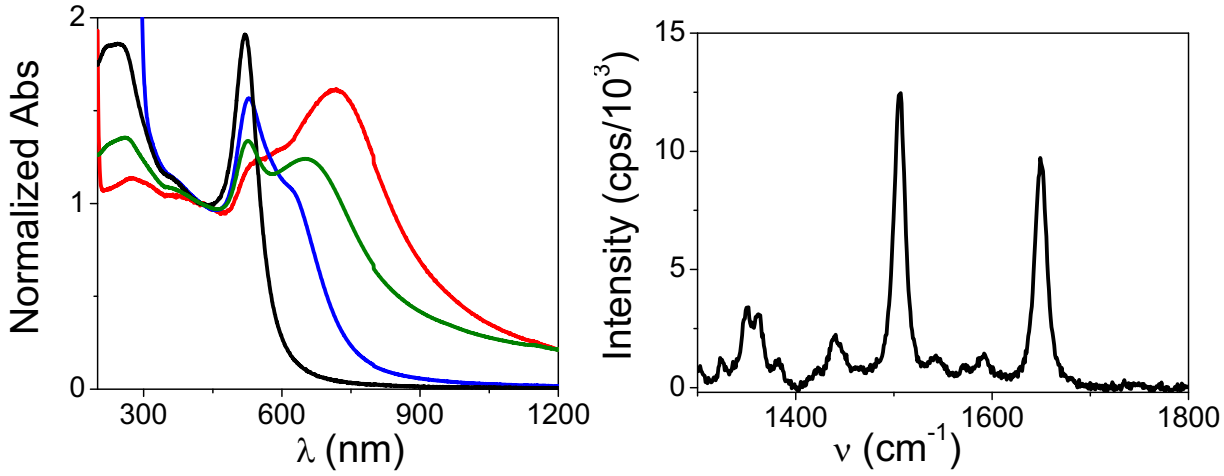

Figure A5. On the left, evolution of the extinction spectra during the assembling steps of the nanostructures: Laser Ablation in Solution of gold nanoparticles (black line), aggregation by centrifugation (green line), labelling with the SERRS reporter (red line) and conjugation of ligands (blue line). On the right, SERRS spectra of the final nanostructures (a) AuNP@GE11^{N} (b) AuNP@GE11^{C} (c) AuNP@PEG-GE11 (d) AuNP@PEG-KKKGG-GE11 (e) AuNP@PEG.

AuNP@Cetuximab

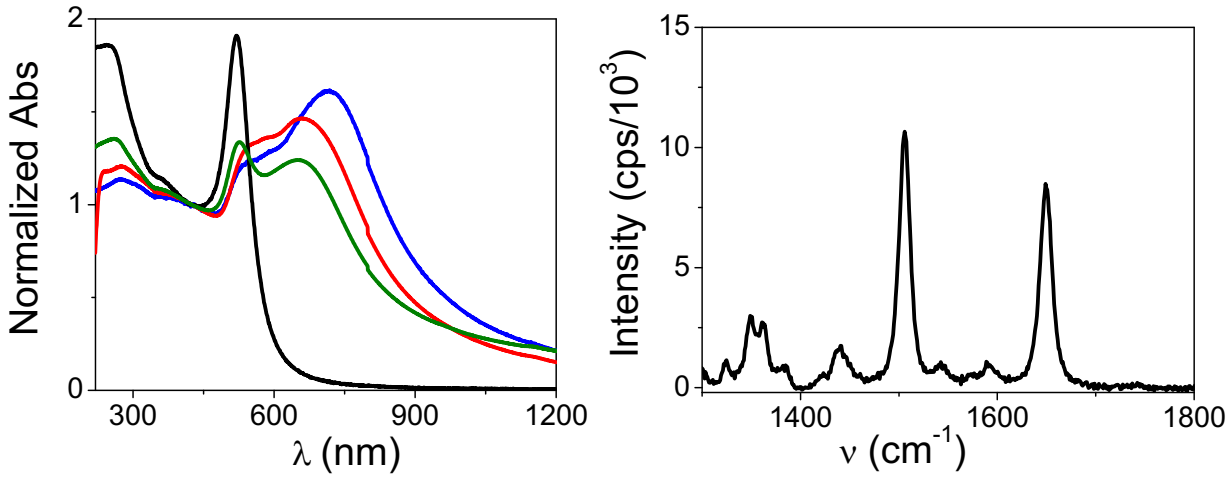

Figure A6. On the left, evolution of the extinction spectra during the assembling steps of the nanostructures: Laser Ablation in Solution of gold nanoparticles (black line), aggregation by centrifugation (green line), labelling with the SERRS reporter (red line) and conjugation of the antibody Cetuximab (blue line). On the right, SERRS spectra of the final nanostructure AuNP@Cetuximab.

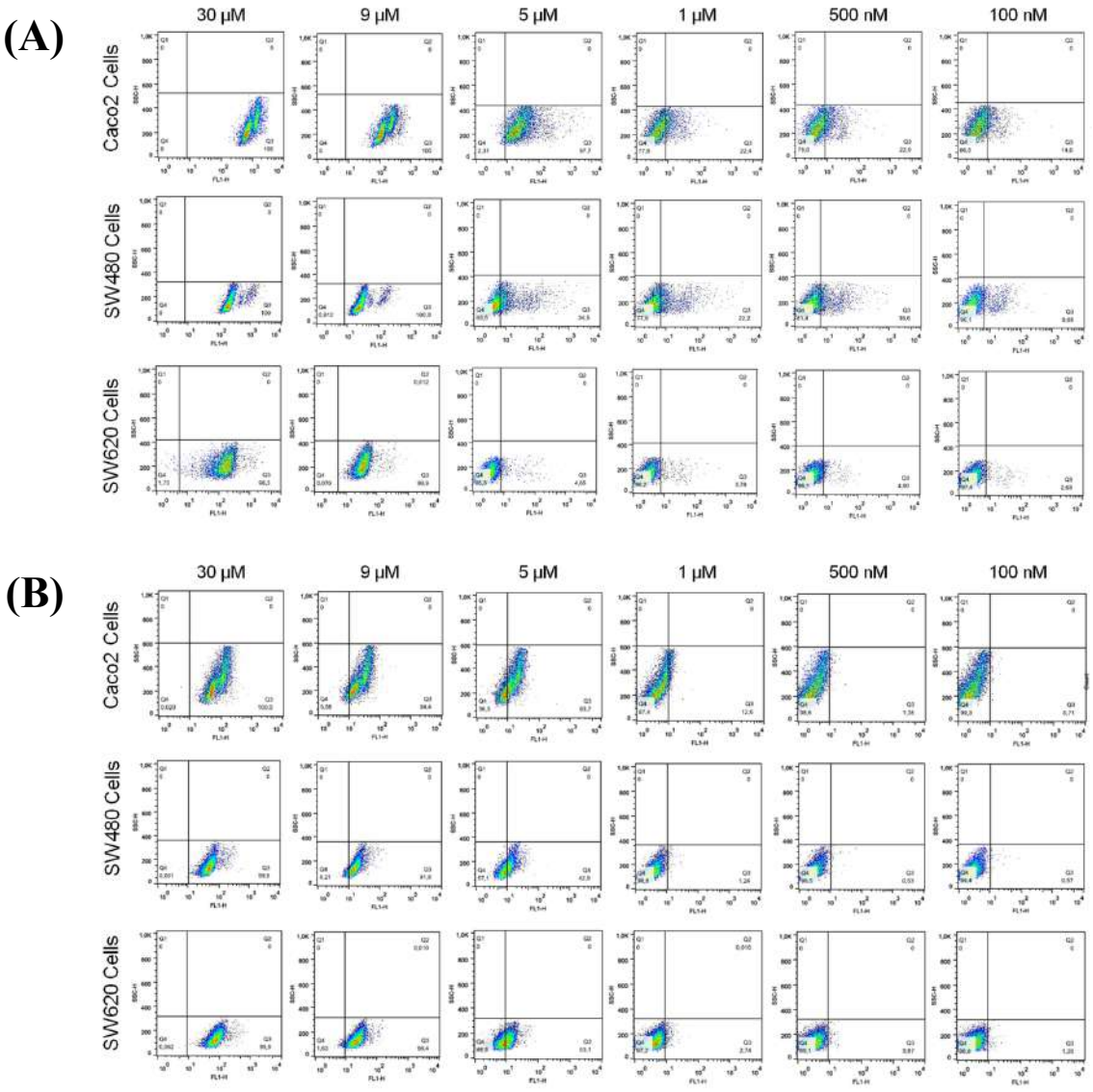

Figure A7. Cytofluorimetric evaluation of Fluo-GE11^{N} (A) and Fluo-GE11^{C} (B) targeting activity on Caco2, SW480 and SW620 cells. Peptides concentration for incubations with cells was varied from 30 µM to 100 nM.

References

1. Li, Z. H., Zhao, R. J., Wu, X. H., Sun, Y., Yao, M., Li, J. J., Xu, Y. H., Gu, J. R., Identification and characterization of a novel peptide ligand of epidermal growth factor receptor for targeted delivery of therapeutics. *Faseb Journal.* **2005**. 19 (14), pp 1978-1985.

2. Vonlaufen, A., Wiedle, G., Borisch, B., Birrer, S., Luder, P., Imhof, B. A., Integrin alpha(v)beta(3) expression in colon carcinoma correlates with survival. *Modern Pathology.* **2001**. 14 (11), pp 1126-1132.

3. Yewale, C., Baradia, D., Vhora, I., Patil, S., Misra, A., Epidermal growth factor receptor targeting in cancer: A review of trends and strategies. *Biomaterials.* **2013**. 34 (34), pp 8690-8707.

4. Liu, B., Fang, M., Schmidt, M., Lu, Y., Mendelsohn, J., Fan, Z., Induction of apoptosis and activation of the caspase cascade by anti-EGF receptor monoclonal antibodies in DiFi human colon cancer cells do not involve the c-jun N-terminal kinase activity. *British Journal of Cancer.* **2000**. 82 (12), pp 1991-1999.

5. Baselga, J., Pfister, D., Cooper, M. R., Cohen, R., Burtness, B., Bos, M., D'Andrea, G., Seidman, A., Norton, L.; Gunnett, K., Falcey, J., Anderson, V., Waksal, H., Mendelsohn, J., Phase I studies of anti-epidermal growth factor receptor chimeric antibody C225 alone and in combination with cisplatin. *Journal of Clinical Oncology.* **2000**. 18 (4), pp 904-914.

6. Nicholson, R. I., Gee, J. M. W., Harper, M. E., EGFR and cancer prognosis. *European Journal of Cancer.* **2000**. 37, pp S9-S15.

7. Azemar, M., Schmidt, M., Arlt, F., Kennel, P., Brandt, B., Papadimitriou, A., Groner, B., Wels, W., Recombinant antibody toxins specific for ERBB2 and EGF receptor inhibit the in vitro growth of human head and neck cancer cells and cause rapid tumor regression in vivo. *International Journal of Cancer.* **2000**. 86 (2), pp 269-275.

8. Papo, N., Seger, D., Makovitzki, A., Kalchenko, V., Eshhar, Z., Degani, H., Shai, Y., Inhibition of tumor growth and elimination of multiple metastases in human prostate and breast xenografts by systemic inoculation of a host defense-like lytic peptide. *Cancer Research* **2006**. 66 (10), pp 5371-5378.

9. Schafer, A., Pahnke, A., Schaffert, D., van Weerden, W. M., de Ridder, C. M. A., Rodl, W., Vetter, A., Spitzweg, C., Kraaij, R., Wagner, E., Ogris, M., Disconnecting the Yin and Yang Relation of Epidermal Growth Factor Receptor (EGFR)-Mediated Delivery: A Fully Synthetic, EGFR-Targeted Gene Transfer System Avoiding Receptor Activation. *Human Gene Therapy.* **2011**. 22 (12), pp 1463-1473.

10. Cardo-Vila, M., Giordano, R. J., Sidman, R. L., Bronk, L. F., Fan, Z., Mendelsohn, J., Arap, W., Pasqualini, R., From combinatorial peptide selection to drug prototype (II): Targeting the epidermal growth factor receptor pathway. *Proceedings of the National Academy of Sciences of the United States of America.* **2010**. 107 (11), pp 5118-5123.

11. Esposito, C. L., Passaro, D., Longobardo, I., Condorelli, G., Marotta, P., Affuso, A., de Franciscis, V., Cerchia, L., A Neutralizing RNA Aptamer against EGFR Causes Selective Apoptotic Cell Death. *Plos One.* **2011**. 6 (9), pp 12.

12. Fan, M. L., Yang, D. B., Liang, X. F., Ao, J. P., Li, Z. H., Wang, H. Y., Shi, B. Z., Design and biological activity of epidermal growth factor receptor-targeted peptide doxorubicin conjugate. *Biomedicine & Pharmacotherapy.* **2015**. 70, pp 268-273.

13. Master, A. M., Qi, Y. Z., Oleinick, N. L., Sen Gupta, A., EGFR-mediated intracellular delivery of Pc 4 nanoformulation for targeted photodynamic therapy of cancer: in vitro studies. *Nanomedicine-Nanotechnology Biology and Medicine.* **2012**. 8 (5), pp 655-664.

14. Chariou, P. L., Lee, K. L., Wen, A. M., Gulati, N. M., Stewart, P. L., Steinmetz, N. F., Detection and Imaging of Aggressive Cancer Cells Using an Epidermal Growth Factor Receptor (EGFR)-Targeted Filamentous Plant Virus-Based Nanoparticle. *Bioconjugate Chemistry.* **2015**. 26 (2), pp 262-269.

15. Abyaneh, H. S., Soleimani, A. H., Vakili, M. R., Soudy, R., Kaur, K., Cuda, F., Tavassoli, A., Lavasanifar, A., Modulation of Hypoxia-Induced Chemoresistance to Polymeric Micellar Cisplatin: The Effect of Ligand Modification of Micellar Carrier Versus Inhibition of the Mediators of Drug Resistance. *Pharmaceutics.* **2018**. 10 (4), pp 18.

16.Zheng, T. T., Feng, H. H., Liu, L., Peng, J., Xiao, H. T., Yu, T., Zhou, Z. Q., Li, Y., Zhang, Y. S., Bai, X. H., Zhao, S. M., Shi, Y., Chen, Y., Enhanced antiproliferative effect of resveratrol in head and neck squamous cell carcinoma using GE11 peptide conjugated liposome. *International Journal of Molecular Medicine.* **2019**. 43 (4), pp 1635-1642.

17. Abdelrehim, A., Shaltiel, L., Zhang, L., Barenholz, Y., High, S., Harris, L. K., The use of tail-anchored protein chimeras to enhance liposomal cargo delivery. *Plos One.* **2019**. 14 (2), pp 17.

18. Du, C., Qi, Y. Q., Zhang, Y. L., Wang, Y. Z., Zhao, X., Min, H., Han, X. X., Lang, J. Y., Qin, H., Shi, Q. W., Zhang, Z. K., Tian, X. D., Anderson, G. J., Zhao, Y., Nie, G. J., Yang, Y. M., Epidermal Growth Factor Receptor-Targeting Peptide Nanoparticles Simultaneously Deliver Gemcitabine and Olaparib To Treat Pancreatic Cancer with Breast Cancer 2 (BRCA2) Mutation. *Acs Nano.* **2018**. 12 (11), pp 10785-10796.

19. Fasolato, C., Giantulli, S., Silvestri, I., Mazzarda, F., Toumia, Y., Ripanti, F., Mura, F., Luongo, F., Costantini, F., Bordi, F., Postorino, P., Domenici, F., Folate-based single cell screening using surface enhanced Raman microimaging. *Nanoscale.* **2016.** 8 (39), pp 17304-17313.

20. Stefanick, J. F., Kiziltepe, T., Bilgicer, B., Improved Peptide-Targeted Liposome Design Through Optimized Peptide Hydrophilicity, Ethylene Glycol Linker Length, and Peptide Density. *Journal of Biomedical Nanotechnology.* **2015**. 11 (8), pp 1418-1430.

21. Wong, S. F., Cetuximab: An epidermal growth factor receptor monoclonal antibody for the treatment of colorectal cancer. *Clinical Therapeutics.* **2005**. 27 (6), pp 684-694.

22. Biscaglia, F., Rajendran, S., Conflitti, P., Benna, C., Sommaggio, R., Litti, L., Mocellin, S., Bocchinfuso, G., Rosato, A., Palleschi, A., Nitti, D., Gobbo, M., Meneghetti, M., Enhanced EGFR targeting activity of plasmonic nanostructure with engineered GE11 peptide. *Advanced Healthcare Materials.* **2017**. 6 (23), pp 1700596-1700604.

23. Meneghetti, M., Scarsi, A., Litti, L., Marcolongo, G., Amendola, V., Gobbo, M., Di Chio, M., Boscaini, A., Fracasso, G., Colombatti, M., Plasmonic Nanostructures for SERRS Multiplexed Identification of Tumor-Associated Antigens. *Small.* **2012**. 8 (24), pp 3733-3738.

24. Kuo, W. T., Lin, W. C., Chang, K. C., Huang, J. Y., Yen, K. C., Young, I. C., Sun, Y. J., Lin, F. H., Quantitative Analysis of Ligand-EGFR Interactions: A Platform for Screening Targeting Molecules. *Plos One* **2015**. 10 (4), pp 1.

25. Walkey, C. D., Olsen, J. B., Guo, H., Emili, A., Chan, W., Nanoparticle size and surface chemistry determine serum protein adsorption and macrophage uptake. *J. Am. Chem. Soc.* **2012**. 134, pp 2130-2147.

26. Wang, M., Thanou, M., Targeting nanoparticles to cancer. *Pharmacological Research.* **2010**. 62 (2), pp 90-99.

27. Stefanick, J. F., Ashley, J. D., Bilgicer, B., Enhanced Cellular Uptake of Peptide-Targeted Nanoparticles through Increased Peptide Hydrophilicity and Optimized Ethylene Glycol Peptide-Linker Length. *Acs Nano.* **2013**. 7 (9), pp 8115-8127.

28. Saha, B., Evers, T. H., Prins, M. W. J., How Antibody Surface Coverage on Nanoparticles Determines the Activity and Kinetics of Antigen Capturing for Biosensing. *Analytical Chemistry.* **2014**. 86 (16), pp 8158-8166.

29.Amendola, V., Meneghetti, M., Size Evaluation of Gold Nanoparticles by UV-vis Spectroscopy. *Journal of Physical Chemistry C.* **2009**. 113 (11), pp 4277-4285.

30. Pall, S., Abraham, M. J., Kutzner, C., Hess, B., Lindahl, E., Int. Conf. on EASC, Solving Software Challenges for Exascale. *Springer- Verlag, Berlin*. **2015**. 8759, pp 3.

31. Oostenbrink, C., Villa, A., Mark, A. E., Van Gunsteren, W. F., A biomolecular force field based on the free enthalpy of hydration and solvation: The GROMOS force-field parameter sets 53A5 and 53A6. *Journal of Computational Chemistry.* **2004**. 25 (13), pp 1656-1676.

32. Fuchs, P. F. J., Hansen, H. S., Hunenberger, P. H., Horta, B. A. C., A GROMOS Parameter Set for Vicinal Diether Functions: Properties of Polyethyleneoxide and Polyethyleneglycol. *Journal of Chemical Theory and Computation.* **2012**. 8 (10), pp 3943-3963.

33. Berendsen, H. J. C., Postma, J. P. M., Van Gunsteren, W. F., Hermans, J., In Intermolecular Forces. Ed: B. *Pullman, Reidel, Dordrecht*. **1981**. pp 331-342.

34. Bocchinfuso, G., Bobone, S., Mazzuca, C., Palleschi, A., Stella, L., Fluorescence spectroscopy and molecular dynamics simulations in studies on the mechanism of membrane destabilization by antimicrobial peptides. *Cellular and Molecular Life Sciences.* **2011**. 68 (13), pp 2281-2301.

35. Bobone, S., Gerelli, Y., De Zotti, M., Bocchinfuso, G., Farrotti, A., Orioni, B., Sebastiani, F., Latter, E., Penfold, J., Senesi, R., Formaggio, F., Palleschi, A., Toniolo, C., Fragneto, G., Stella, L., Membrane thickness and the mechanism of action of the short peptaibol trichogin GA IV. *Biochimica Et Biophysica Acta-Biomembranes.* **2013**. 1828 (3), pp 1013-1024.

36. Farrotti, A., Bocchinfuso, G., Palleschi, A., Rosato, N., Salnikov, E. S., Voievoda, N., Bechinger, B., Stella, L., Molecular dynamics methods to predict peptide locations in membranes: LAH4 as a stringent test case. *Biochimica Et Biophysica Acta-Biomembranes.* **2015**. 1848 (2), pp 581-592.

37. Essmann, U., Perera, L., Berkowitz, M. L., Darden, T., Lee, H., Pedersen, L. G., A smooth particle mesh ewald method. *Journal of Chemical Physics.* **1995**. 103 (19), pp 8577-8593.

38. Berendsen, H. J. C., Postma, J. P. M., Van Gunsteren, W. F., Di Nola, A., Haak, J. R., Molecular dynamics with coupling to an external bath. *Journal of Chemical Physics*. **1984**. 81, pp 3684-3690.

Chapter 4: Understanding the efficient $\alpha_v\beta_3$ integrin targeting of SERRS nanostructures functionalized with engineered cycloRGD peptides

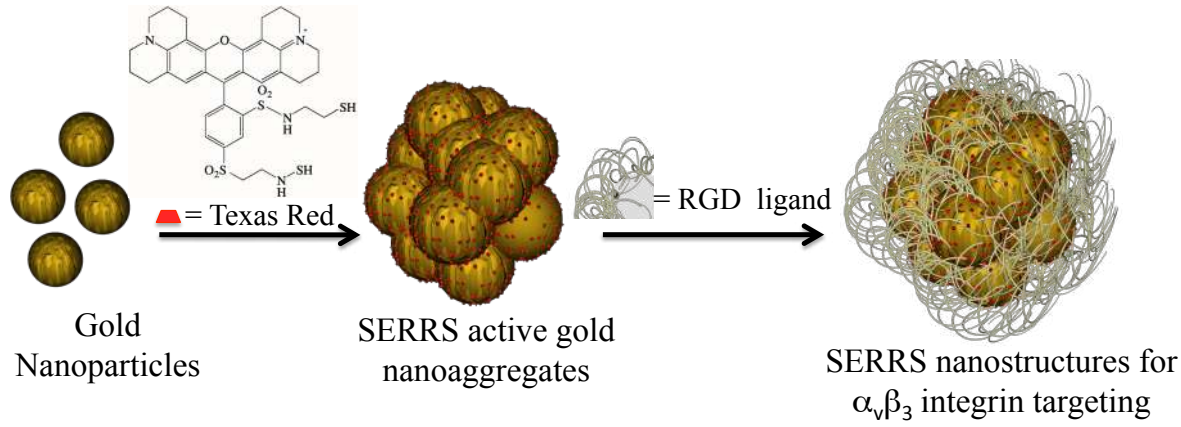

Schematic steps for the preparation of SERRS nanostructures for $\alpha_v\beta_3$ integrin targeting: gold nanoparticles synthesized by LASiS were induced to assemble in SERRS active gold nanoaggregates by functionalization with Texas Red as SERRS label. Then, nanoaggregates were functionalized with RGD peptides as $\alpha_v\beta_3$ targeting ligands.

As deeply discussed in Chapter 1, integrins are a family of adhesion receptors identified in the extracellular matrix [1,2] and in tumour vasculatures [3] involved in many physiological processes such as cells growth and migration. Among different integrins, $\alpha_v\beta_3$ integrin is of a great interest for cancer nanomedicine since high levels of expression are associated with increased cells invasion and metastasis [4]. Up-regulation was observed in breast, pancreatic and colorectal cancer, that is one of the target tumour of this PhD project, of patients who have metastatic disease [5,6]. $\alpha_v\beta_3$ integrin can be recognized by various agents containing the tripeptide sequence Arg-Gly-Asp (RGD) [1,7] and in the last decades a number of nanosystems functionalized with ligands incorporating this targeting motif have been developed for targeted imaging [8-10], drug delivery [11,12] and phototherapy [13,14]. Unfortunately just a few nanosystems have been translated into clinical trials because of their limited delivery to the diseased site and considerable systemic toxicity [15]. This is mainly due to enzymatic degradation, protein adsorption and uptake by the immune system to which nanoparticles are subjected once intravenously injected [16]. The covering of the nanostructures surface with highly hydrophilic and anti-fouling polymers, like PEG, is a widely exploited strategy to deal with these problems. The PEG shell, in fact, minimizes non-specific physical absorption of proteins and reactions with biological species which are responsible of the degradation of the targeting ligands and of the rapid uptake by the immune systems, thus reducing blood retention and limiting the delivery of the nanosystem to the tumour [17-19]. Besides, the influence of the PEG coating on the nanosystems targeting capability has been object of curiosity in many studies in recent literature whose main focus is the engineering of the polymeric layer for the improvement of the sensitivity and the specificity of the receptor binding. Regarding nanostructures functionalized with RGD ligands, several studies have investigated on the effect of the PEG length, achieving not homogenous results. Ge and co-workers showed that the elongation of PEG from 12 to 20 kDa on PEGylated polyplex micelles promotes both the system delivery to the tumour and the cellular uptake. This is due to the increase of PEG crowdedness that contributes to avoid rapid blood clearance [20]. Elongation of PEG length proved also to be useful for the enhancement of either the integrin dependent internalization or the transfection efficiency [21]. On the contrary, the increase of the length of the PEG-linker connecting RGD to the nanostructures from 2 to 5 kDa resulted in irrelevant change in the cellular uptake of the system [22]. In another article PEG shorter than 1 kDa demonstrated to be the most suitable linker [23] since longer PEG chains hinder the peptide proper exposition for the association with the receptor [24]. In addition to the PEG length, an appropriate peptide density on the nanostructures surface plays a key role for an efficient binding between ligands and receptors [25]. In particular it has been demonstrated that increasing the functionalization with PEG, and consequently lowering the RGD peptide density, the uncontrolled adsorption of plasma proteins can be limited thus prolonging the blood retention and

promoting the nanosystem accumulation in the tumour [26,27]. Actually, the effect of the organization of the RGD targeting motifs on nanostructures coated with PEG has not been investigated. With the aim to contribute to increase knowledge on this matter and considering that the presentation on the polymeric layer of another peptide, namely the peptide GE11, proved to strongly influence the binding of the EGFR on colorectal cancer cells (Chapter 3), in this chapter the synthesis of SERRS nanostructures functionalized with different analogues of cyclo[RGDyK] peptide (cRGD) [28] is described. Peptides analogues were rationally designed in order to expose the targeting sequence in different arrangement on the polymer coating the nanosystems. The targeting activity of the nanostructures was studied by incubation with colorectal cancer cells expressing the $\alpha_v\beta_3$ integrin (Caco2 and SW620) thanks to the partnership with the group of Prof. A. Rosato and Prof. S.Mocellin of Department of Surgery Oncology and Gastroenterology of the University of Padova. Engineering of the targeting ligands was found to strongly influence the nanostructures targeting ability and Molecular Dynamics (MD) calculations allowed understanding that these differences rely on the different arrangement of the RGD motif on the nanostructures surface. MD simulations were carried out in collaboration with the group of Prof. A. Palleschi of the Department of Chemical Sciences and Technologies of the University of Roma Tor Vergata. Results presented in this chapter were recently published [29].

Results and Discussion

The strategy of functionalizing PEG coated nanoparticles with RGD peptides, as well as other targeting moieties, has been widely explored in the recent past to achieve nanostructures showing efficient accumulation in the tumour and low systemic toxicity. As discussed in Chapter 2, the most common method of synthesizing these systems involves the direct coupling of the targeting units to nanoparticles pre-coated with PEG. This approach results in batch-to-batch variation in nanoparticles functionalization due to the poor control over the peptide loading, surface homogeneity and reproducibility [30-32]. To correlate the targeting activity of RGD functionalized nanostructures with the presentation of the peptide on the surface, a more stringent control over the functionalization is requested. For this purpose, the strategy of first synthesizing thiolated PEG-peptide conjugates and to link them to SERRS nanoaggregates, whose preparation procedure is reported subsequently, was followed. This approach was previously used to obtain nanostructures functionalized with GE11 analogues for EGFR targeting and proved to ensure a good control over the loading of the targeting units avoiding the presence of extraneous ligands on the particles surface (Chapter 3). Following this procedure, a number of PEG-peptide conjugates were engineered to present the RGD targeting motif in different arrangements on the nanostructures surface. All PEG-peptide conjugates were enriched with an extra thiol group to exploit the sulphur affinity for gold to functionalize the nanosystems as discussed in Chapter 2. At first two ligands were synthesized by modifying the peptide at the amino terminus with different-size PEG chains:

a) the Z-cRGD ligand (**1** in Figure 1), obtained by covalently linking a short PEG chain (MW about 100 Da) to cRGD. A residue of cysteine was added to the sequence in order to insert the thiol group requested for the anchoring of the ligand to the gold surface;

b) the PEG-G-cRGD ligand (**2** in Figure 1), synthesized by covalently linking the cRGD peptide through an extra glycine residue to a thiolated longer PEG chain (MW around 3 kDa).

It is well known that the elongation of the PEG chain could hamper the association between ligands and receptors by burying the targeting units in the polymeric layer [33] even though recent literature have highlighted that the exposition of the targeting motif above the polymeric coating can be fostered by increasing the peptide hydrophilicity, thus promoting the receptor recognition [34]. However, for another peptide used for this PhD project, namely the GE11 peptide specific for the EGFR targeting, it was proved that the hydrophilicity of the targeting unit could be not a sufficient condition for guaranteeing a satisfactory receptor binding. Others features, such as an adequate distance between the peptides to prevent their aggregation and a suitable presentation above the PEG coating, are necessary (Chapters 3). As opposite to GE11, which is a neutral peptide, cRGD is zwitterionic at

physiological pH and is therefore supposed to be more exposed above the PEG layer due to the presence of positive and negative charges. For further promoting the presentation of cRGD above the polymeric coating and evaluate the effect of the increased hydrophilicity of the peptide on the association with the receptor, another ligand was synthesized following the same strategy applied for other targeting sequences (Chapter 3, [25,34]): a short oligolysine linker (GKKK) was inserted between the PEG chain (MW around 3 kDa) and the peptide obtaining the PEG-GKKKG-cRGD ligand (**3** in Figure 1).

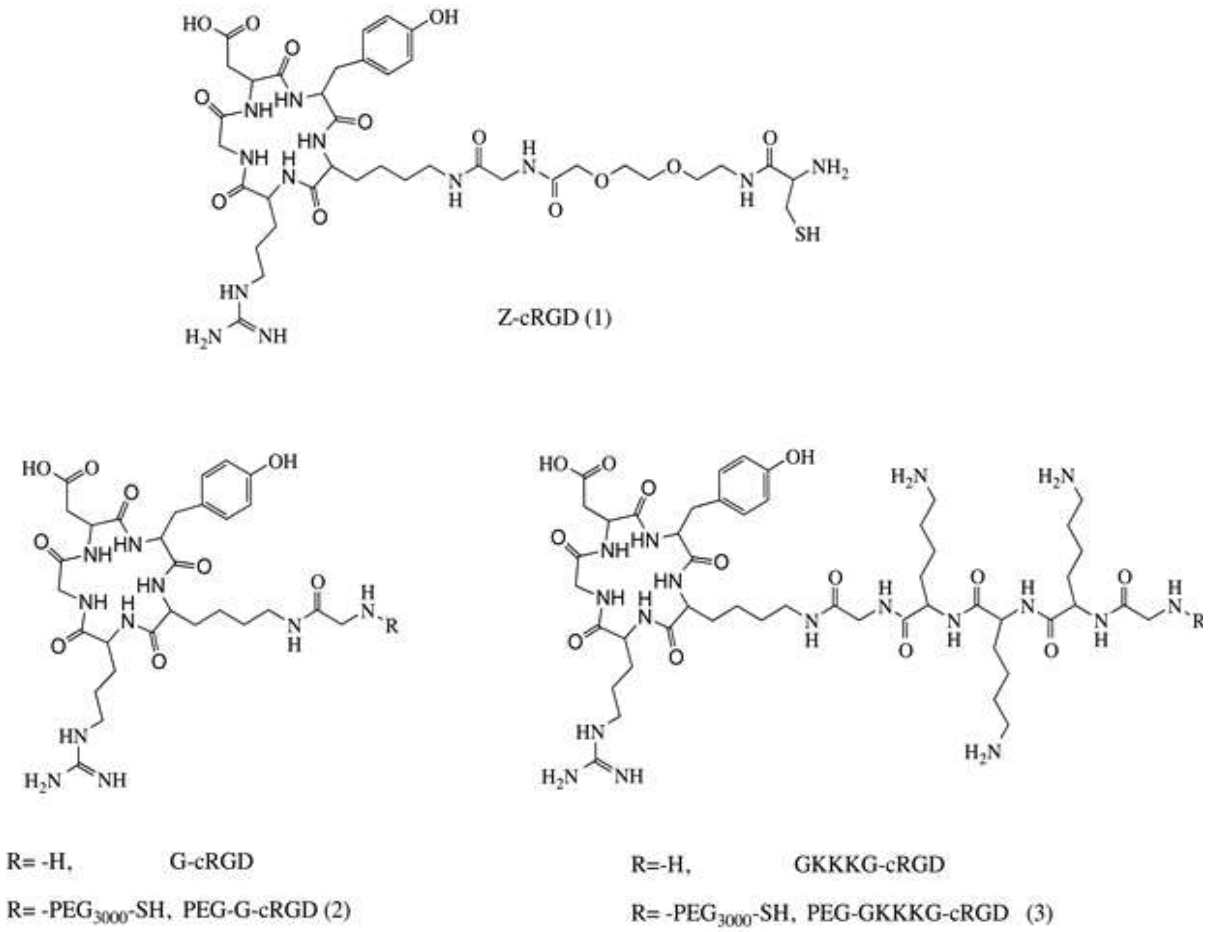

Figure 1. Structures of synthesized peptides and PEG conjugates.

All ligands were synthesized on solid phase and used to prepare the nanosystems AuNP@ Z-cRGD, AuNP@PEG-G-cRGD and AuNP@PEG-GKKKG-cRGD. Experimental procedures and characterizations of peptides and nanosystems are respectively reported in the Experimental Section and in the Appendix of this chapter. Nanosystems were prepared from naked gold nanoparticles

synthesized by laser ablation in solution [35] and induced to assemble in SERRS active nanoaggregates by functionalization with Texas Red (TR) as SERRS reporter. After cleaning from non-reacted TR by centrifugation, the nanoaggregates were functionalized with the ligands. The functionalization was confirmed by Ellman test on the peptide solutions before and after conjugation. This procedure allowed also quantifying the number of ligands covering, on average, each nanoparticle. Around two-three thousands of peptides were found to be linked per nanoparticle (Table 1).

Table 1. Characterization of the nanosystems.

Nanosystems	*Peptides per nanoparticle*	*Hydrodynamic diameter (nm)*	*ζ-potential (mV)*
AuNP@Z-cRGD	2000	132±5	-21±2
AuNP@PEG-G-cRGD	3000	273±15	-53.2±0.5
AuNP@PEG-GKKKG-cRGD	3000	452±13	-16±2

After the final step, the nanosystems were characterized by recording Uv-vis-NIR and SERRS spectra, which confirmed the stability of the aggregates (Fig A3). TEM images (Figure 2) showed that functionalized nanosystems have dimension in the order of 100-200 nm, as also suggested by Dynamic light scattering (DLS) measurements (Table 1). In Chapter 3 it was observed that the hydrodynamic diameter of nanostructures functionalized with PEG-peptides conjugates is smaller than that of nanosystems covered with only the peptides. This was ascribed to the capability of PEG chains to prevent the aggregation among the nanostructures. However, nanosystems decorated with cRGD analogues display the opposite behavior since the hydrodynamic diameter of AuNP@PEG-GKKKG-cRGD and AuNP@PEG-G-cRGD is greater than that of AuNP@Z-cRGD. Moreover, the trend of the number of ligands per nanoparticle is opposite of what previously observed and tentatively explained (Chapter 3), namely that it is lower for nanostructures functionalized with PEG-peptide conjugates because of their larger dimension with respect to the parent peptide. Besides deserving a proper explanation, these unexpected trends are currently not explained and will be thoroughly investigated in the next future. ζ-potentials, as introduced in Chapter 3, are the complex results of a lot of influences deriving from either the nanoaggregates or the ligands on their surface. Despite the trend among the nanostructures is currently not completely understood, negative experimental values support the idea that the nanosystems are stable in solution as colloidal dispersion.

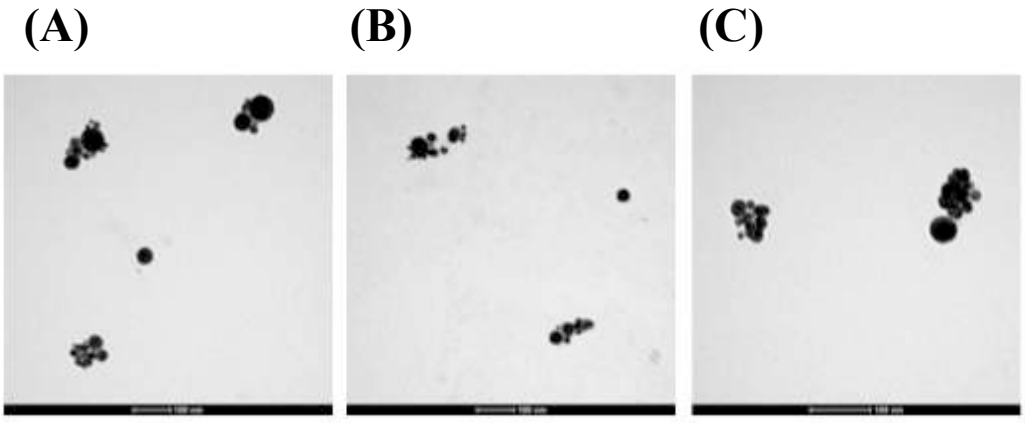

Figure 2. TEM images of the nanosystems: (a) AuNP@Z-cRGD (b) AuNP@PEG-G-cRGD (c) AuNP@PEG-GKKKG-cRGD

The targeting activity of the nanosystems was assessed on colorectal cancer cell lines Caco2 and SW620, whose $\alpha_v\beta_3$ integrin expression was previously verified by flow cytometry (Figure A4). Cells were incubated for 2 h at 37 °C with increasing concentrations of the nanostructures. After then, the nanosystems that did not target cells were discarded by washing and the targeting capability was evaluated by recording SERRS spectra of single cells, totalling on average one hundred of cells. Both SERRS measurements and statistical analysis of the dataset were carried out as described in Chapter 3. For reference, the activity of nanostructures functionalized with PEG only (AuNP@PEG) was also considered. Overall results are summarized in Figure 3. AuNP@Z-cRGD nanostructures bounded sufficiently to both cell lines despite. However, especially for SW620 cells, the targeting activity did not change increasing the concentration of the nanostructures thus proving that the presentation of the targeting peptide is not optimal for the association with the receptor. The targeting activity of AuNP@PEG-G-cRGD nanostructures was found to be very low in both cell lines, right around nanostructures AuNP@PEG that do not present the targeting units and are not expected to recognize $\alpha_v\beta_3$ integrins. Moreover, it did not vary by modifying the nanostructures concentration, as observed for either AuNP@Z-cRGD and AuNP@PEG, suggesting that the targeting motif is not suitably able to interact with the receptor. Recalling that the peptide was supposed to be exposed over the polymeric layer thanks to the good hydrophilicity imparted by the charges, these results clearly proved that the hydrophilicity is not a sufficient condition to assure the proper presentation of the targeting units for good associations with receptors. Peptide ligands on AuNP@PEG-G-cRGD nanostructures are supposed, in fact, to be buried into the PEG coating as already observed for nanostructures functionalized with analogues of GE11 peptide for EGFR targeting described in Chapter 3. By

contrast, AuNP@PEG-GKKKG-cRGD nanostructures showed a remarkable targeting activity achieving sensitivity of almost 100% with SW620 cells at all the explored concentrations. As can be noticed in Figure 3B, the targeting activity raises by increasing the nanostructures concentration reaching sensitivity above 88% with Caco2. The relative sensitivity of recognition of the two cell lines can be ascribed to their different $\alpha_v\beta_3$ integrin expression. Cytofluorometries reported in Figure A4 revealed, in fact, a major expression in SW620 cells that could justify the greater sensitivity of the nanostructures. Anyway, results obtained from both cell lines suggest that the targeting motif on AuNP@PEG-GKKKG-cRGD is properly arranged on the surface to optimally interact with the receptor. The very different results with respect to those of AuNP@PEG-G-cRGD highlighted that the additional charges brought by the three lysines of the linker have beneficial effects on the targeting activity. Interestingly these findings agree with results presented in Chapter 3, pointing out that the different behaviour of the nanosystems enriched or not with the cationic linker can derive from the arrangement of the peptide over the PEG layer. In particular, the addition of the cationic spacer nearby the RGD targeting motif could improve the presentation of the peptide beyond the polymeric coating, enhancing its targeting activity against the receptor. To investigate on several factors influencing the association of the targeting unit with the receptor and, in particular, on the role of the linker on cRGD peptide presentation on the nanostructures surface, MD calculations were performed.

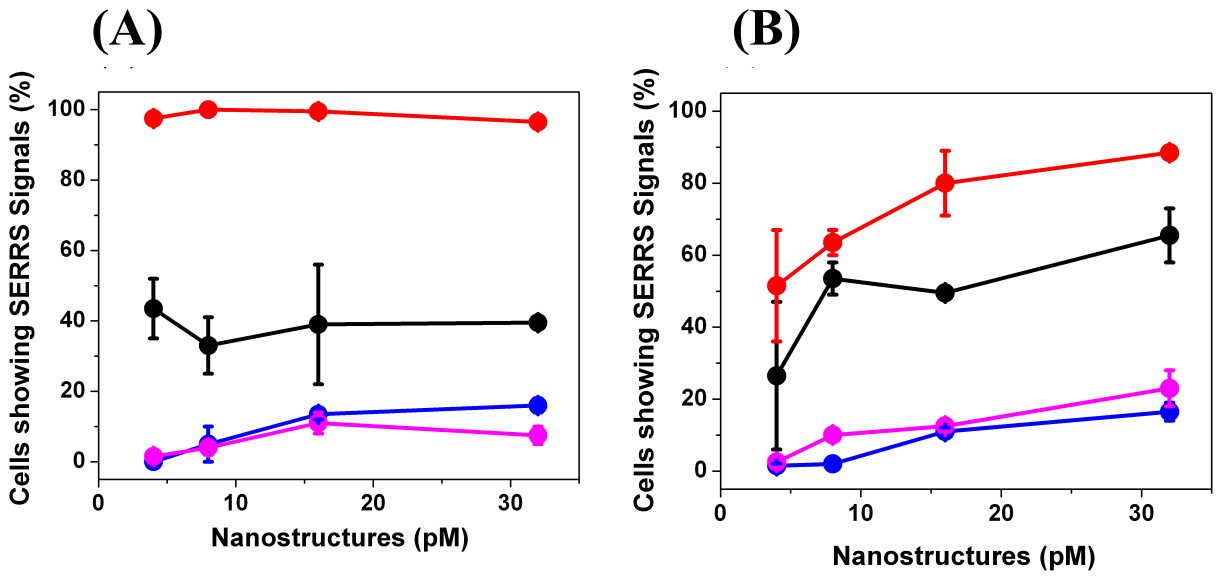

Figure 3. Targeting activity of the nanosystems AuNP@ Z-cRGD (black line), AuNP@PEG-G-cRGD (blue line), AuNP@PEG-GKKKG-cRGD (red line) and AuNP@PEG (magenta line) toward SW620 (A) or Caco2 (B) cells. 100 cells were considered for each measurement and error bars indicate variations of the results for three different selections of 100 cells within two or three preparations.

Simulations were carried out considering two different systems comprised of a planar gold surface of roughly 25 nm^2 and 16 molecules of PEG-G-cRGD or PEG-GKKKG-cRGD. Three independent 200 ns long simulations were performed for each system. In the starting structure, the PEG molecules were inserted in the extended conformation and the cRGD units were taken from the structure with pdb code 1L5G5g [36]. During the simulation range time, the PEG chains slowly loss the starting extended conformation and the number of populated structures with gauche angles increases. This conformational change is coupled with a reduction of the thickness of the PEG layer on the gold plane. In Figure 4 the Z coordinate, where the PEG density falls below 200 kg m^{-3}, is reported as a function of time. Since the reported profiles showed that both the systems reach the equilibrium after roughly 160 ns, only the last 40 ns of the simulations were considered for the analysis. In this interval, the number of virtual torsional angles between four consecutive oxygen atoms which loss the trans conformation in the PEG molecules resulted equal to 90% for both the systems, reflecting the evidence that the presence of the cationic spacer slightly affects the PEG dynamics.

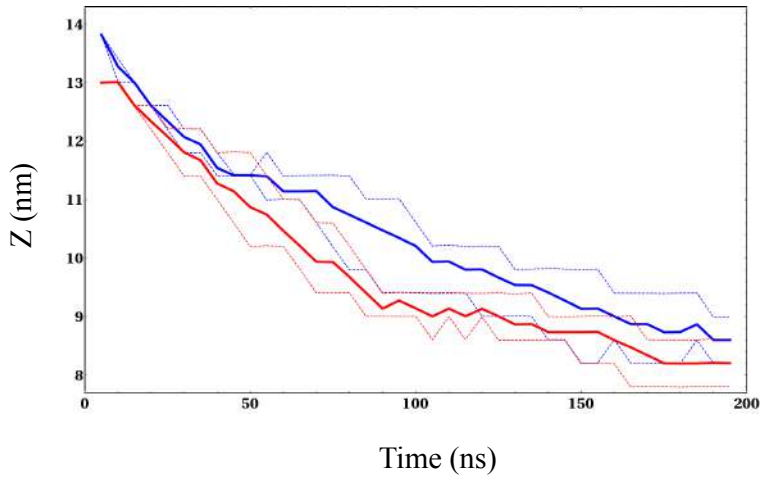

Figure 4. Distance of the PEG/water interface from the gold plane. The reported coordinate corresponds to the Z value where the density of PEG calculated in consecutive intervals of 5 ns is equal to 200 kg m^{-3}. The continuous lines refer to the average value between three independent simulations of the systems containing the G-cRGD (red) and GKKKG-cRGD (blue) bioactive peptides. The dashed lines represent minimum and maximum value registered at each time.

Figure 5 reports the interface between PEG phase and water in the final structure in three replicated calculations for both systems. In all the cases, the peptides localize in the interface region. However, the systems seem showing different water exposure of the cyclopeptides. In the simulations where the cationic spacer is absent the cRGD, besides being located on the external polymeric layer, seems to be more buried, on average, into the PEG phase and less exposed to the water solution than in the simulations where the spacer is present.

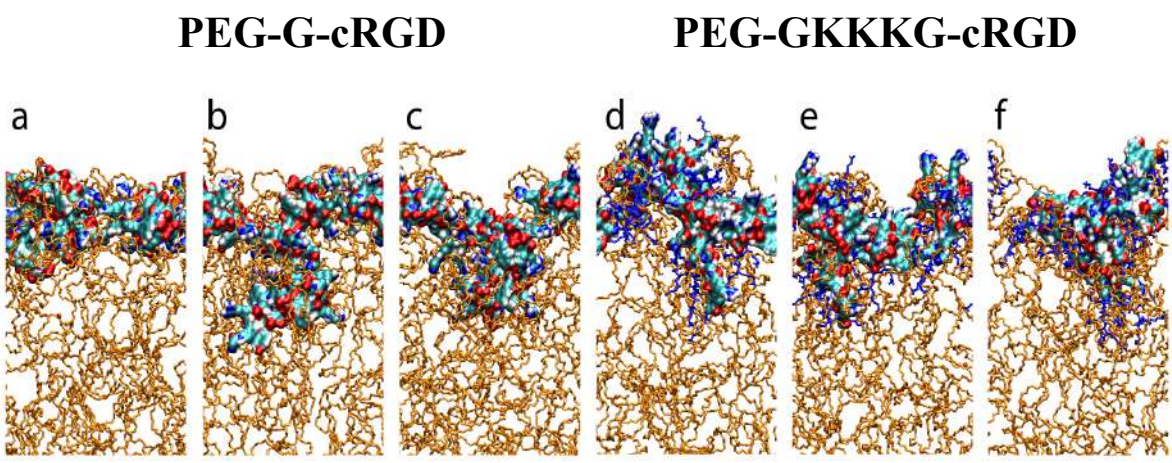

Figure 5. Final structures of the three independent MD simulations for the PEG-G-cRGD (a - c) and PEG-GKKKG-cRGD (d - f) on a gold surface. The PEG chains are shown as orange sticks. The cRGD is represented as surface colored per elements (H, C, N and O in white, cyan, blue and red, respectively). The KKK linker is represented in blue sticks. For sake of clarity, water molecules are not reported.

To quantify this effect, the solvent accessible area of the cRGD peptide and the density profile along the normal to the gold surface of PEG moiety, cyclopeptides, water molecules and the spacers, when present, were calculated in the equilibrated ensembles (Figure 6). The density profile confirmed the differences suggested by the visual inspection of the final structures (Figure 6A): the peptide is completely embedded in the PEG layer in the case of simulations without the spacer (PEG-G-cRGD) while it was observed, together with the cationic spacer, outside the polymeric coating when the spacer is present (PEG-GKKKG-cRGD). The surface of cRGD accessible to water, a direct parameter to quantify the availability of the cyclopeptide in the water phase, is reported in Figure 6B. The data confirmed the general picture above described, with the system containing the cationic spacer definitively more exposed than the corresponding ones without the spacer. A similar scenario was described for nanostructures functionalized with the GE11 peptide for the EGFR targeting (Chapter 3). However, being GE11 not charged at physiological pH, the addition of the cationic linker was expected to increase the peptide exposure to water thus improving its hydrophilicity and consequently its availability for the association with the receptor. On the contrary cRGD is a zwitterionic peptide, so its propensity to remain buried into the PEG layer was not obvious.

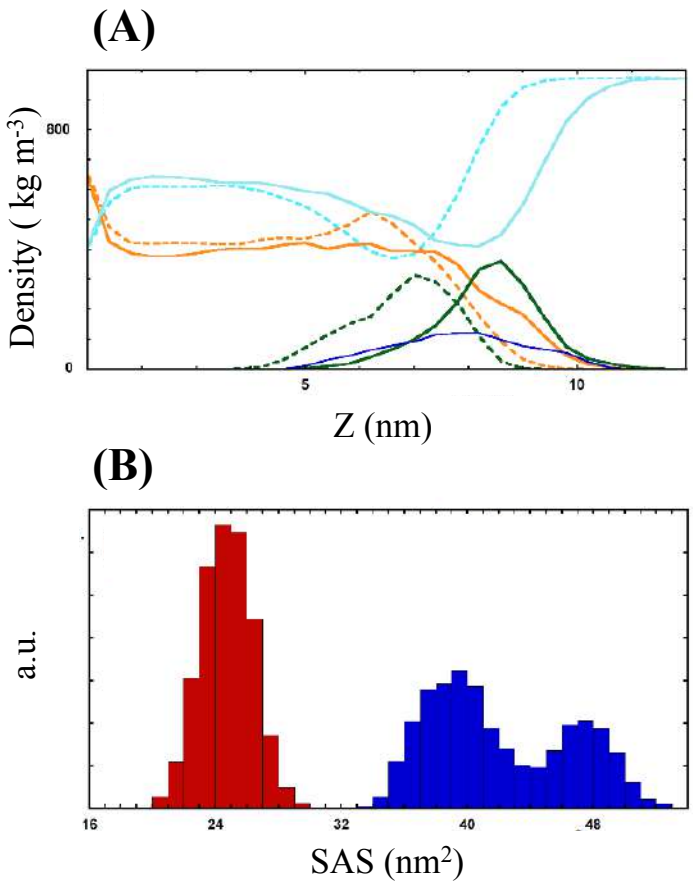

Figure 6. Water exposure of cRGD: density profiles along the normal to the gold plane obtained from MD simulations of PEG-cRGD (dashed lines) and PEG-GKKKG-cRGD (continuous lines). The profiles are calculated on the equilibrated ensembles (last 40 ns of three independent simulations). Light blue, orange, green and blue curves refer to water, PEG, cRGD and GKKKG, respectively (A). Water exposed surfaces of cRGD as calculated on the equilibrated ensemble from the PEG-cRGD (red) and PEG-GKKKG-cRGD (blue) MD simulations (B).

Due to the notable differences determined by the presence or not of the cationic linker, possible contributes of conformational and configurational differences between the two systems were searched. At first, the conformation of cRGD in the two cases was investigated using a global topological parameter that estimates the deviation from the planarity for the cyclopeptide (hereafter, the Index of Planarity). The population of this parameter in the two systems is reported in the Figure 7. Considering the rigidity of the cyclopeptide cRGD [37], it is not surprising that the spacer has no effect on its conformation and that the peptides behaviour is consequently similar in the two systems. On the other hand, by looking at the orientation assumed by the cyclopeptide with respect to the normal to the gold plane (Figure 6), a marked difference between the two systems can be observed. In fact, the more probable angle for GKKKG-cRGD is 125°, whilst for cRGD is 85°. This finding suggested that the linker affects the configurational properties of the targeting motif on the nanosystems. During the simulations, the cationic linkers showed a low tendency to make intermolecular H-bonds. Structural connections between the linker and the orientation of the

cyclopeptide have not been individuated. In the primary sequence of PEG-GKKKG-cRGD, the linker is closer to the surface with respect to the cyclopeptide, but in the density profile it is co-localized with cRGD. Probably this feature determines the different dynamical properties of the cyclopeptide observed between the two systems.

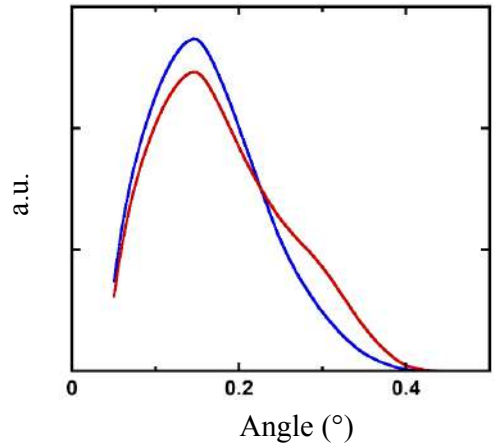

Figure 7. Distribution of the Index of Planarity for the cRGD with (blue) and without (red) cationic linker during the MD simulations. The distributions are calculated on the equilibrated ensembles (last 40 ns of three independent simulations).

In conclusion, in this chapter the importance of optimizing design elements of cRGD peptide for the functionalization of the nanostructures to achieve an effective and selective targeting of $\alpha_v\beta_3$ integrin overexpressed on colorectal cancer cells was demonstrated. Molecular Dynamics calculations allowed rationalizing that rather than the hydrophilicity, the configurational and conformational properties of the targeting motif on the nanostructures surface play a key role for assuring a satisfactory association with the receptor. Moreover, overall results clearly show that the proper presentation of the peptides above a stealth layer, such as the PEG coating, is crucial to gain effective targeting activities. The role of PEG in increasing either the sensitivity or the specificity of the receptor recognition will be deeply discussed in the following chapter.

Experimental Section

Materials and Methods

Unless differently specified, all chemicals were commercial products and were used without further purification. Bovin Serum Albumin (BSA), 9-Fluorenylmethoxycarbonyl (Fmoc)-amino acids and all other chemicals for the solid phase peptide synthesis were purchased from Sigma Aldrich. Fmoc-Asp(Wang resin)-OAll (loading 0.3 mmol/g), Fmoc-8-amino-3,6-dioxaoctanoic acid (Fmoc-O2Oc-OH) and Fmoc-5-amino-3-oxapentanoic acid (Fmoc-O1Pen-OH) were provided by Iris Biotech GMBH. S-Trityl-thioPEG N-hydroxysuccinimide ester (TrtS-PEG-NHS MW ~3000 Da) and α-Methoxy-ω-mercapto PEG (CH_3O-PEG-SH MW ~2000 Da) from Rapp Polymer. Sulforhodamine 101-bis-cysteamide (TR-SH) was prepared according to a previously published procedure [35]. Anti-integrin $\alpha_v\beta_3$ Antibody, clone LM609, Phycoerythrin (PE) conjugated was provided by Merck Millipore.

Analytical HPLC separations were carried out as described in Chapter 3. Except otherwise indicated, the elution condition was: isocratic 5% B for 3 min; linear gradient 5-65% B for 30 min. Semipreparative HPLC separation, mass spectral analysis, DLS and ζ-potential measurements were performed as described in Chapter 3 as well as UV–vis-NIR and SERRS spectra. TEM images were recorded at 100 kV with a FEI TECNAI G2 transmission electron microscope.

Synthesis of Peptides and Conjugates

General Method: Z-cRGD {cyclo[RGDyK(*N*$^{\varepsilon}$*G*-O2Oc-C)]}, G-cRGD {cyclo[RGDyK(*N*$^{\varepsilon}$G)]}, and GKKKG-cRGD {cyclo[RGDyK(*N*$^{\varepsilon}$GKKKG)]} were prepared by on resin-cyclization of the protected linear peptide, previously synthesized starting from Fmoc-Asp(Wang resin)-OAll (0.06 mmoles) on an automated Advanced Chemtech 348 Ω peptide synthesizer. Fmoc-amino acids side chains were protected by the *tert*-butyl (tBu) group (Tyrosine), the 2,2,4,6,7-pentamethyldihydrobenzofuran-5-sulfonyl (Pbf) group (Arginine), the 1-(4,4-dimethyl-2,6-dioxocyclohex-1-ylidene)isovaleryl (ivDde) group (Lysine), the *tert*-butyloxycarbonyl (Boc) protecting group (Lysine), the allyl ester (OAll) group (Aspartic acid) or the trityl (Trt) group (Cysteine). Except otherwise indicated, the procedure already reported in Chapter 3 was followed for the synthesis of peptides. Following completion of the pentapeptide sequence the allyl ester was removed according to the literature [38]. The linear peptide still anchored to the resin was cyclized in DMF in presence of benzotriazol-1-yl-oxytripyrrolidinophosphonium hexafluorophosphate (PyBOP), HOBt and DIEA (1: 1: 2 eq). The ivDde protecting group on the lysine side chain was removed by treatment with 2% hydrazine in DMF. The synthesis continued on the cyclic peptide, still attached to the solid support. Residual amino acids of each peptide sequence were then assembled on

the cyclic peptide and, after removal of the Fmoc group from the last amino acid, the protected derivative was a) conjugated to TrtS-PEG-NHS (G-cRGD and GKKKG-cRGD, see below); b) Z-cRGD was deprotected and detached from the resin. Final deprotection and detachment from the resin were achieved as described in Chapter 3. Peptides were purified by semi-preparative HPLC and characterized as shown in Table A1 and Figure A1-2. Before conjugation to PEG, the quality of G-cRGD and GKKKG-cRGD sequences was checked on a small sample detached from the resin in acid conditions as previously described (Table A1 and Figure A1).

PEG-peptide conjugates: TrtS-PEG-NHS (0.047 mmol in 1 mL of DMF) was reacted with the N^{ε} (for G-cRGD) or N^{α} (for GKKKG-cRGD)-amino group of the cyclic peptide still attached to the resin (0.007 mmoles). The mixture was stirred for 24 h at RT. After then, the solution containing the unreacted PEG was filtered off and the resin was repeatedly washed with DMF and DCM. Cleavage and deprotection were achieved by treatment with a TFA: triisopropylsilane: H_2O: 1,2-ethanedithiol mixture (94 : 1 : 2.5 : 2.5 v/v/v/v) for 90 min at RT. The resin was filtered off and the filtrate was reduced to a small volume. Addition of cold diethyl ether yielded the crude peptide, which was purified by semi-preparative HPLC and characterized by analytical HPLC and MALDI-TOF MS as reported in Table A1 and Figure A2.

Preparation of SERRS targeted nanostructures

Synthesis of gold nanoparticles and functionalization with the SERRS reporter: Naked gold nanoparticles were synthesized with Laser Ablation Synthesis in Solution (LASiS) methodology [35] and were found to have an average diameter of 20 nm, hydrodynamic diameters of order of 35 nm and ζ-potentials larger than −30 mV. Aggregation and labelling with the thiol functionalized SERRS Reporter (TR) were performed by mixing 1 mL of the colloidal solution of nanoparticles (6 nM) with 50 μL of a 34 μM alcoholic solution of TR in mild sonication in order to maximize the presence of hot spots useful for a strong SERRS enhancement. After half an hour gold nanoparticle were centrifuged at 25000 g for 10 min and the supernatant containing the SERRS reporter in excess was discarded. The functionalized nanoaggregates were redispersed in PBS buffer at nanomolar concentration. The extent of aggregation and the presence of the characteristic SERRS signals were controlled by recording UV-Vis-NIR and Raman spectra of the resulting colloidal solution.

Functionalization of Nanoaggregates with Peptide and PEG Ligands: The functionalization of nanostructures with peptide ligands was achieved by simply mixing 1 mL of the colloidal solution of gold nanoaggregates (4 nM), previously centrifuged at 25000 g for 10 min, with 40 μM solution of the peptide derivative ligand in 1 ml of PBS. The mixture was gently shaken for 3 h at RT and stored overnight at 4 °C. The excess of ligands was removed by centrifugation and the nanostructures were

re-dispersed in 1 mL of PBS containing 5 mg of bovine serum albumin (BSA) as conditioning step prior the incubation in biological media [35,39]. The average number of peptide ligands linked to nanoparticles was estimated by the Ellman test before and after the removal of nanoparticles by centrifugation (See Table 1). UV-Vis-NIR spectra recorded at each step of the preparation and the final SERRS spectra are reported in Figure A3. The fully functionalized SERRS nanostructures were also characterized by DLS and ζ-potential measurements (See Table 1). Nanosystems coated only with PEG (AuNP@PEG) were prepared according to the procedure described in Chapter 3. Characterizations are reported in Chapter 3.

Cell Lines and Receptor Expression Assay

Caco2 and SW620 cell lines were provided by CLS Cell Lines Service GmbH (Eppelheim, Germany) and were cultured as described in Chapter 3.

Flow Cytometry Analysis: Caco2 and SW620 cells were grown in T75 flasks until about 80% confluency at which point they were subcultivated. A 1:1 (v/v) solution of 0.25% trypsin and 0.02% ethylenediaminetetraacetic acid (EDTA) in PBS was used to loosen the adherent cells and the cell pellet was washed with PBS. 500000 cells were incubated with 1µg of Anti-integrin $\alpha_v\beta_3$ Antibody, clone LM609, Phycoerythrin (PE) conjugated in the dark for 15 min at room temperature and then unbound antibodies were removed by washing with PBS. The samples were analysed using the FACS BD Calibur instrument (BD biosciences San Jose, CA, USA) and unmarked cells as negative control. The results were compared for relative $\alpha_v\beta_3$ expression and analysed with FlowJo software, TreeStar Inc. (Figure A4).

Cells Incubation with Nanoparticles and SERRS Measurements

Caco2 and SW620 cells were seeded at a density of 50000 per well in 8 well chamber slides (Sigma-Aldrich, Irvine, UK) and allowed to grow overnight. Then the normal growth medium was aspirated and the medium containing different concentrations of nanoparticles (320, 160, 80, 40 pM) was added and incubated for 2 h at 37 °C. After incubation, the medium was removed and cells were repeatedly washed with PBS and fixed with 2% paraformaldehyde for 15 min at 4 °C. The fixed cells were then washed with sterile water three times to remove unbound nanoparticles before the SERRS measurements, performed as described in Chapter 3 as well as the statistical analysis of the dataset.

Molecular Dynamics Simulations

Molecular Dynamics (MD) simulations were carried out using the software package Gromacs v5.0.7[40]. Peptides force field parameters were taken from the Gromos53a6 [41] while PEG parameters

from Fuchs et al. [42]. The starting configuration was obtained considering a flat surface of Au atoms (FCC 111) [43]. 16 molecules composed by a 3 kDa PEG chain in an extended conformation modified at the terminus with a thiol group and a G-cRGD or a GKKKG-cRGD peptides were inserted in the simulation box. The starting conformation for cRGD was taken from the structure with pdb code 1L5G [36] of a FXRGD cyclopeptide [X stands for N-methylated Val (MVA)] whose side chains of the F and X residues were changed by using the Chimera tools [44] to obtain the YKRGD sequence. The S-Au bonds were mimed by constraining the Z-coordinates of the sulphur atoms at 0.265 nm far from the Au layer [45] by means of a harmonic potential with force constants equal to 1000 kJ mol^{-1} nm^{-2}. The positions of Au atoms where harmonically constrained to their starting values with force constants equal to 10000 kJ mol^{-1} nm^{-2}. Initially, the simulation box has dimension of 5 x 5 x 40 nm and roughly 28500 water molecules (SPC model [46]). During the equilibration time, the PEG chains lost the extended conformation and the thickness of the PEG phase dramatically reduced. In order to improve the computational performances, after 30 ns the Z dimensions were reduced to 20 nm and the number of water molecules to 13000. All the simulations were carried out by slightly changing a protocol previously used for peptides simulations [47-49]. In brief, electrostatic interactions were calculated with the particle mesh Ewald (PME) algorithm [50] (cut-off 1.4 nm) and chloride ions were added to ensure the electroneutrality of the system. A cut-off scheme was used for the van der Waals interactions (1.4 nm). Temperature was kept constant using the Velocity Rescale scheme [51] and pressure using the Berendsen algorithm [52]. Three independent simulations, each one 200 ns long, were carried out for each system. Convergence was evaluated by following the Z coordinate corresponding to a density of PEG equal to 200 kg m^{-3} and calculated in consecutive intervals of 5 ns during the simulation time. The last 40 ns of each replica were merged and analysed for each system. The structural figures were produced by means of the VMD software [53]. The density profile and the solvent accessible surface area (SAS) were evaluated by using the density and SAS tools in the GROMACS software package. The Index of Planarity, the angle between the plane of the cyclopeptide and the Z-axis (perpendicular to the surface) were calculated by means of homemade program. The normal vector to the average plane of the five C_α atoms in the cycle was considered to evaluate the orientation of the cyclopeptide. The Index of Planarity was defined as the square root of the summation of the square distances between the five C_α atoms in the cycle and the average plane passing through the same C_α atoms.

Appendix

(a) Z-cRGD {cyclo[RGDyK(N^{ε}G-O_2Oc-C)]}

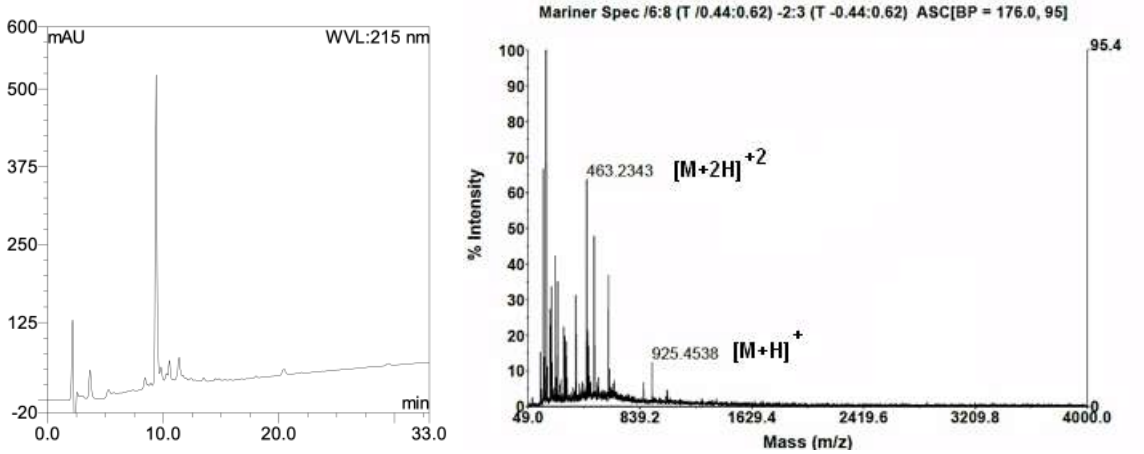

(b) G-cRGD {cyclo[RGDyK(N^{ε}G)]}

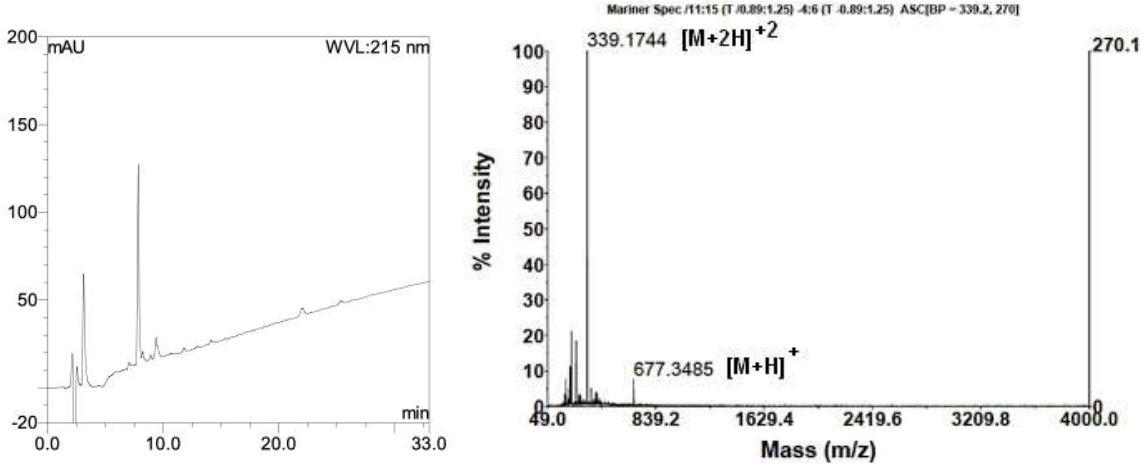

(c) GKKKG-cRGD {cyclo[RGDyK(*N*$^{\varepsilon}$GKKKG)]}

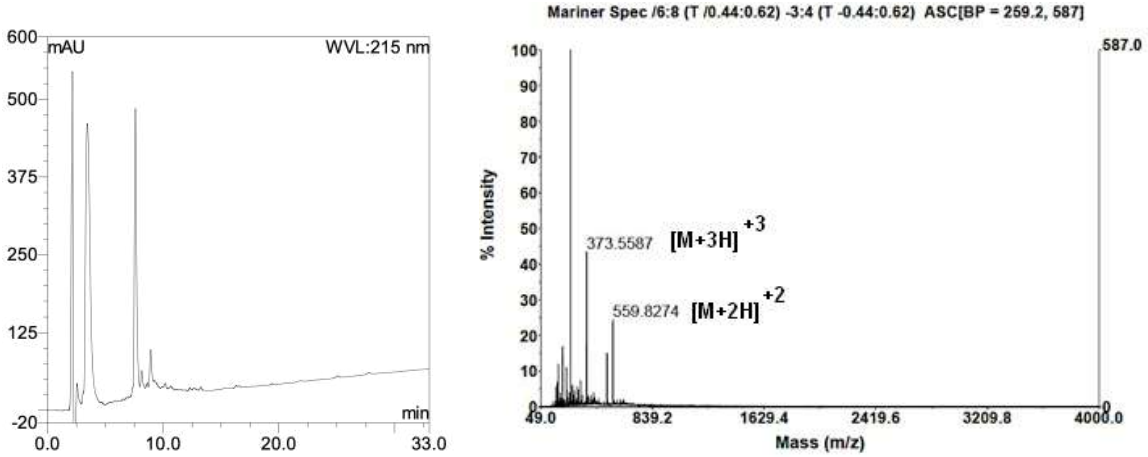

Figure A1. Analytical HPLC and ESI-MS spectra of peptides (a) Z-cRGD (b) G-cRGD (c) GKKKG-cRGD. Analytical HPLC separations were performed on a Vydac 218TP54 column (250 x 4.6 mm, 5 μm, flow rate at 1.5 ml/min). The elution condition was: isocratic 5% B for 3 min; linear gradient 5-65% B for 30 min. For preparing binary gradients the mobile phase A (aqueous 0.1% Trifluoroacetic acid (TFA)) and B (90% aqueous acetonitrile containing 0.1%TFA) were used. Mass spectral analyses were carried out on a Mariner API-TOF workstation operating in a positive mode with the ESI technique.

(a) PEG-G-cRGD {cyclo[RGDyK(N^{ε}G-PEG_{3000}-SH)]}

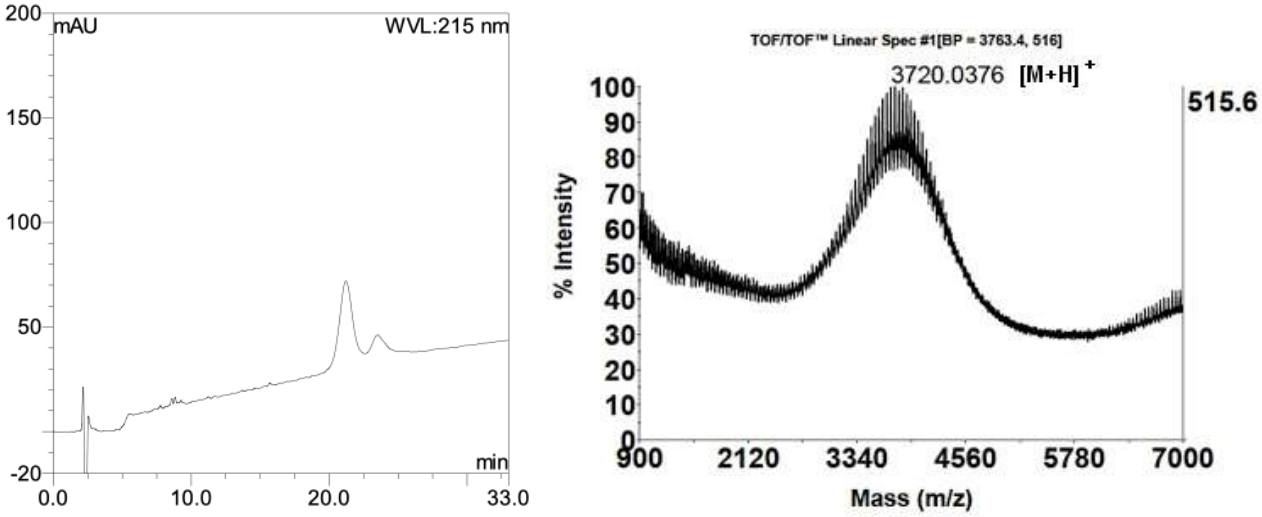

(b) PEG-GKKKG-cRGD {cyclo[RGDyK(N^{ε}GKKKG-PEG_{3000}-SH)]}

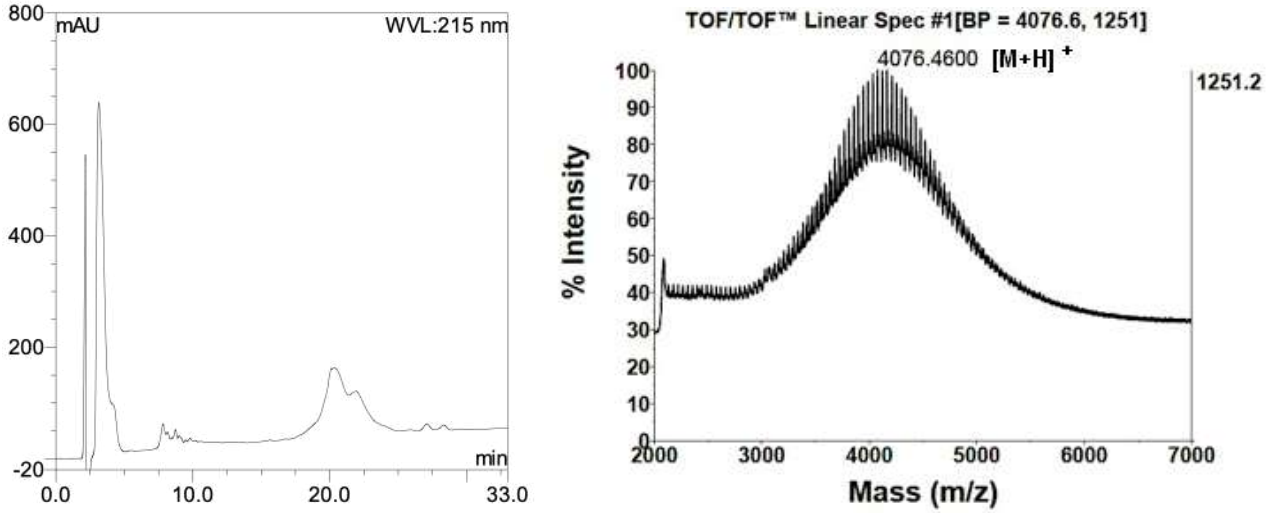

Figure A2. Analytical HPLC and MALDI TOF-TOF spectra of ligands (a) PEG-G-cRGD and (b) PEG-GKKKG-cRGD. Analytical HPLC separations were carried out in the same conditions described in Figure A1. Mass spectral analyses were performed on a MALDI TOF/TOF Analyser, operating in positive mode in the linear mid-mass range (2,5-dihydroxybenzoic acid as matrix).

Table A1. Analytical data of the synthesized peptides and PEG conjugates.

Tag	*Sequence* [a]	*Yield %*	*HPLC*[b] *t_R (min)*	*Expected Mass $[M+H]^+$*	*Found Mass*[b] *m/z*
Z-cRGD	cyclo[RGDyK(N^{ε}G-O_2Oc-C)]	87	9.39	924.51	925.45$[M+H]^{+1}$, 463.23$[M+2H]^{+2}$
G-cRGD	cyclo[RGDyK(N^{ε}G)]	77	7.81	676.33	677.35$[M+H]^{+1}$, 339.17$[M+2H]^{+2}$
GKKKG-cRGD	cyclo[RGDyK(N^{ε}GKKKG)]	75	7.59	1117.64	559.83$[M+2H]^{+2}$, 373.56$[M+3H]^{+3}$
PEG-G-cRGD	cyclo[RGDyK(N^{ε}G-PEG_{3000}-SH)]	87	21.21, 23.54	3677	3720 $[M+H]^{+1}$
PEG-GKKKG-cRGD	cyclo[RGDyK(N^{ε}GKKKG-PEG_{3000}-SH)]	78	20.35, 21.92	4118	4076 $[M+H]^{+1}$

[a] Abbreviations: Amino acids are represented by one letter symbol. y is D-tyrosine. O_2Oc is 8-amino-3,6-dioxoactanoic acid and O1Pen is 5-amino-3-oxapentanoic acid.

[b] For Analytical HPLC and MS spectra see Figures A1-2.

(a) AuNP@ Z-cRGD

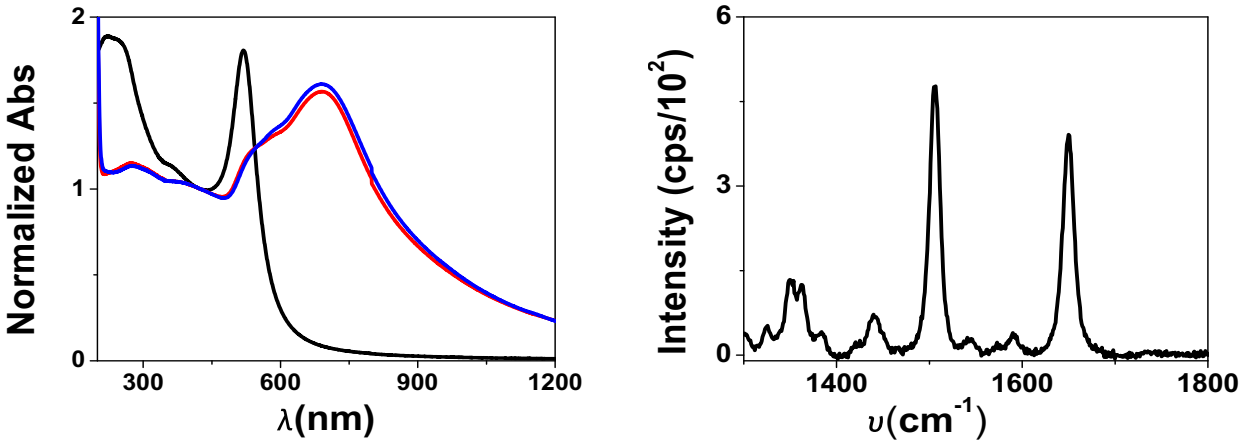

(b) AuNP@ PEG-G-cRGD

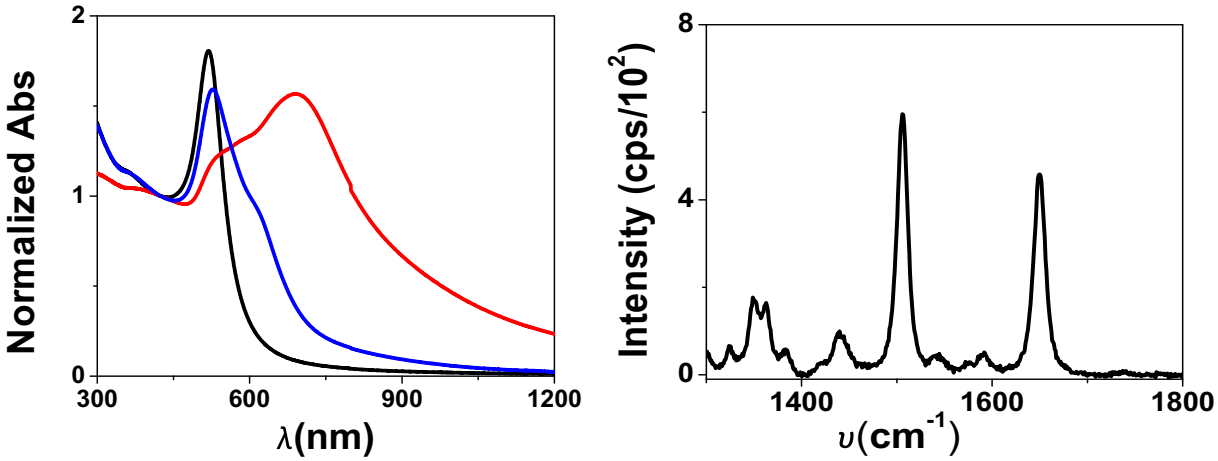

(c) AuNP@ PEG-GKKKG-cRGD

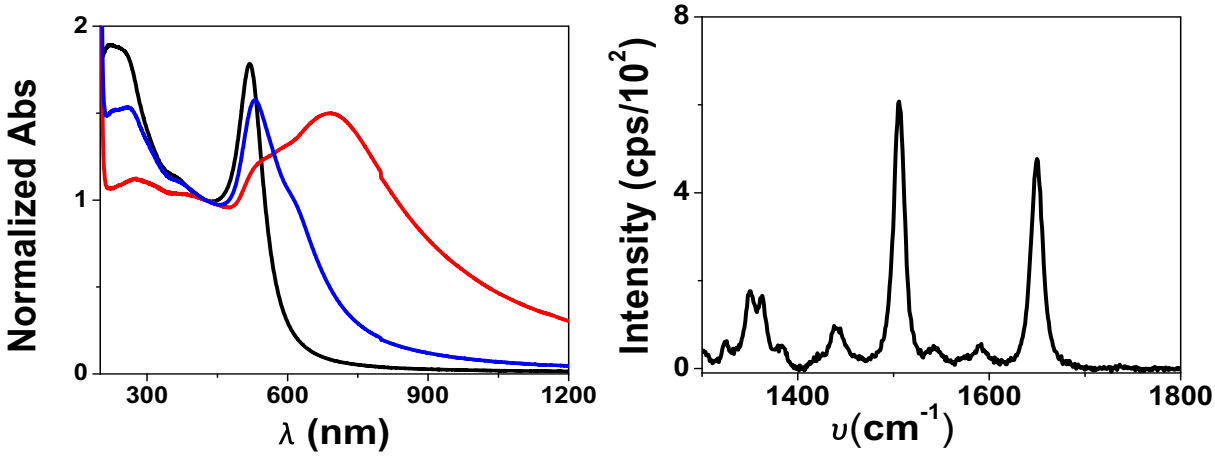

Figure A3. On the left, evolution of the extinction spectra during the assembling steps of the nanostructures: Laser Ablation in Solution of gold nanoparticles (black line), aggregation and labelling with the SERRS reporter (red line) and conjugation of peptide ligands (blue line). On the right, SERRS spectra of the final nanostructures (a) AuNP@ Z-cRGD (b) AuNP@ PEG-G-cRGD (c) AuNP@ PEG-GKKKG-cRGD.

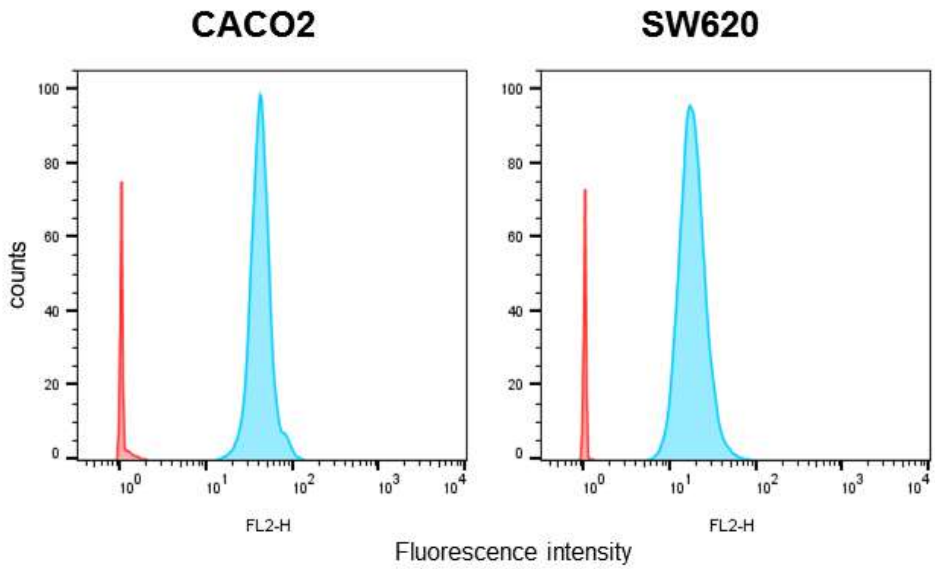

Figure A4. Integrin expression in Caco2 and SW620 cells determined by flow cytometry. Cells marked with Anti-integrin $\alpha_v\beta_3$ Antibody, clone LM 609, Phycoerythrin conjugated are represented in blue while unmarked cells in red.

References

1. Jin, H., Varner, J., Integrins: roles in cancer development and as treatment targets. *British Journal of Cancer.* **2004**. 90 (3), pp 561-565.

2. Hwang, R.,Varner, J., The role of integrins in tumor angiogenesis. *Hematology-Oncology Clinics of North America.* **2004**. 18 (5), pp 991-1006.

3. Brooks, P. C., Clark, R. A. F., Cheresh, D. A., Requirement of vascular integrin alpha(v)beta(3) for angiogenesis. *Science* **1994**. 264 (5158), pp 569-571.

4. Pilch, J., Habermann, R., Felding-Habermann, B., Unique ability of integrin alpha(v)beta(3) to support tumor cell arrest under dynamic flow conditions. *Journal of Biological Chemistry.* **2002**. 277 (24), pp 21930-21938.

5. Vonlaufen, A., Wiedle, G., Borisch, B., Birrer, S., Luder, P., Imhof, B. A., Integrin alpha(v)beta(3) expression in colon carcinoma correlates with survival. *Modern Pathology.* **2001**. 14 (11), pp 1126-1132.

6. Funahashi, H., Takeyama, H., Sawai, H., Furuta, A., Sato, M., Okada, Y., Hayakawa, T., Tanaka, M., Manabe, T., Alteration of integrin expression by glial cell line-derived neurotrophic factor (GDNF) in human pancreatic cancer cells. *Pancreas.* **2003**. 27 (2), pp 190-196.

7. Hynes, R. O., A reevaluation of integrins as regulators of angiogenesis. *Nature Medicine.* **2002**. 8 (9), pp 918-921.

8. Sanchez, A., Paredes, K. O., Ruiz-Cabello, J., Martinez-Ruiz, P., Pingarron, J. M., Villalonga, R., Filice, M., Hybrid Decorated Core@Shell Janus Nanoparticles as a Flexible Platform for Targeted Multimodal Molecular Bioimaging of Cancer. *Acs Applied Materials & Interfaces.* **2018**. 10 (37), pp 3 032-31043.

9. Kim, M., Sahu, A., Kim, G. B., Nam, G. H., Um, W., Shin, S. J., Jeong, Y. Y., Kim, I. S., Kim, K., Kwon, I. C., Tae, G., Comparison of in vivo targeting ability between cRGD and collagen-targeting peptide conjugated nano-carriers for atherosclerosis. *Journal of Controlled Release.* **2018**. 269, pp 337-346.

10. Zhu, T. T., Xiong, J., Xue, Z. B., Su, Y., Sun, F. N., Chai, R., Xu, J. L., Feng, Y. Q., Meng, S. X., A novel amphiphilic fluorescent probe BODIPY-O-CMC-cRGD as a biomarker and nanoparticle vector. *Rsc Advances.* **2018**. 8 (36), pp 20087-20094.

11. Mo, J. B., He, L. Z., Ma, B.; Chen, T. F., Tailoring Particle Size of Mesoporous Silica Nanosystem To Antagonize Glioblastoma and Overcome Blood-Brain Barrier. *Acs Applied Materials & Interfaces.* **2016**. 8 (11), pp 6811-6825.

12. Murugan, C., Rayappan, K., Thangam, R., Bhanumathi, R., Shanthi, K., Vivek, R., Thirumurugan, R., Bhattacharyya, A., Sivasubramanian, S., Gunasekaran, P., Kannan, S., Combinatorial nanocarrier based drug delivery approach for amalgamation of anti-tumor agents in bresat cancer cells: an improved nanomedicine strategies. *Scientific Reports.* **2016**. 6 (17), pp 34053-34069.

13. Kim, S. K., Lee, J. M., Oh, K. T., Lee, E. S., Extremely small-sized globular poly(ethylene glycol)-cyclic RGD conjugates targeting integrin alpha(v)beta(3) in tumor cells. *International Journal of Pharmaceutics.* **2017**. 528 (1-2), pp 1-7.

14. Shi, S. R., Zhang, L. Y., Zhu, M. Q., Wan, G. Y., Li, C. Y., Zhang, J., Wang, Y., Wang, Y. S., Reactive Oxygen Species-Responsive Nanoparticles Based on PEGlated Prodrug for Targeted Treatment of Oral Tongue Squamous Cell Carcinoma by Combining Photodynamic Therapy and Chemotherapy. *Acs Applied Materials & Interfaces.* **2018**. 10 (35), pp 29260-29272.

15. Yu, M. X., Zheng, J., Clearance Pathways and Tumor Targeting of Imaging Nanoparticles. *Acs Nano.* **2015**. 9 (7), pp 6655-6674.

16. Nie, S. M., Understanding and overcoming major barriers in cancer nanomedicine. *Nanomedicine.* **2010**. 5 (4), pp 523-528.

17. Jeon, S. I., Lee, J. H., Andrade, J. D., Degennes, P. G., Protein surface interactions in the presence of polyethylene oxide .1. simplified theory. *Journal of Colloid and Interface Science.* **1991**. 142 (1), pp 149-158.

18. Suk, J. S., Xu, Q. G., Kim, N., Hanes, J., Ensign, L. M., PEGylation as a strategy for improving nanoparticle-based drug and gene delivery. *Advanced Drug Delivery Reviews.* **2016**. 99, pp 28-51.

19.J okerst, J. V., Lobovkina, T., Zare, R. N., Gambhir, S. S., Nanoparticle PEGylation for imaging and therapy. *Nanomedicine.* **2011**. 6 (4), pp 715-728.

20. Ge, Z. S., Chen, Q. X., Osada, K., Liu, X. Y., Tockary, T. A., Uchida, S., Dirisala, A., Ishii, T., Nomoto, T., Toh, K., Matsumoto, Y., Oba, M., Kano, M. R., Itaka, K., Kataoka, K., Targeted gene delivery by polyplex micelles with crowded PEG palisade and cRGD moiety for systemic treatment of pancreatic tumors. *Biomaterials.* **2014**. 35 (10), pp 3416-3426.

21. Mickler, F. M., Vachutinsky, Y., Oba, M., Miyata, K., Nishiyama, N., Kataoka, K., Brauchle, C., Ruthardt, N., Effect of integrin targeting and PEG shielding on polyplex micelle internalization studied by live-cell imaging. *Journal of Controlled Release.* **2011**. 156 (3), pp 364-373.

22. Hada, T., Sakurai, Y., Harashima, H., Optimization of a siRNA Carrier Modified with a pH-Sensitive Cationic Lipid and a Cyclic RGD Peptide for Efficiently Targeting Tumor Endothelial Cells. *Pharmaceutics.* **2015**. 7 (3), pp 320-333.

23. Yamamoto, S., Sakurai, Y., Harashima, H., Failure of active targeting by a cholesterol-anchored ligand and improvement by altering the lipid composition to prevent ligand desorption. *International Journal of Pharmaceutics.* **2018**. 536 (1), pp 42-49.

24. Shuhendler, A. J., Prasad, P., Leung, M., Rauth, A. M., DaCosta, R. S., Wu, X. Y., A Novel Solid Lipid Nanoparticle Formulation for Active Targeting to Tumor alpha(v)beta(3) Integrin Receptors Reveals Cyclic RGD as A Double-Edged Sword. *Advanced Healthcare Materials.* **2012**. 1 (5), pp 600-608.

25. Stefanick, J. F., Kiziltepe, T., Bilgicer, B., Improved Peptide-Targeted Liposome Design Through Optimized Peptide Hydrophilicity, Ethylene Glycol Linker Length, and Peptide Density. *Journal of Biomedical Nanotechnology.* **2015**. 11 (8), pp 1418-1430.

26. Yang, X., Chen, Q. X., Yang, J. J., Wu, S. D., Liu, J., Li, Z., Liu, D. Q., Chen, X. Y., Qiu, Y. M., Tumor-Targeted Accumulation of Ligand-Installed Polymeric Micelles Influenced by Surface PEGylation Crowdedness. *Acs Applied Materials & Interfaces.* **2017**. 9 (50), pp 44045-44052.

27. Gref, R., Luck, M., Quellec, P., Marchand, M., Dellacherie, E., Harnisch, S., Blunk, T., Muller, R. H., 'Stealth' corona-core nanoparticles surface modified by polyethylene glycol (PEG): influences of the corona (PEG chain length and surface density) and of the core composition on phagocytic uptake and plasma protein adsorption. *Colloids and Surfaces B-Biointerfaces.* **2000**. 18 (3-4), pp 301-313.

28. Schottelius, M., Laufer, B., Kessler, H., Wester, H. J., Ligands for Mapping alpha(v)beta(3)-Integrin Expression in Vivo. *Accounts of Chemical Research.* **2009**. 42 (7), pp 969-980.

29. Biscaglia, F., Ripani, G., Rajendran, S., Benna, C., Mocellin, S., Bocchinfuso, G., Meneghetti, M., Palleschi, A., Gobbo, M., Gold Nanoparticle Aggregates Functionalized with Cyclic RGD Peptides for Targeting and Imaging of Colorectal Cancer Cells. *Acs Applied Nano Materials.* **2019**. 2 (10), pp 6436-6444.

30. Veronese, F. M., Peptide and protein PEGylation: a review of problems and solutions. *Biomaterials.* **2001**. 22 (5), pp 405-417.

31. Ikeda, Y., Nagasaki, Y., PEGylation Technology in Nanomedicine. In *Polymers in Nanomedicine*. Eds. Springer-Verlag Berlin. **2012**. 247, pp 115-140.

32. Nobs, L., Buchegger, F., Gurny, R., Allemann, E., Current methods for attaching targeting ligands to liposomes and nanoparticles. *Journal of Pharmaceutical Sciences.* **2004**. 93 (8), pp 1980-1992.

33. Stefanick, J. F., Ashley, J. D., Kiziltepe, T., Bilgicer, B., A Systematic Analysis of Peptide Linker Length and Liposomal Polyethylene Glycol Coating on Cellular Uptake of Peptide-Targeted Liposomes. *Acs Nano.* **2013**. 7 (4), pp 2935-2947.

34. Stefanick, J. F., Ashley, J. D., Bilgicer, B., Enhanced Cellular Uptake of Peptide-Targeted Nanoparticles through Increased Peptide Hydrophilicity and Optimized Ethylene Glycol Peptide-Linker Length. *Acs Nano.* **2013**. 7 (9), pp 8115-8127.

35. Meneghetti, M., Scarsi, A., Litti, L., Marcolongo, G., Amendola, V., Gobbo, M., Di Chio, M., Boscaini, A., Fracasso, G., Colombatti, M., Plasmonic Nanostructures for SERRS Multiplexed Identification of Tumor-Associated Antigens. *Small.* **2012**. 8 (24), pp 3733-3738.

36. Xiong, J. P., Stehle, T., Zhang, R. G., Joachimiak, A., Frech, M., Goodman, S. L., Arnaout, M. A., Crystal structure of the extracellular segment of integrin alpha V beta 3 in complex with an Arg-Gly-Asp ligand. *Science.* **2002**. 296 (5565), pp 151-155.

37. Haubner, R., Gratias, R., Diefenbach, B., Goodman, S. L., Jonczyk, A., Kessler, H., Structural and functional aspects of RGD-containing cyclic pentapeptides as highly potent and selective integrin alpha(v)beta(3) antagonists. *Journal of the American Chemical Society.* **1996**. 118 (32), pp 7461-7472.

38. Alcaro, M. C., Sabatino, G., Uziel, J., Chelli, M., Ginanneschi, M., Rovero, P., Papini, A. M., On-resin head-to-tail cyclization of cyclotetrapeptides: Optimization of crucial parameters. *Journal of Peptide Science.* **2004**. 10 (4), pp 218-228.

39. Chanana, M., Gil, P. R., Correa-Duarte, M. A., Liz-Marzan, L. M., Parak, W. J., Physicochemical Properties of Protein-Coated Gold Nanoparticles in Biological Fluids and Cells before and after Proteolytic Digestion. *Angewandte Chemie-International Edition.* **2013**. 52 (15), pp 4179-4183.

40. Abraham, M. J., Murtola, T., Schulz, R., Páil, S., Smith, J. C., Hess, B., Lindahl , E., GROMACS: High performance molecular simulations through multi-level parallelism from laptops to supercomputer. *SoftwareX*. **2015**. 1(C), pp 19-25.

41. Oostenbrink, C.,Villa, A., Mark, A. E., Van Gunsteren, W. F., A biomolecular force field based on the free enthalpy of hydration and solvation: The GROMOS force-field parameter sets 53A5 and 53A6. *Journal of Computational Chemistry.* **2004**. 25 (13), pp 1656-1676.

42. Fuchs, P. F. J., Hansen, H. S., Hunenberger, P. H., Horta, B. A. C., A GROMOS Parameter Set for Vicinal Diether Functions: Properties of Polyethyleneoxide and Polyethyleneglycol. *Journal of Chemical Theory and Computation.* **2012**. 8 (10), pp 3943-3963.

43. Pu, Q., Leng, Y. S., Zhao, X. C., Cummings, P. T., Molecular simulations of stretching gold nanowires in solvents. *Nanotechnology.* **2007**. 18 (42), pp 424007-424011.

44. Pettersen, E. F., Goddard, T. D., Huang, C. C., Couch, G. S., Greenblatt, D. M., Meng, E. C., Ferrin, T. E., UCSF chimera - A visualization system for exploratory research and analysis. *Journal of Computational Chemistry.* **2004**. 25 (13), pp 1605-1612.

45. Tupper, K. J., Brenner, D. W., Compression-induced structural transition in a self-assembled monolayer. *Langmuir.* **1994**. 10 (7), pp 2335-2338.

46. Berendsen, H. J. C., Postma, J. P. M., Van Gunsteren, W. F., Hermans, J., In Intermolecular Forces. *Pullman, Reidel, Dordrecht*. **1981**. Ed: B, pp 331-342.

47. Bocchinfuso, G., Bobone, S., Mazzuca, C., Palleschi, A., Stella, L., Fluorescence spectroscopy and molecular dynamics simulations in studies on the mechanism of membrane destabilization by antimicrobial peptides. *Cellular and Molecular Life Sciences.* **2011**. 68 (13), pp 2281-2301.

48. Bobone, S., Gerelli, Y., De Zotti, M., Bocchinfuso, G., Farrotti, A., Orioni, B., Sebastiani, F., Latter, E., Penfold, J., Senesi, R., Formaggio, F., Palleschi, A., Toniolo, C., Fragneto, G., Stella, L., Membrane thickness and the mechanism of action of the short peptaibol trichogin GA IV. *Biochimica Et Biophysica Acta-Biomembranes.* **2013**. 1828 (3), pp 1013-1024.

49. Farrotti, A., Bocchinfuso, G., Palleschi, A., Rosato, N, Salnikov, E. S., Voievoda, N., Bechinger, B., Stella, L., Molecular dynamics methods to predict peptide locations in membranes: LAH4 as a stringent test case. *Biochimica Et Biophysica Acta-Biomembranes.* **2015**. 1848 (2), pp 581-592.

50. Essmann, U., Perera, L., Berkowitz, M. L., Darden, T., Lee, H., Pedersen, L. G., A smooth particle mesh ewald method. *Journal of Chemical Physics.* **1995**. 103 (19), pp 8577-8593.

51. Bussi, G., Donadio, D., Parrinello, M., Canonical sampling through velocity rescaling. *Journal of Chemical Physics.* **2007**. 126 (1), pp 014101-014107.

52. Berendsen, H. J. C., Postma, J. P. M., Van Gunsteren, W. F., Di Nola, A., Haak, J. R., Molecular dynamics with coupling to an external bath. *Journal of Chemical Physics*. **1984**. 81, pp 3684-3690.

53. Humphrey, W., Dalke, A., Schulten, K., VMD: Visual Molecular Dynamics. *Journal of Molecular Graphics*. **1996**. 14, pp 33-38.

Chapter 5: The pivotal role of PEG on the targeting activity of SERRS nanostructures

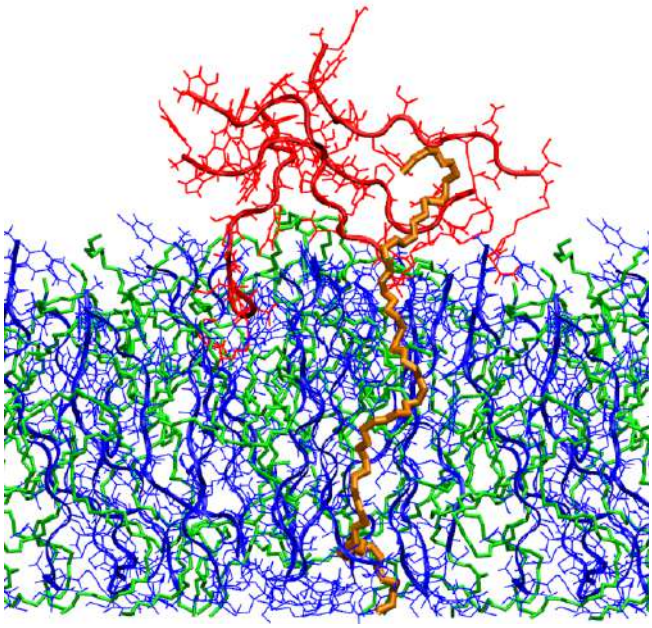

Side-view snapshot of a GE11 aggregate (red) lying on a monolayer constituted by PEG (light green) and GE11 (blue) in molar ratio 1:1. One PEG chain (orange) interacts with the aggregate.

In Chapters 3 and 4 it was demonstrated that an efficient targeting activity could be achieved by controlling the organization of the targeting units on the surface of gold nanostructures. In particular, the effect on the receptor binding of different arrangements of the targeting motif on the nanoparticles was evaluated by loading the system with properly engineered analogues of peptides GE11 and cycloRGD chosen to target, respectively, the EGFR and $\alpha_v\beta_3$ integrins overexpressed on colorectal cancer cells. The most effective activity for both peptides was achieved by covalently linking the targeting motif to long thiolated PEG chains through a cationic spacer constituted by three lysines and two glicines. The targeting capability of these nanostructures proved to be more sensitive and selective than that of nanosystems obtained by directly linking the peptides to a PEG coating or to the nanoparticles surface. The overall results clearly highlighted that the presence of both the PEG and the linker is crucial to improve the receptor recognition. If the effect of the cationic linker on the association with receptors was deeply investigated by means of Molecular Dynamics calculations (Chapters 3 and 4), the role of PEG on the nanostructures targeting capabilities is already known in literature. Among several polymers, PEG is the most common for improving the efficiency of the delivery to the tumor site for the stealth function due to its hydrophilicity and flexibility. The coating of the nanoparticles surface with PEG, a process already known as PEGylation, prevents the interactions between the nanoparticles each other and with plasma proteins or other components of biological fluids. This on one hand inhibits the nanoparticles aggregation improving the colloidal stability of the nanosystem. On the other avoids the adsorption of several biomolecules to form the so called “protein corona”, that critically affects the pathophysiology of the systems and masks the ability of targeted nanoparticles to bind specific receptors. Moreover, forming a protective layer, PEG limits the nanostructures uptake by the Reticulo Endothelial System thus prolonging blood circulation times. PEG’s size and density are key features for an efficient accumulation in tumors [1-4].

The nanoparticle surface co-functionalization with ligands of different chemistry and lengths, such as PEG and peptides, ensuring their biological functionality is the challenge of several works in literature. Two are the most employed strategy for the surface co-functionalization. The first is based on the use of hetero-bifunctional PEG linkers, such as described in Chapters 3, 4 and 7 and in numerous studies [5-7]. This approach has the benefit to completely cover the nanostructure surface with PEG. Moreover, since the targeting moieties are situated at the end of the polymer, they are supposed to be available for the association with receptors. Unfortunately, many works report that this methodology lead to instable nanostructures since the PEG linker reduces the stability of the conjugate and promotes opsonization imparting an anti-PEG effect [8]. This drawback has encouraged the spread of the latter methodology, that is the formation of mixed monolayer. In fact, stable nanosystems can be synthesized following this strategy simply by choosing a proper PEG length and

content [9]. Exploiting hydrophobic spacers, the stability in biological media can be also further enhanced [10]. However, if nanoparticles are functionalized with multiple targeting peptides, they should have similar length in order to be available for the interaction with specific receptors [11]. On the contrary, the use of PEG chains longer than that of peptides is encouraged to reduce cell toxicity and prolongs blood circulation time [6]. Unfortunately, the control over the layer composition is still quite challenging despite it is crucial to assure the reproducibility of the synthetic process.

For this work several nanosystems were loaded with different stochiometric mixture of PEGs and GE11 peptides. Experimental conditions assured a good control over the formation of the mixed monolayer. The targeting activity of the nanostructures, once evaluated against two different lines of colorectal cancer cells that overexpressed or minimally expressed the EGFR (Caco2 and SW620 respectively), was compared to those of nanostructures coated only with PEG or GE11. Results showed that the introduction of PEG together with the peptide leads to an improvement of the targeting capability with respect to nanoparticles functionalized only with GE11. Moreover, the amount of PEG was found to strongly influence the specificity and the sensitivity of the receptor binding. Results were rationalized by studying the interaction between PEG and GE11, the aggregation property of the peptide and the organization of both GE11 and PEG on the nanoparticles surface through a combination of spectroscopic measurements and MD simulations. In vitro experiments were carried out in collaboration with the group of Prof. S. Mocellin of Department of Surgery Oncology and Gastroenterology of the University of Padova while spectroscopic analysis and MD calculations thanks to the partnership with the group of Prof. A. Palleschi of the Department of Chemical Sciences and Technologies of the University of Roma Tor Vergata. The work presented in this chapter has been recently published [12].

Results and Discussion

Gold nanostructures were prepared following the protocol already described in Chapter 4 and reported in the Experimental Section along with other synthetic and analytical procedures. Characterizations of peptides and nanosystems are contained in the Appendix. Briefly, nanoparticles synthesized by laser ablation of bulk gold under water were mixed with a tiny amount of Texas Red as SERRS reporter to obtain SERRS active nanostructures. Aggregation and labelling were monitored by recording Uv-vis-NIR and Raman spectra (Figure A2). The number of peptides and PEG chains on each nanoparticle was controlled by mixing ligands and particles at specific stoichiometry and estimated, on average, by measuring the Uv-vis absorbance and by performing the Ellman test on the solution before and after the removal of nanoparticles by centrifugation.

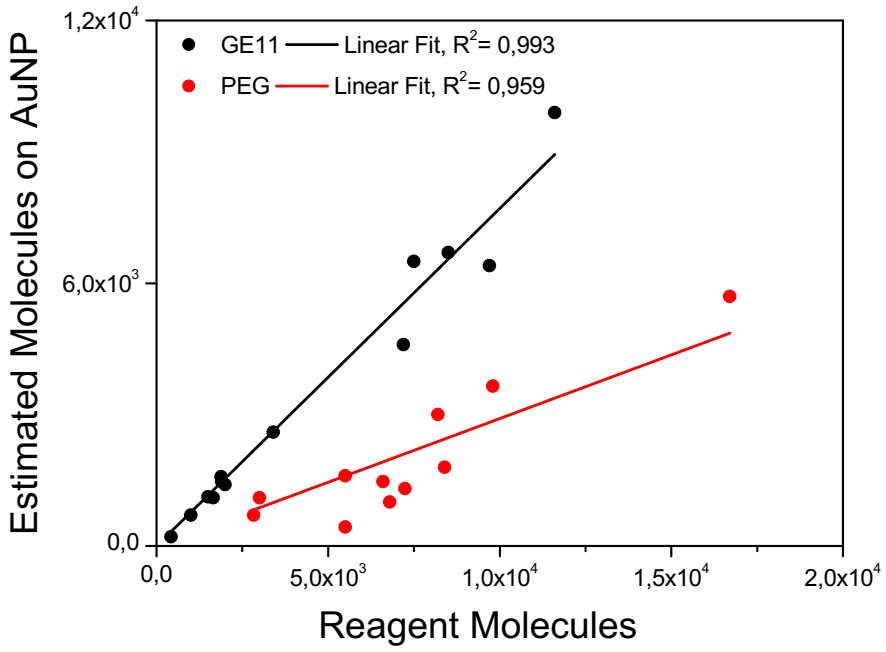

Figure 1. Curve trends describing the nanostructures functionalization with the ligands.

In Figure 1 the curve trends, describing the nanostructures functionalization with the ligands, are shown and it can be observed that are quite linear. The number of molecules binding the nanosystems surface with respect to those introduced for the functionalization, estimated in percentage, resulted as follows: 77±3 % for GE11 and 29±4 % for PEG. Results highlighted that the peptide is more prone to react than PEG molecules. This is probably due to the greater presence of functional groups, such as carboxyl groups or amines, interacting with gold. Despite the functionalization process can be

controlled by properly choosing the number of reacting molecules, an accurate prediction is, however, quite difficult.

Among several synthesized nanostructures, five of them were chosen for this study: AuNP@GE11 and AuNP@PEG, nanosystems functionalized only with GE11 and PEG, respectively; AuNP@GE11/PEG_1, 2 and 3 that are assemblies loaded with variable contents of the two molecules (Table 1). The nanostructures were characterized by Uv-vis-NIR and Raman spectra (Figure A2). ζ-potential and DLS measurements revealed that nanosystems have negative potentials, providing their colloidal stability, and hydrodynamic diameters ranging from around 50 to 120 nm (Table 1).

Nanostructures targeting properties were evaluated as a function of their concentration on two colorectal cancer cell lines overexpressing or not the EGFR (Caco2 and SW620, respectively) and following the procedure already described in Chapters 3 and 4. As expected, nanostructures coated with only PEG (AuNP@PEG) exhibited sensitivity lower than 10% at the highest concentration while nanosystems functionalized only with GE11 (AuNP@GE11) showed sensitivity higher than 90% but specificity below 60%. The best results (specificity above 90% and sensitivity above 85%) were achieved at the highest explored concentration when the peptide is in strong excess with respect to PEG (AuNP@GE11/PEG_1). The targeting activity did not change by varying the nanostructures concentration suggesting that the ligand arrangement on the surface is optimal for the association with the receptor. For lower GE11/PEG molar ratios, the targeting activity approached that of the nanostructure functionalized with PEG only. At the highest concentration AuNP@GE11/PEG_2, namely nanostructures loaded with a twice amount of GE11 with respect to the polymer, achieved sensitivity of 77% and specificity of 16%. Comparing the targeting activity of either AuNP@GE11/PEG_1 and AuNP@GE11/PEG_2 to that of AuNP@GE11, it can be noticed that it is possible to enhance the specificity by introducing an amount of PEG into the peptide layer. This finding was in accordance to expectation being the result of the stealth function of the polymer. However, if PEG was in strong excess with respect to the peptide (AuNP@GE11/PEG_3) the sensitivity dramatically decreased, and the targeting activity became comparable to that of nanosystems entirely coated with the polymer. The targeting motif on AuNP@GE11/PEG_3 was supposed to be buried in the PEG layer and therefore not available for interacting with the receptor. These results pointed out that both specificity and sensitivity can be strongly enhanced by carefully defining the GE11/PEG molar ratio.

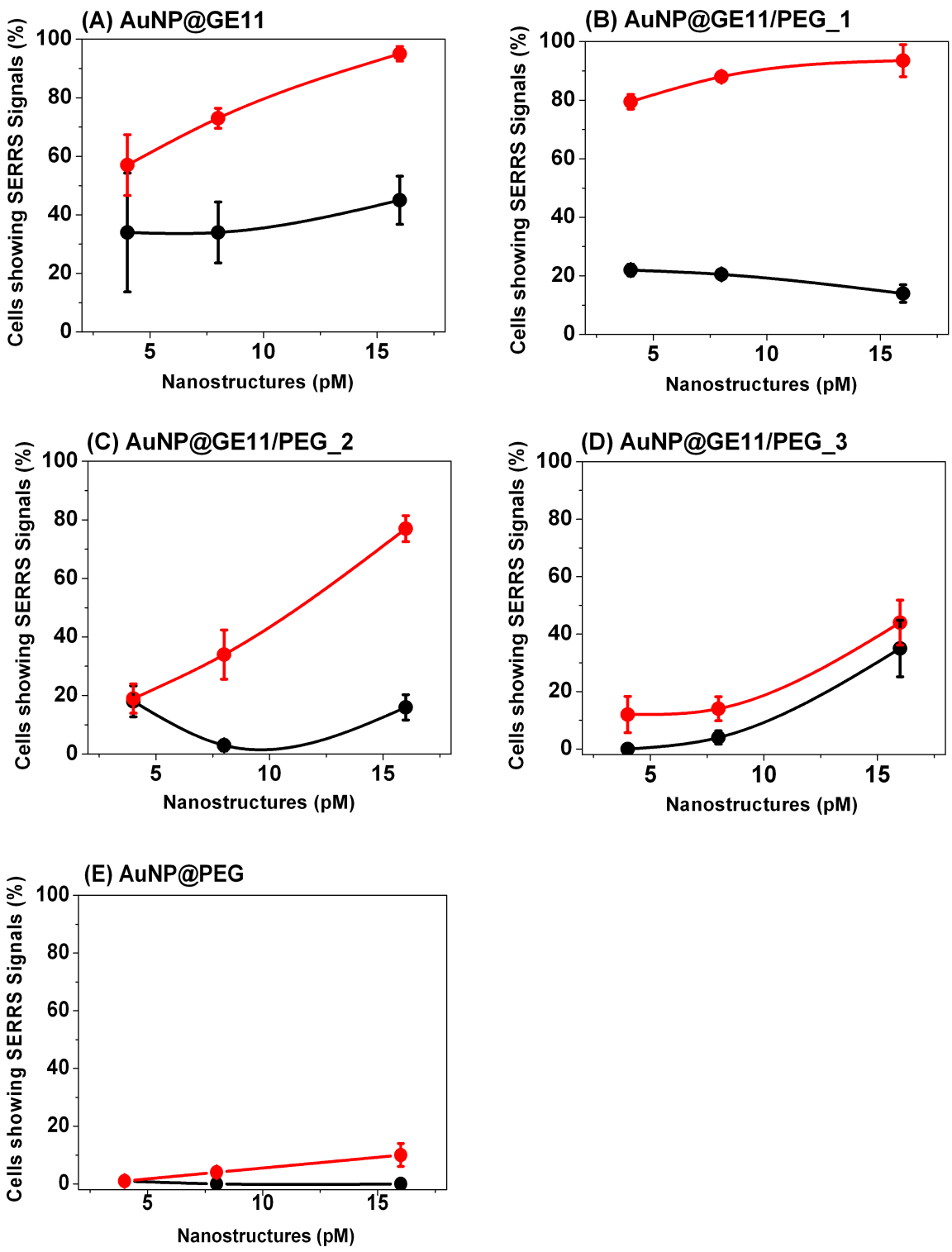

Figure 2. Targeting activity of synthesized nanostructures (A) AuNP@GE11 (B) AuNP@GE11/PEG_1 (C) AuNP@GE11/PEG_2 (D) AuNP@GE11/PEG_3 (E) AuNP@PEG for Caco2 (red lines) and SW620 (black lines) cells. 100 cells were considered for each measurement and error bars indicate variations of the results for three different selections of 100 cells within two or three preparations.

Besides the targeting activity, nanostructures physical properties changed by varying the ratio between the two ligands (see Table 1) indicating that the co-presence of both ligands plays a key role in the nanosystem coating and assembling.

Table 1. Nanostructures and their characterization.

Nanostructure	*GE11 per Nanoparticle*	*PEG per Nanoparticle*	*GE11/PEG Molar ratio*	*Hydrodynamic diameter (nm)*	*ζ-potential (mV)*
AuNP@GE11	5500	0	1:0	87±4	-24±3
AuNP@GE11/PEG_1	9180	492	19:1	123±4	-36.3±0.1
AuNP@GE11/PEG_2	1850	1016	1.7:1	99±17	-32±8
AuNP@GE11/PEG_3	810	2860	0.3:1	51±1	-27±7
AuNP@PEG	0	5700	0:1	64±1	-15±1

As can be observed in Table 1, the hydrodynamic diameter of AuNP@GE11/PEG_1, namely nanosystems mainly loaded with peptides rather than PEG, is major than that of the nanostructures entirely covered with peptides, AuNP@GE11. One can speculate that the introduction of a small amount of PEG destroys the aggregation between peptide chains. As a consequence, the conformation of the GE11 peptide becomes more extended and more available to interact with the receptor. On the contrary, the dimension of AuNP@GE11/PEG_3, mainly coated with the polymer, is minor than that of the nanostructures totally covered with PEG, AuNP@PEG. ζ-potentials measurements revealed negative values, supporting the idea that the nanosystems are stable in solution as colloidal dispersion thanks to the repulsion interactions between the nanoparticles. However, ζ-potentials trend is currently not explained. Deserving a proper explanation, these evidences will be thoroughly investigated in the next future. As can be observed in Table 1, the total number of molecules per nanoparticle also showed to be strongly dependent on the layer composition. In case of a single ligand about 5000 molecules, regardless the type, were estimated per nanoparticle. On the contrary, when PEG and GE11 are mixed, the number of total molecules on the system significantly varied. The most interesting case is that of AuNP@GE11/PEG_1: characterized by a strong excess of the peptide with respect to PEG (19:1 GE11/ PEG ratio), this assembly exhibited a number of peptides on the surface

that is almost the double of that shown by nanostructures functionalized only with GE11, AuNP@GE11. Since the presence of almost 5000 ligands per nanoparticle is in accordance to that estimated by theoretical models based on the steric hindrance of molecules covalently linked to the surface of nanoparticles of 20 nm (the average diameter of particles synthesized by LASiS), the total attached molecules for AuNP@GE11/PEG_1 exceeds the amount of ligands that can be allocated on the system. A molecular organization on the surface should, therefore, make possible the placement of the higher number of molecules. The basic hypothesis was that monolayers of ligands on the gold surface could strongly interact with peptides in solution allowing the localization of other peptidic assemblies on the yet formed layer. To confirm this hypothesis, monolayers constituted by GE11 or PEG only or by a mixture of GE11 and PEG in 1:1 molar ratio were studied by performing MD simulations and by using different spectroscopic techniques by the group of Prof. Palleschi of the University of Roma Tor Vergata.

In Figure 3, the density profile along the Z-axis of peptidic aggregates approaching different monolayers is reported.

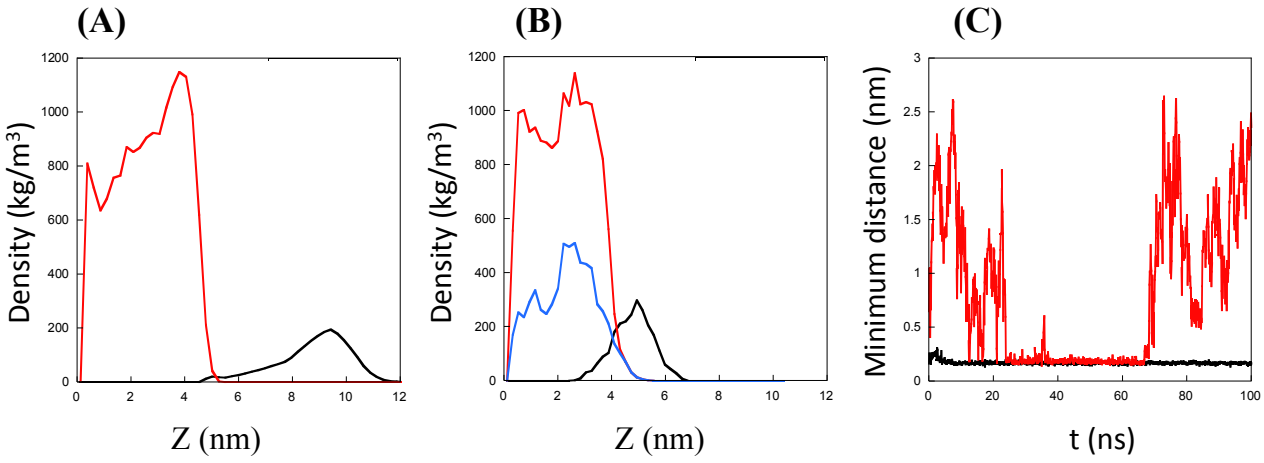

Figure 3. Partial density values along z-axis of GE11 in solution (black), GE11 in the monolayer (red) and PEG in the monolayer (blue), when only GE11 (A) and both GE11 and PEG in molar ratio 1:1 (B) are linked to surface. Minimum distance from any atoms of peptides in solution and any atoms of monolayer formed by only GE11 (red) and both GE11 and PEG in molar ratio 1:1 (black) during simulations (C).

If the monolayer is constituted only of GE11 (Fig. 3A), the density profile shows that peptides in solution approach the surface but, slightly interacting with the layer, remain quite distant from that. On the contrary, in the case of a monolayer constituted of GE11 and PEG in molar ratio 1:1 (Fig. 3B), aggregated peptides migrate from the solution to the monolayer and interact with both peptides and polymers. This is evident either from the overlap of the density profiles along Z-axis of GE11 in

solution and PEG in the 2.5-5 nm range (Fig. 3C). In this process the PEG plays a pivotal role since, being able to anchor peptides from the solution, allow layers constituted by both PEG and GE11 ligands to coordinate a higher number of molecules than those present in the monolayer, generating, in turn, an outer second layer on the nanosystem. To better understand the PEG role and to deep insight into the mechanism that rules the different targeting activity of the nanostructures, interactions between GE11 and PEG were investigated in detail.

Initially, the behaviour of GE11 and PEG in solution was studied by means of fluorescence anisotropy and steady state fluorescence experiments in order to understand whether the nanostructures coating derives from an aggregative process already present in solution or not. Results clearly indicated the formation of aggregates of dimension in the range of 0.9– 1.1 nm, compatible with the presence of 5–8 peptides, both in the presence of the polymer or not. Moreover, the analyses of peptide conformation using spectroscopic techniques (Circular Dichroism spectroscopy in solution and FTIR-ATR experiments on SAM) and MD calculations confirmed the hypothesis that the PEG does not substantially alter the the propensity of the whole peptide to assume several different conformations rather than a unique prevailing secondary structure (Data shown in ref [12]).

Details concerning the interactions between GE11 and PEG either in solution or on the nanostructures surface were obtained by MD simulations. Regarding the behaviour of GE11 in solution, calculations in the presence or not of PEG molecules indicated that the formation of large aggregates is not favoured and that the structural features of peptidic assemblies are not substantially influenced by the presence of the polymer, in agreement with experimental results. This can be explained by the fact that in absence of PEG the surface of peptidic aggregates is positively charged due to the presence of charged amino terminal groups exposed to water, as shown in the snapshot of the final frame of simulation (Fig. 4A). Electrostatic interactions established by the outer high surface charge inhibit the growth of the already formed assemblies. The presence of PEG does not substantially change this behavior, as shown in Fig. 4B. Besides, a peculiar structural feature of aggregates including a PEG chain should be noted: the polymer is located on the surface of the aggregates in all the simulations. Additional simulations were performed on monolayer constituted of PEG or GE11 only. MD simulations carried out on a monolayer constituted of PEG only showed that the polymers form a carpet on the gold surface, thus inhibiting any further specific binding (data not shown).

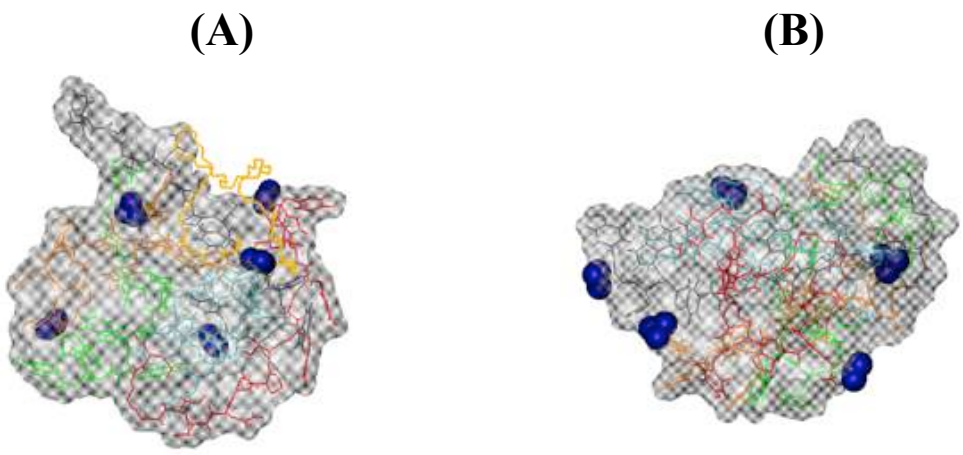

Figure 4. GE11 aggregates (n. 5) in the presence (A) and in the absence (B) of 1 molecule of PEG. The positive amino charged residues are represented in blue while PEG is colored in orange, peptides in green, gray, red, light blue and orange using bonds representation in VMD program.

As it concerns layer of only GE11, MD calculations showed that all peptides are covalently linked to the surface through their thiol group and some regions in the sequence assume a parallel β -*sheet* conformation, as shown in Figure 5. As will be discussed later, this finding explains the lower selectivity of AuNP@GE11 with respect to AuNP@GE11/PEG.

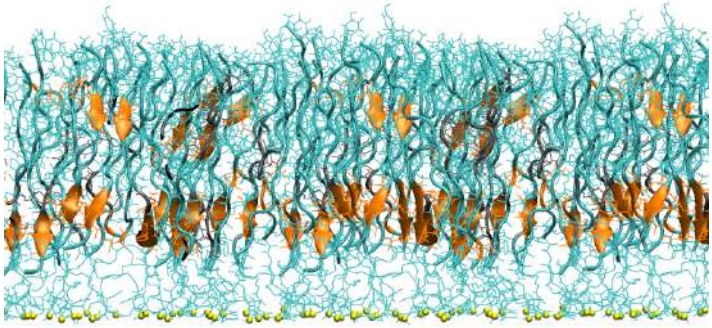

Figure 5. Compact monolayer of GE11 chemisorbed on the gold surface. S atoms are colored in yellow. All the other atoms are colored in cyan. β-sheet conformation is represented in New Cartoon and colored in orange.

Simulations of the monolayer containing PEG and GE11 in molar ratio 1:1 showed that the addition of PEG destabilizes GE11 assemblies leading to a decrease in the population of parallel β -*sheet* secondary structures. The irregular mixture that is consequently formed in the gold surface coating could explain why the excess of PEG on the nanostructures AuNP@GE11/PEG_2,3 reduces the efficiency of the targeting activity.

The linking process of GE11 and/or PEG to the gold surface was then studied by simulating a cluster formed by 9 molecules of GE11 and 1 molecule of PEG. During the simulation time the aggregates, already constituted in solution, are able to reach the surface and form several S-Au bonds, consequently changing their morphology and shape. The bonding to the surface is not influenced by the presence of PEG. Interestingly, when only one aggregate is linked to the surface, the second one, which is still in solution, is able to merge with it only if the PEG is present forming a dense monolayer. On the contrary, in absence of the polymer the aggregates remain quite apart. These results proved that PEG plays a key role in the formation of the monolayer (Figure 6). MD calculations also indicated that not all peptides are covalently linked to the surface and that many of them form an external second layer. On one hand this finding justifies the higher density of ligands on the nanostructures surface. On the other it could explain the good targeting activity of the nanostructure AuNP@GE11/PEG_1. In this system, in fact, the large number of peptides exposed above those directly linked to the surface, being more free to adapt their conformation, could be responsible of the good sensitivity of the interaction with receptors on cells. Increasing the concentration of PEG, as in the nanostructures AuNP@GE11/PEG_2 and AuNP@GE11/PEG_3, the number of GE11 molecules on the surface is limited and, therefore, the targeting activity is reduced. However, a tiny amount of PEG is necessary since, being mostly located on the surface of GE11 aggregates, is responsible for the decrease of non-specific interactions with cells. This feature explains the higher selectivity of the nanostructure AuNP@GE11/PEG_1 with respect to AuNP@GE11.

To conclude, in this chapter the huge impact of PEG on the targeting activity of GE11 functionalized nanostructures was demonstrated by combining experimental analysis with MD simulations of gold nanostructures loaded with different amounts of GE11 and PEG. Results were compared to those of nanostructures coated only with PEG or GE11. Small peptidic aggregates were found to be already formed in solution, stabilized by external positive charges that also inhibit their growth, and are maintained in response to interactions with the gold surface. The introduction of PEG chains together with the peptides has a small influence on aggregates features, either in solution or on the system surface. Moreover, by anchoring the molecules from the solution, the polymer promotes the organization of small peptidic aggregates on the gold surface forming an external assembly that is responsible for the improvement of the nanostructures targeting activity. These more exposed peptides have, in fact, a more flexible conformation that can be adapted to optimize the interactions with receptors on cells with respect to those in the internal layer.

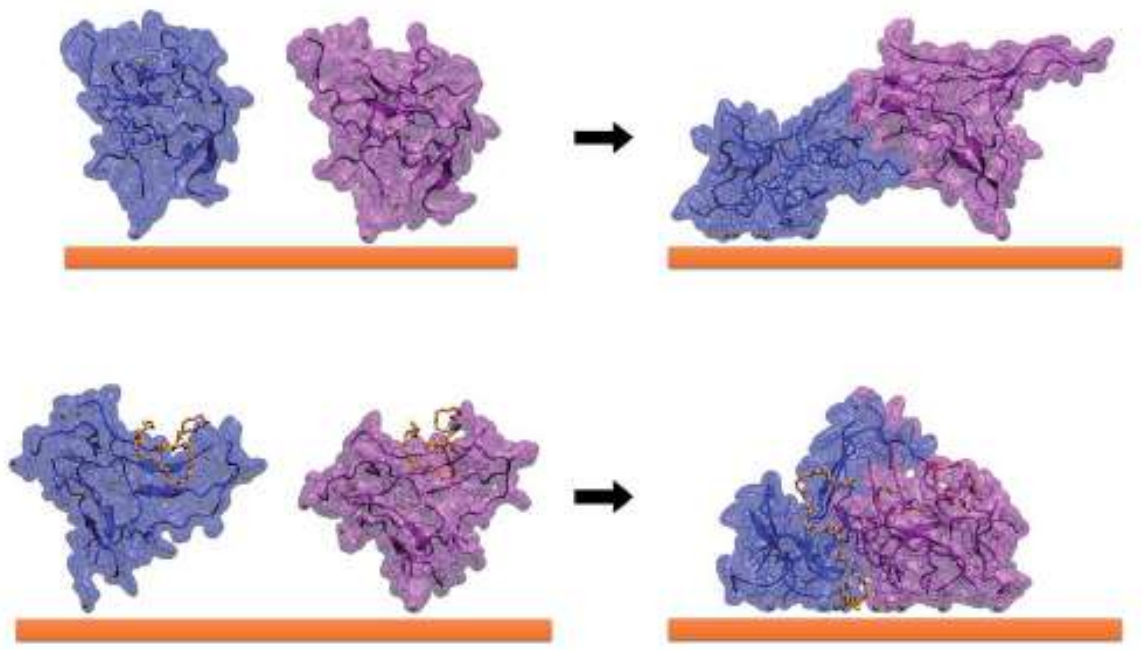

Figure 6. Features of 2 aggregates (colored in blue and purple) constituted by 9 molecules of GE11, with (bottom) or without 1 molecule of PEG per aggregate (top) on the gold surface in the starting (left) and in the final (right) frames of simulations. PEG is colored in orange, with bonds style in VDM representation. Lines, New Cartoon and Quicksurface representations were used for peptides. For sake of clarity, water molecules are not represented.

Experimental Section

Materials and Methods

Unless differently specified, all chemicals were commercial products and were used without further purification. Bovin Serum Albumin (BSA), Poly (ethylene glycol) methyl ether thiol (PEG, MW 800), 3-Carboxy-4-nitrophenyl disulphide, 9-Fluorenylmethoxycarbonyl (Fmoc)-amino acids and all other chemicals for the solid phase peptide synthesis were provided by Sigma-Aldrich. Rink Amide MBHA Resin (loading 0.64 mmol/g) was purchased from Novabiochem EMD Millipore and Fmoc-8-amino-3,6-dioxaoctanoic acid (Fmoc-O_2Oc-OH) from Iris Biotech GMBH. Sulforhodamine 101-bis-cysteamide (TR) was prepared according to a previously published procedure [13].

Analytical high-performance liquid chromatography (HPLC) separations, Semipreparative HPLC separations, mass spectral analysis, DLS and ζ-potential measurements were performed as described in Chapter 3 as well as UV–vis-NIR and SERRS spectra.

Synthesis of Peptide GE11

The peptide sequence YHWYGYTPQNVI-O_2Oc-C-NH_2 (GE11) was prepared following the procedures already reported in Chapter 3. The peptide was purified by semipreparative HPLC using the elution condition: isocratic 27% B for 5 min: linear gradient 27–25% B for 20 min. The purified product was characterized by analytical HPLC and ESI-MS (Table A1 and Figures A1).

Preparation of SERRS nanostructures

Synthesis of SERRS Nanoaggregates and of the Reference AuNP@PEG Nanostructure. According to a previously published procedure [14], gold nanoparticles were synthesized by LASiS technology. Size (average diameter of 20 nm) and concentration (4 nM) of the nanoparticles in the colloidal solution were determined by fitting their Uv-vis-NIR spectrum. [15] Aggregation and labelling with the thiol functionalized SERRS Reporter Sulforhodamine 101-bis-cysteamide (TR) was performed as described in Chapter 4. The extent of aggregation and the presence of the characteristic Raman signals were controlled by recording the UV-Vis-NIR and Raman spectra (Figure A3) of the resulting colloidal solution. Nanosystems coated only with PEG (AuNP@PEG) were prepared according to the procedure already discussed in Chapter 3. Characterizations are reported in Table 1 and Figure A2.

Functionalization of Nanoaggregates with Ligands: 1 mL of the colloidal solution of gold nanoaggregates (4 nM) was centrifuged at 25 000 g for 10 min and redispersed in 1 ml of PBS containing the peptide GE11 and PEG. By changing the concentration of the ligands in the

micromolar range, nanostructures functionalized with different molar ratios of peptides and polymers were obtained (Table 1). The mixture was shaken for 3 h at room temperature and stored at 4 °C overnight. The excess of ligand was removed by centrifugation and the nanoaggregates were re-dispersed in 1 mL of PBS. The number of ligands covering, on average, each nanoparticle was estimated by measuring the absorbance at 280 nm of the ligand solution (ε(GE11) 5350 M^{-1} cm^{-1}; ε(PEG) 86 M^{-1} cm^{-1}) and by performing Ellman test for thiol before and after removal of nanoparticles by centrifugation (Table 1). At each step, UV–Vis–NIR and Raman Spectra were recorded (Figure A2) and the fully functionalized nanostructures were also characterized by DLS and ζ-potential measurements (Table 1). BSA (5 mg) was added to the solution just before incubation with cells.

Cell Lines and Incubation with Nanoparticles: Caco2 (EGFR+) and SW620 (EGFR-) colorectal cancer cell lines were purchased from CLS Cell Lines Service GmbH (Eppelheim, Germany). Cells were cultured and incubated with nanosystems as described in Chapter 3.

SERRS Measurements: SERRS spectra were collected from each single cell (20x objective) using an automated homemade procedure. Two replicas were done for each experiment randomly choosing 100 cells among about 50000 cells present in a well. SERRS spectra were collected from four different positions on each cell. The presence of the characteristic Raman signals was evaluated with a Pearson correlation coefficient of 0.6. The error bars in Figure R1 indicate 95% confidence intervals. The statistical analysis of the dataset was carried out as described in Chapter 3.

Molecular Dynamics Calculations

MD simulations were carried out using the GROMACS v5.0.7 software package [18]. GROMOS53A6 force field parameters were used for peptides while parameters required for PEG were taken from Fuchs et al. [19]. Simulations were performed at constant pressure and temperature ensemble (NPT) with periodic boundaries conditions. First, only the solvent was energy minimized and after that the solute (peptide and polymer) was considered. Then, the solvent was equilibrated for 150 ps at 50 K (δ_t=0.5 fs). All the systems were gradually heated from 50 to 300 K in a 1.1 ns MD, and then production runs were performed, using a time step of 2 fs. The particle mesh Ewald (PME) algorithm [20,21] was used for the electrostatic interactions (cut-off = 1.4 nm). Explicit simple point-charge (SPC) water molecules [22] were used to solvate the simulation box. Chloride ions were added to assure the electroneutrality. For the van der Waals interactions (1.4 nm), a cut-off was used. In all the simulations, the velocity rescale scheme [23] was exploited to keep the temperature constant (coupling

constant τ_T=0.6 ps). The Berendsen algorithm [24] was used with isotropic conditions for pressure coupling (τ_P=1 ps), except where specified. All results were obtained when the systems were equilibrated. Secondary structure analyses were performed using the DSSP (define secondary structures of proteins) GROMACS tool [25]. The visual molecular dynamics (VMD) program [26] was used to visualize the structures.

MD Calculations in solution: The simulated systems were obtained with different number of peptides (n. 1, 2, 5, 8, 9 and 20) and in the absence or presence of one molecule of PEG. A cubic box of 5 nm lengths was solvated with water molecules. Both peptides and polymers were randomly placed in the box in an extended conformation as starting configuration. For each system three replicas of 250 ns time long were performed. The features of the aggregates were analyzed using the *gyrate* (for radius of gyration and moments of inertia calculations), *rms* (for root mean square deviations) and *mindist* tools of GROMACS.

Symmetry factor: To characterize the shape of peptidic aggregates, a symmetry factor (I_s) defined as follows was used:

$$I_s = \frac{2\,I_1 - I_2 - I_3}{I_1 + I_2 + I_3}$$

Equation 3. Symmetry factor

I_1, I_2 e I_3 are respectively the major, intermediate and minor tensor components of the second moment of the mass distribution. According to this definition, for example, I_s=0 if the aggregate has a spherical form, while I_s=2 in the case of a linear aggregate.

MD Calculations on Au surface: Simulations were performed placing all the molecules in extended conformation and perpendicular to the gold surface. The positions on the Z-coordinate of S atoms were restrained at 2.95 Å from the surface to mimic the Au-S covalent bonds during simulations. Aligned molecules were solvated with water molecules and placed in the simulation box of 5 x 5 x 12 nm^3. For all the simulations three replicas of at least 200 ns time long were performed. The Lennard-Jones parameters for the Au atom were taken from Pu et all [27]. In order to study interactions between bulk peptides and the monolayer, additional simulations were carried out by randomly placing 4 molecules of peptides in the same simulation box. Peptides were placed without any restrain at distance greater than 2 nm from the monolayer already formed (as previously reported). All the features were analyzed using the *density*, *rms* and *mindist* tools of GROMACS.

MD Calculations with wall potential: To study the diffusion process of the molecules from the solution to the surface, a double wall potential along Z-axis was used. No explicit Au atoms are needed with this approach. The atom type of the first wall (Z=0) was chosen according to Wright et al. [28] to mimic the chemical Au-S bond. The periodic boundary conditions were applied only to the

X- and Y-coordinates due to the doubly defined wall along Z-axis. A semi-isotropic Berendsen algorithm [24] was chosen for pressure coupling. Two replicas of at least 100 ns long were performed for each simulated system, obtained with different number of peptides (n. 8, 9) and in the absence or presence of one molecule of PEG. A box of 6 x 6 x 12 nm^3 length was solvated with water molecules. Also, in this case both peptides and PEG were placed randomly in the box in an extended conformation as starting configuration. The system features were analyzed using the *sasa* (for solvent accessible surface analysis) and *mindist* tools of GROMACS.

Appendix

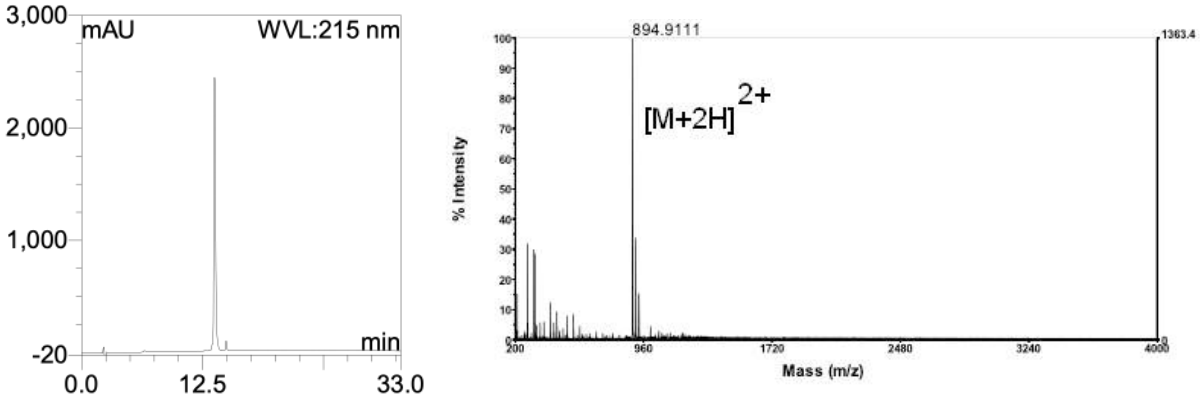

Figure A1. Analytical HPLC and ESI-MS spectra of the peptide GE11. Analytical HPLC separation was performed on a Vydac 218TP54 column (250 x 4.6 mm, 5 µm, flow rate at 1.5 ml/min). The elution condition was: isocratic 10% B for 3 min; linear gradient 10-90% B for 30 min. For preparing binary gradients the mobile phase A (aqueous 0.1% Trifluoroacetic acid (TFA)) and B (90% aqueous acetonitrile containing 0.1%TFA) were used. Mass spectral analyses were carried out on a Mariner API-TOF workstation operating in a positive mode with the ESI technique.

Table A1. Analytical data of the synthesized ligand.

Peptide	*Sequence*	*Yield %*	*HPLC[b] t_R (min)*	*Expected Mass $[M+H]^+$*	*Found Mass m/z[b]*
GE11	YHWYGYTPQNVI-O_2Oc-C-NH_2	92	13.65	1787.9	894.9 $[M+2H]^{+2}$

[a] Abbreviations: O_2Oc, 8-amino-3,6-dioxoactanoic acid. In the sequence, the one-letter symbols for amino acids have been used. [b] For Analytical HPLC and ESI-MS spectra see Figure A1.

(a) AuNP@GE11

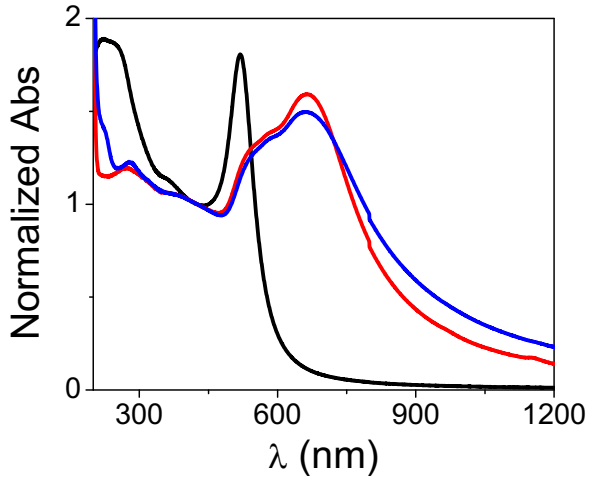

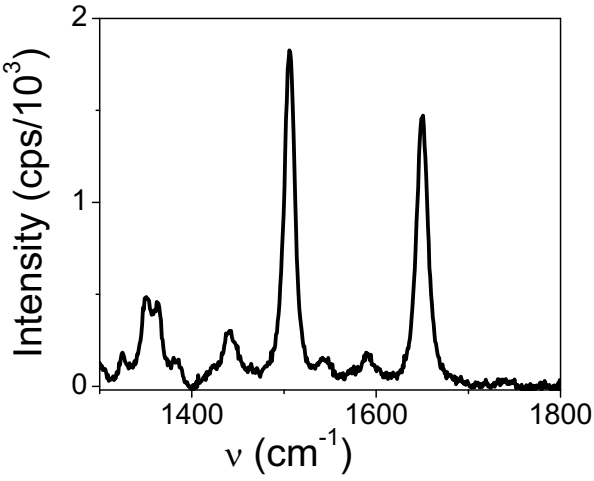

(b) AuNP@GE11/PEG_1

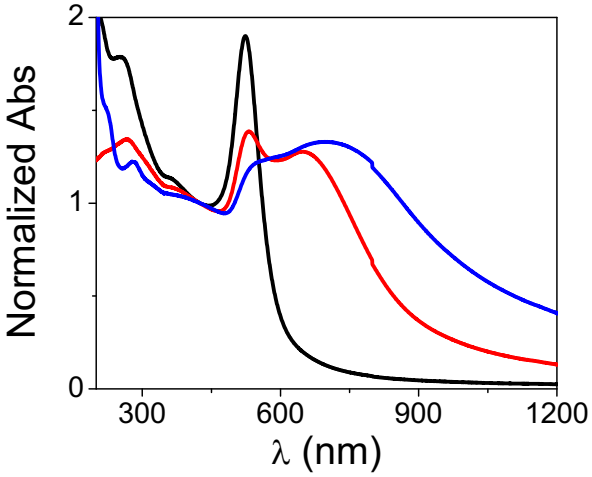

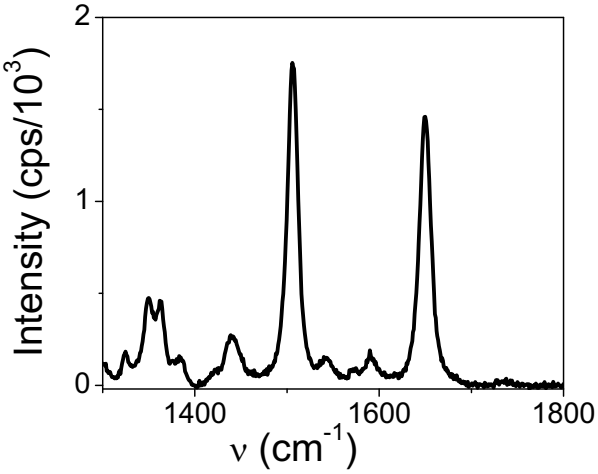

(c) AuNP@GE11/PEG_2

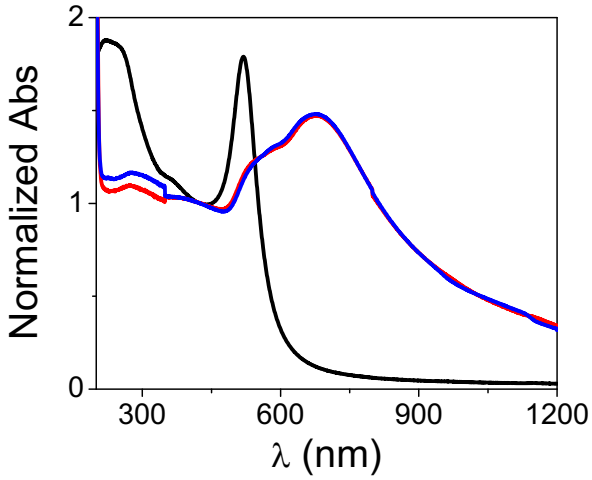

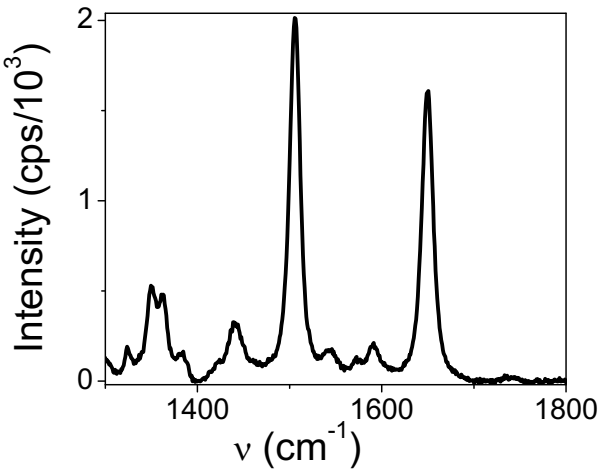

(d) AuNP@GE11/PEG_3

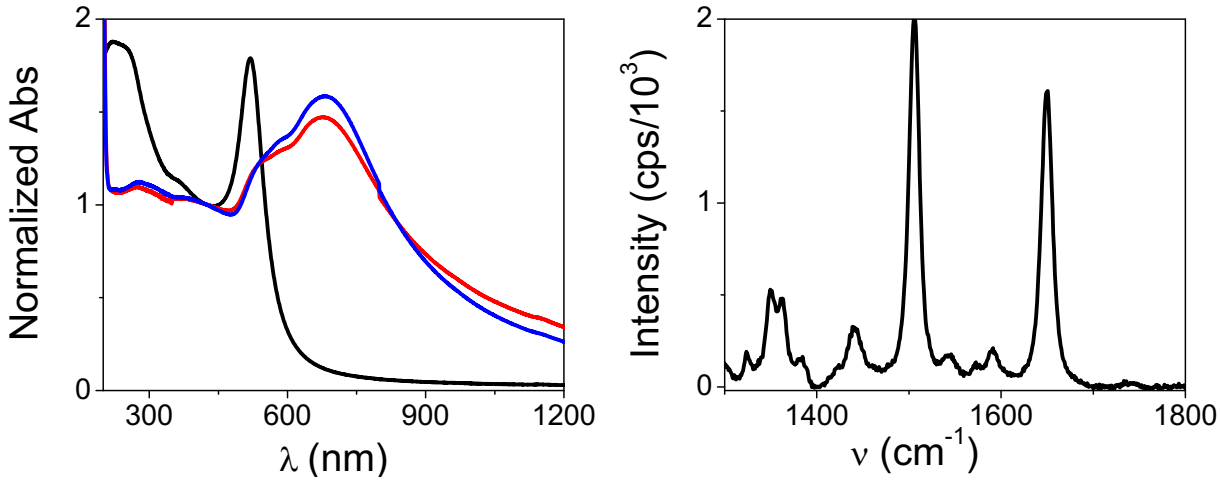

(e) AuNP@PEG

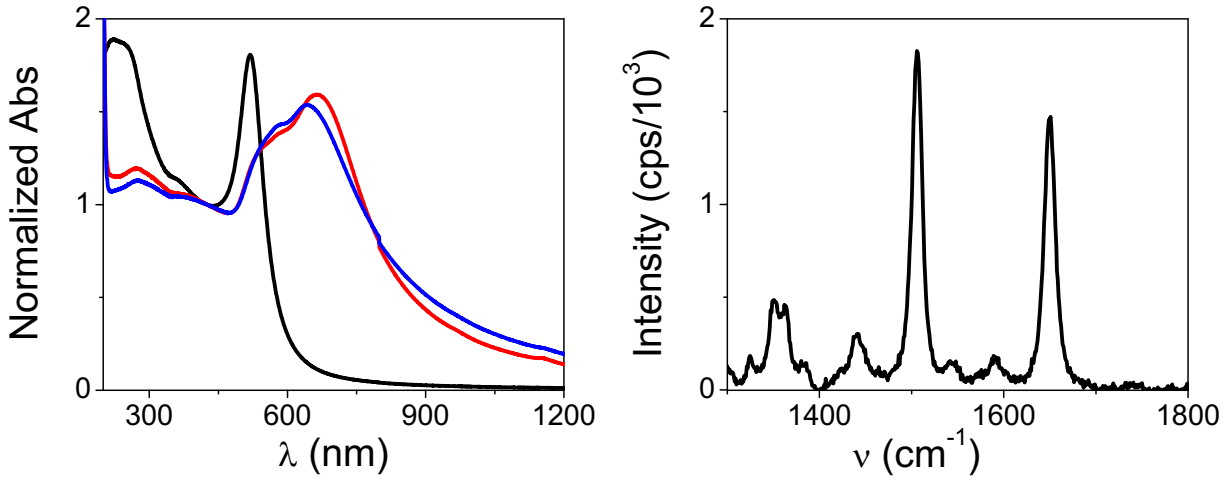

Figure A2. On the left, evolution of the extinction spectra during the assembling steps of the nanostructures: Laser Ablation in Solution of gold nanoparticles (black line), aggregation and labelling with the SERRS reporter (red line) and conjugation of ligands (blue line). On the right, SERRS spectra of the final nanostructures (a) AuNP@GE11 (b) AuNP@GE11/PEG_1 (c) AuNP@GE11/PEG_2 (d) AuNP@GE11/PEG_3 (e) AuNP@PEG

References

1 .Suk, J. S., Xu, Q. G., Kim, N., Hanes, J., Ensign, L. M., PEGylation as a strategy for improving nanoparticle-based drug and gene delivery. *Advanced Drug Delivery Reviews.* **2016**. 99, pp 28-51.

2. Wang, M., Thanou, M., Targeting nanoparticles to cancer. *Pharmacological Research.* **2010**. 62 (2), pp 90-99.

3. Dai, Q., Walkey, C., Chan, W. C. W., Polyethylene Glycol Backfilling Mitigates the Negative Impact of the Protein Corona on Nanoparticle Cell Targeting. *Angewandte Chemie-International Edition.* **2014**. 53 (20), pp 5093-5096.

4. Tenzer, S., Docter, D., Kuharev, J., Musyanovych, A., Fetz, V., Hecht, R., Schlenk, F., Fischer, D., Kiouptsi, K., Reinhardt, C., Landfester, K., Schild, H., Maskos, M., Knauer, S. K., Stauber, R. H., Rapid formation of plasma protein corona critically affects nanoparticle pathophysiology. *Nature Nanotechnology.* **2013**. 8 (10), pp 772-U1000.

5. Maus, L., Dick, O., Bading, H., Spatz, J. P., Fiammengo, R., Conjugation of Peptides to the Passivation Shell of Gold Nanoparticles for Targeting of Cell-Surface Receptors. *Acs Nano.* **2010**. 4 (11), pp 6617-6628.

6. Harrison, E., Nicol, J. R., Macias-Montero, M., Burke, G. A., Coulter, J. A., Meenan, B. J., Dixon, D., A comparison of gold nanoparticle surface co-functionalization approaches using Polyethylene Glycol (PEG) and the effect on stability, non-specific protein adsorption and internalization. *Materials Science & Engineering C-Materials for Biological Applications.* **2016**. 62, pp 710-718.

7. Harrison, E., Coulter, J. A., Dixon, D., Gold nanoparticle surface functionalization: mixed monolayer versus hetero bifunctional peg linker. *Nanomedicine.* **2016**. 11 (7), pp 851-865.

8. Kumar, D., Meenan, B. J., Dixon, D., Glutathione-mediated release of Bodipy (R) from PEG cofunctionalized gold nanoparticles. *International Journal of Nanomedicine.* **2012**. 7, pp 4007-4022.

9. Liu, Y. L., Shipton, M. K., Ryan, J., Kaufman, E. D., Franzen, S., Feldheim, D. L., Synthesis, stability, and cellular internalization of gold nanoparticles containing mixed peptide-poly(ethylene glycol) monolayers. *Analytical Chemistry.* **2007**. 79 (6), pp 2221-2229.

10. Schulz, F., Dahl, G. T., Besztejan, S., Schroer, M. A., Lehmkuhler, F., Grubel, G., Vossmeyer, T., Lange, H., Ligand Layer Engineering To Control Stability and Interfacial Properties of Nanoparticles. *Langmuir.* **2016**. 32 (31), pp 7897-7907.

11. Mandal, D., Maran, A., Yaszemski, M. J., Bolander, M. E., Sarkar, G., Cellular uptake of gold nanoparticles directly cross-linked with carrier peptides by osteosarcoma cells. *Journal of Materials Science-Materials in Medicine.* **2009**. 20 (1), pp 347-350.

12. Mazzuca, C., Di Napoli, B., Biscaglia, F., Ripani, G., Rajendran, S., Braga, A., Benna, C., Mocellin, S., Gobbo, M., Meneghetti, M., Palleschi, A., Understanding the good and poor cell targeting activity of gold nanostructures functionalized with molecular units for the epidermal growth factor receptor. *Nanoscale Advances.* **2019**. 1 (5), pp 1970-1979.

13. Meneghetti, M., Scarsi, A., Litti, L., Marcolongo, G., Amendola, V., Gobbo, M., Di Chio, M., Boscaini, A., Fracasso, G., Colombatti, M., Plasmonic Nanostructures for SERRS Multiplexed Identification of Tumor-Associated Antigens. *Small.* **2012**. 8 (24), pp 3733-3738.

14. Amendola, V., Meneghetti, M., Controlled size manipulation of free gold nanoparticles by laser irradiation and their facile bioconjugation. *Journal of Materials Chemistry.* **2007**. 17 (44), pp 4705-4710.

15. Amendola, V., Meneghetti, M., Size Evaluation of Gold Nanoparticles by UV-vis Spectroscopy. *Journal of Physical Chemistry C.* **2009**. 113 (11), pp 4277-4285.

16. Caruso, M., Placidi, E., Gatto, E., Mazzuca, C., Stella, L., Bocchinfuso, G., Palleschi, A., Formaggio, F., Toniolo, C., Venanzi, M., Fibrils or Globules? Tuning the Morphology of Peptide Aggregates from Helical Building Blocks. *Journal of Physical Chemistry B.* **2013**. 117 (18), pp 5448-5459.

17. Bocchinfuso, G., Conflitti, P., Raniolo, S., Caruso, M., Mazzuca, C., Gatto, E., Placidi, E., Formaggio, F., Toniolo, C., Venanzi, M., Palleschi, A., Aggregation propensity of Aib homo-peptides of different length: an insight from molecular dynamics simulations. *Journal of Peptide Science.* **2014**. 20 (7), pp 494-507.

18. Abraham, M. J., Murtola, T., Schulz, R., Páil, S., Smith, J. C., Hess, B., Lindahl , E., GROMACS: High performance molecular simulations through multi-level parallelism from laptops to supercomputer. *SoftwareX*. **2015**. 1(C), pp 19-25.

19. Fuchs, P. F. J., Hansen, H. S., Hunenberger, P. H., Horta, B. A. C., A GROMOS Parameter Set for Vicinal Diether Functions: Properties of Polyethyleneoxide and Polyethyleneglycol. *Journal of Chemical Theory and Computation.* **2012**. 8 (10), pp 3943-3963.

20. York, D. M., Darden, T. A., Pedersen, L. G., The effect of long-range electrostatic interactions in simulations of macromolecular crystals - a comparison of the ewald and truncated list methods. *Journal of Chemical Physics.* **1993**. 99 (10), pp 8345-8348.

21. Essmann, U., Perera, L., Berkowitz, M. L., Darden, T., Lee, H., Pedersen, L. G., A smooth particle mesh ewald method. *Journal of Chemical Physics.* **1995**. 103 (19), pp 8577-8593.

22. Berendsen, H. J. C., Postma, J. P. M., Van Gunsteren, W. F., Hermans, J., In Intermolecular Forces. *Pullman, Reidel, Dordrecht.* **1981**. Ed.B, pp 331-342.

23. Bussi, G., Donadio, D., Parrinello, M., Canonical sampling through velocity rescaling. *Journal of Chemical Physics.* **2007**. 126 (1), pp 014101-014107.

24. Berendsen, H. J. C., Postma, J. P. M., Van Gunsteren, W. F., Di Nola, A., Haak, J. R., Molecular dynamics with coupling to an external bath. *Journal of Chemical Physics*. **1984**. 81, pp 3684-3690.

25.Kabsch, W., Sander, C., Dictionary of protein secondary structure: Pattern recognition of hydrogen-bonded and geometrical features. *Biopolymers*. **1983**. 22, pp 2577-2637.

26. Humphrey, W., Dalke, A., Schulten, K., VMD: Visual Molecular Dynamics. *Journal of Molecular Graphics*. **1996**. 14, pp 33-38.

27. Pu, Q., Leng, Y. S., Zhao, X. C., Cummings, P. T., Molecular simulations of stretching gold nanowires in solvents. *Nanotechnology.* **2007**. 18 (42), pp 424007-424011.

28. Wright, L. B., Rodger, P. M., Corni, S., Walsh, T. R., GoIP-CHARMM: First-Principles Based Force Fields for the Interaction of Proteins with Au(111) and Au(100). *Journal of Chemical Theory and Computation.* **2013**. 9 (3), pp 1616-1630.

Chapter 6: Stability to proteolysis of engineered GE11 peptide analogues on SERRS nanostructures

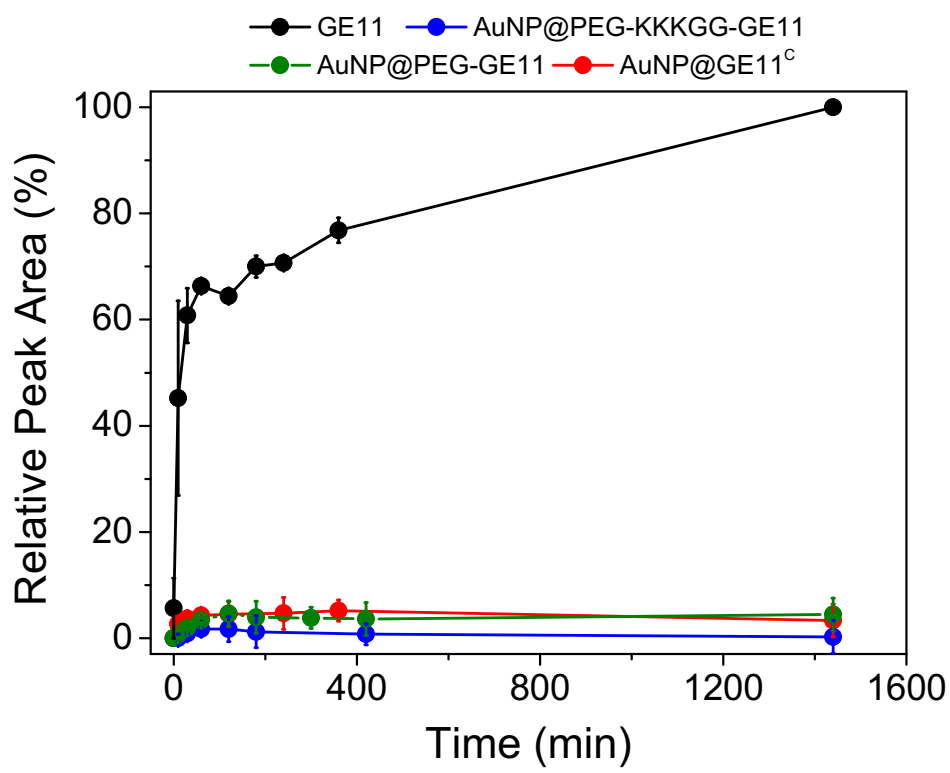

Degradation of GE11 peptide and its nanostructures with Chymotrypsin expressed as normalized peak area of the diagnostic fragment GYTPQNVI-NH_2 relative to the area of the same fragment at 24 h.

As already discussed in previous Chapters, the specific delivery of nanoparticles to tumor tissues is necessary to achieve high imaging and therapeutic efficacy and to limit adverse side-effects resulting from an unintended accumulation in healthy tissues. To address these purposes the so-called "active targeting", which is based on the mechanism of ligand-receptor recognition, is a widely accepted strategy and many different ligands have been employed to decorate the nanoparticles surface [1-4]. Among them peptides have emerged due to their efficacy and selectivity, large range of cellular target, deep tissue penetration, scarce immunogenicity and fast synthesis at reasonable costs [5,6]. However, in spite of the good results one can obtain, the widespread use of peptides is hampered by intrinsic weakness as the rapid elimination from the blood circulation due to renal filtration, uptake by the reticuloendothelial system, enzymatic digestion and accumulation in non-targeted tissues [7,8]. As obvious, beneficial effects derived by the use of peptides as targeting ligands can be lost if they are rapidly degraded in biological environments. To overcome these problems many approaches have been developed including D-amino acid replacement [9], modification of the N- or C- terminus as N-acetylation and C-amidation [10,11], molecular self-assembly [12-15] and cyclization [16]. Interesting results have been reported for peptidomimetics of the targeting peptides, as retro-inverso analogues, that bind the receptor with an affinity comparable to that of the original peptide but are not recognized by the proteases [17,18]. One of the main diffuse strategy is the polymer conjugation. Despite hydrophobic polymers formed by fatty acids of various chain lengths have been successfully used [3], hydrophilic polymers are more exploited indeed since they are capable of prolonging the blood circulation time by a combination of two mechanisms. The first is the improvement of the stability to proteases due to a steric hindrance that minimizes the physical absorption of proteolytic enzymes. The second is the decreasing of renal excretion by the increase of the peptide size and molecular mass [8]. Examples of hydrophilic polymers are polysialic acids, polymers of the N-acetylneuraminic acid, that are available in nature, biodegradable and have not receptors in the human body [19]. The most employed is, however, certainly the PEG because of its numerous useful properties for biomedical applications, as lack of toxicity and immunogenicity, high water solubility and high mobility in solution [20,21]. Recently, the stability to proteases of peptides anchored to nanoparticles has received considerable attention within the scientific community but not many works have been published about this topic at the state of art of current literature. For instance, Boge et all reported that the association of antimicrobial peptides to dispersed cubic liquid crystalline gel (cubosomes) successfully protects them against the enzymatic attack compared to unformulated peptides while preserving, or sometimes even slightly enhancing, the bactericidal effect [22]. Another study showed a lower susceptibility to enzymatic digestion of peptides once loaded on lipid-disk nanoparticles [23]. A popular statement is that the presence of a high density of ligands on the nanostructures surface sterically hinders the

action of the enzymes [24-26]. However, over functionalization can promote premature clearance by the reticuloendothelial system and, if peptides are used to deliver the nanoparticles to a specific area, a high density does not necessarily correspond to an efficient targeting [27-30].

In Chapter 3 gold nanostructures AuNP@GE11^{C} and AuNP@PEG-KKKGG-GE11, presenting the targeting peptide GE11 in different arrangements on the surface, were introduced. The nanostructures proved an efficient in vitro targeting activity against colorectal cancer cells expressing the EGFR receptor. With the view to use these nanosystems as biosensors for in vivo diagnostic of EGFR-expressing tumours, the stability in biological fluids is requested to assure a long enough half-life and consequently the delivery to the target. For this reason, the nanostructures stability against two of the most abundant enzymes in human serum, Chymotrypsin and Trypsin, pancreatic endoproteases catalyzing the hydrolysis of peptide bonds of protein foods in the mammalian gut [31], was studied by 24 h of incubation. Usually, the enzymatic stability of peptides is evaluated monitoring the decrease of the HPLC peak area of the intact peptides [20,32,33]. As evident, this approach can not be applied if peptides are bound to nanoparticles. After 24 h of hydrolysis the nanostructures stability against proteases was therefore verified using an alternative method based on the detection by HPLC-MS of peptide fragments detached from the nanostructures and pour in solution as a consequence of the enzymes action. Finally, the preservation of the targeting ability after 24 h incubation in the presence of Chymotrypsin or human serum was confirmed in vitro on cancer cells expressing the EGFR receptor thanks to the collaboration with the group of Prof. F. Rizzolio of the Department of Molecular Sciences and Nanosystems of the University Ca' Foscari in Venezia and Dr. I. Caligiuri of the Pathology unit of Centro di Riferimento Oncologico (CRO) in Aviano.

Results and Discussion

The most popular method used to evaluate the stability of peptides in biological media is based on the decrease of the HPLC peak area of the intact peptides [20,32,33]. As previoulsy introduced, this approach can not be applied if peptides are bound to nanoparticles. For this reason, in this work the enzymatic degradation of peptides decordating the nanosystems was studied by monitoring in HPLC-MS the proteolytic fragments detached from the gold surface as a result of the enzymes attack. Initially, the hydrolysis of the targeting peptide (GE11) was investigated by incubation in 20% human serum. As can be observed in Figure 1, the peptide begins deteriorating immediately after the addition to the serum and quickly and completely degrades. Unfortunately, useful proteolytic fragments to monitor the peptide digestion did not emerged.

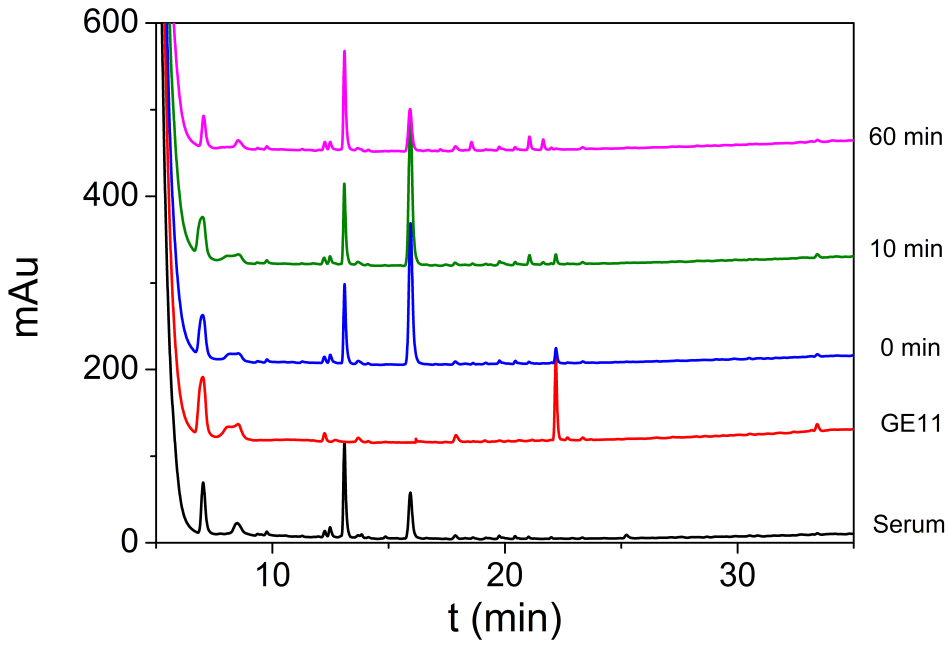

Figure 1. HPLC chromatograms of products of GE11 digestion in 20% human serum. From the bottom: 20% aqueous serum (black line); parent peptide without serum as reference (red line); other lines: aliquots collected at the indicated time. For elution conditions see the Experimental Section.

Taking these results into account and bearing in mind that human serum is rich of various enzymes, the peptide GE11 and its elongated analogue (KKKGG-GE11) were subjected to enzymatic digestion using two serine-proteases, Chymotrypsin and Trypsin respectively. In contrast to many similarities as similar arrangement of the catalytic residue and mechanism, the only major difference between Chymotrypsin and Trypsin is the characteristic specificity. Chymotrypsin, in fact, cleaves the peptide backbone mainly at the carboxylic side of aromatic amino acids (Phe, Tyr and Trp) but, showing a

rather broader specificity, slowly reacts on aliphatic amino acids with hydrophobic side chains as methionine, leucine, valine and alanine [34]. Trypsin, on the other hand, selectively cuts at the carboxylic side of basic amino acids (Lys and Arg) [35]. The slightly different structure between the enzymes is responsible of the selection of the specific amino acids prior to getting them into the active site, where the mechanism of action is exactly the same for both the proteases. The main structural difference occurs at position 189 since for Chymotrypsin the amino acid residue is a Serine whereas for Trypsin an Aspartic Acid [31]. The potential cleavage sites on GE11 and its elongated analogue are indicated in Figure 2.

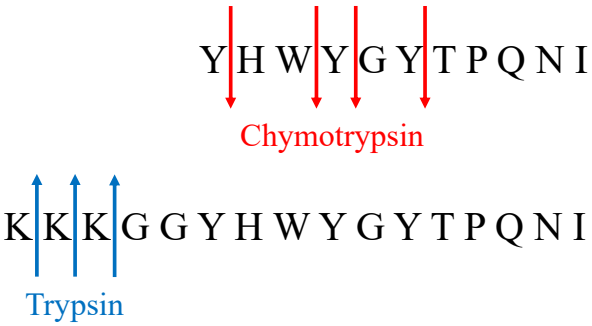

Figure 2. Potential cleavage sites on GE11 (up) and its elongated analogue (down) of Chymotrypsin and Trypsin proteases.

The enzymatic digestion was carried out incubating the peptides GE11 and KKKGG-GE11 for 24 hours at 37 °C respectively with Chymotrypsin or Trypsin. To identify by HPLC-MS the respective proteolytic fragments (Table 1 and 2), aliquots were withdrawn from the incubation solutions at different times and acidified to block the digestion. Despite both peptides were rapidly digested by the enzymes, approximately within 10 min (Figure 3), two diagnostic fragments were identified enabling the evaluation of the nanostructures stability to proteases: the (5-12) fragment (GYTPQNVI-NH_2, Figure 3A and Table 2) in the digestion of GE11 with Chymotrypsin and the (4-17) fragment (GG-GE11, Figure 3B and Table 1) in the digestion of KKKGG-GE11 with Trypsin.

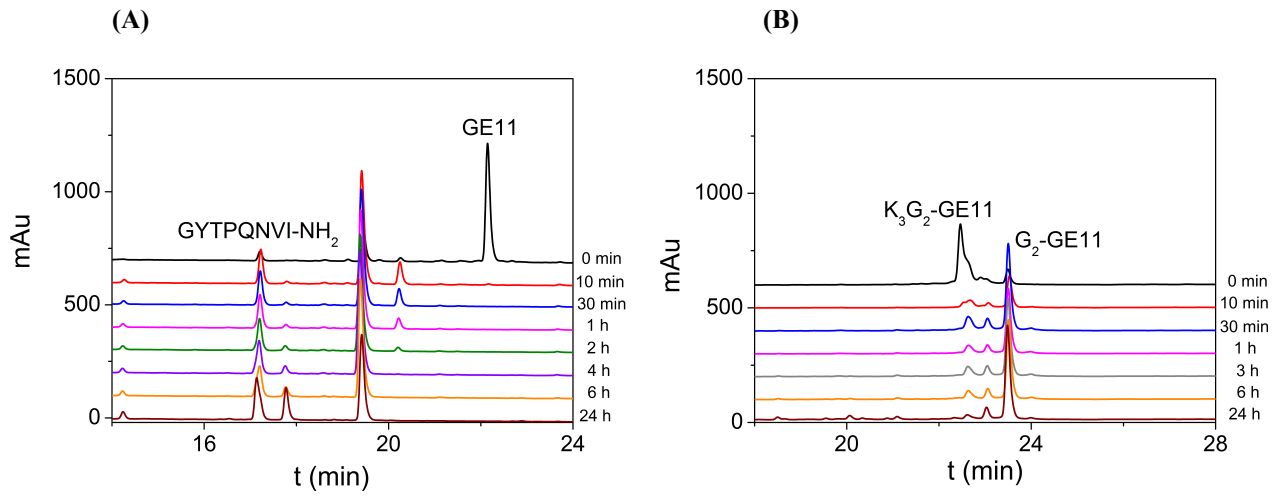

Figure 3. HPLC chromatograms of aliquots withdrawn at the indicated time from digestion of GE11 (A) and KKKGG-GE11 (B) respectively with Chymotrypsin or Trypsin. For elution conditions see the Experimental Section.

Table 1. Characterization of main fragments emerged from proteolysis of peptide KKKGG-GE11 with Trypsin.

Parent peptide or fragment[a]	*Peptide sequence*	*HPLC*[b] *t_R (min)*	*Monoisotopic Calculated*	*Mass*[c] *(Da) Found*
KKKGG-GE11 (1-17)	KKKGGYHWYGYTPQNVI-NH_2	22.7	2037.06	2036.9
2-17	KKGGYHWYGYTPQNVI-NH_2	22.8	1908.96	1908.8
3-17	KGGYHWYGYTPQNVI-NH_2	23.1	1780.87	1780.8
4-17 (GG-GE11)	GGYHWYGYTPQNVI-NH_2	23.6	1652.77	1652.7

[a] Numbers refer to the residue number of the parent peptide.

[b] Column and elution conditions see the experimental section.

[c] Monoisotopic masses were identified using LC-MS.

Table 2. Characterization of main fragments emerged from proteolysis of peptide GE11 with Chymotrypsin.

Parent peptide or fragment[a]	*Peptide sequence*	*HPLC*[b] t_R *(min)*	*Monoisotopic Calculated*	*Mass*[c] *(Da) Found*
GE11 (1-12)	YHWYGYTPQNVI-NH_2	22.1	1538.73	1538.7
5-12	GYTPQNVI-NH_2	17.2	889.47	889.5
7-12	TPQNVI-NH_2	14.2	669.38	669.4
1-6	YHWYGY-OH	20.2	887.36	887.4
1-4	YHWY-OH	19.4	667.27	667.3
1-3	YHW-OH	17.8	504.21	504.2

[a] Numbers refer to the residue number of the parent peptide.

[b] Column and elution conditions see the experimental section.

[c] Monoisotopic masses were identified using HPLC-MS.

AuNP@GE11[C] and AuNP@PEG-KKKGG-GE11 nanostructures were prepared following the two steps protocol already described in Chapter 3. Experimental procedures and characterizations of peptides and nanosystems are respectively reported in the Experimental Section and in the Appendix of this chapter. The enzymatic degradation was performed in the same experimental conditions used for free peptides. Aliquots collected at different time from the incubation solutions were acidified to block the action of the enzyme, centrifuged to remove the nanoparticles and injected in HPLC-MS to detect the presence of the diagnostic fragments. Regarding the enzymatic degradation of AuNP@PEG-KKKGG-GE11 with Trypsin, no significant peak emerged from the HPLC-MS chromatograms (Figure 4A) suggesting that the peptide was not attacked by the enzyme. This can be explained considering that modification with polymers shields peptides from proteolysis due to the steric hindrance that minimizes the physical absorption of the proteases [20,36]. Moreover Molecular Dynamics studies about the organization of the ligands on the surface of the AuNP@PEG-KKKGG-GE11 nanostructures highlighted that the KKKGG sequence, the trypsin sensitive region, is almost completely embedded in the PEG layer (see Chapter 3). As a consequence, it is not easily accessible to the enzyme.

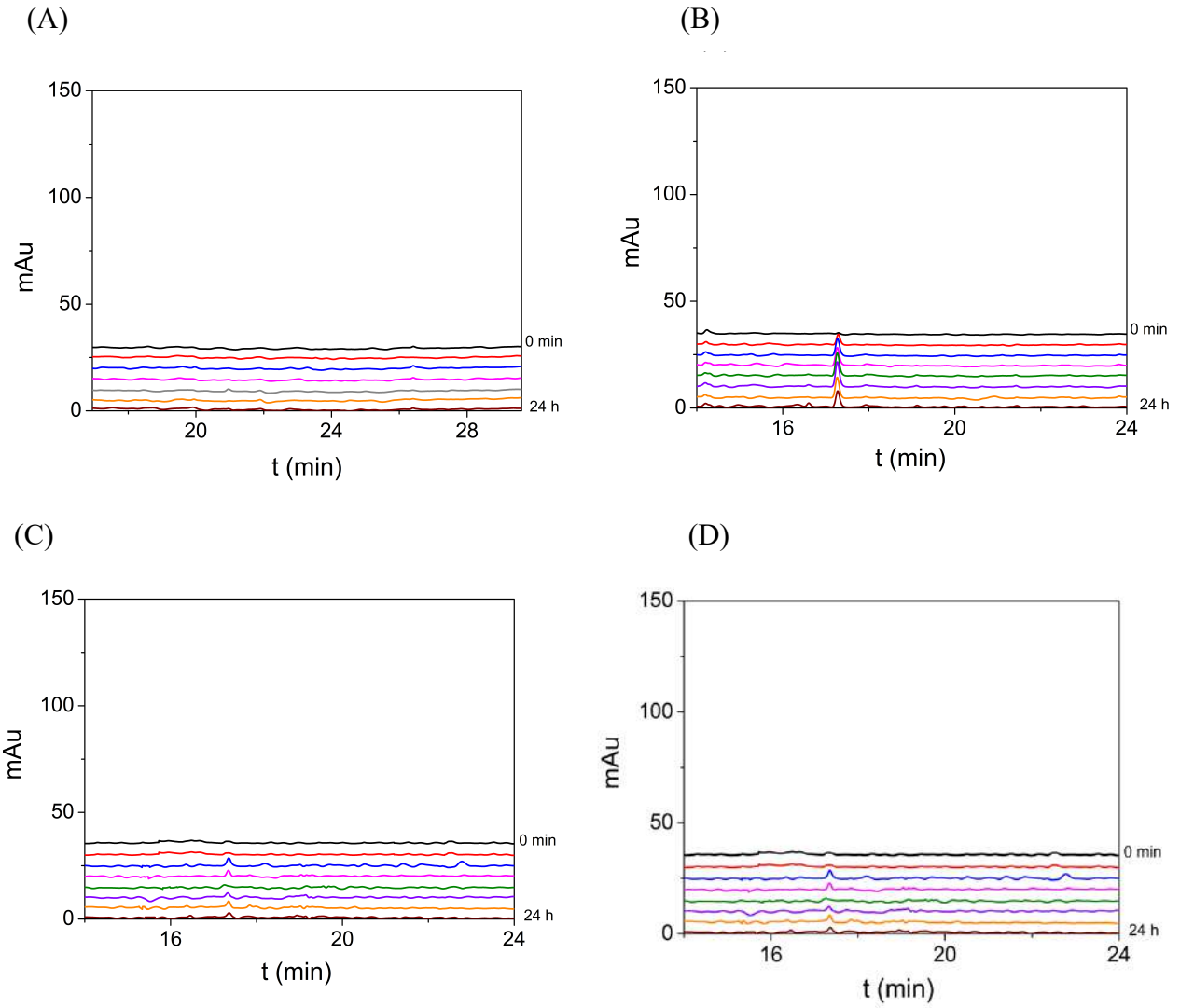

Figure 4. HPLC chromatograms of aliquots withdrawn at the indicated time from digestion of AuNP@PEG-KKKGG-GE11 with Trypsin (A), AuNP@GE11C (B) AuNP@PEG-KKKGG-GE11 (C) and AuNP@PEG-GE11 (D) with Chymotrypsin. For elution conditions see the Experimental Section.

The stability of the targeting peptide to the action of Chymotrypsin was initially investigated on AuNP@GE11^{C} and AuNP@PEG-KKKGG-GE11 nanostructures. For both nanostructures, a very small amount of the (5-12) fragment (GYTPQNVI-NH_2) was detected. The release of the fragment was constant over time (Figures 4B and 4C) and by comparison of the 24 h normalized peak area coming from the digestion of the GE11 in solution with that one coming from the nanostructures, the loss of the targeting peptide was estimated around 3% from AuNP@GE11^{C} and less than 1% from AuNP@PEG-KKKGG-GE11 (Figure 5). The high density of peptides on AuNP@GE11^{C} nanostructures could explain the improved resistance to proteolysis due to steric hindrance to the action of the enzymes. The peptide modification with PEG is supposed to enhance the stability to proteases of AuNP@PEG-KKKGG-GE11, proving that PEG-peptide conjugation could be a successful strategy to achieve an efficient in vivo targeting activity.

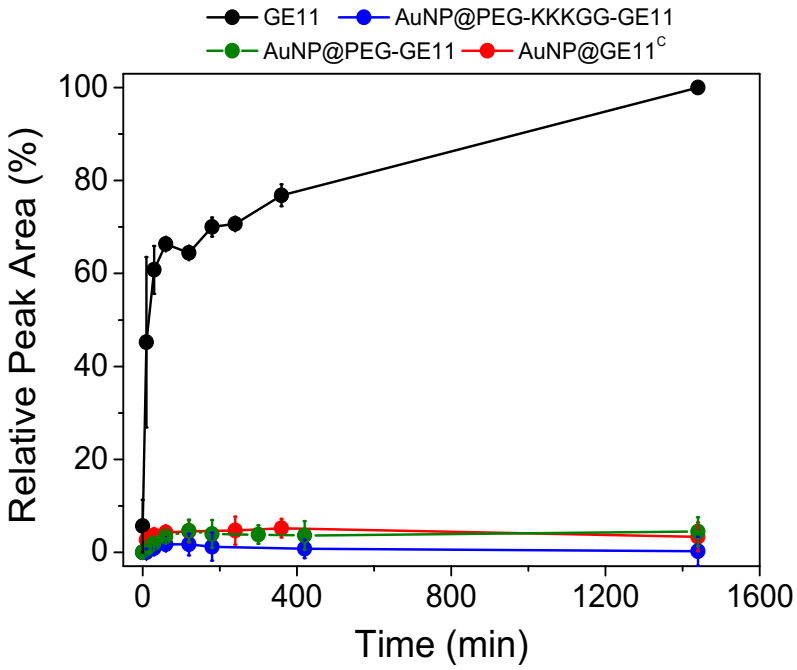

Figure 5. Degradation of GE11 peptide and its nanostructures with chymotrypsin expressed as normalized peak area of the fragment GYTPQNVI-NH_2 relative to the area of the same fragment at 24 h (A).

However, in Chapter 3 it was proved that the simply covalently linking of the targeting motif to the polymer could be a tricky approach. In fact, when the peptide GE11 was directly conjugated to the PEG the resulting nanostructures, AuNP@PEG-GE11, showed a poor targeting activity in vitro. Molecular Dynamics calculation allowed to understand that this was because the targeting peptide was entrapped within the PEG layer and was consequently not available for the association with the receptor. A suitable presentation of the targeting units above the polymeric coating was achieved by inserting a cationic sequence between the PEG and the peptide, obtaining AuNP@PEG-KKKGG-GE11 nanostructures that showed a remarkable targeting activity with respect to AuNP@PEG-GE11. Moreover, as above-described, AuNP@PEG-KKKGG-GE11 demonstrated also to be stable against proteases. According to the statements that peptides buried into a PEG coating are not easily accessible for the interactions with receptors, peptides on AuNP@PEG-GE11 nanostructures are supposed to be also stable to proteolysis. To test this hypothesis AuNP@PEG-GE11 nanostructures were subjected to enzymatic digestion using Chymotrypsin. AuNP@PEG-GE11 were prepared following the protocol already described in Chapter 3 whereas experimental procedures and characterizations are respectively reported in the Experimental Section and in the Appendix of this chapter. The enzymatic degradation was performed in the same experimental conditions used for AuNP@$GE11^C$ and AuNP@PEG-KKKGG-GE11 nanostructures. As can be observed in Figure 5D, an unexpected and constant over time release of the fragment (5-12) fragment (GYTPQNVI-NH_2)

was detected and a loss of the targeting peptide around 4% at 24 h was estimated. This result suggests that Chymotrypsin is capable of interacting with peptides hidden into the polymeric layer. Molecular Dynamics calculations could be helpful to understand the enzyme action in such conditions. Anyway, as can be observed in Figure 5, if a huge different stability against proteases between the isolated peptide and all the nanostructures was revealed, slight differences were observed among the nanosystems. The peptides anchoring to the gold surface might therefore be the main reason of the improved enzymatic stability of the nanostructures.

To confirm the enzymatic stability of the peptides decorating the nanostructure surface, the targeting activity of AuNP@PEG-KKKGG-GE11 was assessed in vitro after 24 h of incubation with Chymotrypsin or human serum. The nanostructures AuNP@GE11^{C} were not considered for this purpose due to their significantly worse specificity with respect to AuNP@PEG-KKKGG-GE11 (see Chapter 3) that could hamper the evaluation. On the contrary, AuNP@PEG-GE11 were not considered because of their far worse sensitivity (see Chapter 3). Incubations were performed in the same conditions previously described. After 24 h the nanosystems were collected from the incubation mixture by centrifugation, washed with PBS and incubated with colorectal cancer cells overexpressing (SW480) or not (SW620) the EGFR for 2h at 37 °C under defined concentration of the nanostructures. As reference, AuNP@PEG-KKKGG-GE11 not subjected to proteolysis were also incubated with cells. Cells were then washed and transferred on a glass slide and the nanosystems SERRS signals were exploited as sensitive probes. SERRS spectra were collected from each single cell, for one hundred cells at each concentration. As shown in Figure 6 all nanostructures efficiently target the EGFR with a sensitivity higher than 80%. The targeting specificity is lower than 80% only for AuNP@PEG-KKKGG-GE11 incubated in serum, probably as a consequence of the protein corona covering the nanostructures in this complex biological fluid, which can increase the non-specific interactions with cells not expressing the EGFR. However, taking into account that the sensitivity, observed with SW480 cells, is increased for the serum incubated nanostructures, probably due to the same non-specific interactions, one concludes that the activity also in this case is similar to the nanostructures treated with Chymotrypsin.

These results confirmed that the targeting activity of the nanostructures is preserved also after the treatment with proteases, thus further proving the stability of the peptide on the nanosystems against the enzymes digestion.

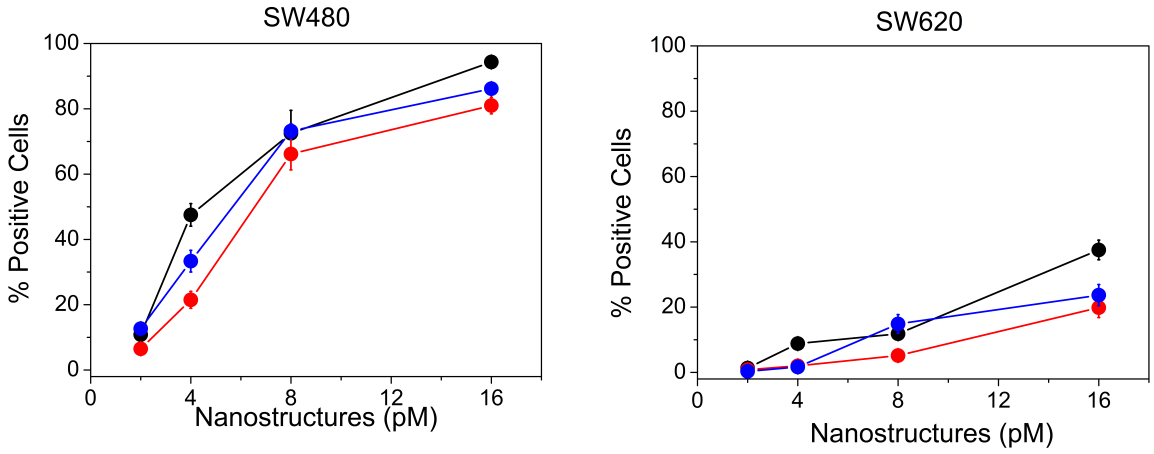

Figure 6. Targeting activity of AuNP@PEG-KKKGG-GE11 nanostructures untreated (blue line), after 24 h incubation in 20% serum (black line) or with chymotrypsin (red line) on colorectal cancer cells overexpressing the EGFR (SW480, on the left) and not expressing the receptor (SW620, on the right).

To conclude, in this chapter the stability to proteases of peptides anchored to gold nanostructures as targeting ligands was evaluated using an alternative approach based on the detection by HPLC-MS of proteolytic fragments detached from the surface as a consequence of the enzymes action. Overall results clearly demonstrated the greater stability, with respect to free peptides in solution, of the peptide functionalized nanostructures. Moreover, it has been proved that the nanosystems preserve the targeting ability also after the treatment with proteases opening the possibility for in vivo applications.

Experimental Section

Materials and Methods

All chemicals are commercial products and used without further purification, unless differently specified. 9-Fluorenylmethoxycarbonyl(Fmoc)-amino acids and all other chemicals for the solid phase synthesis are products of Sigma-Aldrich. Trt-S-C_2H_4-CONH-PEG-O-C_3H_6-CONHS (Trt-S-PEG-NHS MW. 3000 Da) was purchased by Rapp Polymer; Fmoc-8-amino-3,6-dioxaoctanoic acid (Fmoc-PEG_1-OH), Rink Amide MBHA resin (0.9-0.55 mmol g^{-1}) or Rink amide PEGA (0.03 mmoles) by Iris Biotech GMBH. α-Chymotrypsin from bovine pancreas, trypsin from porcine pancreas and Bovin Serum Albumin (BSA) are Sigma Aldrich. Sulforhodamine 101-bis-cysteamide (TR-SH) is synthesized according to a procedure described in a previous study [37]. Human Serum was obtained by a blood sample collected from a volunteer donor. The sample was clotted into a serum vacuum gel separator tube and the specimen was centrifuged for 20 minutes at 3.000 rpm at RT. The supernatant serum was then collected.

Analytical HPLC analysis, Preparative HPLC separations and mass spectral analysis were performed as described in Chapter 3. LC-MS separations were performed on an Agilent 6000 Series LC/MS System using a Vydac 218TP54 column (250x4.6 mm, 5 □m, flow rate at 1 ml/min). Elutions were carried out with binary gradients combining mobile phases A (aqueous 0.1% Trifluoroacetic acid (TFA)) and B (100% aqueous acetonitrile containing 0.1%TFA). Unless otherwise indicated, the elution condition was: isocratic 5%B for 5 min; linear gradient 5-50%B for 30 min. DLS and ζ-potential measurements were performed as described in Chapter 3 as well as UV–vis-NIR and SERRS spectra.

Synthesis of Peptides and Peptide Conjugates

The peptide sequences (GE11, $GE11^C$, KKKGG-GE11) and the peptide conjugates PEG- KKKGG-GE11 and PEG-GE11 were synthesized using Fmoc Chemistry as described in detail in Chapter 3. Peptides were purified by semipreparative HPLC using the elution condition: isocratic 27% B for 5 min: linear gradient 27–25% B for 20 min. The purified product was characterized by analytical HPLC and ESI-MS (Figures A1-3 and Table A1)

Preparation of SEERS nanostructures

Naked gold nanoparticles were synthesized with Laser Ablation Solution Synthesis methodology [37, 38]. Aggregation and labelling with the thiol functionalized SERRS Reporter, Sulforhodamine 101-bis-cysteamide (TR-SH), as well as the conjugation with peptide ligands, was performed according

to the procedure described in Chapter 3. The average number of peptides linked to nanoparticles was estimated by recording the UV-Vis spectra before and after incubation of nanoparticles with the ligands (see Table A2). At each step, UV-Vis-NIR and Raman Spectra were recorded (See Figure A4) and the fully functionalized nanostructures were also characterized by TEM, DLS and Zeta-potential measurements (See Table A2).

Enzymatic hydrolysis using chymotrypsin

Peptide GE11 was dissolved in 1 ml of TRIS Buffer 100 mM, pH 8 up to a concentration of 0.07 mg mL^{-1}. A freshly made solution of the enzyme Chymotripsin a in HCl 1 mM was prepared simultaneously. An aliquot with the corresponding amount of enzyme to afford a final peptide to enzyme ratio of 60:1 was added to the solution of the peptide. The mixture was incubated in a thermally controlled water bath at 37 °C for 24 h. 100 µL of the mixture were withdrawn at different times during the incubation time and diluted with 100 µL of TRIS Buffer. Enzymatic hydrolysis was quenched by adding 10 µL of HCl 1M. Solutions were analysed by analytical reverse phase LC-MS as described in Materials and Methods. The signals in the raw chromatograms, corresponding to the peptide and its degradation products, were baseline corrected and integrated. Areas were normalized to the peptide concentration.

The same procedure was followed for the nanostructures Au@GE11^{C}, AuNP@PEG-KKKGG-GE11 and AuNP@PEG-GE11. Several aliquots of each kind of nanostructures were prepared and collected in 1 ml of TRIS Buffer in order to obtain a concentration of peptides of 0.07 mg mL^{-1}. The enzyme activity was quenched as described above. The solutions were centrifuged for 10 min at 25000 RCF to remove the nanostructures. The collected supernatants, containing the degradation products, were analysed by LC-MS as described in Materials and Methods.

Enzymatic hydrolysis using trypsin

Peptide KKKGG-GE11 was dissolved in 1 ml of Ammonium Bicarbonate Buffer 100 mM, pH 8 up to a concentration of 0.07 mg mL−. A freshly made solution of the enzyme in HCl 1 mM solution was contemporary prepared. An aliquot with the corresponding amount of enzyme to afford a final peptide to enzyme ratio of 200:1 was added to the peptide solution. The mixture was incubated in a thermally controlled water bath at 37 °C for 24 h. 100 µL aliquots of the mixture were withdrawn during the incubation time at different times and diluted with 100 µL of water. Enzymatic degradation was stopped by adding 20 µL of HCl 1M. Solutions were analysed by analytical reverse phase LC-MS. The signals corresponding to the peptide and its degradation products in the raw chromatograms were baseline corrected and integrated. Areas were normalized to the peptide concentration.

The same procedure was followed for the nanostructures AuNP@PEG-KKKGG-GE11. Several aliquots of each kind of nanostructures were prepared and collected in 1 ml of Ammonium Bicarbonate Buffer to obtain a concentration of peptides of 0.07 mg mL^{-1}. The enzyme activity was stopped as described previously. The solutions were centrifuged for 10 min at 25000 RCF to remove the nanostructures. The collected supernatants, containing the degradation products, were analysed by LC-MS as described in Materials and Methods.

Proteolysis in human serum

Peptide GE11 was dissolved in 1 ml of 20% aqueous human serum up to a concentration of 0.07 mg mL^{-1} and the resulting mixture was incubated in a thermally controlled water bath at 37 °C for 24 h. 100 μL aliquots of the mixture were withdrawn during the incubation time at different times. Each aliquot was diluted with 200 μL of 15% aqueous Tricloroacetic acid and cooled in ice to stop the enzymatic proteolysis. The solutions were centrifuged for 10 min at 25000 RCF to precipitate serum proteins. The collected supernatants, containing the degradation products, were analysed by LC-MS as described in Materials and Methods.

Cell Lines and Incubation with AuNP@PEG-KKKGG-GE11: SW480(EGFR+) and SW620(EGFR-) colorectal cancer cell lines were cultured and incubated with the nanostructures as described in Chapter 3. Before incubation Three solutions of AuNP@PEG-KKKGG-GE11 nanostructures were synthesized. Two of them were subjected using to 24 h of enzymatic proteolysis with chymotrypsin or human serum following the procedure previously described. After 24 h, the nanostructures were centrifuged at 25000 RCF for 10 min and resuspended in 1 ml of PBS for three times. The third solution, as reference, was not subjected to enzymatic degradation.

SERRS Measurements: SERRS spectra were collected, processed and statistically analysed as described in Chapter 3.

Appendix

GE11^{C}

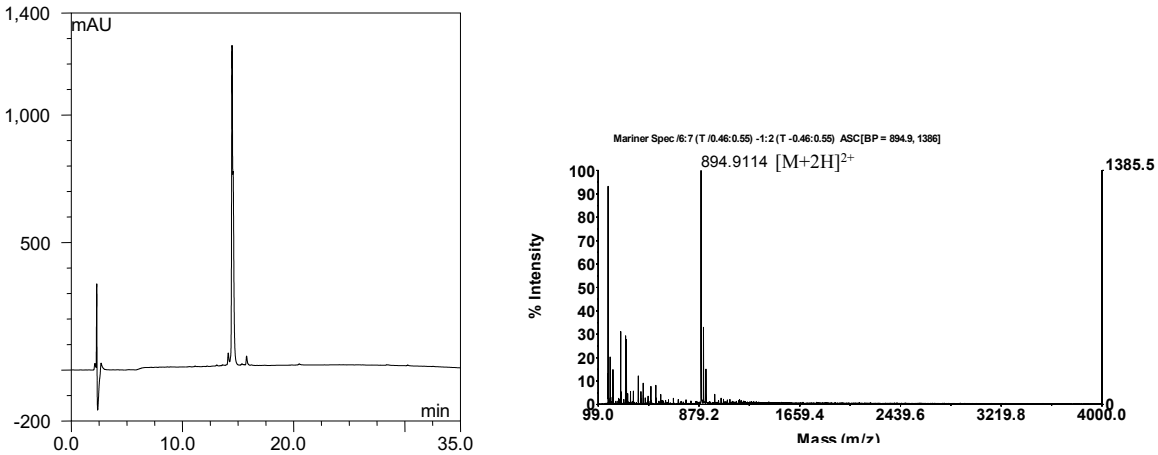

Figure A1. Analytical HPLC and ESI-MS spectra of peptide GE11^{C}. Analytical HPLC separations were performed on a Vydac 218TP54 column (250 x 4.6 mm, 5 µm, flow rate at 1.5 ml/min). The elution condition was: isocratic 10% B for 3 min; linear gradient 10-90% B for 30 min. For preparing binary gradients the mobile phase A (aqueous 0.1% Trifluoroacetic acid (TFA)) and B (90% aqueous acetonitrile containing 0.1%TFA) were used. Mass spectral analyses were carried out on a Mariner API-TOF workstation operating in a positive mode with the ESI technique.

(a) GE11

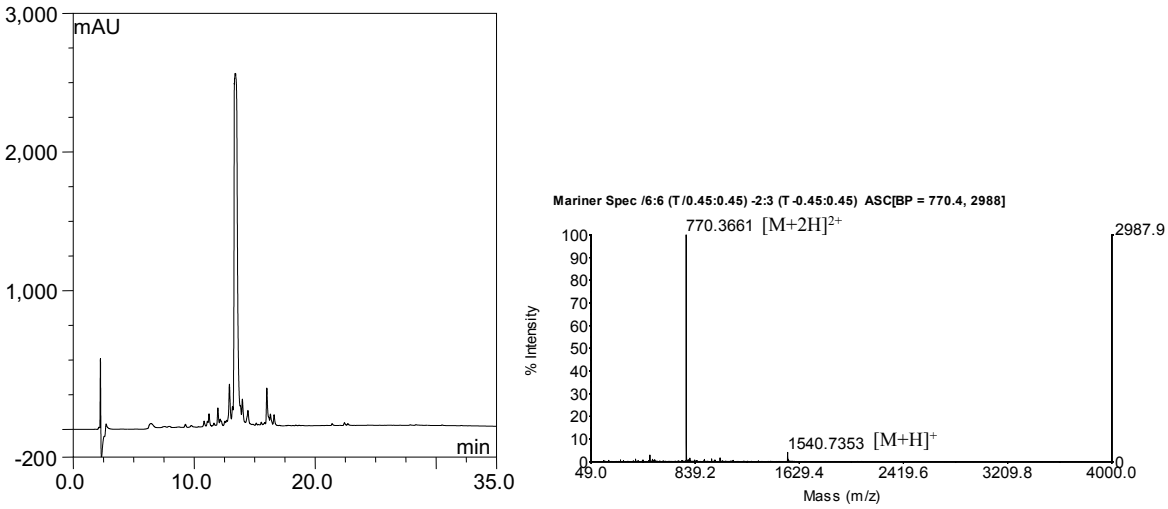

(b) KKKGG-GE11

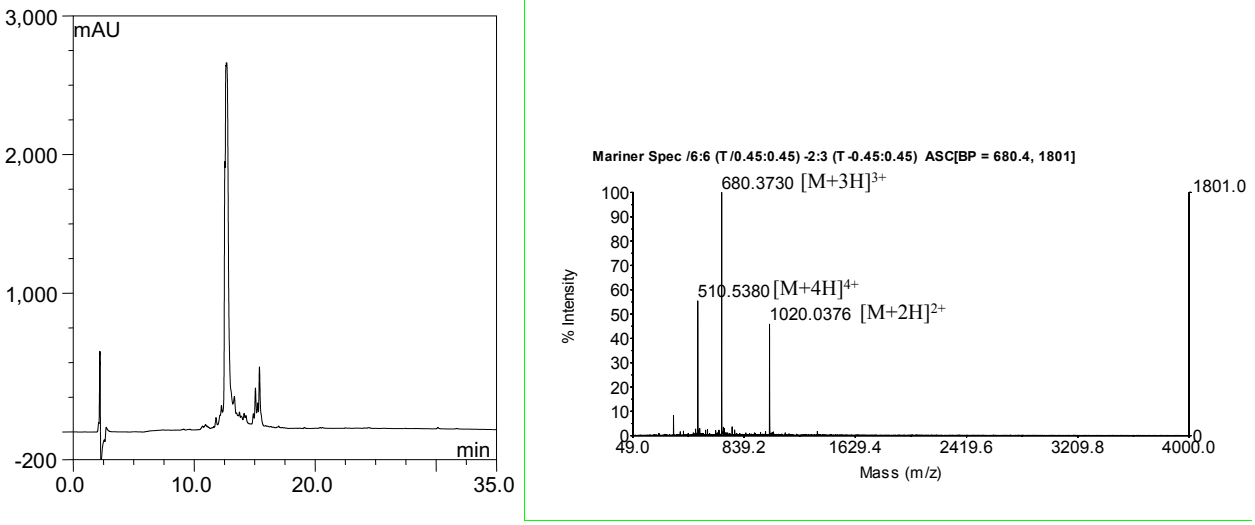

Figure A2. Analytical HPLC and ESI-MS spectra of peptides: (a) GE11 (b) KKKGG-GE11. Analytical HPLC separations and mass spectral analyses were carried out in the same conditions described in Fig. A1.

(a) PEG-GE11

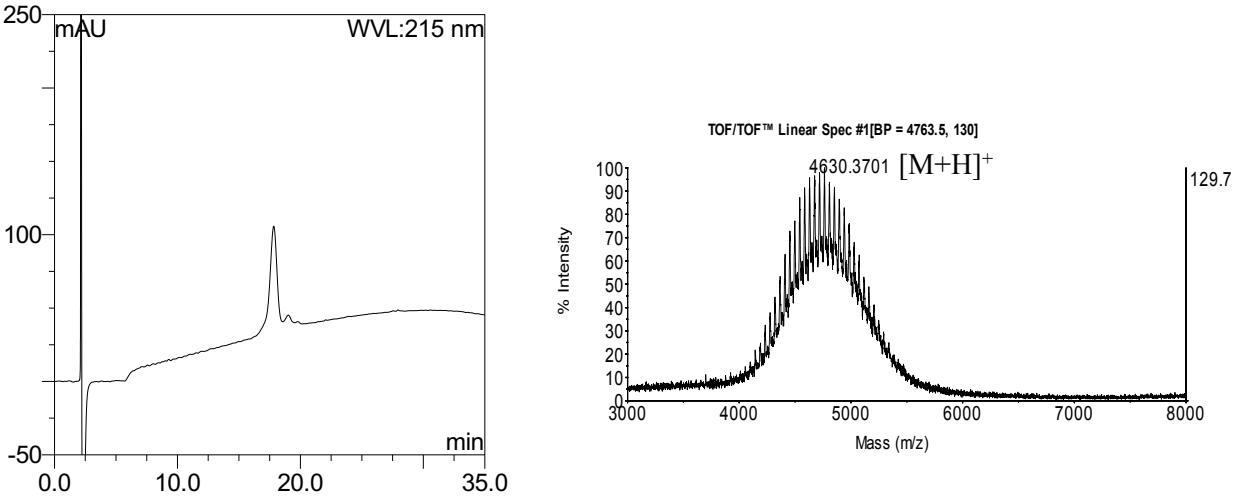

(b) PEG-KKKGG-GE11

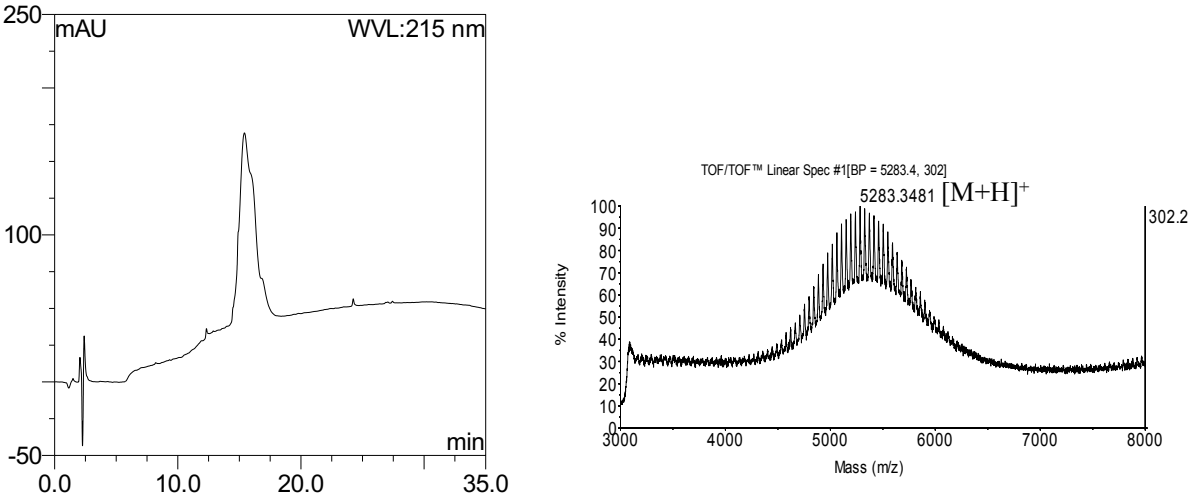

Figure A3. Analytical HPLC and MALDI TOF-TOF spectra of conjugates (a) PEG-GE11 (b) PEG-KKKGG-GE11. Analytical HPLC separations were carried out in the same conditions described in Fig. A1. Mass spectral analyses were performed on a MALDI TOF/TOF Analyser, operating in positive mode in the linear mid-mass range (2,5-dihydroxybenzoic acid as matrix).

Table A1

Peptide	*Sequence*	*Yield %*	*HPLC[b] t_R (min)*	*Expected Mass*	*Found Mass*
GE11[C]	C-PEG1-YHWYGYTPQNVI- NH_2	92	23.69	1787.886$[M+H]^+$	894.9114 $[M+2H]^{+2}$
KKKGG-GE11	H-KKKGGYHWYGYTPQNVI-NH_2	91	12.70	2038.066$[M+H]^+$	1020.0376$[M+2H]^{+2}$, 680.3730$[M+3H]^{+3}$, 510.5380$[M+4H]^{+4}$
GE11	H-YHWYGYTPQNVI-NH2	94	13.39	1539.738[M+H]+	1540.7353 $[M+H]^{+1}$, 770.3661 $[M+2H]^{+2}$
PEG-GE11	HS-PEG-YHWYGYTPQNVI-NH_2	91	17.84	4729 $[M+H]^+$	4630 $[M+H]^+$
PEG-KKKGG-GE11	HS-PEG-KKKGG-YHWYGYTPQNVI-NH2	94	15.41	5226 [M+H]+	5283 $[M+H]^{+1}$

Abbreviations: PEG_1, 8-amino-3,6-dioxoactanoic acid

[a] In the sequences, the one-letter symbols for amino acids have been used.

[b] For Analytical HPLC and MS spectra see Figure A1-3

(a) AuNP@GE11^{C}

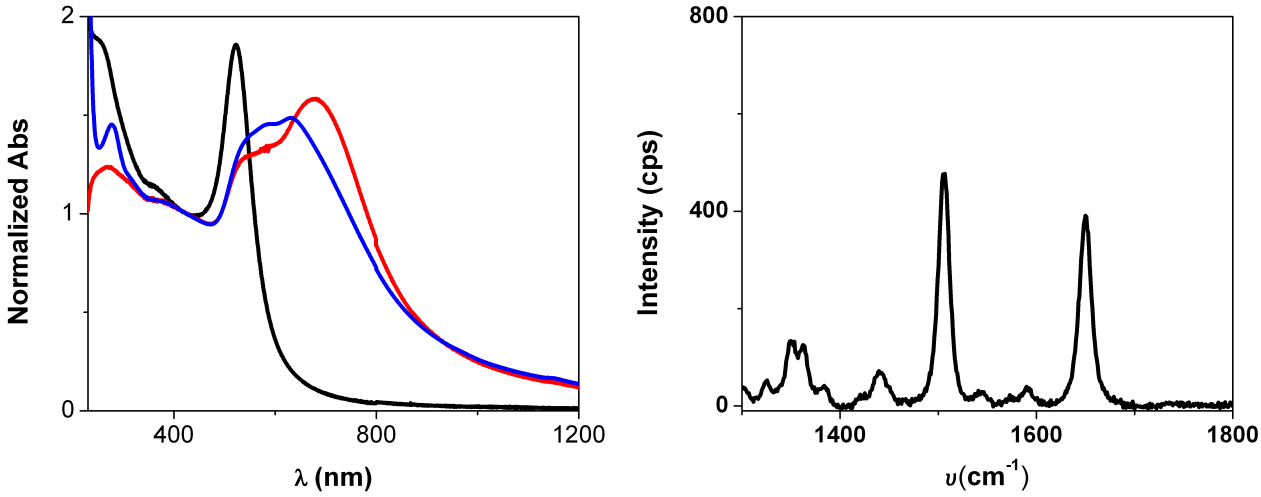

(b) AuNP@PEG-KKKGG-GE11

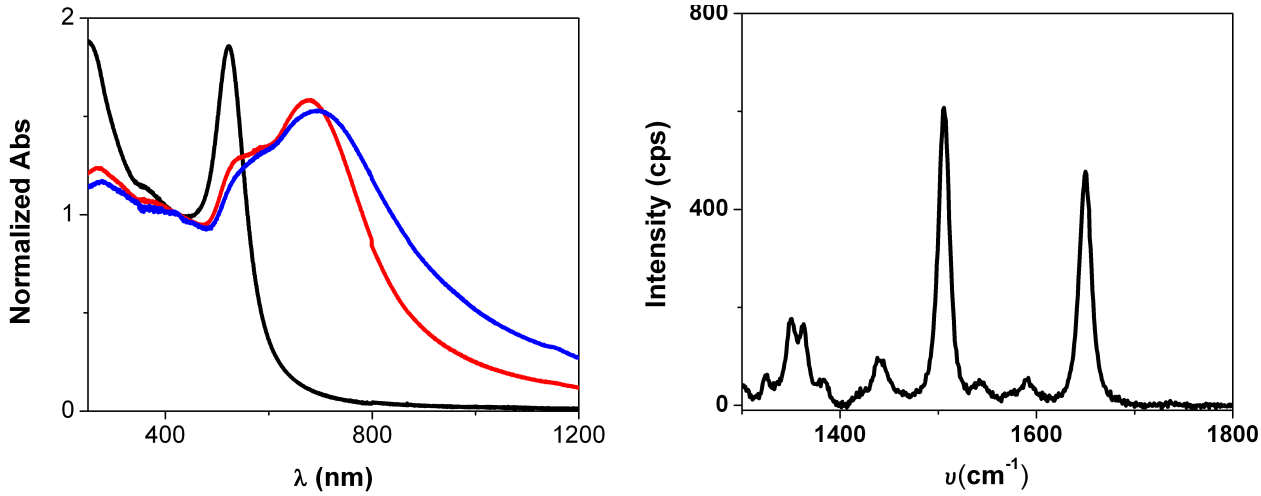

(c) AuNP@PEG-GE11

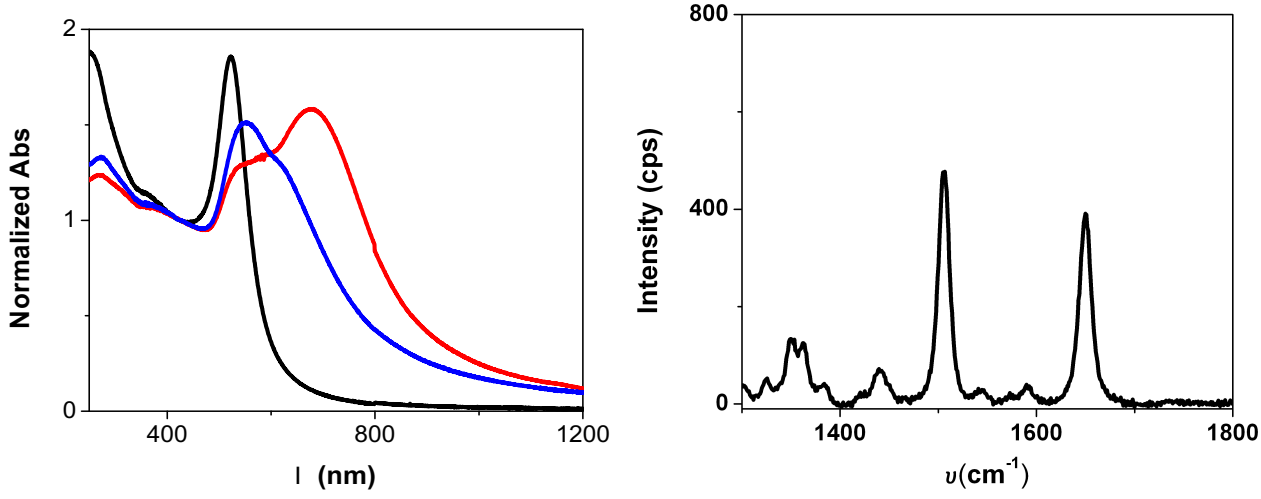

Figure A4. On the left, evolution of the extinction spectra during the assembling steps of the nanostructures: Laser Ablation in Solution of gold nanoparticles (black line), aggregation and labelling with the SERRS reporter (red line) and conjugation of peptide ligands (blue line). On the right, SERRS spectra of the final nanostructures (a) AuNP@GE11^{C} (b) AuNP@PEG-KKKGG-GE11 (c) AuNP@PEG-GE11

Table A2

Nanostructure	*Peptides per nanoparticle*	*Hydrodynamic diameter (nm)*	*Zeta-potential (mV)*
AuNP@GE11^{C}	10000	70±8	-13.9±0.2
AuNP@PEG-GE11	3000	120±5	4±1
AuNP@PEG-KKKGG-GE11	2200	100±6	13.9±2.2

References

1. Zhang, X. Q., Xu, X., Bertrand, N., Pridgen, E., Swami, A., Farokhzad, O. C., Interactions of nanomaterials and biological systems: Implications to personalized nanomedicine. *Advanced Drug Delivery Reviews.* **2012**. 64 (13), pp 1363-1384.

2. Allen, T. M., Ligand-targeted therapeutics in anticancer therapy. *Nature Reviews Cancer.* **2002**. 2 (10), pp 750-763.

3. Dasgupta, P., Singh, A., Mukherjee, R., N-terminal acylation of somatostatin analog with long chain fatty acids enhances its stability and anti-proliferative activity in human breast adenocarcinoma cells. *Biological & Pharmaceutical Bulletin.* **2002**. 25 (1), pp 29-36.

4. Huynh, N. T., Roger, E., Lautram, N., Benoit, J. P., Passirani, C., The rise and rise of stealth nanocarriers for cancer therapy: passive versus active targeting. *Nanomedicine.* **2010**. 5 (9), pp 1415-1433.

5. Bellmann-Sickert, K., Beck-Sickinger, A. G., Peptide drugs to target G protein-coupled receptors. *Trends in Pharmacological Sciences.* **2010**. 31 (9), pp 434-441.

6. Lau, J. L., Dunn, M. K., Therapeutic peptides: Historical perspectives, current development trends, and future directions. *Bioorganic & Medicinal Chemistry.* **2018**. 26 (10), pp 2700-2707.

7. Tu, Z. G., Ha, J., Kharldia, R., Meng, X. G., Liang, J. F., Improved stability and selectivity of lytic peptides through self-assembly. *Biochemical and Biophysical Research Communications.* **2007**. 361 (3), pp 712-717.

8. Werle, M., Bernkop-Schnurch, A., Strategies to improve plasma half life time of peptide and protein drugs. *Amino Acids.* **2006**. 30 (4), pp 351-367.

9. Janek, K., Rothemund, S., Gast, K., Beyermann, M., Zipper, J., Fabian, H., Bienert, M., Krause, E., Study of the conformational transition of A beta(1-42) using D-amino acid replacement analogues. *Biochemistry.* **2001**. 40 (18), pp 5457-5463.

10. Brinckerhoff, L. H., Kalashnikov, V. V., Thompson, L. W., Yamshchikov, G. V., Pierce, R. A., Galavotti, H. S., Engelhard, V. H., Slingluff, C. L., Terminal modifications inhibit proteolytic degradation of an immunogenic MART-1(27-35) peptide: Implications for peptide vaccines. *International Journal of Cancer.* **1999**. 83 (3), pp 326-334.

11. Green, B. D., Mooney, M. H., Gault, V. A., Irwin, N., Bailey, C. J., Harriott, P., Greer, B., O'Harte, F. P. M., Flatt, P. R., N-terminal His(7)-modification of glucagon-like peptide-1(7-36) amide generates dipeptidyl peptidase IV-stable analogues with potent antihyperglycaemic activity. *Journal of Endocrinology.* **2004**. 180 (3), pp 379-388.

12. Gelain, F., Bottai, D., Vescovi, A., Zhang, S. G., Designer Self-Assembling Peptide Nanofiber Scaffolds for Adult Mouse Neural Stem Cell 3-Dimensional Cultures. *Plos One.* **2006**. 1 (2), pp 11.
13. Nagai, Y., Unsworth, L. D., Koutsopoulos, S., Zhang, S. G., Slow release of molecules in self-assembling peptide nanofiber scaffold. *Journal of Controlled Release.* **2006**. 115 (1), pp 18-25.
14. Toft, D. J., Moyer, T. J., Standley, S. M., Ruff, Y., Ugolkov, A., Stupp, S. I., Cryns, V. L., Coassembled Cytotoxic and Pegylated Peptide Amphiphiles Form Filamentous Nanostructures with Potent Antitumor Activity in Models of Breast Cancer. *Acs Nano.* **2012**. 6 (9), pp 7956-7965.
15. Zhou, X. R., Cao, Y. M., Zhang, Q., Tian, X. B., Dong, H., Chen, L., Luo, S. Z., Self-assembly nanostructure controlled sustained release, activity and stability of peptide drugs. *International Journal of Pharmaceutics.* **2017**. 528 (1-2), pp 723-731.
16. Rozek, A., Powers, J. P. S., Friedrich, C. L., Hancock, R. E. W., Structure-based design of an indolicidin peptide analogue with increased protease stability. *Biochemistry.* **2003**. 42 (48), pp 14130-14138.
17. Ying, M., Shen, Q., Liu, Y., Yan, Z. Q., Wei, X. L., Zhan, C. Y., Gao, J., Xie, C., Yao, B. X., Lu, W. Y., Stabilized Heptapeptide A7R for Enhanced Multifunctional Liposome-Based Tumor-Targeted Drug Delivery. *Acs Applied Materials & Interfaces.* **2016**. 8 (21), pp 13232-13241.
18. Tang, J. J., Wang, Q. T., Yu, Q. W., Qiu, Y., Mei, L., Wan, D. D., Wang, X. H., Li, M., He, Q., A stabilized retro-inverso peptide ligand of transferrin receptor for enhanced liposome-based hepatocellular carcinoma-targeted drug delivery. *Acta Biomaterialia.* **2019**. 83, pp 379-389.
19. Gregoriadis, G., Fernandes, A., Mital, M., McCormack, B., Polysialic acids: potential in improving the stability and pharmacokinetics of proteins and other therapeutics. *Cellular and Molecular Life Sciences.* **2000**. 57 (13-14), pp 1964-1969.
20. Grunwald, J., Rejtar, T., Sawant, R., Wang, Z. X., Torchilin, V. P., TAT Peptide and Its Conjugates: Proteolytic Stability. *Bioconjugate Chemistry.* **2009**. 20 (8), pp 1531-1537.
21. Pasut, G., Veronese, F. M., State of the art in PEGylation: The great versatility achieved after forty years of research. *Journal of Controlled Release.* **2012**. 161 (2), pp 461-472.
22. Boge, L., Umerska, A., Matougui, N., Bysell, H., Ringstad, L., Davoudi, M., Eriksson, J., Edwards, K., Andersson, M., Cubosomes post-loaded with antimicrobial peptides: characterization, bactericidal effect and proteolytic stability. *International Journal of Pharmaceutics.* **2017**. 526 (1-2), pp 400-412.
23. Zetterberg, M. M., Reijmar, K., Pranting, M., Engstrom, A., Andersson, D. I., Edwards, K., PEG-stabilized lipid disks as carriers for amphiphilic antimicrobial peptides. *Journal of Controlled Release.* **2011**. 156 (3), pp 323-328.

24. Rai, A., Pinto, S., Evangelista, M. B., Gil, H., Kallip, S., Ferreira, M. G. S., Ferreira, L., High-density antimicrobial peptide coating with broad activity and low cytotoxicity against human cells. *Acta Biomaterialia.* **2016**. 33, pp 64-77.

25. Yan, J., He, W. X., Yan, S. Q., Niu, F., Liu, T. Y., Ma, B. H., Shao, Y. P., Yan, Y. W., Yang, G., Lu, W. Y., Du, Y. P., Lei, B., Ma, P. X., Self-Assembled Peptide-Lanthanide Nanoclusters for Safe Tumor Therapy: Overcoming and Utilizing Biological Barriers to Peptide Drug Delivery. *Acs Nano.* **2018**. 12 (2), pp 2017-2026.

26. Niu, F., Yan, J., Ma, B. H., Li, S. C., Shao, Y. P., He, P. C., Zhang, W. G., He, W. X., Ma, P. X., Lu, W. Y., Lanthanide-doped nanoparticles conjugated with an anti-CD33 antibody and a p53-activating peptide for acute myeloid leukemia therapy. *Biomaterials.* **2018**. 167, pp 132-142.

27. Goutayer, M., Dufort, S., Josserand, V., Royere, A., Heinrich, E., Vinet, F., Bibette, J., Coll, J. L., Texier, I., Tumor targeting of functionalized lipid nanoparticles: Assessment by in vivo fluorescence imaging. *European Journal of Pharmaceutics and Biopharmaceutics.* **2010**. 75 (2), pp 137-147.

28. Su, Z. G., Shi, Y. P., Xiao, Y. Y., Sun, M. J., Ping, Q. N., Zong, L., Li, S., Niu, J. X., Huang, A. W., You, W. L., Chen, Y. A., Chen, X., Fei, J., Tian, J., Effect of octreotide surface density on receptor-mediated endocytosis in vitro and anticancer efficacy of modified nanocarrier in vivo after optimization. *International Journal of Pharmaceutics.* **2013**. 447 (1-2), pp 281-292.

29. Accardo, A., Aloj, L., Aurilio, M., Morelli, G., Tesauro, D., Receptor binding peptides for target-selective delivery of nanoparticles encapsulated drugs. *International Journal of Nanomedicine.* **2014**. 9, pp 1537-1557.

30. Stefanick, J. F., Kiziltepe, T., Bilgicer, B., Improved Peptide-Targeted Liposome Design Through Optimized Peptide Hydrophilicity, Ethylene Glycol Linker Length, and Peptide Density. *Journal of Biomedical Nanotechnology.* **2015**. 11 (8), pp 1418-1430.

31. Rawlings, N. D., Salvesen, G., Handbook of Proteolyic Enzymes. *Academic Press*. **2013**. 3rd Edition.

32. Gobbo, M., Benincasa, M., Bertoloni, G., Biondi, B., Dosselli, R., Papini, E., Reddi, E., Rocchi, R., Tavano, R., Gennaro, R., Substitution of the Arginine/Leucine Residues in Apidaecin Ib with Peptoid Residues: Effect on Antimicrobial Activity, Cellular Uptake, and Proteolytic Degradation. *Journal of Medicinal Chemistry.* **2009**. 52 (16), pp 5197-5206.

33. Berthold, N., Czihal, P., Fritsche, S., Sauer, U., Schiffer, G., Knappe, D., Alber, G., Hoffmann, R., Novel Apidaecin 1b Analogs with Superior Serum Stabilities for Treatment of Infections by Gram-Negative Pathogens. *Antimicrobial Agents and Chemotherapy.* **2013**. 57 (1), pp 402-409.

34. Blow, D. M., Structure and mechanism of chymotrypsin. *Acc. Chem. Res.* **1976**. 9, pp 145-152.

35. Inagami, T., Mitsuda, H., The Mechanism of the Specificity of Trypsin Catalysis. *The Journal of Biological Chemistry*. **1964**. 239, pp 1388-1405.
36.Ikeda, Y., Nagasaki, Y., PEGylation Technology in Nanomedicine. *Polymers in Nanomedicine*. *Eds. Springer-Verlag Berlin*. **2012**. 247, pp 115-140.
37. Meneghetti, M., Scarsi, A., Litti, L., Marcolongo, G., Amendola, V., Gobbo, M., Di Chio, M., Boscaini, A., Fracasso, G., Colombatti, M., Plasmonic Nanostructures for SERRS Multiplexed Identification of Tumor-Associated Antigens. *Small.* **2012**. 8 (24), pp 3733-3738.
38. Litti, L., Ramundo, A., Biscaglia, F., Toffoli, G., Gobbo, M., Meneghetti, M., A surface enhanced Raman scattering based colloid nanosensor for developing therapeutic drug monitoring. *Journal of Colloid and Interface Science.* **2019**. 533, pp 621-626.

Chapter 7: Efficient Liver Cancer Targeting and SERRS Imaging with PreS1 Peptide-Functionalized Gold Nanostructures

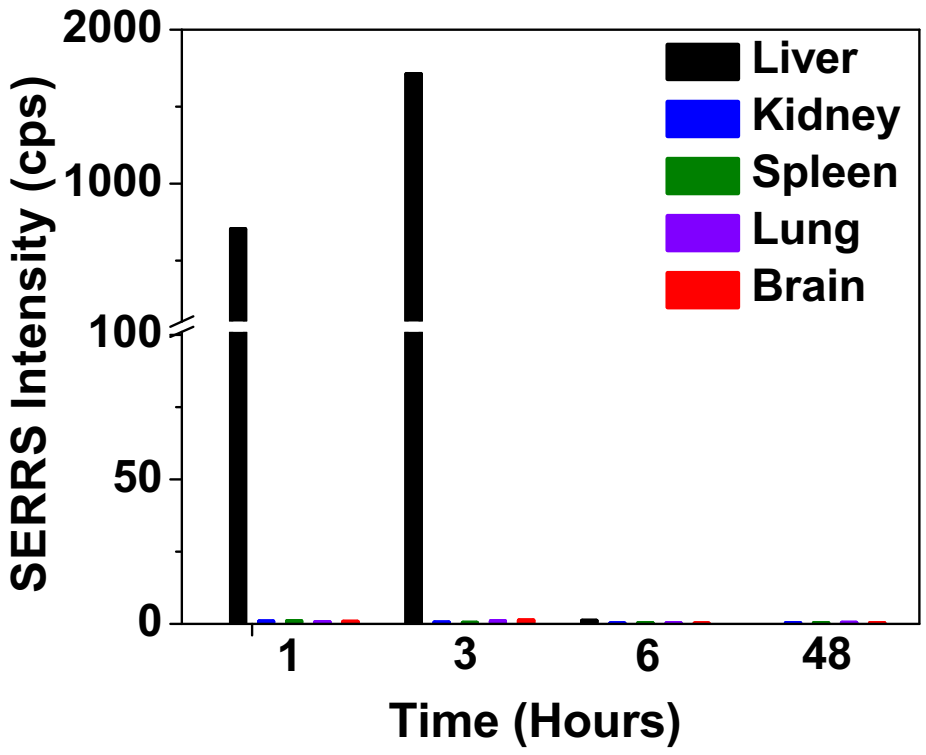

Variation of SERRS Intensity as a function of time over a period of 48 hours in organ lysates of SerpinB3 transgenic mice after injection of PreS1 functionalized nanostructures.

The goal of this PhD project, as introduced in Chapter 1, is the engineering of gold nanostructures to be used as SERRS biosensors for colorectal and liver cancer diagnostics by functionalization with peptides as specific ligands of tumor associated receptors. Colorectal cancer cells targeting was achieved by loading the nanosystems with GE11 (Chapters 3,5,6) and cycloRGD (Chapter 4) peptides that respectively bind the EGFR and $\alpha_v\beta_3$ integrin overexpressed by these cells. Several aspects regarding the association of the nanostructures with receptors were investigated and discussed in detail in the previous chapters. Herein the possibility to exploit SERRS nanostructures for liver cancer targeting and early stage screening is explored. As anticipated in Chapter 2, the target protein chosen for this purpose is the Squamous Cell Carcinoma Antigen 1, named also SerpinB3 (SB3), which is a soluble serine protease inhibitor of the ovalbumin−serine protease family (ov-serpins) frequently overexpressed in numerous dysplastic nodules, in the hepatocellular carcinoma (HCC) and in the hepatoblastoma. Being not expressed in healthy hepatocytes, SB3 up-regulation is a wake up call of early events of hepatocarcinogenesis and metastatic processes [1]. Interestingly, SB3 is also a target of the hepatitis B virus (HBV), which involves the N-terminal PreS1(21–47) sequence (PLGFFPDHQLDPAFGANSNNPDWDFNP-NH_2), from here on PreS1, of its envelope for cells attachment and internalization [2,3]. Several recent studies have exploited the SB3/PreS1 affinity for different purposes. For instance, PreS1 was linked to a 9-mer-Arginine peptide, that mediates translocation through the cell membrane, to deliver siRNA to hepatocytes and induce post-transcriptional silencing inhibiting the replication of the HBV [4]. Moreover, a number of PreS1-functionalized nanosystems were developed for targeted biotechnological applications, including imaging and delivering of anticancer drugs. As an example, PreS1 was used to deliver 2 nm gold nanoparticles [5], hyperthermophilic responsive protein-based nanocage [6] and drug loaded PEGylated liposomes [7] or polysaccharides [8] to human hepatoma cells (HepG2). Actually, the SB3/PreS1 affinity has not been yet exploited in imaging techniques to detect early events in liver cell carcinomatous transformations and monitoring of cancer [9]. Because of the many advantages over other emerging techniques, as deeply discussed in Chapter 2, Raman imaging using SERRS nanoparticles is very promising [10-16] and was therefore chosen to develop biosensors for early stage detection of the SB3 antigen overexpressed on liver cancer cells. Nanosensors were obtained by decorating SERRS active gold nanostructures with PreS1 peptides as targeting units. Previous studies for other peptide sequences (Chapters 3-5) demonstrated the huge impact of the organization of the targeting motif on the nanostructures surface for the binding of the receptor. Taking this finding in account, a number of PreS1 analogues were rationally designed and synthesized so that the targeting unit could be exposed in different arrangement on the nanostructures. Thanks to the collaboration with the group of Prof. P.Pontisso of the Department of Medicine DIMED of the University of Padova, the targeting

ability was studied both in vitro on hepatoma cells, expressing or not the SB3 antigen, and in vivo in healthy mice and mice genetically modified to express the SB3 protein. Overall results demonstrated that the nanostructures functionalized with the PreS1 peptide represent an efficient approach for SB3 targeted diagnostic and imaging activities. Results presented in this Chapter were recently published [17].

Results and Discussion

SERRS nanostructures preparation was carried out following the two steps protocol used for obtaining nanosystems functionalized with GE11 or cycloRGD peptides described in Chapters 4,5 and 6. Experimental procedures and characterizations of peptides and nanosystems are respectively reported in the Experimental Section and in the Appendix of this chapter. Briefly, the synthesis started from a colloidal solution of naked gold nanoparticles (AuNP), obtained by the LASiS (laser ablation synthesis in solution) technique [18], induced to assemble in SERRS active nanoaggregates by functionalization with the thiolated derivative of Texas Red (TR) as SERRS label. After cleaning from non-reacted TR by centrifugation, nanoaggregates were functionalized with the 28-residue PreS1 peptide exploiting the stable bond between gold and the thiol group added to the sequence. By comparing the absorbance of the ligand solution before and after the functionalization of the nanostructures, hundreds to thousands of PreS1 peptides were estimated to be linked per nanoparticle (Table 1). This large number of peptides is important for achieving an efficient targeting since increases the nanostructures avidity, as also suggested comparing the different affinity for the SB3 protein between the isolated peptide PreS1 and a tetravalent peptide arrangement [19]. Fully functionalized nanostructures were characterized by recording Uv-vis-NIR and SERRS spectra (Figure A4). Dimensions of the aggregates were found to be in the order of 100 nm, as confirmed by DLS measurements. ζ-potentials showed negative values supporting the nanostructures stability as colloidal dispersion. The ζ-potentials trend among the nanosystems is currently not understood. Being the results of several factors, which rely on both the nanoparticles and the ligands on their surface, they will be object of future studies. (Table 1).

Table 1. Characterization of the synthesized nanostructures.

Nanostructure	*Ligands per nanoparticle*	*Hydrodynamic diameter (nm)*	*ζ-potential (mV)*
AuNP@PreS1^{N}	2000	257±5	-17±1
AuNP@PreS1^{C}	2000	231±4	-45±2
AuNP@PEG-PreS1	1600	136±1	-34±1

In order to investigate if the orientation of the peptide on nanoparticles can affect the SB3 protein recognition, two PreS1 analogues bearing an extra cysteine residue at the C- or N-terminal end ($PreS1^N$ and $PreS1^C$, respectively) were synthesized. Nanostructures coated with the peptide anchored with opposite orientation (Au@$PreS1^N$ and Au@$PreS1^C$) were prepared by simply mixing the colloidal solution of aggregates with the ligands.

The strategy of coating the nanostructures surface with a PEG layer is known to be useful to reduce non-specific adsorption of proteins in biological fluids, that promotes clearance of nanoparticles by the reticuloendothelial system [20] and impart stability against proteolytic enzymes [21] (Chapter 6). Moreover, in Chapters 3-5 of this thesis, the presence of PEG on peptide functionalized nanostructures demonstrated to be useful to improve the association of the targeting motif with the receptor and to reduce non-specific interactions with cells. The hydrophilicity of the targeting peptide, although it is not the only condition, proved to be essential to gain access to the environment above the PEG coating, which is the basic condition for the receptor recognition. The presence of four aspartic acid residues in the PreS1 sequence makes the peptide high hydrophilic and should impart little propensity to stay buried into the polymeric layer. Therefore, a bifunctional PEG chain (MW around 3 kDa), ending with a masked thiol group, was conjugated to the amino terminus of the PreS1 peptide still attached to the solid support. Final removal of the conjugate from the resin, in acid conditions, released also the thiol group on the polymer for the functionalization of the nanostructures, Au@PEG-PreS1.

As already observed for other nanosystems (Chapter 3), nanostructures decorated with PEG-peptide conjugates showed a lower dimension than that of nanostructures functionalized with only the peptides (Table 1). In fact, if Au@PEG-PreS1 nanosystems displayed a hydrodynamic diameter around 135 nm, that of AuNP@$PreS1^N$ and AuNP@$PreS1^C$ was on average quantified around 245 nm. This can be explained considering that the presence of the PEG avoids further aggregation among the nanostructures. Moreover, Au@PEG-PreS1 showed a lower number of ligands per nanoparticles compared to AuNP@$PreS1^N$ and AuNP@$PreS1^C$, probably as a consequence of the larger dimension of the PEG-peptide conjugates with respect to the parent peptides.

To detect nonspecific interactions with cells, nanostructures without targeting units, AuNP@mPEG, were also prepared and used as control. The targeting properties of the synthesized nanostructures were assessed on HepG2 cells stably transfected with SB3 (HepG2/SB3) and HepG2 cells devoid of the wild-type SB3 gene (HepG2/CTR). At first, the ability of the isolated PreS1 peptide to interact with the target protein on both cell lines was evaluated by a Fluorimetric assay. Two fluoresceinated analogues of PreS1 were synthesized for this purpose by modifying the N- or the C-terminus with the dye (Fluo-PreS1 and PreS1-Fluo, respectively). In both cases the specific binding resulted very weak,

according to that suggested by literature data [5,19]. Surface Plasmon Resonance (SPR) analysis was also carried out (Figure A6): SB3 protein was immobilized on a sensor-chip and increasing concentrations of PreS1 were passed over the sensor. Results confirmed a weak binding of the isolated peptide with the target protein (K_D= 3.8 x 10^{-5} M). The incubation of increasing concentrations of the functionalized nanostructures with HepG2/SB3 and HepG2/CTR cells (2 h at 37°C), on the contrary, showed a very interesting targeting activity. Recording SERRS spectra from each single cell and analysing the dataset using the reference spectrum of the SERRS reporter, the presence of the nanosystems was estimated. Clearly, the signal of the SERRS label was found only if cells were targeted by the nanostructures. SERRS measurements and statistical analysis of the dataset were carried out as described in Chapter 3. As shown in Figure 2, AuNP@PreS1^N and AuNP@PreS1^C strongly bind to HepG2/SB3 because more than 50% of cells exhibit SERRS signals at the highest explored concentration. Taking into account similar findings obtained for other targeting moieties (Chapter 3) and considering the large dissociation constant for the binding of PreS1 to SerpinB3 measured by SPR in comparison to the high binding affinity of a tetravalent conjugate of PreS1 [19], these results highlight the importance of the presence of a large number of peptides on the nanostructures to achieve a good targeting activity. The presence of multiple copies of the peptide is supposed to significantly enhance the target-specific avidity through multivalent interactions [22,23].

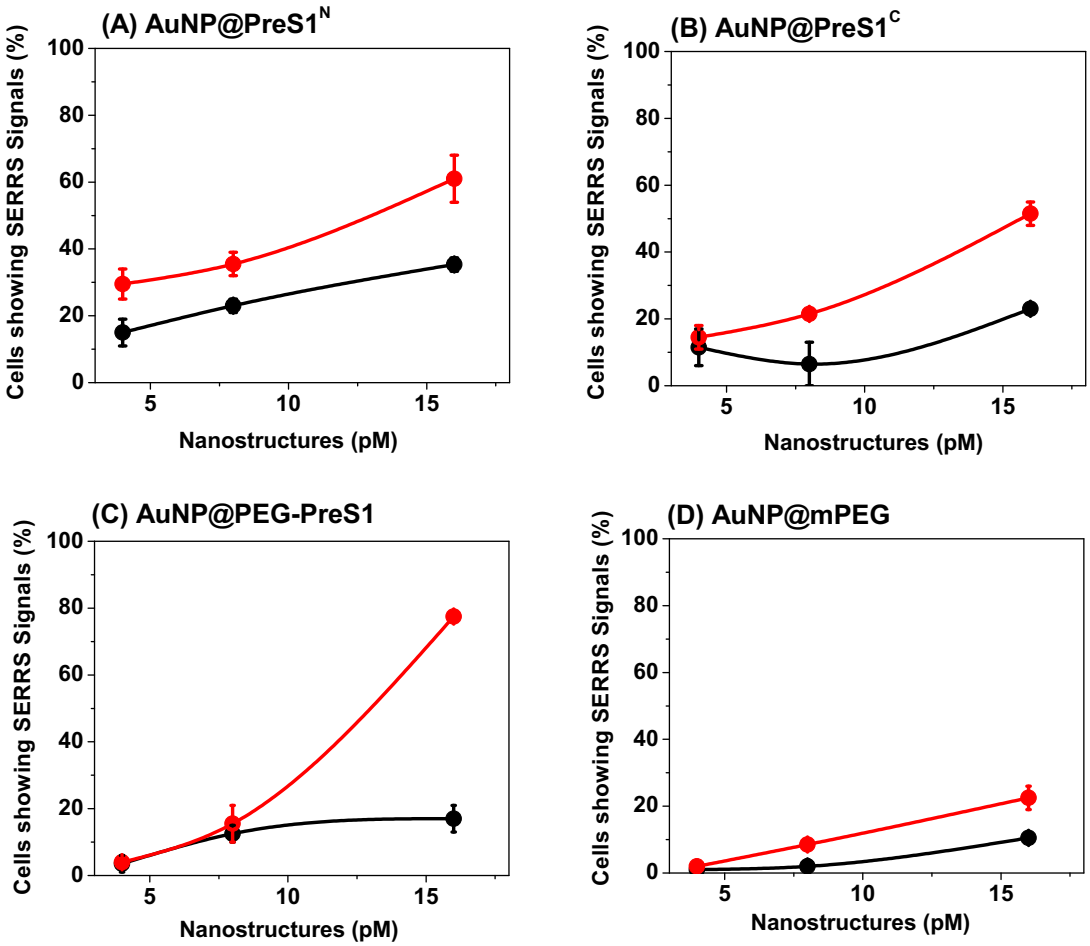

Figure 1. Targeting activity of the nanosystems (A-D) toward HepG2/CTR (black lines) or HepG2/SB3 (red lines). A cell is considered positive when it shows SERRS signals. 100 cells were considered for each measurement and error bars indicate variations of the results for three different selections of 100 cells within two or three preparations.

As already observed for nanostructures loaded with the peptide GE11 for the EGFR targeting (Chapter 3), the orientation of the peptide on the nanoparticles weakly affects the targeting activity. However, the nanostructures, in particular AuNP@PreS1^{N}, exhibited some nonspecific interactions with HepG2/CTR cells. AuNP@PEG-PreS1^{C} nanostructures showed a remarkably activity compared to nanosystems without PEG (AuNP@PreS1^{N} and AuNP@PreS1^{C}) binding up to 83% of HepG2/SB3 cells but only 17% of HepG2/CTR cells, as shown in Figure 2C. Moreover, the interaction with HepG2/CTR cells resulted comparable to that shown by AuNP@mPEG nanostructures, used as control. Considering that PreS1 is a hydrophilic peptide with a net negative charge at physiological pH, the good targeting activity is supposed to take advantage of a better presentation of the targeting motif on the nanosystems, that improves the association with the receptor, and the anti-fouling effect of the PEG coating, that enhances the selectivity of the targeting. This result confirmed similar and

as much interesting findings achieved for other targeting peptides (Chapters 3 and 4), namely that the properly designing of targeted nanostructures is crucial to obtain SERRS biosensors for detection and imaging of cancer cells.

In the perspective to test the AuNP@PEG-PreS1 nanostructures in vivo, really promising for the detection of liver cell carcinomatous transformation particularly in patients with chronic liver diseases, the stability in biological environments and the possible toxicity were evaluated. Proteolytic degradation is the major weakness limiting the widespread of peptide therapeutics for clinical use despite the several advantages offered with respect to antibodies or other targeting ligands [24]. Even if efficient targeting activity is achieved in vitro, in fact, many peptides do not circulate in blood for more than few minutes since they suffer from sensitivity to proteolytic enzymes and required to be stabilized against proteases [25,26]. The stability of PreS1 was evaluated incubating the peptide in 20% aqueous human serum and aliquots sampled at various time points were analysed by HPLC and ESI-MS to determine degradation patterns (Figure A7). The analyses showed that the predominant signal always corresponds to the intact peptide, proving that PreS1 is very stable in the presence of proteases. Moreover, the stability of PreS1 on the nanostructures is expected to be further enhanced because the presence of thousands of nearby peptides per nanoparticle contrasts the action of the enzymes [27].

The stability of the nanostructures in biological environments and their possible toxicity are other important issues for successful in vivo applications. The nanostructures stability was evaluated in human serum by monitoring Uv-vis-NIR and Raman spectra for 48 hours: no significant changes in the spectra were observed, demonstrating the nanostructures stability in the biological fluid (Figure A8). The cellular toxicity was investigated by xCELLigence real-time cell analysis, monitoring the cell growth curves upon incubation with increasing concentration of AuNP@PEG-PreS1 or AuNP@mPEG, as control. Figure 2 shows that no cytotoxicity was induced by the nanostructures.

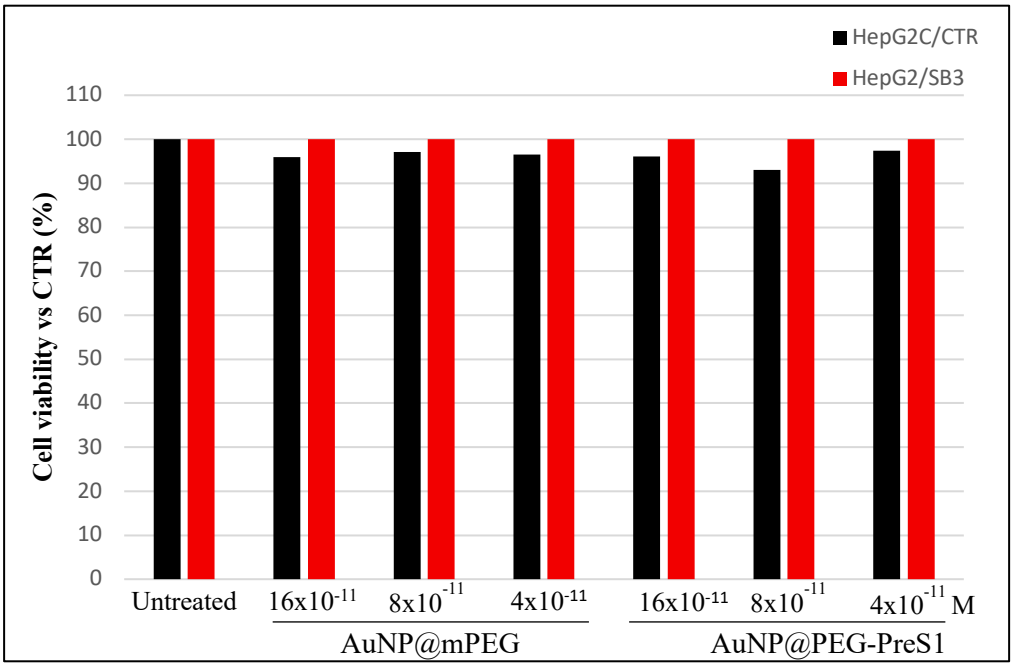

Figure 2. Cytotoxicity assay. Percentage of cell viability of HepG2/SB3 and HepG2/CTR treated for 2 hours with increasing concentration of AuNP@PEG-PreS1 and AuNP@mPEG, as control.

A more realistic evaluation of the stability in vivo of AuNP@PEG-PreS1 nanostructures was performed in animal models of adult C57BL/6J transgenic mice expressing the human SerpinB3 (TG-SB3) [28] and C57BL/6J mice not expressing SB3 (WT). Experiments were performed by injecting the nanostructures in the mice tail vein and harvesting known aliquots of lysates from different organs (liver, spleen, lung, brain and kidney) after 1, 3, 6 and 48 hours after the injection. Lysates were analysed to detect SERRS signals associated to the presence of nanostructures. Negligible SERRS signals were detected in all tested organs except in livers. As shown in Figure 3, targeted nanostructures gradually accumulated in the liver of TG-SB3 mice. The signals peaked after 3 hours and were completely cleared off six hours after injection. Their retarded accumulation in the liver can be interpreted as a consequence of the presence of low concentrations of the SB3 protein in other organs in addition to the liver of TG-SB3 mice [28]. Considering negligible SERRS signals detected in the liver of WT mice, these preliminary results proved that AuNP@PEG-PreS1 nanostructures target SB3 in vivo with high affinity. The low retention in healthy mice and fast clearance from the body, demonstrate they represent a promising tool for the early stage detection of HCC.

In conclusion in this chapter biocompatible SERRS nanosensors functionalized with the PreS1 peptide to detect the presence of the SB3 antigen overexpressed in liver tumor cells have been proposed. The peptide was rationally engineered and synthesized to obtain different arrangements of the targeting units in the nanosystem, which strongly influence the association with the receptor as already observed for other targeting moieties (Chapters 3 and 4). The best targeting activity in vitro

was found for nanostructures functionalized with the peptide PreS1 linked to a 3 kDa PEG chain. The biodistribution of the nanostructures in healthy mice and mice genetically modified to overexpress the SB3 antigen was also evaluated. The accumulation of nanosystems in the liver of transgenic mice demonstrated that these sensors represent an effective approach for the early stage detection of liver cancer diagnosis and imaging, which could improve the efficacy of therapeutic treatments and enhance the quality of life and overall survival of patients.

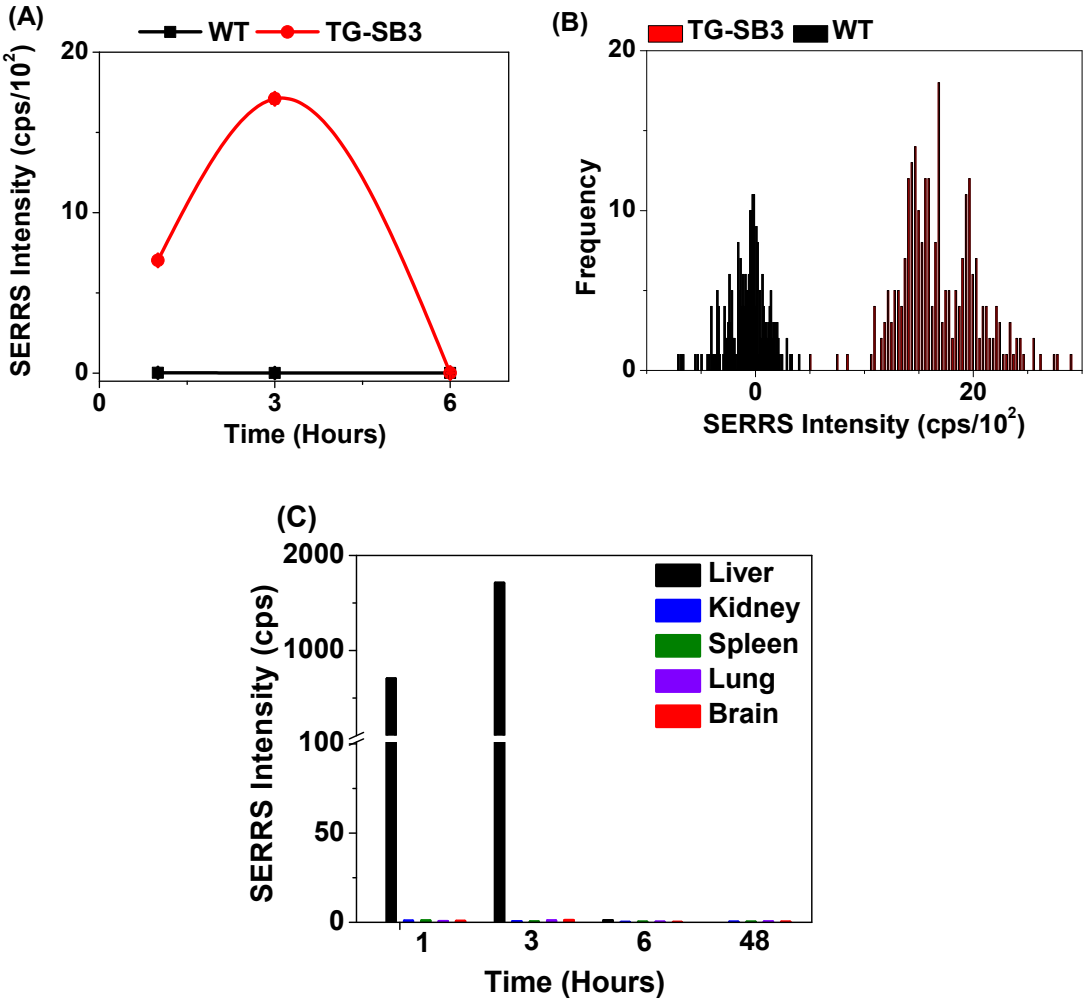

Figure 3. A) Variation of SERRS Intensity as a function of time in liver lysates of "TG-SB3" (Red line) or "WT" (Black Line) mice, after injection of AuNP@PEG-PreS1 nanostructures. SERRS intensity was monitored over a period of 48 hours. B) SERRS intensities (after baseline subtraction) of liver lysates three hours post injection, in different spots for "TG-SB3" mice (Red line) and "WT" (Black Line) mice. C) Variation of SERRS Intensity as a function of time over a period of 48 hours in organ lysates of SerpinB3 transgenic mice after injection of PreS1 functionalized nanostructures.

Experimental Section

Materials and Methods

Unless differently specified, all chemicals were commercial products and were used without further purification. 5(6)-Carboxyfluorescein, Fluorescein-5-maleimide, Bovin Serum Albumin (BSA), 9-Fluorenylmethoxycarbonyl (Fmoc)-amino acids and all other chemicals for the solid phase peptide synthesis were purchased from Sigma-Aldrich. Rink Amide MBHA resin (loading 0.52 mmol/g) and Rink Amide PEGA resin (loading 0.35 mmol/g) were provided by Iris Biotech GMBH. S-Trityl-thioPEG N-hydroxysuccinimide ester (TrtS-PEG-NHS MW ≅ 3000 Da from Rapp Polymer. Sulforhodamine 101-bis-cysteamide (TR) was prepared according to a previously published procedure [29]. Rabbit polyclonal antibody against recombinant SerpinB3 (Hepa-Ab) was purchased from Xeptagen while 488 AlexaFluor anti-rabbit secondary antibody and RNasy Trizol from Invitrogen. DAPI for cellular nuclei counterstaining and ELVANOL for slides mounting were provided by Sigma-Aldrich. Analytical HPLC separations were carried as described in Chapter 3. Except otherwise indicated, the elution condition was: isocratic 5% B for 3 min; linear gradient 5-65% B for 30 min. Semipreparative HPLC separations and mass spectral analyses operating with ESI or MALDI technique were performed as described in Chapter 3. UV-Vis-NIR and SERRS spectra were recorded in the same experimental condition described in Chapter 3 as well as DLS and ζ-potential measurements. TEM images were recorded at 100 kV with a FEI TECNAI G2 transmission electron microscope.

Synthesis of Peptides and Conjugates

General Method: PreS1 (PLGFFPDHQLDPAFGANSNNPDWDFNP) and its analogues were synthesized starting from Rink amide MBHA resin (0.04 mmoles) or Rink amide PEGA (0.03 mmoles) on an automated Advanced Chemtech 348 Ω peptide synthesizer. Fmoc-amino acids side chains were protected by the *tert*-butyl group (aspartic acid and serine), the *tert*-butyloxycarbonyl group (tryptophan) or the trityl group (asparagine, glutamine, histidine and cysteine). Except otherwise indicated, the procedures already reported in Chapter 3 was followed for peptides synthesis, deprotection and cleavage from the resin. An optimized protocol to minimize well-known side-reactions that could engage aspartic acid residues [30] was taken also into account. Peptides were purified by semi-preparative HPLC and characterized as shown in Table A1 and Figure A1.

Fluoresceinated peptides: PreS1 fluoresceinated at C-terminus (PreS1-Fluo) was prepared by reacting the cysteine thiol group in $PreS1^N$ (0.002 mmol) with fluorescein-5-maleimide (0.010 mmol) dissolved in 1 mL of DMF-10 mM phosphate buffer (50 : 50 v/v). The mixture was stirred at RT for

5 h under inert atmosphere and then the unreacted fluorescein-5-maleimide was quenched with an excess of cysteine. The crude peptide was purified by semi-preparative HPLC (isocratic 35% B for 5 min; linear gradient 35-60%B in 20 min) and characterized as reported in Table A1 and Figure A2. PreS1 fluoresceinated at N-terminus (Fluo-PreS1) was prepared by reacting the $PreS1^{C}$ peptide (0.011 mmol), still anchored to the solid support, with a DMF solution containing 5(6)-carboxyfluorescein, diisopropylcarbodiimide and HOBt (0.029 mmol each one) under shaking overnight. The fluoresceinated peptide was washed to remove unreacted reagents and then deprotected and cleaved from the resin as described in the General Procedure. Then it was purified by semi-preparative HPLC as described for PreS1-Fluo and characterized by analytical HPLC and ESI-MS (Table A1 and Figure A2).

PEG-PreS1 Conjugate: TrtS-PEG-NHS (0.014 mmol in 0.5 mL of DMF) was reacted with the amino terminal group of the PreS1 peptide still attached to the resin (0.007 mmoles) for 24 h at RT under stirring. After then, the solution containing the unreacted PEG was filtered off and the resin was repeatedly washed with DMF and DCM. Final deprotection and removal from the solid support were performed as described in the General Procedure. The conjugate was characterized by analytical HPLC and MALDI-TOF MS (Table A1 Figure A3)**.**

Plate Fluorimetric Assay

To estimate the PreS1 binding affinity to the target SB3 protein, flat-bottomed plates (Optiplate,Perkin Elmer) were coated with 8 µg/mL of SB3 or phosphate buffer pH 7.4, as control, and incubated overnight at 4 °C. After then, the plates were washed with PBS-Tween 0.05% for three times and the blocking buffer (10 mg/mL BSA) was added for 2h at RT. After washing, the fluoresceinated peptide (Fluo-PreS1 or PreS1-Fluo) or BSA was added to the wells at different dilutions (range 200-3.15 µg/mL) and incubated for 1 h at RT. Plates were washed and read in fluorescence mode on a plate reader (Ensight, Perkin Elmer) using 485 nm excitation filter and a 535 nm emission filter.

Surface Plasmon Resonance Analysis

A Biocore T 100 instrument (GE Healthcare, Uppsala,Sween) was used to measure molecular interactions between PreS1 and SB3. Recombinant SB3, produced by cloning human SB3 c-DNA in the directional expression vector pET101, was covalently linked to a Sensor Chip CM5 (carboxymethylated dextrane surface) by exploiting amine coupling chemistry [31]. SB3 (0.1 mg/mL) in 10 mM sodium acetate (pH.5) was immobilized on the activated chip surface at a flow rate of 10 µl/mL (720 sec. contact time) to obtain an immobilization level of "Final Response" of 15000

resonance units (RU). Solutions of PreS1 were injected over the surface at 25 °C at a flow rate of 10 µl/mL in HBS running buffer (10 mM Hepes pH 7.4, 150 mM NaCl, 3 mM EDTA, 0.005% P20 surfactant). Different concentrations of PreS1, ranging from 0 to 200 µM, were passed for 120 sec over sensor chip with immobilized SB3 to evaluate the stoichiometry of the SB3-PreS1 interaction. Surface regeneration was accomplished by injecting 1 M NaCl (30 sec contact time). All analyte solutions were run simultaneously over a control flow cell containing a blank surface, with no immobilized protein. SPR signal was normalized to the corresponding control flow cell at each time course. Interaction rate constant of PreS1 was calculated by using Biacore T100 evaluation software version 2.0.3 and expressed as mean for three separate experiments.

Preparation of SERRS targeted nanostructures

Synthesis of gold nanoparticles and functionalization with the SERRS reporter: Gold nanoparticles were synthesized by LASiS technology [18] as described in previous chapters. Aggregation and labelling with the thiol functionalized SERRS label, Sulforhodamine 101-bis-cysteamide (TR), was performed as described in Chapter 4. The extent of aggregation and the presence of the characteristic Raman signals were controlled by recording UV-Vis-NIR and Raman spectra of the colloidal solutions of the gold nanoaggregates (Figure A4).

Functionalization of Nanoaggregates with Peptide and PEG Ligands: 1 mL of the colloidal solution of gold nanoaggregates (4 nM) was centrifuged at 25000 g for 10 min and re-dispersed in a 20 µM solution of the peptide ligands in 1 ml of PBS. The mixture was gently shaken for 3 h at RT and stored overnight at 4 °C. The excess of ligands was discarded by centrifugation and the nanostructures were re-dispersed in 1 mL of PBS containing 5 mg of BSA as conditioning step prior to the incubation in biological media [29,32]. The average number of peptide ligands linked to each nanoparticle was estimated by measuring the absorbance at 280 nm of the peptide solution (ε_{PreS1} 5663 M^{-1} cm^{-1}) before and after the conjugation to the nanostructures and by performing the Ellman test for thiols (See Table 1). The UV-Vis-NIR spectra recorded at each steps of the preparation and the SERRS spectra of the final nanostructures are reported in Figure A4. The fully functionalized SERRS nanostructures were also characterized by DLS and ζ-potential measurements (See Table 1). Nanosystems coated only with PEG (AuNP@PEG) were prepared according to the procedure already described in Chapter 3. Characterizations are reported in Chapter 3.

Cell Lines and Receptor Expression Assay

HepG2 cell line (LGC Standards) was stably transfected with the plasmid vector pcDNA3.1 carrying the wild-type SerpinB3 gene (HepG2/SB3) or with the plasmid vector alone (HepG2/CTR), as

negative control, and used as target cells. The expression of the target SerpinB3 was analyzed at protein and mRNA level by immunofluorescence and real-time PCR before each individual experiment (Figure A5 as an example).

Immunofluorescence: Cells were seeded on slides (5000 cells/well, in a 12 wells plate) and cultured overnight. Then, cells were fixed in 4% paraformaldehyde, permeabilized with 0.2% Triton X 100 and blocked with 5% Goat serum in 1% BSA in PBS. Slides were incubated with 8 µg/mL of a rabbit polyclonal antibody against recombinant SerpinB3 (Hepa-Ab, Xeptagen), washed with 0.1% Tween 20 in PBS and incubated with 488 Alexa Fluor anti-rabbit secondary antibody (1:500 dilution). Cellular nuclei were counterstained with DAPI and sides were mounted with ELVANOL and analyzed by using the optical sectioning of Apotome.2 of a fluorescence microscope (Axiovert 200M, Carl Zeiss MicroImaging GmbH).

Quantitative real-time RT-PCR: The levels of SerpinB3 mRNA were measured in cultured cells by real-time PCR using the SYBR® green method. Total RNA was extracted using RNasy Trizol according to the manufacturer's instructions and its purity and integrity was determinated. Complementary DNA synthesis and quantitative real-time PCR reactions (RT-PCR) were carried out as described in a previously published procedure [33] by using the CFX96 Real-Time instrument (Bio-Rad Laboratories Inc). The relative gene expression was generated for each sample by calculating $2^{-\Delta Ct}$ [34]. The designed oligonucleotide sequences of the primers were the following: sense 5'-GCA AAT GCT CCA GAA GAA AG-3, reverse 5'-CGA GGC AAA ATGAAAA AGA TG-3'. Glyceraldehyde-3-phosphate dehydrogenase (GAPDH) was used as internal reference and co-amplified with target samples using identical real-time PCR conditions.

Cell Culture and SERRS Measurements

Cells were incubated the day after seeding with 160, 80 and 40 pM nanoparticles in culture medium for 2 h at 37 °C. Then the slides were washed twice with PBS, fixed with 4% PFA and washed three times with distilled water to remove unbound nanoparticles before SERRS measurements. Both SERRS measurements and analysis of the dataset were carried out using the procedures described in Chapter 3.

Serum stability of the targeting peptide and nanostructures

The stability of the PreS1 peptide in serum was evaluated according to literature [35]. In brief, 1 mg of the peptide PreS1 was dissolved in 1 ml of 20% aqueous human serum and incubated at 37 °C for 24 h. After 0, 10 min, 30 min, 1 h, 2 h, 6 h and 24 h of incubation, samples of 100 µl were withdrawn and serum proteins were precipitated by adding 200 µl of 15% aqueous trichloroacetic acid. The samples were centrifuged at 25000 g for 10 min and the supernatants were immediately cooled down

on ice. 200 µl of each supernatant were analysed by HPLC and ESI-MS to identify potential digestion products (Figure A7).

The stability of AuNP@PEG-PreS1 was determined by centrifuging the nanostructures at 25000 g for 10 min, redispersing in 1 mL of 100 % human serum and incubating over a period of 48 h at 37 ° C under gentle shaking. After 0, 2 h, 24 h and 48 h of incubation, Uv-vis-NIR spectra and SERRS spectra were registered to monitor possible aggregation/disaggregation phenomena and to evaluate the stability of the signal associated to the presence of the SERRS label, respectively (Figure A8).

Cytotoxicity assay

The nanostructures cytotoxicity at the experimental dose-range was analysed by xCELLigence real-time cell analysis (RTCA) (ACEA). Cells were seeded at (20000 cells/well) onto the appropriate E-plates and the day after were treated with 160, 80 and 40 pM solutions of nanoparticles in culture medium for 2 h. The response profiles were followed over time and, as show in Figure 3, revealed none toxicity effect for the whole time of treatment.

In vivo experiments

In vivo studies were carried out in adult males C57BL/6J mice, aged 12-14 weeks with a weight range of 25-30 g and transgenic for human SerpinB3 (TG-SB3) with the insert located under the α1-antitripsin promoter [28]. Mice were maintained under a 12 h light/dark cycle at 22 ° C± 3 °C and bred at the Animal Care Facility of the Experimental Surgery Division of the University of Padua. After 1h, 3h, 6h and 48 h after tail vein injection with 200 µl of a 10 nM AuNP@PEG-PreS1 solution in PBS, the animals were sacrificed. The experimental protocol was approved by the Animal Investigation Committee of the Italian Ministry of Health with the accreditation number 667/2016-PR. All measures were taken to minimize any pain or discomfort for the animals and conducted in accordance with the European guidelines.

Preparation of organ extracts and SERRS Measurements. Specimens of liver, lung, kidney, spleen and brain were processed by placing 30 mg of frozen samples in a tube containing ceramic beads of 1.4 mm mean diameter (MagNA Lyser Green Beads, Roche) and 1 mL of 1X RIPA lysis buffer was added (20 mM Tris-HCl pH 7.5; 150 mM NaCl; 1 mM Na_2EDTA; 1 mM EGTA; 1% NP-40; 1% sodium deoxycholate; 2.5 mM sodium pyrophosphate; 1 mM b-glycerophosphate; 1 mM Na_3VO_4; 1 µg/mL leupeptin). The samples were homogenized by using the MagNA Lyser Instrument (Roche) at RT 2 minutes at 6000 g. Lysates of excised organs were homogenously spread on a well and, to reveal the presence of the nanostructures, the SERRS spectra were recorded with a Raman point mapping method. The samples were mapped along the x and y axes in 0.4-µm steps totaling 55 µm.

The dataset, consisting on each spectrum recorded for the Raman map, was analysed following the procedure already described for the statistical analysis of SERRS measurements of cells in Chapter 3. Data are reported in Figure 4 as the characteristic SERRS signals at 1505 cm^{-1} of the Raman reporter averaged over the whole sample area of each lysate at the indicated time points.

Appendix

(a) PreS1^{N} (PLGFFPDHQLDPAFGANSNNPDWDFNPC-NH_2)

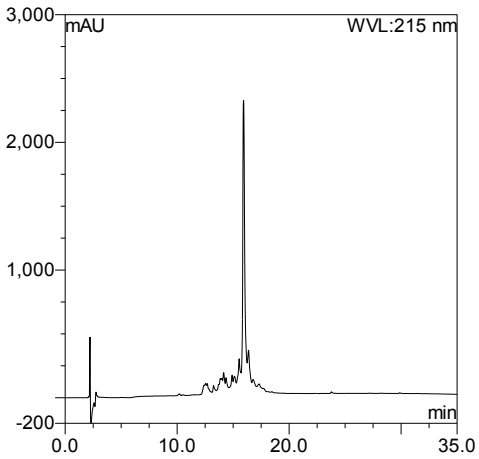

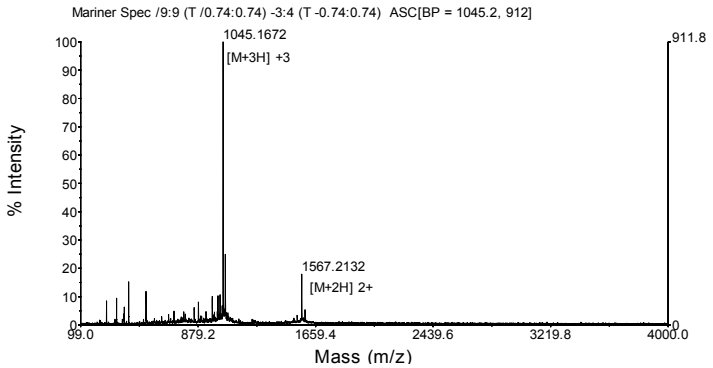

(b) PreS1^{C} (CPLGFFPDHQLDPAFGANSNNPDWDFNP-NH_2)

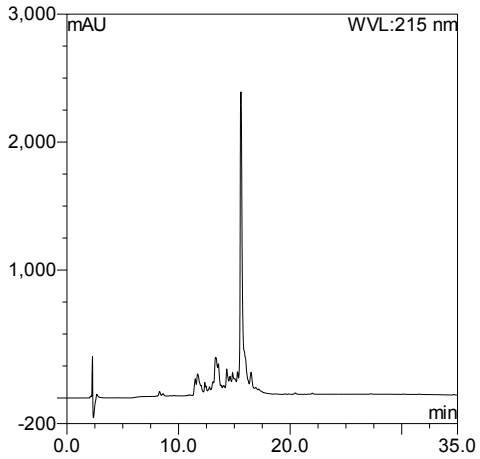

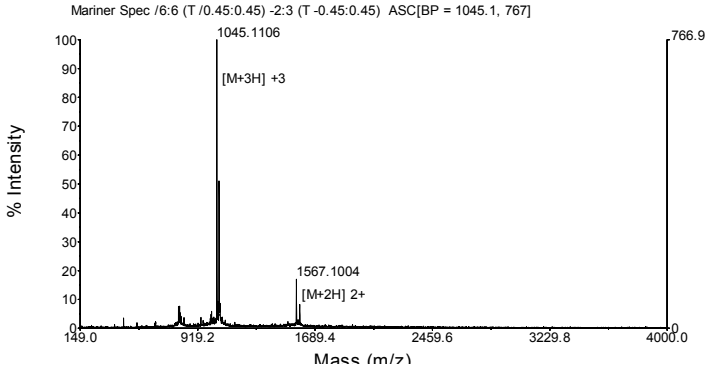

(c) PreS1 (PLGFFPDHQLDPAFGANSNNPDWDFNP-NH_2)

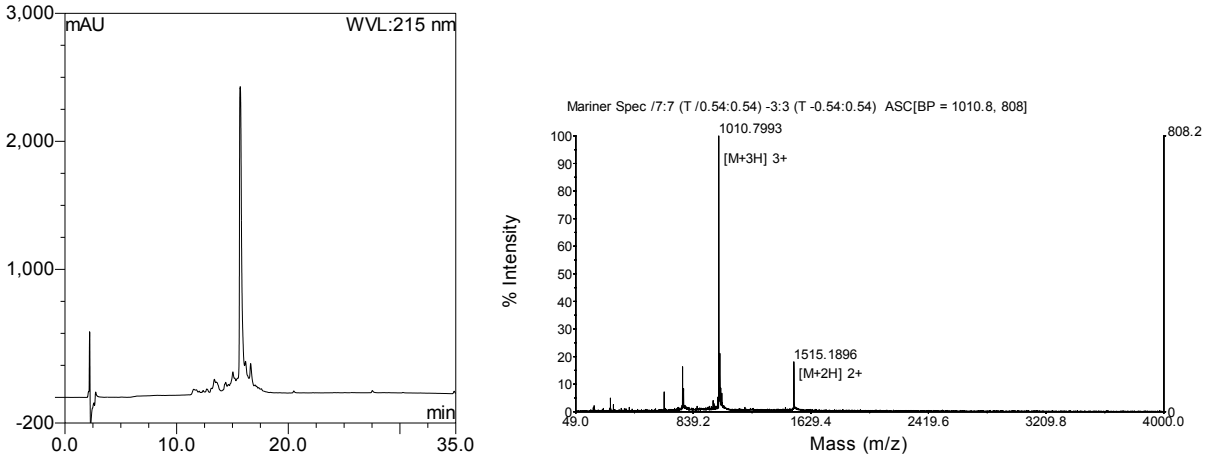

Figure A1. Analytical HPLC and ESI-MS spectra of peptides: (a) $PreS1^N$ (b) $PreS1^C$ (c) PreS1. Analytical HPLC separations were performed on a Vydac 218TP54 column (250 x 4.6 mm, 5 µm, flow rate at 1.5 ml/min). The elution condition was: isocratic 10% B for 3 min; linear gradient 10-90% B for 30 min. For preparing binary gradients the mobile phase A (aqueous 0.1% Trifluoroacetic acid (TFA)) and B (90% aqueous acetonitrile containing 0.1%TFA) were used. Mass spectral analyses were carried out on a Mariner API-TOF workstation operating in a positive mode with the ESI technique.

(a) PreS1-Fluo (PLGFFPDHQLDPAFGANSNNPDWDFNPC(Fluo)-NH_2)

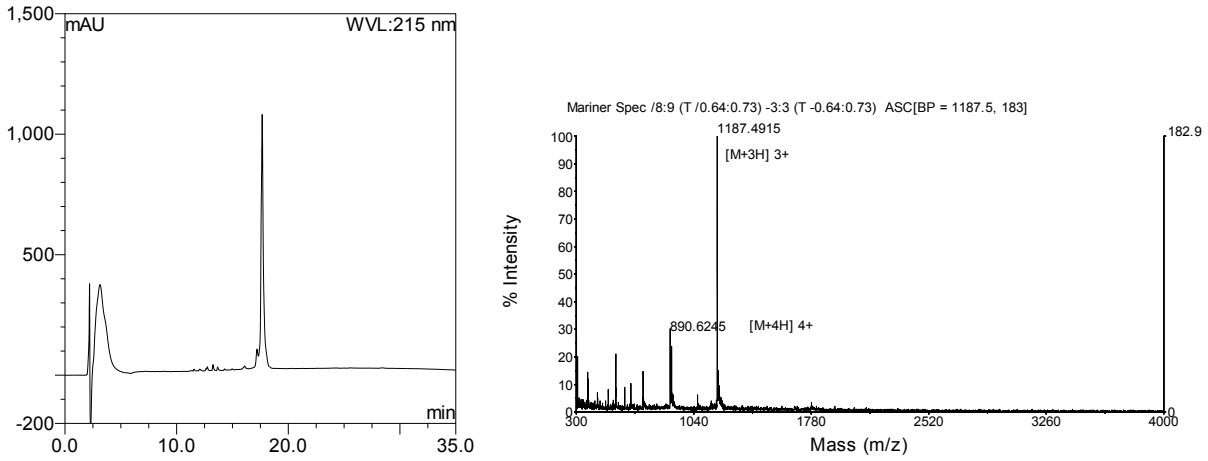

(b) Fluo-PreS1 (Fluo-PLGFFPDHQLDPAFGANSNNPDWDFNP-NH_2)

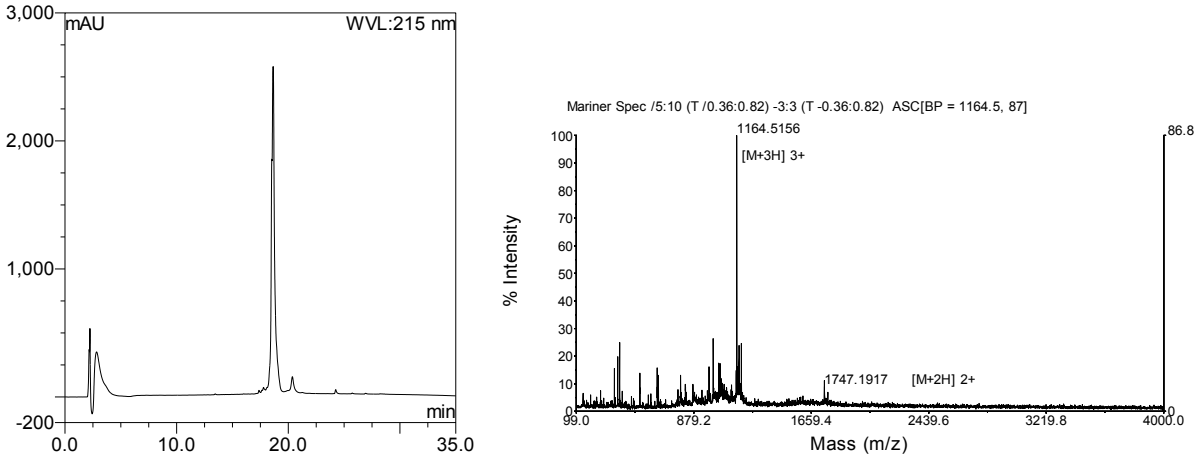

Figure A2. Analytical HPLC and ESI-MS spectra of fluoresceinated peptides: (a) PreS1-Fluo (b) Fluo-PreS1. Analytical HPLC separations and mass spectral analyses were carried out in the same conditions described in Figure A1.

PEG-PreS1 (HS-PEG- PLGFFPDHQLDPAFGANSNNPDWDFNP-NH_2)

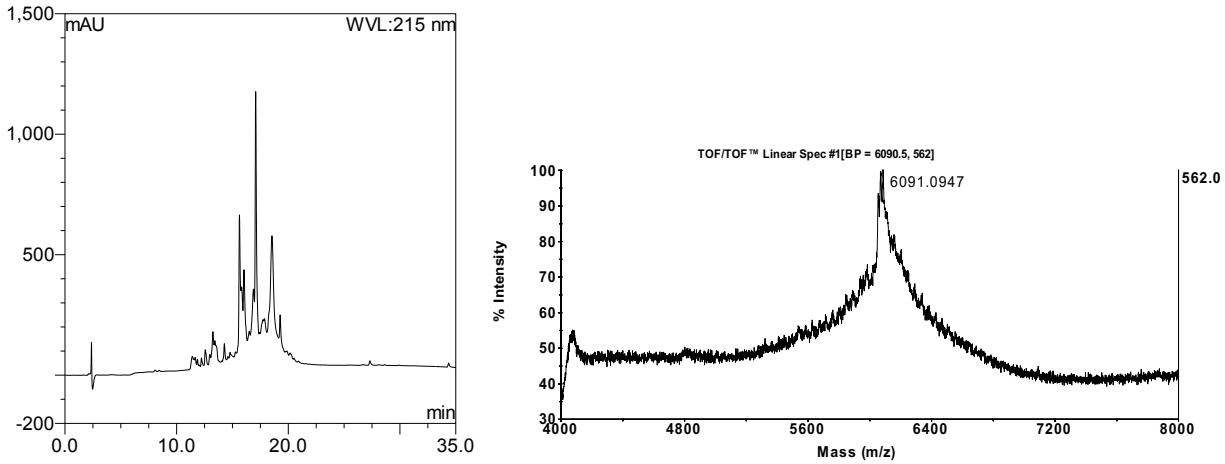

Figure A3. Analytical HPLC and MALDI TOF-TOF spectra of PEG-PreS1 conjugate. Analytical HPLC separations were carried out in the same conditions described in Figure A1. Mass spectral analyses were performed on a MALDI TOF/TOF Analyser, operating in positive mode in the linear mid-mass range (2,5-dihydroxybenzoic acid as matrix).

Table A1. Analytical data of the synthesized ligands.

Peptide	Sequence [a]	Yield %	HPLC[b] t_R (min)	Expected Mass $[M+H]^+$	Found Mass[b] m/z
$PreS1^C$	CPLGFFPDHQLDPAFGANSNNPD WDFNP-NH_2	77	15.6	3131.4	1566.7$[M+2H]^{+2}$ 1044.8 $[M+3H]^{+3}$
$PreS1^N$	PLGFFPDHQLDPAFGANSNNPD WDFNPC-NH_2	100	15.9	3131.4	1566.7$[M+2H]^{+2}$ 1044.5 $[M+3H]^{+3}$
PreS1	PLGFFPDHQLDPAFGANSNNPD WDFNP-NH_2	41	15.7	3028.4	1515.2$[M+2H]^{+2}$, 1010.5$[M+3H]^{+3}$
PreS1-Fluo	PLGFFPDHQLDPAFGANSNNPD WDFNPC(Fluo)-NH2	70	17.7	3558.8	1187.1$[M+3H]^{+3}$ 890.6$[M+4H]^{+4}$
Fluo-PreS1	Fluo-PLGFFPDHQLDPAFGANSNNPD WDFNP-NH_2	77	18.6	3489.7	1745.7$[M+2H]^{+2}$ 1164.2$[M+3H]^{+3}$
PEG-PreS1	HS-PEG_{3000}-PLGFFPDHQLDPAFGANSNNPD WDFNP-NH_2	40	16.2	6028.4	6091.1$[M+H]^{+1}$

[a] Abbreviations: Amino acids are represented by one letter symbol and Fluo is 5(6)-carboxyfluorescein

[b] For Analytical HPLC and MS spectra see Figures A1-A3.

(a) AuNP@PreS1^{N}

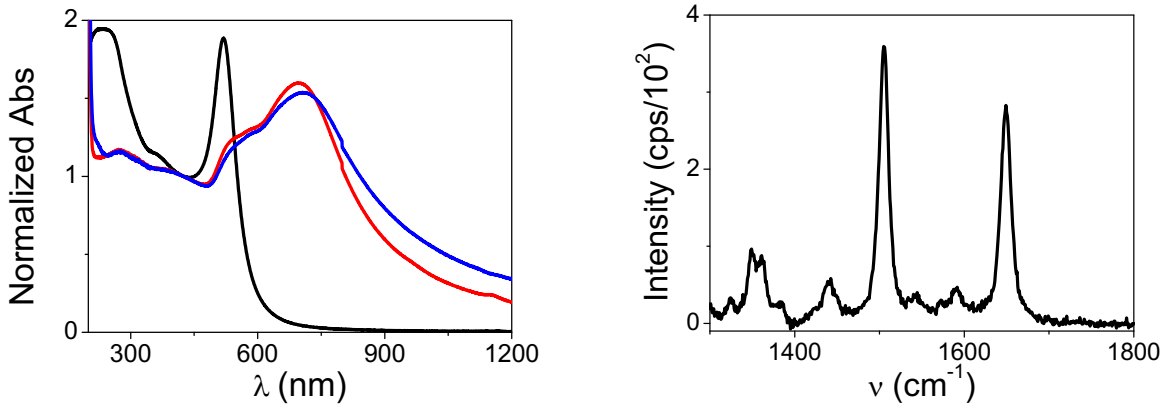

(b) AuNP@PreS1^{C}

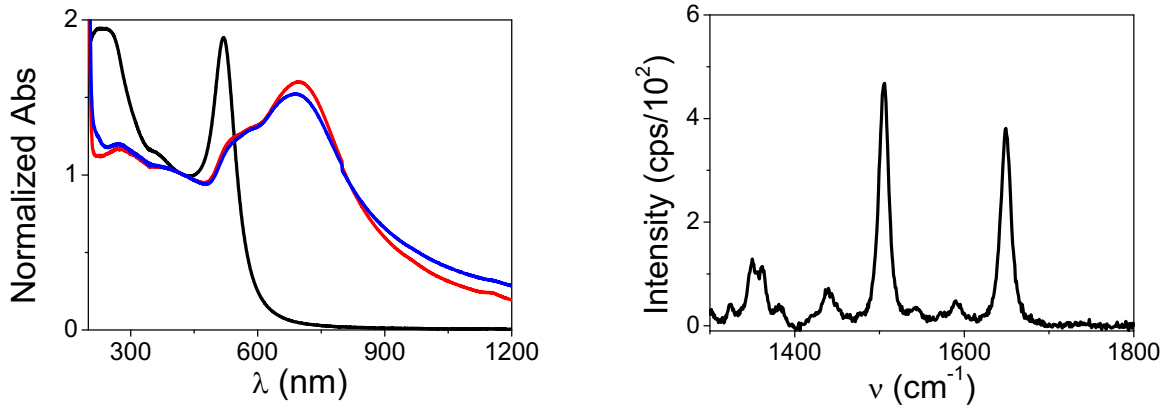

(c) AuNP@PEG-PreS1

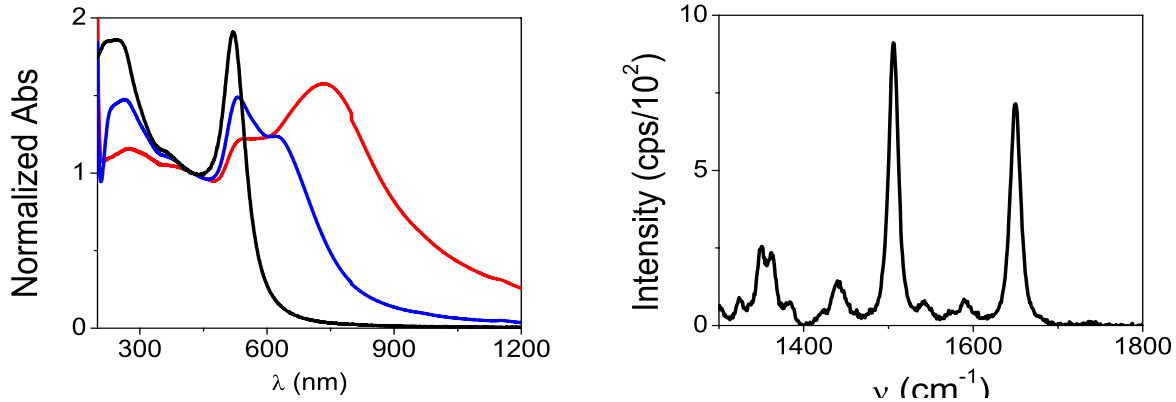

Figure A4. On the left, evolution of the extinction spectra during the assembling steps of the nanostructures: Laser Ablation in Solution of gold nanoparticles (black line), aggregation and labelling with the SERRS reporter (red line) and conjugation of peptide ligands (blue line). On the right, SERRS spectra of the final nanostructures (a) AuNP@PreS1^{N} (b) AuNP@PreS1^{C} (c) AuNP@PEG-PreS1.

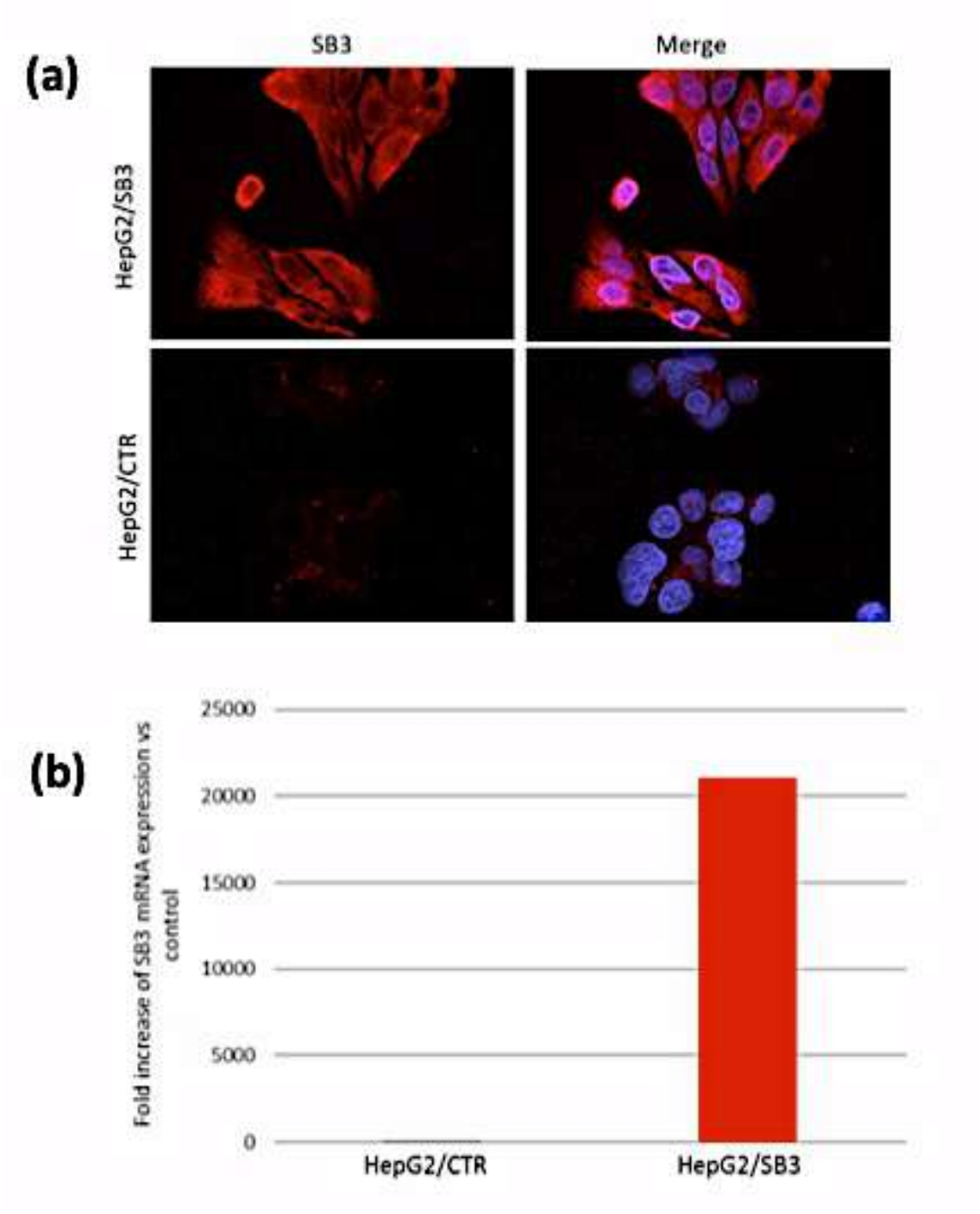

Figure A5 a**)** Immunofluorescence analysis of SB3 expression (63x objective). The cells were immunostained with anti-SB3 antibody and the nuclei were counterstained with DAPI. Images were obtained by fluorescence microscopy Axiovert 200 after optical sectioning with Apotome 2 (Zeiss). b) SB3 mRNA expression. Analysis of SB3 transcripts in HepG2/SB3 transfected cells and in HepG2/CTR cells by quantitative real-time PCR (Q-PCR).

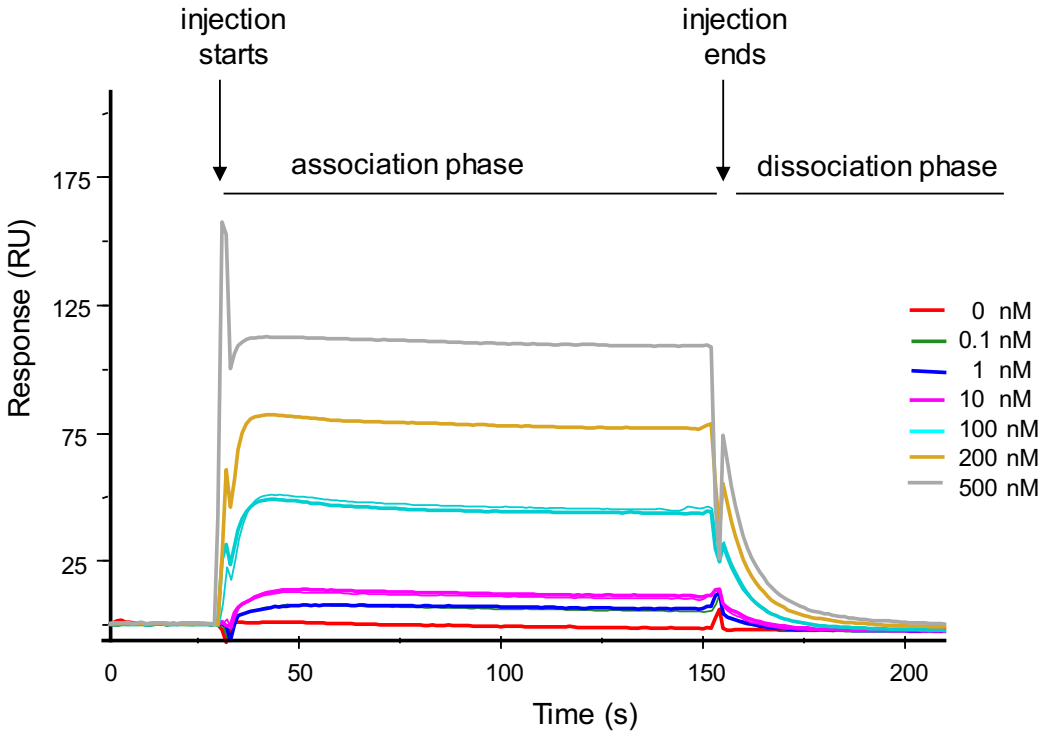

Figure A6. SPR analysis of the interaction between SB3 and PreS1 peptide. SB3 was immobilized on the chip surface while PreS1 peptide was injected in the solution and flowed over the surface at different nM concentrations. Representative sensorgrams (colored lines) are shown after subtraction of the signal obtained on a control surface. Abbreviation: RU, resonance units.

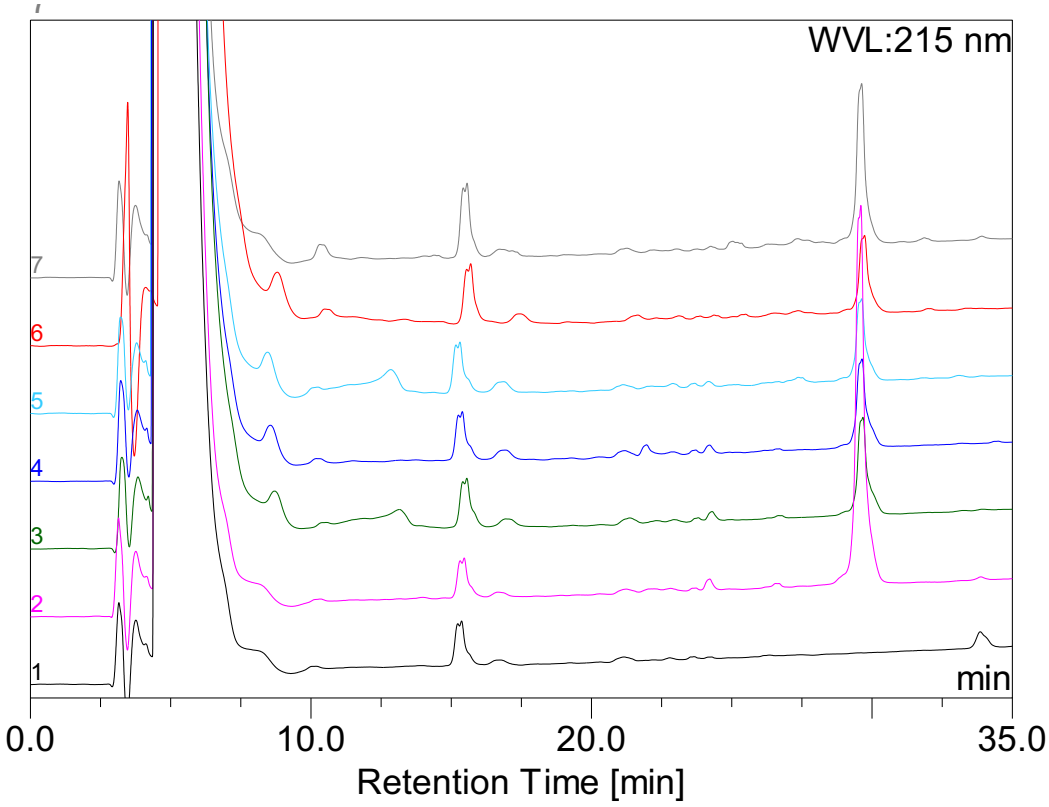

Figure A7. Analytical HPLC of aliquots of the peptide PreS1 ^{C} taken up after 0 (magenta line), 10 min (green line), 30 min (blue line), 2h (pale blue line), 6 h (red line) and 24 hours (grey line) of incubation in 20% aqueous human serum. As reference 20% aqueous human serum (black line). Analytical HPLC separations were performed on a Vydac 218TP54 column (250 x 4.6 mm, 5 µm, flow rate at 1.5 ml/min). The elution condition was: isocratic 5% B for 3 min; linear gradient 5-50% B for 30 min. For preparing binary gradients the mobile phase A (aqueous 0.1% Trifluoroacetic acid (TFA)) and B (90% aqueous acetonitrile containing 0.1%TFA) were used.

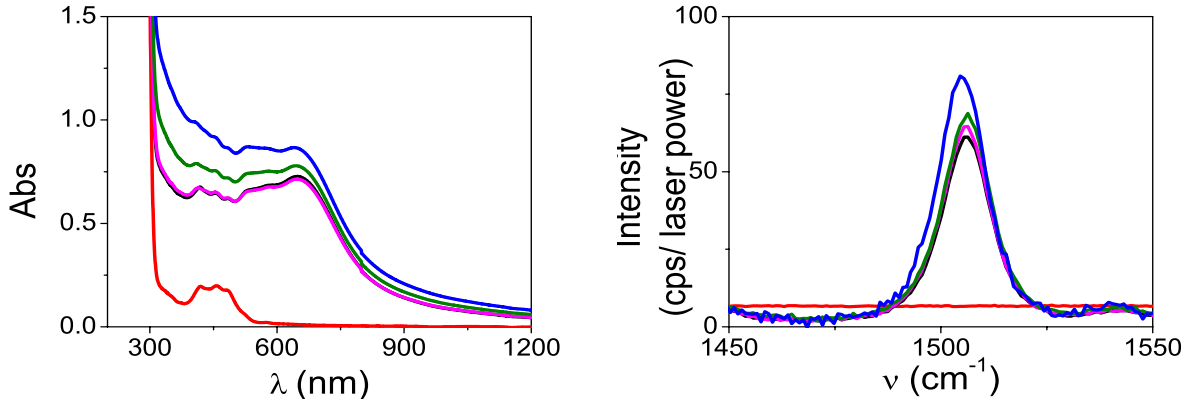

Figure A8. On the right, zoom of the spectral fingerprint of the SERRS reporter and, on the left, evolution of the extinction spectra of the nanostructure AuNP@PEG-PreS1 in incubation with serum over a period of: 2h (magenta line), 24h (green line) and 48 h (blue line). As reference human serum (red line) and AuNP@PEG-PreS1 (black line) in PBS.

References

1. Guido, M., Roskam, T., Pontisso, P., Fassan, M., Thung, S. N., Giacomelli, L., Sergio, A., Farinati, F., Cillo, U., Rugge, M., Squamous cell carcinoma antigen in human liver carcinogenesis. *J. Clin. Pathol.* **2008**. 61 (4), pp 445-447.

2. Dash, S., Rao, K. V. N., Panda, S. K., Receptor for Pre-S1(21-47) component of hepatitis-B on the liver-cell-role in virus-cell interaction. *J. Med. Virol.* **1992**. 37 (2), pp 116-121.

3. Deng, Q., Zhai, Q., Michel, M. L., Zhang, J., Qin, J., Kong, J. J., Zhang, X. X., Budkowska, A., Tiollais, P., Wang, Y., Xie, Y. H., Identification and characterisation of peptides that interact with hepatitis B virus via the putative receptor binding site. *J. Virol.* **2007**. 81, pp 4244–54.

4. Huang, Y. H., Li, X., Yi, M., Zhu, S., Chen, W., Targeted delivery of siRNA against hepatitis B virus by pres1 peptide molecular ligand. *Hepatology Research.* **2014**. 44, pp 897–906.

5. Jha, S., Ramadori, F., Quarta, S., Biasiolo, A., Fabris, E., Baldan, P., Guarino, G., Ruvoletto, M., Villano, G., Turato, C., Gatta, A., Mancin, F., Pontisso, P., Scrimin, P., Binding and uptake into human hepatocellular carcinoma cells of peptide-functionalized gold nanoparticles. *Bioconjugate Chem.* **2017**. 28, pp 222-229.

6. Murata, M., Narahara, S., Umezaki, K., Toita, R., Tabata, S., Piao, J. S., Abe, K., Kang, J. H., Ohuchida, K., Cui, L., Hashizume, M., Liver cell specific targeting by the pres1 domain of hepatitis B virus surface antigen displayed on protein nanocages. *International Journal of Nanomedicine.* **2012**. 7, pp 4353-4363.

7. Zhang, Q., Zhang, X., Chen, T., Wang, X., Fu, Y., Jin, Y., Sun, X., Gong, T., Zhang, Z., A safe and efficient hepatocyte-selective carrier system based on myristoylated preS1/21-47 domain of hepatitis B virus. *Nanoscale.* **2015**. 7, pp 9298–9310.

8. Balasso, A., Salmaso, S., Pontisso, P., Rosato, A., Quarta, S., Malfanti, A., Mastrotto, F., Caliceti, P., Re-programming pullulan for targeting and controlled release of doxorubicin to the hepatocellular carcinoma cells. *European Journal of Pharmaceutical Sciences.* **2017**. 103, pp 104–115.

9. Roberts, L. R., Sirlin, C. B., Zaiem, F., Almasri, J., Prokop, L. J., Heimbach, J. K., Murad, M. H., Mohammed, K., Imaging for the diagnosis of hepatocellular carcinoma: A systematic review and meta-analysis. *Hepatology.* **2018**. 67 (1), pp 401-421.

10. Fabris, L., Gold-based SERS tags for biomedical imaging. *Journal of Optics.* **2015**. 17 (11), pp 114002-114016.

11. Zavaleta, C. L., Kircher, M. F., Gambhir, S. S., Raman's "Effect" on Molecular Imaging. *Journal of Nuclear Medicine.* **2011**. 52 (12), pp 1839-1844.

12. Wang, L., Guo, T., Lu, Q., Yan, X. L., Zhong, D. X., Zhang, Z. P., Ni, Y. F., Han, Y., Cui, D. X., Li, X. F., Huang, L. J., Sea-Urchin-Like Au Nanocluster with Surface-Enhanced Raman Scattering in Detecting Epidermal Growth Factor Receptor (EGFR) Mutation Status of Malignant Pleural Effusion. *Acs Applied Materials & Interfaces.* **2015**. 7 (1), pp 359-369.
13. Liu, M. H., Zheng, C. H., Cui, M. L., Zhang, X. Y., Yang, D. P., Wang, X. S., Cui, D. X., Graphene oxide wrapped with gold nanorods as a tag in a SERS based immunoassay for the hepatitis B surface antigen. *Microchimica Acta.* **2018**. 185 (10), pp 458-465.
14. Chen, Y. S., Cheng, S. L., Zhang, A., Song, J., Chang, J., Wang, K., Gao, G., Zhang, Y. X., Li, S. J., Liu, H. M., Alfranca, G., Aslam, M. A., Chu, B. F., Wang, C., Pan, F., Ma, L. J., de la Fuente, J. M., Ni, J., Cui, D. X., Salivary Analysis Based on Surface Enhanced Raman Scattering Sensors Distinguishes Early and Advanced Gastric Cancer Patients from Healthy Persons. *Journal of Biomedical Nanotechnology.* **2018**. 14 (10), pp 1773-1784.
15. Tian, F. R., Conde, J., Bao, C. C., Chen, Y. S., Curtin, J., Cui, D. X., Gold nanostars for efficient in vitro and in vivo real-time SERS detection and drug delivery via plasmonic-tunable Raman/FTIR imaging. *Biomaterials.* **2016**. 106, pp 87-97.
16. Chen, Y. S., Zhang, Y. X., Pan, F., Liu, J., Wang, K., Zhang, C. L., Cheng, S. L., Lu, L. G., Zhang, W., Zhang, Z., Zhi, X., Zhang, Q., Alfranca, G., de la Fuente, J. M., Chen, D., Cui, D. X., Breath Analysis Based on Surface-Enhanced Raman Scattering Sensors Distinguishes Early and Advanced Gastric Cancer Patients from Healthy Persons. *Acs Nano.* **2016**. 10 (9), pp 8169-8179.
17. Biscaglia, F., Quarta, S., Villano, G., Turato, C., Biasiolo, A., Litti, L., Ruzzene, M., Meneghetti, M., Pontisso, P., Gobbo, M., PreS1 peptide-functionalized gold nanostructures with SERRS tags for efficient liver cancer cell targeting. *Materials Science & Engineering C-Materials for Biological Applications.* **2019**. 103.
18. Amendola, V., Meneghetti, M., Controlled size manipulation of free gold nanoparticles by laser irradiation and their facile bioconjugation. *Journal of Materials Chemistry.* **2007**. 17 (44), pp 4705-4710.
19. De Falco, S., Ruvoletto, M. G., Verdoliva, A., Ruvo, M., Raucci, A., Marino, M., Senatore, S., Cassani, G., Alberti, A., Pontisso, P., Fassina, G., Cloning and expression of a novel hepatitis B virus-binding protein from HepG2 cells. *Journal of Biological Chemistry.* **2001**. 276 (39), pp 36613-36623.
20. Blanco, E., Shen, H., Ferrari, M., Principles of nanoparticle design for overcoming biological barriers to drug delivery. *Nature Biotechnology.* **2015**. 33 (9), pp 941-951.
21. Grunwald, J., Rejtar, T., Sawant, R., Wang, Z. X., Torchilin, V. P., TAT Peptide and Its Conjugates: Proteolytic Stability. *Bioconjugate Chemistry.* **2009**. 20 (8), pp 1531-1537.

22. Tassa, C., Duffner, J. L., Lewis, T. A., Weissleder, R., Schreiber, S. L., Koehler, A. N., Shaw, S. Y., Binding Affinity and Kinetic Analysis of Targeted Small Molecule-Modified Nanoparticles. *Bioconjugate Chemistry.* **2010**. 21 (1), pp 14-19.

23. Fasting, C., Schalley, C. A., Weber, M., Seitz, O., Hecht, S., Koksch, B., Dernedde, J., Graf, C., Knapp, E. W., Haag, R., Multivalency as a Chemical Organization and Action Principle. *Angewandte Chemie-International Edition.* **2012**. 51 (42), pp 10472-10498.

24. Fosgerau, K., Hoffmann, T., Peptide therapeutics: current status and future directions. *Drug Discovery Today.* **2015**. 20 (1), pp 122-128.

25. Ngambenjawong, C., Gustafson, H. H., Pineda, J. M., Kacherovsky, N. A., Cieslewicz, M., Pun, S. H., Serum Stability and Affinity Optimization of an M2 Macrophage-Targeting Peptide (M2pep). *Theranostics.* **2016**. 6 (9), pp 1403-1414.

26. Ngambenjawong, C., Pun, S. H., Multivalent Polymers Displaying M2 Macrophage-Targeting Peptides Improve Target Binding Avidity and Serum Stability. *Acs Biomaterials Science & Engineering.* **2017**. 3 (9), pp 2050-2053.

27. Acar, H., Ting, J. M., Srivastava, S., LaBelle, J. L., Tirrell, M. V., Molecular engineering solutions for therapeutic peptide delivery. *Chemical Society Reviews.* **2017**. 46 (21), pp 6553-6569.

28. Villano, G., Quarta, S., Ruvoletto, M. G., Turato, C., Vidalino, L., Biasiolo, A., Tono, N., Lunardi, F., Calabrese, F., Dall'olmo, L., Dedja, A., Fassina, G., Gatta, A., Pontisso, P., Role of squamous cell carcinoma antigen-1 on liver cells after partial hepatectomy in transgenic mice. *International Journal of Molecular Medicine.* **2010**. 25 (1), pp 137-143.

29. Meneghetti, M., Scarsi, A., Litti, L., Marcolongo, G., Amendola, V., Gobbo, M., Di Chio, M., Boscaini, A., Fracasso, G., Colombatti, M., Plasmonic Nanostructures for SERRS Multiplexed Identification of Tumor-Associated Antigens. *Small.* **2012**. 8 (24), pp 3733-3738.

30. Subiros-Funosas, R., El-Faham, A., Albericio, F., Aspartimide formation in peptide chemistry: occurrence, prevention strategies and the role of N-hydroxylamines. *Tetrahedron.* **2011**. 67 (45), pp 8595-8606.

31. Ruzzene, M., Brunati, A. M., Sarno, S., Donella-Deana, A., Pinna, L. A., Hematopoietic lineage cell specific protein 1 associates with and down-regulates protein kinase CK2. *Febs Letters.* **1999**. 461 (1-2), pp 32-36.

32. Chanana, M., Gil, P. R., Correa-Duarte, M. A., Liz-Marzan, L. M., Parak, W. J., Physicochemical Properties of Protein-Coated Gold Nanoparticles in Biological Fluids and Cells before and after Proteolytic Digestion. *Angewandte Chemie-International Edition.* **2013**. 52 (15), pp 4179-4183.

33. Turato, C., Vitale, A., Fasolato, S., Ruvoletto, M., Terrin, L., Quarta, S., Morales, R. R., Biasiolo, A., Zanus, G., Zali, N., Tan, P. S., Hoshida, Y., Gatta, A., Cillo, U., Pontisso, P., SERPINB3 is

associated with TGF-beta 1 and cytoplasmic beta-catenin expression in hepatocellular carcinomas with poor prognosis. *British Journal of Cancer.* **2014**. 110 (11), pp 2708-2715.

34. Livak, K. J., Schmittgen, T. D., Analysis of relative gene expression data using real-time quantitative PCR and the 2(T)(-Delta Delta C) method. *Methods.* **2001**. 25 (4), pp 402-408.

35. Cudic, M., Condie, B. A., Weiner, D. J., Lysenko, E. S., Xiang, Z. Q., Insug, O., Bulet, P., Otvos, L., Development of novel antibacterial peptides that kill resistant isolates. *Peptides.* **2002**. 23 (12), pp 2071-2083.

Conclusions

In the wide panorama of cancer research, nanomaterials are emerging as promising tools for overcoming common difficulties of traditional medicine. Some are already commercially available and used in the clinical settings. Novel nanomaterials continue to be synthesized, like in the present Ph.D. thesis, and they show great promises. A challenging gap between the preclinical development and the regulatory requirements slows down many times their clinical use, but their importance will certainly emerge in the near future.

In this Ph.D. thesis an overview of nanomaterials was given in the introduction. A particular attention was payed to gold nanoparticles since, due to their useful optical properties and recognized biocompatibility, their application in cancer nanotechnology has raised steadily in the recent past.

In the following chapters successful protocols for assembling gold nanostructures that find application in cancer nanomedicine, as Surface-Enhanced Raman Resonance Scattering (SERRS) biosensors for colorectal and liver cancer diagnostics, are presented. The SERRS detection approach offers many advantages over other more common techniques, as fluorescence, providing narrow signals, that allow easy multiplexing measurements. Moreover, being not affected by bleaching and by auto-fluorescence of biological components, it is particularly useful for in vivo studies. Nanostructures were obtained with surfactants-free gold nanoparticles synthesized with a green technique, the Laser Ablation in Solution of bulk gold, and induced to assemble into aggregates of 10 to 20 nanoparticles in order to achieve strong SERRS signals. The nanoaggregates were decorated with peptides, as specific ligands (active targeting agents) of tumor associated receptors, chosen among many targeting ligands because of their relatively low synthetic cost, low toxicity and low immunogenicity profiles: GE11 and RGD peptides, respectively specific for the Epidermal Growth Factor Receptor and $\alpha_v\beta_3$ Integrins which are receptors overexpressed in many cancer cells and tissues, and PreS1 peptide, specific ligand of the Squamous Cell Carcinoma Antigen 1 that is overexpressed in hepatoma and hepatoblastoma. Aiming to investigate on different aspects that can influence the receptor recognition, several peptide analogues were conveniently engineered so that the targeting motif could to be organized with different arrangements on the gold surface. The nanostructures targeting properties were studied both *in vitro* on cancer cells and *in vivo* on murine tumour models achieving very positive results. Among many ligands, those properly engineered by conjugating the peptide to polyethylene glycol (PEG), chosen among many polymers for its numerous useful properties for biomedical applications such as the capability of prolonging the blood circulation time and improve the stability to proteases, showed the best targeting activity. Recent

literature highlights that the peptide hydrophilicity could be a sufficient condition to assure the presentation of the targeting motif above the PEG coating thus guaranteeing a satisfactory receptor binding. By contrast, experimental results combined with Molecular Dynamics (MD) calculations and spectroscopic analysis reported in this Ph.D. thesis demonstrated that other features are necessary for a good association with the receptor. Suitable configurational and conformational properties of the targeting motif GE11 and cRGD and the avoidance of peptides aggregation are requested for an effective receptor recognition (Chapters 3 and 4). Moreover, by optimizing design elements of the GE11 peptide ligand, a targeting activity even better than that of nanosystems functionalized with specific antibodies, was achieved (Chapter 3).

As the PEG was observed to have a huge impact on increasing either the sensitivity or the specificity of the receptor recognition, its role was investigated in dept by combining experimental studies of the targeting activity of nanostructures loaded with mixed amounts of PEG and GE11 peptides with MD simulations. The introduction of PEG chains together with the peptides on the gold surface revealed to promote the organization of an external peptide assembly since the PEG acts anchoring peptide molecules from the solution. The more exposed peptides, owning a flexible conformation that can be more easily adapted to optimize the interactions with receptors on cells with respect to those forming the internal layer, are responsible of the improvement of the nanostructures targeting activity (Chapter 5).

Good stability to proteases is a fundamental feature for the nanostructures' in vivo application since assures their delivery to the target. With the perspective of exploiting GE11 peptide functionalized nanostructures in vivo, their stability to proteolysis was evaluated by incubation with different proteolytic enzymes and in serum. Proteolytic fragments detached from the nanostructures as a consequence of the enzymes action were revealed by HPLC-MS thus allowing the estimation of the proteolytic stability of the peptide ligands. Experimental results clearly pointed out the greater stability of peptides loaded on the gold surface with respect to those free in solution. The nanosystems proved also to preserve the targeting activity after the treatment with proteases, opening wide possibilities for in vivo applications (Chapter 6).

As already observed for other targeting moieties (Chapters 3 and 4), also the best in vitro targeting activity of nanostructures functionalized with the peptide PreS1 was obtained by linking the peptide to a PEG chain. The nanostructures biodistribution was evaluated in mice genetically modified to overexpress the SB3 antigen and in healthy mice as reference. The accumulation in the liver of transgenic mice demonstrated that these nanostructures represent an effective approach for the early stage detection of liver cancer diagnosis, which could improve the quality of life and overall survival of patients.

Not least, overall results highlight the importance of the cooperation of experts in different research fields, in the chemical synthesis of the engineered peptides, and their assembling within nanostructures, the rationalization by model calculations of the nanostructures, and the work of biomedical laboratories for assessing the results. The obtained successful results show that an interdisciplinary approach is very important in the biotechnological research field.

The work presented in this thesis can be considered a step closer to the use of nanomaterials for efficient cancer diagnostic.

Publications

1. Biscaglia, F., Frezza, E., Zurlo, E., Gobbo, M., Linker dependent chirality of solvent induced selfassembled structures of porphyrin–α-helical peptide conjugates. *Org. Biomol. Chem*., **2016**. 14, pp 9568-9577

2. Biscaglia, F., Rajendran, S., Conflitti, P., Benna, C., Sommaggio, R., Litti, L., Mocellin, S., Bocchinfuso, G., Rosato, A., Palleschi, A., Nitti, D., Gobbo, M., Meneghetti, M., Enhanced EGFR targeting activity of plasmonic nanostructure with engineered GE11 peptide. *Advanced Healthcare Materials,* **2017**. 6 (23), pp 1700596-1700604.

3. F.Biscaglia, M.Gobbo, Porphyrin–peptide conjugates in biomedical applications. *Peptide Science*. **2018**. e24038

4. Biscaglia, F., Ripani, G., Rajendran, S., Benna, C., Mocellin, S., Bocchinfuso, G., Meneghetti, M., Palleschi, A., Gobbo, M., Gold Nanoparticle Aggregates Functionalized with Cyclic RGD Peptides for Targeting and Imaging of Colorectal Cancer Cells. *Acs Applied Nano Materials,* **2019**. 2 (10), pp 6436-6444.

5. Biscaglia, F., Quarta, S., Villano, G., Turato, C., Biasiolo, A., Litti, L., Ruzzene, M., Meneghetti, M., Pontisso, P., Gobbo, M., PreS1 peptide-functionalized gold nanostructures with SERRS tags for efficient liver cancer cell targeting. *Materials Science & Engineering C-Materials for Biological Applications.* **2019**, 103, pp 109762-109770

6. Litti, L., Ramundo, A., Biscaglia, F., Toffoli, G., Gobbo, M., Meneghetti, M., A surface enhanced Raman scattering based colloid nanosensor for developing therapeutic drug monitoring. *Journal of Colloid and Interface Science.* **2019**. 533, pp 621-626.

7. Mazzuca, C., Di Napoli, B., Biscaglia, F., Ripani, G., Rajendran, S., Braga, A., Benna, C., Mocellin, S., Gobbo, M., Meneghetti, M., Palleschi, A., Understanding the good and poor cell targeting activity of gold nanostructures functionalized with molecular units for the epidermal growth factor receptor. *Nanoscale Advances.* **2019**. 1 (5), pp 1970-1979.

8. Cimino, R., Grelloni, E., Magna, G., Monti, D., Stefanelli, M., Gatto, E., Placidi, E., Biscaglia, F., Gobbo, M., Venanzi, M., Tuning the morphology of mesoscopic structures of porphyrin macrocycles functionalized by an antimicrobial peptide. *Journal of Porphyrins and Phthalocyanines*. **2020**. 24, PP 920-928.

9. Biscaglia, F., Caligiuri, I., Rizzolio, F., Meneghetti, M., Gobbo, M., Stability to proteolysis of peptide targeted gold nanostructures. *Submitted*.

10. Meneghin, E., Biscaglia, F., Volpato, A., Bolzonello, L., Pedron, D., Frezza, E., Ferrarini, A., Gobbo, M., Collini, E., Biomimetic nanoarchitectures for light-harvesting: self-assembly of pyropheophorbide-peptide conjugates. *Submitted.*.

11. Dugaria, S., Zanetti, E., Biscaglia, F., Agresti, F., Fedele, L., Meneghetti, M., Del Col, D., Experimental study of nanofluids circulating in a volumetric solar receiver. *Submitted.*